Efficient and automated calculation schemes for chemical reaction rates.

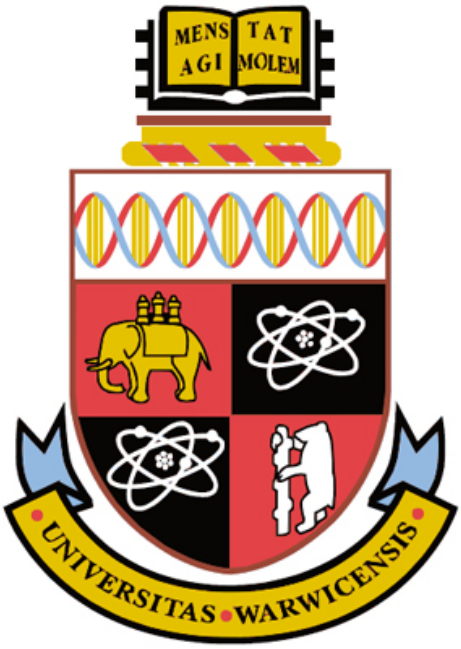

Raphaël Chantreau Majérus

A thesis submitted in partial fulfilment of the requirements for the degree of Doctor of Philosophy in Analytical Science.

University of Warwick

Department of Chemistry

September 2022

Contents

List of Figures

List of Tables

Abbreviations

MEP	Minimum Energy Path
CRN	Chemical Reaction Network
ARD	Automated Reaction Discovery
PES	Potential Energy Surface
TS	Transition State
NEB	Nudged Elastic Band
GSM	Growing String Method
TST	Transition State Theory
RPH	Reaction Path Hamiltonian
TSSCDS	Transition State Search Chemical Dynamics Simulations
AFIR	Artifical Force Induced Reaction
SEGDS	Single Ended Graph Driven Search
DEGDS	Double Ended Graph Driven Search
MD	Molecular Dynamics
VTST	Variational Transition State Theory
CVTST	Canonical Variational Transition State Theory
ICVTST	Improved Canonical Variational Transition State Theory
BFGS	Broyden-Fletcher-Goldfarb-Shanno
TS-BFGS	Transition State Broyden-Fletcher-Goldfarb-Shanno
SR1	Symmetric Rank-1
PSB	Powell-Symmetric-Broyden
CFD	Compact Finite Difference
CFD-SR1	Compact Finite Difference Symmetric Rank-1
CFD-PSB	Compact Finite Difference Powell-Symmetric-Broyden
CFD-Bofill	Compact Finite Difference Bofill
DFT	Density Functional Theory
P-NSM	Projected Navigation String Method
A-NSM	Adiabatic Navigation String Method
IDPP	Image Dependent Pair Potential
RMSD-PP	Root Mean Square Deviation Push Pull
CI-NEB	Climbing Image Nudged Elastic Band
LST	Linear Synchronous Transit
RESD	Restrained Distance
QM/MM	Quantum Mechanic / Molecular Mechanic
cRMSD	Coordinate Root-Mean Square Deviation
IRC	Intrinsic Reaction Coordinate

Acknowledgements

Firstly, I would like to thank Scott Habershon for the continued support, guidance and advice throughout these last four years. I am grateful for having been given the opportunity to be a part of his research group and working on interesting and novel ideas. Over the years, he has pushed me to become more independent as a scientist while still being available along the way for any questions or problems encountered. I truly believe that, under his guidance, I have both grown as a scientist and person.

I would also like to extend my thanks to the Habershon Group, in particular Christopher Robertson who was crucial in my development as a PhD student for the first years. I am extremely grateful for his guidance and help, especially during the early stages of the reaction path Hamiltonian code implementation, where many hours were sunk.

I would like to thank the University of Warwick and the Centre for Scientific Computing for the resources and infrastructure that I was able to use during my research. I would also like to thank the Molecular Analytical Centre for Doctoral Training and the Engineering and Physical Sciences Research Council for funding my project and allowing me to carry out my research.

To Mum, Dad, Zoe, Maxime and Alexis, thank you for your constant support and encouragements along the way, all of which was much appreciated.

To Theo, Tom, Mark, Sam, Warren, thank you for the late night gaming sessions over the years which were always enjoyable and fun even when we were 0-3 in clash...

To Veronica and Ruben, thank you for the very early gym sessions which were filled with laughter.

To Abbie, thank you for encouraging me and helping me all throughout my PhD, even with the little things. Watching how hard you worked as well always grounding me in reality, immensely helped with the completion of the PhD.

Declaration

This thesis is submitted to the University of Warwick in support of my application for the degree of Doctor of Philosophy. It has been composed by myself and has not been submitted in any previous application for any degree. The work presented (including data generated and data analysis) was carried out entirely by myself.

Parts of this thesis have been published by the author:

1. R. Chantreau Majerus, C. Robertson, and S. Habershon, *Assessing and rationalizing the performance of Hessian update schemes for reaction path Hamiltonian rate calculations*, The Journal of Chemical Physics 155, 204112 (2021).

2. I. Ismail, R. Chantreau Majerus, and S. Habershon, *Graph-driven reaction discovery: Progress, challenges, and future opportunities*, The Journal of Physical Chemistry, (2022), *In Press*

Abstract

With the development of automated reaction discovery (ARD) methods as a tool to generate and describe chemical reaction networks, the need for rapid and accurate screening of either undesirable or unfeasible chemical reactions has become essential. Two common ways to screen through chemical reactions include using reaction rates, typically determined using transition state theory (TST), and characteristics of the minimum energy path such as energy barriers. Whilst TST is a popular method for determining reaction rates, the no recrossing assumption can lead to important differences in the dynamically correct reaction rate. As an alternative, the reaction path Hamiltonian (RPH) coupled to reactive flux dynamics has been shown to be able to account for recrossing occurring in the reaction, resulting in the dynamically correct reaction rate. However, the determination of the dynamically correct reaction using the RPH comes at a significant computational cost which makes this method unfeasible in the context of ARD. As such, in this work, a novel way to reduce the computational cost associated with constructing the RPH by implementing update Hessian schemes is used. The advantage of using update Hessian schemes to construct the RPH lies within the significant reduction Hessian evaluations, which are essential to the RPH. Results for this implementation were very positive, where a significant improvement on the computational cost was demonstrated, while keeping a similar level of accuracy depending on which update Hessian scheme was used. In addition to this work, the RPH is used to investigate dynamical effects in the Heck–Breslow mechanism for alkene hydroformylation with a cobalt catalyst, both in gas-phase and in solvent-phase. Moreover, the RPH reaction rates were compared to the TST reaction rates in the determination of the rate law to assess the importance of accounting for recrossing effects. Our results showed evidence of recrossing in the catalytic cycle, however, the kinetic simulations and the rate law showed little to no difference between TST and RPH reaction rates. Finally, as a way of improving on initial paths for nudged elastic band to determine minimum energy paths, we present two novel methods which use a navigation function as a driving force to determine a reaction path. The two novel methods are compared to other popular methods with the same goal and their performance is assessed in the context of computational cost required and overall accuracy.

Chapter 1

Introduction

> Impossible? We did a lot of impossible things on this journey. I'm tired of hearing that things are impossible or useless. Those words mean nothing to us.
>
> *JoJo's Bizarre Adventure Stardust Crusaders*, Hirohiko Araki

Summary

This Chapter provides an overview of the field in which the work presented here is set. The importance of the minimum energy path (MEP) as the lowest energy reaction path from which essential dynamic and mechanistic properties can be derived is discussed. Furthermore, an overview of the current work being done related to chemical reaction networks (CRN), specifically using automated reaction discovery (ARD) methods and the issues linked to screening the reaction network during ARD, is also discussed. Finally, we outline the aims and objectives for this work and provide a short overview detailing the contents and layout of the chapters to follow.

1.1 Introduction

Understanding the dynamics at play in chemical reactions has always been a key issue to solve in chemistry. It was only during the second half of the 20th century, where a "boom" in the atomic scale viewpoint of chemistry was witnessed,[1] as experimental methods to investigate chemical dynamics such as molecular spectroscopy,[2] the laser[3,4] and molecular beams[5,6] established themselves. The development of these experimental tools resulted in a growth in chemical dynamics insight, however, it was the advent of high-power computing[7] which propelled the field of chemical dynamics to a new level. This was mainly due to the issue for experimental methods to obtain detailed mechanistic and dynamic descriptions of more complex chemical reactions. For example, being limited to detecting and describing reactants, products and stable intermediates, and failing to account for any other species with short lifetimes. As such, combined with theoretical methods, a much clearer picture of reaction dynamics could be obtained.

Central to the improvements in theoretical understanding of chemical dynamics was the Born-Oppenheimer approximation, whereby, in the full electrons-plus-nuclei Hamiltonian operator $\hat{H}$ shown in Equation 1.1, the time-scales with which the electrons and nuclei move (vibrate and rotate) are usually quite different.[8]

$$\begin{aligned}\hat{H} = \sum_i \left\{ -\frac{\hbar^2}{2\mathrm{m}_e}\frac{\partial^2}{\partial \mathbf{q}_i^2} + \frac{1}{2}\sum_j \frac{e^2}{r_{i,j}} - \sum_a \frac{\mathrm{Z}_a e^2}{r_{i,a}} \right\} \\ + \sum_a \left\{ -\frac{\hbar^2}{2\mathrm{m}_a}\frac{\partial^2}{\partial \mathbf{q}_a^2} - \frac{1}{2}\sum_b \frac{\mathrm{Z}_a \mathrm{Z}_b e^2}{r_{a,b}} \right\},\end{aligned} \tag{1.1}$$

where m_e denotes the mass of an electron, q_i denotes the coordinates of the electrons, Z_a denotes the charges nuclei and m_a denotes the nuclear mass.

As such, the heavy nuclei move more slowly than the lighter electrons, with even the nucleus in a hydrogen atom nearly 2000 times more heavy than what an electron weighs, and so the electrons are able to essentially adjust their motion to the slowly moving nuclei. With this approximation, the Schrodinger equation can be solved for the movement of the electrons in the presence of fixed nuclei for a few physical systems (e.g the free particle, the particle in the box, certain kinds of rotating bodies, the harmonic oscillator) resulting in a representation of the fully adjusted state of the electrons at any fixed positions of the nuclei.

The electronic Hamiltonian which relates to the allowed states of the electrons in the presence of fixed nuclei, Equation 1.2, results in energies $\mathrm{E}_K(\mathrm{q}_a)$ as eigenvalues that depend on where the nuclei are located, $\{\mathrm{q}_a\}$, Equation 1.3. These energies are what is known as the potential energy surface (PES).

$$\hat{H} = \sum_i \left\{ -\frac{\hbar^2}{2\mathrm{m}_e}\frac{\partial^2}{\partial \mathbf{q}_i^2} + \frac{1}{2}\sum_j \frac{e^2}{r_{i,j}} - \sum_a \frac{\mathrm{Z}_a e^2}{r_{i,a}} \right\}, \tag{1.2}$$

$$\hat{H}\psi_K(\mathbf{q}_j|\mathbf{q}_a) = E_K(\mathbf{q}_a)\psi_K(\mathbf{q}_j|\mathbf{q}_a). \tag{1.3}$$

Understanding the PES, which is a direct result of the Born-Oppenheimer approximation, is key in order to investigate chemical dynamics as it describes changes in the potential energy of a chemical species during the course of the chemical reaction. On the PES lie minima, points where the first derivatives of the energy with respect to the coordinates is zero and the surface has a positive curvature, which represent geometries of stable molecular structures. As well as minima, the PES will contain multiple configurations and intermediate species, referred to as saddle-points (where the first derivatives of the energy with respect to the coordinates is zero in all but one direction, resulting in negative curvature) which connect the minima. These features, which lie on the PES, are shown in the 2D Müller-Brown PES in Figure 1.1. The Müller-Brown PES is defined in Equation 1.4;

$$V(x,y) = \sum_{i=1}^{4} A_i e^{a_i(x-x_i^0)^2 + b_i(x-x_i^0)(y-y_i^0) + c_i(y-y_i^0)^2}, \tag{1.4}$$

where,

$$\mathbf{A} = [-200.0, -100.0, -170.0, 15.0] \quad \mathbf{a} = [-1.0, -1.0, -6.5, 0.7]$$
$$\mathbf{b} = [0.0, 0.0, 11.0, 0.6] \quad \mathbf{c} = [-10.0, -10.0, -6.5, 0.7]$$
$$\mathbf{x^0} = [1.0, 0.0, -0.5, -1.0] \quad \mathbf{y^0} = [0.0, 0.5, 1.5, 1.0].$$

Whichever reaction path connecting the minima through a saddle-point is the lowest in energy, the reaction path then corresponds to a minimum energy path (MEP), where the saddle-point is known as the transition state (TS) for the given reaction.

In this context, the TS corresponds to the highest energy point along the MEP located between the reactant and product minima, and as such is crucial in chemical dynamics. It can be noted that extensive knowledge of the MEP (shape around the reactant and product minima as well as the shape around the TS stationary point) and at times the full PES is also required to investigate chemical dynamics. However, despite its importance, calculating and characterising the MEP for a given chemical reaction represents a significant challenge in the field of theoretical chemistry. Therefore, calculating an accurate MEP is essential if one wants to derive accurate chemical reaction dynamics, such as reaction rates, which reflect

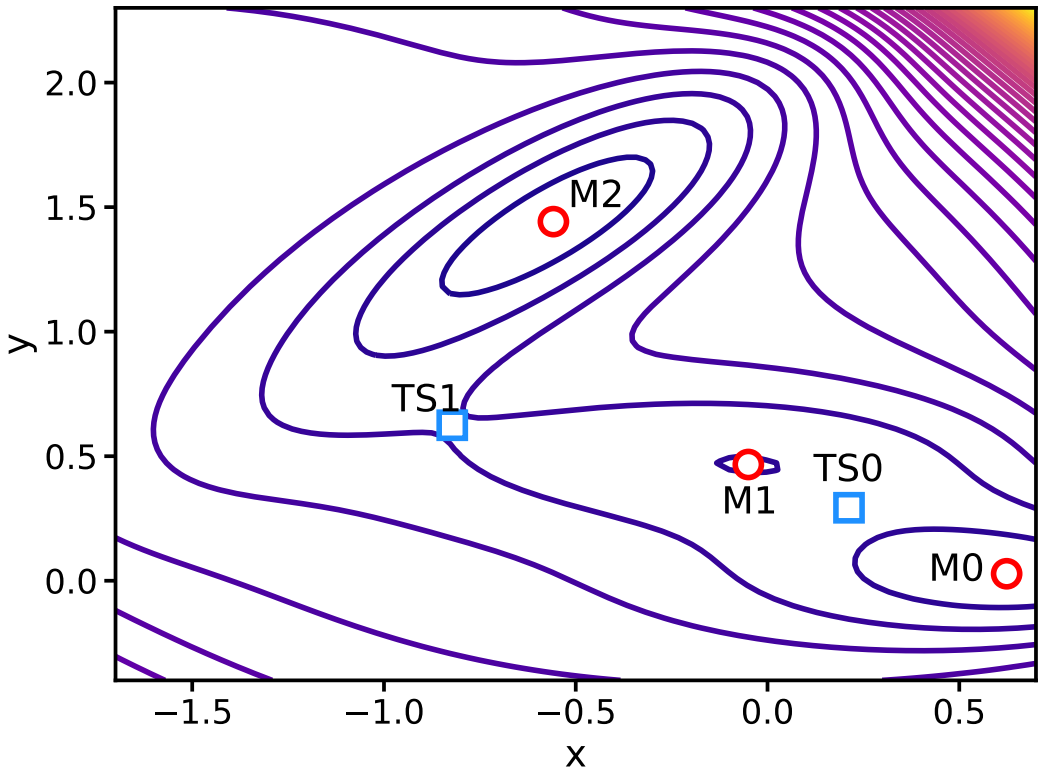

Figure 1.1: Müller-Brown PES featuring the three minima labelled M0, M1, M2 and the two transition states labelled TS0 and TS1. Parameters taken from Mehta *et al.*[9]

reality. As such, computational methods, such as nudged elastic band (NEB), growing string method(GSM) and their derivatives, have emerged in order to determine the MEP for a given reaction. With the MEP determined, and the energy barrier being known, reaction rates can be calculated using methods such as transition state theory (TST) or its different variations and the reaction path Hamiltonian (RPH), all of which will be expanded upon in the next chapter.

In the recent decades, the drive to generate and describe chemical reaction networks (CRN) capable of characterizing the full set of reactions and chemical species in a reactive system in order to predict and explore how complex chemical systems evolve has motivated the development of methods capable of doing so.[10–21] One of these methods developed to generate and characterise CRNs has been using automated reaction discovery (ARD).[16,18,19,21–38] ARD methods can typically be split into two branches, the first branch consisting of replacing the molecular structural detail with string-based representations of molecular species[20,38–43] and reactions and the second branch, which has seen rapid growth, consisting of using molecular structural models, in combination with *ab initio* quantum chemistry to generate and characterise CRNs.

Within the second branch, a distinction can be made between methods where (i) molecular dynamics or related sampling methods are used to generate new molecu-

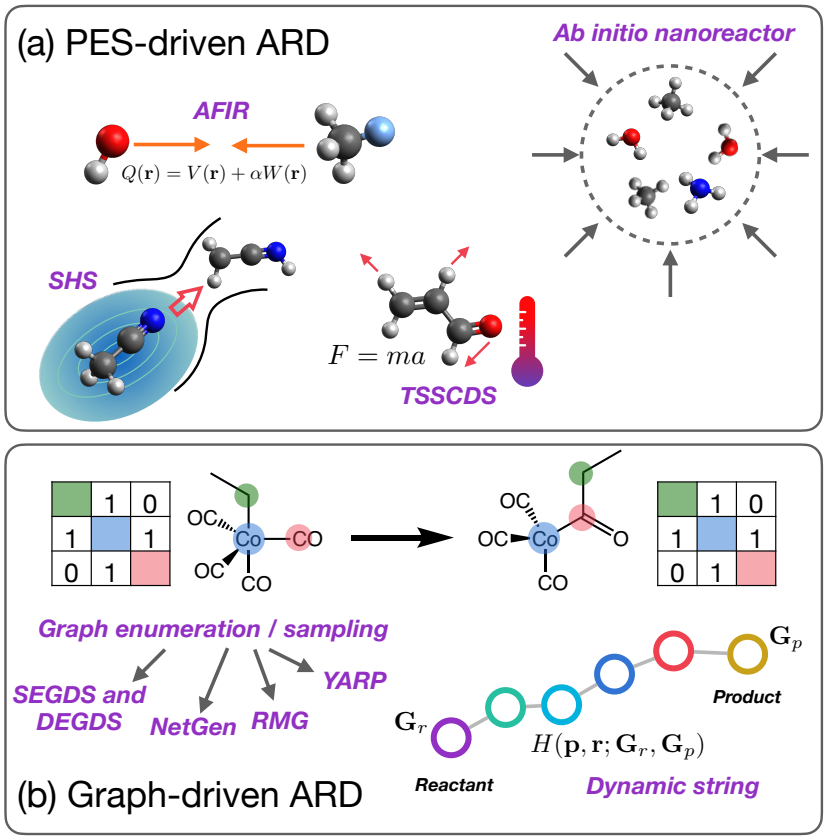

Figure 1.2: Overview of (a) PES-driven ARD schemes (e.g. AFIR, *ab initio* nanoreactor, SHS and TSSCDS), and (b) graph-driven ARD schemes (e.g. single-ended and double-ended graph-driven sampling (SEGDS, DEGDS respectively), NetGen, RMG, YARP)

lar species, and those that use (ii) discretised molecular representations, in the form of adjacency matrices or bond-order matrices, also referred to as graphs, shown in Figure 1.2. For methods using molecular dynamics or related sampling methods, multiple approaches have been developed including the ab initio nanoreactor approach,[27,44] the transition-state search using chemical dynamics simulations (TSSCDS)[30–33,45] and the artificial force induced reaction (AFIR) method.[36] For methods using concepts of molecular graphs, such as single/double ended graph driven search (SEGDS, DEGDS) and dynamic string among others, graphs such as bonding matrices allow for a simple description of the chemical bonding in a collection of molecules identifying which atoms are bonded to which.[24,46–50] With this description, the chemical reactions can be viewed via the changes in the bonding matrix which show new bond arrangements and new chemical species, and CRNs can be generated through the sequence of the bonding matrix changes.

One can imagine that in complex chemical reactions, the sequence of the bonding matrix changes can rapidly become very large and not an accurate representation of the chemistry occurring in the reaction. One possible way to deal with this issue and reduce the growth of the CRN, thus limiting exploration to the region of chem-

ical interest, is to use thermodynamic (i.e enthalpy changes) and kinetic parameters (i.e rate constants) to essentially filter out unfeasible or unrealistic bonding matrix changes.[51–53] In addition, machine learning methods have been used as a way for the rapid determination of thermodynamic properties, such as activation energies, however accuracy and more importantly transferability of the machine learnt model remain a challenge, as models trained on specific CRNs will have to be re-trained depending on the type of CRNs investigated.[54–65] Another way to deal with the problem is to generate targeted product species given a set of reactants using allowed connectivity changes defined by the user and then use automated ab initio schemes to determine and characterise the MEP and TS.[28,29] This results in a complete and detailed picture of the CRN within the region of chemical space by the allowed connectivity changes. Lastly, sorting through reaction products based on graph driven changes to connectivity by using semi-empirical methods is another way to simplify the final CRN.[59] These methods all showcase the need of an intuitive chemistry based way of screening connectivity changes in the bonding matrix, but more importantly they highlight the need for accurate and fast ways to do such screening.

1.2 Aims and objectives

The requirement for determining the MEP during typical CRN construction represents an essential piece of the puzzle in order to derive an understanding of chemical reactions, in particular the dynamic and mechanistic properties. With ARD methods becoming more prevalent where screening techniques using some intuitive chemistry based way are common, the limitations linked to determining the MEP become significant. Typical chemically intuitive screening methods include but are not limited to characteristics of the MEP such as barrier heights, or kinetic information derived by the MEP.

Current methods used to determine the MEP for reactions are associated with high computational costs, in the form of a large number of force evaluations required to determine a reaction path even close to the MEP, as is the case for GSM and NEB methods. This requirement, does not scale well with larger and more complex systems but also with the level of theory used for the calculation. In addition to MEP finding methods, determining reaction rates from the MEP using transition state theory (TST) also has limitations in the assumptions used in the method but also linked to the MEP. The primary limitation in terms of the assumptions lies within the no-recrossing assumption which results in an ill-defined description of the reaction rate which could lead to screening problems in the context of ARD.

This is why there is still a drive to address the limitations associated with MEP

and reaction rate determination and to explore new methods for reaction path finding and reaction rate determination but also possibly improving on current methods. These will be explored and discussed in this work, where the aims and objective are outlined below:

1. Implement the RPH into a functional code where transmission coefficients and reaction rates can be determined.

2. Integrate several different update Hessian schemes into the RPH framework in order to reduce the computational cost while keeping the accuracy of the calculation.

3. Explore dynamical effects in organometallic catalysis using the RPH approach.

4. Develop novel methods to generate reaction paths which can be used as good initial guesses for subsequent MEP refinement.

5. Compare and contrast the resulting reaction paths generated by the novel methods developed to current initial reaction path finding methods.

6. Compare and contrast the TS optimisation capabilities using the resulting reaction paths generated by the novel methods developed to current initial reaction path finding methods.

We also note that accuracy of the electronic structure method has not been discussed as we are exploring and using methods to either determine reaction rates or reaction paths with the assumption that the underlying PES is sufficiently accurate with the most appropriate level of theory.

Chapter 2

Theory

"You're going to be all right. You just stumbled over a stone in the road. It means nothing. Your goal lies far beyond this. Doesn't it? I'm sure you'll overcome this. You'll walk again... soon."

Berserk, Kentaro Muira

Summary

This Chapter will be split into two sections. The first section will discuss the conventional ways to determine chemical reaction rates using Transition State Theory (TST) or other variations, molecular dynamics (MD) and reactive flux. The second section will introduce and discuss the Reaction Path Hamiltonian (RPH) and its role in determining chemical reaction rates.

2.1 Transition state theory

TST has been around for nearly a century, since its initial publication almost simultaneously by Eyring, Evans and Polanyi in 1935,[66–69] and has achieved a wide spread acceptance as the go to method to determine chemical reaction rates. Moreover, the method itself has seen numerous improvements and extensions over the years showing how relevant the underlying theory is to this day. The simplicity of the resulting rate equation calculated via TST remains essential in providing a framework for even complicated reactions to be understood.

The TST Rate Equation can be derived in a number of different ways, but we present here the two most common derivations: the first derivation is that of Wynne-Jones and Eyring,[70] and the second derivation is that of Eyring and Evans and Polanyi.[66,69] Both of these derivations view the motion across the barrier differently; be it vibrational or translational motion, however, they are essentially the same derivation. The first derivation views the crossing of the dividing surface as a very loose vibration, whereas the second derivation views this passage as a free translation. Again, these two views are basically the same, because if a vibrating particle has a restoring force that is reaching zero then it can be treated as a translation.

2.1.1 Derivation of the TST rate equation

In the Wynne-Jones and Eyring derivation, the equilibrium between the initial and activated states is considered, and the motion through the dividing surface is described as a very loose vibration.[68] The equilibrium between two reactants, A and B, and the activated complex, $X^{\ddagger}$, is given by Equation 2.1:

$$\frac{[X^{\ddagger}]}{[A][B]} = K_c^{\ddagger}, \tag{2.1}$$

where $K_c^{\ddagger}$ is the concentration equilibrium constant. The equilibrium constant can also be described using Equation 2.2, by relating the dimensionless equilibrium constant to the molar partition function and the Gibbs free energy, assuming ideal gas conditions,

$$K_c^{\ddagger} = \frac{q^{\ddagger}}{q_A q_B} e^{-E_0/RT}, \tag{2.2}$$

where E_0 is the activation energy at absolute zero (Figure 2.1), and so

$$\frac{[X^{\ddagger}]}{[A][B]} = \frac{q^{\ddagger}}{q_A q_B} e^{-E_0/RT}. \tag{2.3}$$

If we assume that both molecules A and B have N_A and N_B atoms, then the activated complex, $X^{\ddagger}$, has N_A+N_B atoms. The activated complex then has, as well as 3 degrees of rotational freedom, $3(N_A + N_B) - 6$ degrees of vibrational freedom, if it is nonlinear, or $3(N_A + N_B) - 5$ degrees of vibrational freedom, if it is linear. Of the vibrational degrees of freedom, one of them corresponds to a loose vibration which results in no restoring force allowing the complex to freely form products. And so, for this vibrational degree of freedom, ν, instead of using the ordinary partition function $(1 - e^{h\upsilon/k_bT})^{-1}$, the value of this function calculated at the limit where ν approaches zero can be used (under the condition that $\nu << T$ according to the kinetic theory of gases), as shown in Equation 2.4 below;

$$\lim_{\nu\to 0} \frac{1}{1 - e^{h\upsilon/k_bT}} = \frac{1}{1 - (1 - h\upsilon/k_bT)} = \frac{kT}{h\nu}. \tag{2.4}$$

This expression can then be included in $q^{\ddagger}$ as

$$q^{\ddagger} = q_{\ddagger}\frac{k_bT}{h\nu}, \tag{2.5}$$

where $q_{\ddagger}$ is the product of factors. Note that this happens at low temperature for loose vibrations. Substituting Equation 2.5 into Equation 2.3 results in

$$\frac{[X^{\ddagger}]}{[A][B]} = \frac{q_{\ddagger}(k_bT/h\nu)}{q_Aq_B}e^{-E_0/RT}, \tag{2.6}$$

and can be rearranged into the following equation

$$\nu[X^{\ddagger}] = [A][B]\frac{k_bT}{h}\frac{q_{\ddagger}}{q_Aq_B}e^{-E_0/RT}, \tag{2.7}$$

where ν is the frequency of vibration of the activated complexes which corresponds to the product forming.The rate of reaction υ is then given as

$$\upsilon = [A][B]\frac{k_bT}{h}\frac{q_{\ddagger}}{q_Aq_B}e^{-E_0/RT}, \tag{2.8}$$

and finally, the rate constant, which is defined by $\upsilon \equiv k[A][B]$, is given by

$$k = \frac{k_bT}{h}\frac{q_{\ddagger}}{q_Aq_B}e^{-E_0/RT}. \tag{2.9}$$

To reiterate, the above derivation expressed the motion across the dividing surface as vibrational motion, assuming ideal gases and weak coupling. The following derivation is the original derivation by Eyring, Evans and Polanyi which views the motion across the dividing surface as a translational motion.[68]

If we imagine that all activated complexes lie on top of the potential energy barrier, within the arbitrary length δ, and that the translational partition function corresponding to the motion of a particle of mass, $m_{\ddagger}$, in a one-dimensional box of length δ is given as

$$q_t = \frac{(2\pi m_{\ddagger} k_b T)^{1/2}}{h}\delta, \tag{2.10}$$

The partition function, $q^{\ddagger}$, for the activated complexes is then given as

$$q^{\ddagger} = \frac{(2\pi m_{\ddagger} k_b T)^{1/2}\delta}{h} q_{\ddagger}, \tag{2.11}$$

where $q_{\ddagger}$ is the partition function for all the motions except for the one which crosses the dividing barrier, which is a point typically chosen to be where the TS lies on the MEP for a given reaction. Substituting this partition function into Equation 2.3 results in the following expression

$$[X^{\ddagger}] = [A][B]\frac{(2\pi m_{\ddagger} k_b T)^{1/2}}{h}\delta\frac{q_{\ddagger}}{q_A q_B}e^{-E_0/RT}. \tag{2.12}$$

Kinetic theory states that the average speed of particles moving across the barrier from left to right can be expressed as:

$$\dot{\mathrm{x}} = \left(\frac{k_b T}{2\pi m_{\ddagger}}\right)^{1/2}. \tag{2.13}$$

And so, the frequency at which the activated complexes cross the barrier corresponds to the speed divided by the, length δ:

$$\nu = \left(\frac{k_b T}{2\pi m_{\ddagger}}\right)^{1/2}\frac{1}{\delta}. \tag{2.14}$$

Finally, multiplying Equation 2.12 by the frequency results in the rate constant:

$$[X^{\ddagger}] = [A][B]\frac{(2\pi m_{\ddagger} k_b T)^{1/2}}{h}\delta\left(\frac{k_b T}{2\pi m_{\ddagger}}\right)^{1/2}\frac{1}{\delta}\frac{q_{\ddagger}}{q_A q_B}e^{-E_0/RT}, \tag{2.15}$$

$$\mathrm{k} = [A][B]\frac{k_b T}{h}\frac{q_{\ddagger}}{q_A q_B}e^{-E_0/RT}. \tag{2.16}$$

It is important to note that the length, δ, cancels out and so its magnitude is irrelevant.

2.1.2 Assumptions and limitations of TST

Fundamentally, TST is based upon a series of assumptions,[71] which are the following:

1. Molecular systems that have crossed the dividing barrier, typically the transition state, can no longer recross this dividing surface to form the reactant molecules again.

2. The energy distribution among the reactant molecules can be described with the Maxwell-Boltzmann distribution. Moreover, it is assumed that even when the whole system is not at equilibrium, the concentration of the activated complexes that are becoming products can also be calculated using equilibrium theory.

3. The motion of the system over the dividing surface can be separated from other motions associated with the activated complex.

4. The chemical reaction can be described in terms of classical motion over the barrier and quantum effects can be ignored.

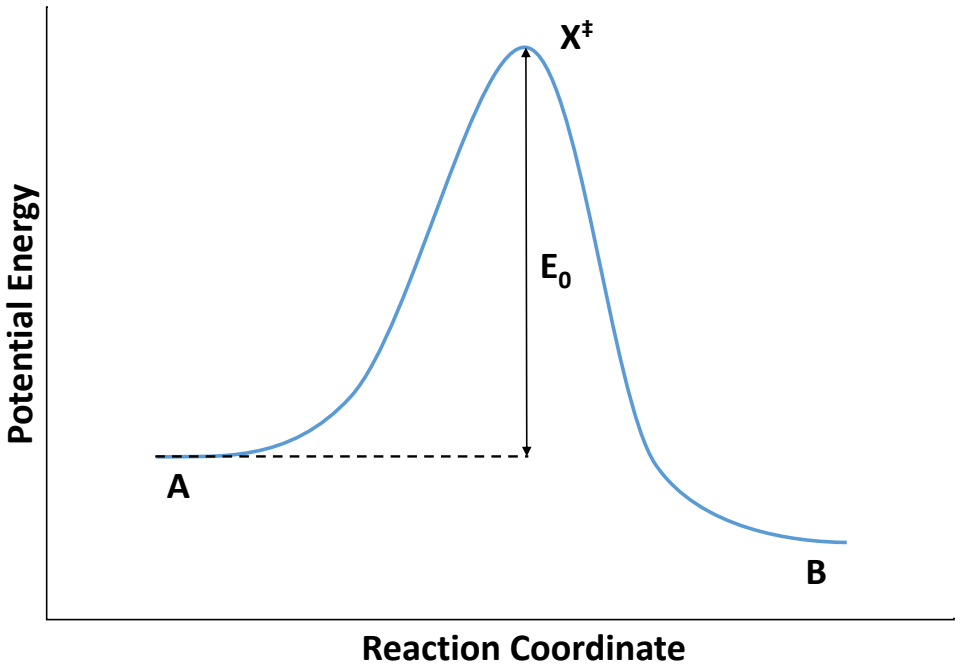

Figure 2.1: Potential energy diagram with the reactant (A), the product (B), the transition state ($X^{\ddagger}$) and the activation energy (E_0) labelled, all of which are necessary for reaction determination using TST.

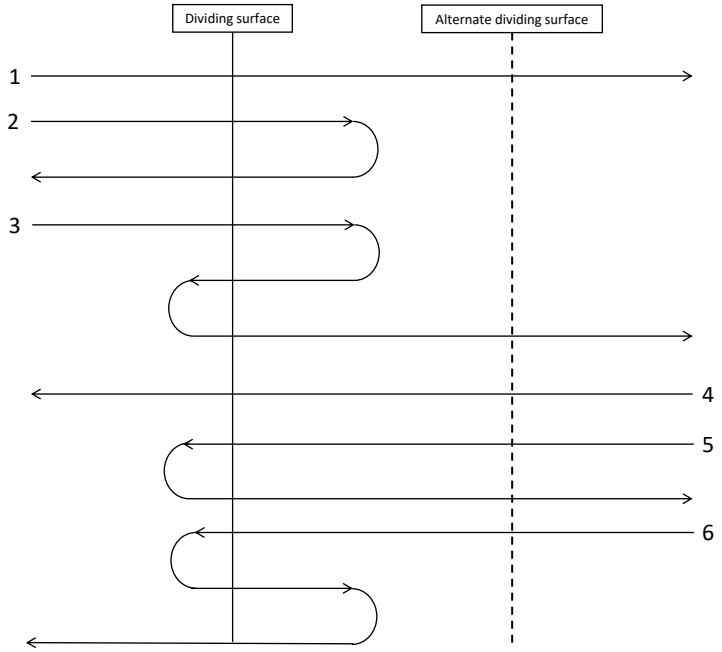

Figure 2.2: Six schematic trajectories of molecules crossing the two different dividing surfaces at the saddle point on a PES. The left hand side corresponds to the reactants and the right hand side corresponds to the products.

In this section, we will explore these assumptions in more details and see how some of these assumptions may act as limitations.

No-recrossing

The first two assumptions are perhaps the most essential to TST. These are: that there can be no multiple crossings of the dividing surface by any one trajectory and that the concentrations of activated complexes may be calculated using the equilibrium theory. To understand how these assumptions can lead to limitations, we consider an argument,[72] shown in Figure 2.2. Figure 2.2 shows six different trajectories which cross the dividing surface on a PES. The first three trajectories originate from the reactant valley, while the last three trajectories originate from the product valley. Trajectories one and four correspond to a simple linear trajectory which crosses the dividing surface and does not recross. Trajectory two starts in the reactant valley and crosses the dividing surface but bounces back towards the reactant valley having recrossed the dividing surface. Trajectory five is essentially the same as trajectory two except it originates from the product valley and finishes in the product valley. Lastly, trajectory three and six originate in the reactant valley and product valley respectively and end in the other valley, however they cross the dividing surface three times. TST assumes that any trajectory crossing the dividing surface is essentially a trajectory which looks like trajectory one or four.

However, we can see that for most of the trajectories in Figure 2.2 there are multiple crossings and thus as a result of these re-crossings, reaction rates derived from TST are typically higher than they should be.

To overcome this, the position of the dividing barrier can be changed in order to better identify trajectories which end in either of the minima. Figure 2.2 also shows an alternate dividing surface which is placed further away than the original dividing surface. This alternate dividing surface reduces the error due to multiple crossings of the dividing barrier as the trajectory doing the crossing would be closer to ending. This method of varying the position of the dividing surface is the basis of Variational Transition State Theory and will be expanded upon in Section 2.2.

There are multiple reasons as to why a trajectory may not finish in the product valley when it has originated from the reactant valley. One possible reason is that there might be a basin at the junction of the two valleys, and a system that enters it might get stuck until it finds a way to leave the basin. Once it leaves it, it is highly likely that the system would return to the reactant valley and so not form a product. Another possible reason arises if the shape of the PES resembles that of a wall resulting in the activated complexes to bounce back into the reactant valley. Furthermore, if solvent effects are included in TST calculations, a system will inevitably interact with the solvent, where energy is exchanged between the system and the solvent. As a result, depending on when this energy exchange occurs during the trajectory, the trajectory could recross and never make it back into the product valley.[73]

Separability of motion

The third assumption of TST is the separability of the motion of the system, as it crosses the dividing surface on the PES, from all the other motions. This assumption is critical for both of the derivations shown in Section 2.1.1, as one particular vibrational factor contributing to the partition function for the activated complex is of a different character from the rest of them. In the first derivation, this particular vibration is treated as a very loose vibration, whereas it is treated as a translation in the second derivation.[68]

Quantum effects

The final assumption of TST is that the motion over the dividing surface on the potential energy surface can be described as classical motion and any quantum effects present can be ignored. As mentioned in 2.1.2, quantisation of the motion leads to some errors with the separability of motion, however it also allows for the possibility that the system may tunnel through the PES.[74–76,76–78] When tunnelling occurs, the

system does not have enough energy to go over the energy barrier and so it moves part way up the entrance channel and tunnels through the energy barrier into the exit channel. As a result, the effective activation energy is reduced compared to if the system had gone over the energy barrier and the reaction rate is thus faster.

2.2 Variational transition state theory

Variational transition state theory (VTST) is a modification to the conventional TST, first presented in a general context but subsequently developed by Truhlar and co-workers[79–82] in an effort to account for recrossing effects. The underlying theory behind VTST is that instead of using the saddle point of the PES as the dividing surface, the dividing surface can be varied at different positions along the reaction path in order to try and reduce recrossing of the dividing surface. The dividing surface which results in the lowest rate is then reported as it would correspond to a dividing surface where recrossing has been minimised.

VTST can be expressed in three ways:

1. Microcanonical variational (NVE ensemble) transition state theory (μVTST). This is when the microcanonical rate constant is calculated for various dividing surfaces and the smallest rate constant is subsequently inserted into in the canonical rate constant equation in order to determine the thermal rate constant.

2. Canonical variational (NVT ensemble) transition state theory (CVTST). This is when the canonical rate constant is calculated using the canonical rate constant for various dividing surfaces and using the minimum value of canonical rate constant as the best estimate.

3. Improved canonical variational (NVE ensemble) transition state theory (ICVTST). This is a modification to CVTST where the position of the dividing surface corresponds to the microcanonical variational transition state when energies are below the threshold energy. As a result, microcanonical rate constant values are equal to zero below the threshold energy and a compromise dividing surface is then chosen in order to minimise the contributions to the rate constant made by reactants having higher energies.

VTST has been shown to determine better reaction rates than conventional TST, especially at higher temperatures where recrossing effects are more important. When TST methods, such as conventional TST, μVTST, CVTST and ICVTST, are used and compared to exact classical dynamical simulations in reactions where recrossing effects are present,[68] greater errors are found when conventional TST

is used compared to any of the VTST methods. Moreover, in the example of a hydrogen atom transfer between heavy atoms at high temperature, such as C_4H_9 + H−C_4H_9 ⟶ C_4H_9−H + C_4H_9, TST overestimates the rate by a factor of 11.4 whereas mVTST, CVTST and ICVTST only overestimate the rate by a factor of 1.7, 2.0 and 1.9 respectively.[68] However we do note that classical dynamical simulations do not take into account tunnelling effects similarly to these TST methods.

2.3 Reactive flux method

The reaction rate can be expressed as the microscopic reaction rate which can account for recrossing effects in a better way than previously discussed. In order to do so, the reaction coordinate, $\xi(\mathbf{r}^N)$, is defined as a function of the coordinates of the reacting system which is positive for products and negative for reactants. Furthermore, the dividing plane, where $\xi = 0$, is defined as the transition state between the products and reactants. If we consider a system with a low solute concentration, where the reacting molecules are not interacting, then each molecule behaves identically and so we can focus on a single molecule. The probability, $\langle p \rangle$, for a single molecule to be in the product state is then determined by summing over all the trajectories where the product state is reached,

$$\langle p \rangle = \int \theta[\xi(\Gamma^N)] e^{[-\beta H \xi(\Gamma^N)]} d\Gamma^N = \langle \theta(\xi) \rangle \,, \tag{2.17}$$

where H is the Hamiltonian of the system and θ is the Heaviside step function,

$$\theta(\xi) = \begin{cases} 0 & \text{if } \xi < 0 \\ 1 & \text{if } \xi > 0 \end{cases}.$$

In order to get the expectation value of the fraction of reactants, a similar equation as Equation 2.17 is used but with replacing ξ for $-\xi$. The expectation value of the number of product molecules, and its time derivative, will hardly depend on the chosen reaction coordinate, since the Boltzmann factor is very small near the top of the energy barrier. The deviation from equilibrium for any realisation is then shown in Equation 2.18,

$$\Delta p = \Delta\theta\big[\xi(\Gamma^N)\big] = \theta\big[\xi(\Gamma^N)\big] - \langle \theta(\xi) \rangle \,, \tag{2.18}$$

where Γ^N is defined as a point on the reaction coordinate with coordinates and momenta, $\Gamma^N = (r_1, \ldots, r_N, p_1, \ldots, p_N)$. By inserting Equation 2.18 into Onsager's

regression hypothesis,[83] Equation 2.19, and using the macroscopic law, Equation 2.20, we get Equation 2.21,

$$\langle \Delta f(t) \Delta f(0) \rangle = \langle \Delta f^2(0) \rangle \, \phi(t), \tag{2.19}$$

where t is time, f is the microscopic analogue of a macroscopic property F and ϕ is the macroscopic response function.

$$\Delta p(t) = \Delta P(0) e^{\lambda t}, \tag{2.20}$$

where λ is the rate constant.

$$\frac{\langle \Delta\theta\big[\xi(t)\big] \Delta\theta\big[\xi(0)\big] \rangle}{\langle \Delta\theta^2\big[\xi(0)\big] \rangle} = e^{-\lambda t}. \tag{2.21}$$

Differentiating Equation 2.21 with respect to time, t, gives,

$$\frac{\langle \dot{\theta}\big[\xi(t)\big] \Delta\theta\big[\xi(0)\big] \rangle}{\langle \Delta\theta^2\big[\xi(0)\big] \rangle} = -\lambda e^{-\lambda t}. \tag{2.22}$$

If this expression is evaluated at a time t in the interval of $\tau_v < t < \frac{1}{\lambda}$, where Onsager's regression hypothesis does not hold on the short time scale of molecular vibrations, τ_v, and where at time $\frac{1}{\lambda}$ the numerator of Equation 2.22 will be unity, then,

$$\lambda = \frac{\langle \theta\big[\xi(t)\big] \dot{\xi}(0) \delta\big[\xi(0)\big] \rangle}{\langle \Delta\theta^2\big[\xi(0)\big] \rangle}, \tag{2.23}$$

where $\dot{\xi}(0)$ is the derivative with respect to time of the reaction coordinate at the dividing surface and the Dirac delta function, $\delta\big[\xi(0)\big]$ is due to the derivative of the Heaviside function where,

$$\delta(\xi) = 0 \text{ if } \xi \neq 0, \tag{2.24}$$

and

$$\int_a^b \delta(\xi) d\xi = 1 \text{ if } a < 0 < b. \tag{2.25}$$

From Equation 2.17, one infers that,

$$\langle \Delta\theta^2 \rangle = \langle \theta^2 \rangle - \langle \theta \rangle^2 = \langle r \rangle \langle p \rangle , \tag{2.26}$$

using $\langle \Delta\theta^2 \rangle = \langle \Delta\theta \rangle$ and $\langle r \rangle + \langle p \rangle = 1$. Finally, combining Equation 2.23, 2.26 and the forward rate constant, k_f, related to the overall relaxation rate defined as,

$$\mathrm{k}_f = \lambda \frac{P_{eq}}{R_{eq} + P_{eq}}, \tag{2.27}$$

results in the reactive flux expression, $\mathrm{k}_f^{RF}(t)$, Equation 2.28, first proposed by Yamamoto;[84]

$$\mathrm{k}_f^{RF}(t) = \frac{\langle \theta\big[\xi(t)\big] \dot{\xi}(0) \delta\big[\xi(t)\big] \rangle}{\langle \theta\big[-\xi(0)\big] \rangle}, \tag{2.28}$$

where the numerator corresponds to the average velocity of molecules that cross the transition state at $t = 0$ and finish in the product minimum and the denominator corresponds to the equilibrium reactant fraction.

We also note that in the limit of time t going to zero, Equation 2.28 now becomes,

$$\mathrm{k}_f^{TST} = \frac{\langle \theta\big[\xi(t)\big] \dot{\xi}(0) \delta\big[\xi(0)\big] \rangle}{\langle \theta\big[-\xi(0)\big] \rangle}, \tag{2.29}$$

which can be shown to be the TST expression for the reaction rate. Unlike in Equation 2.28, the flux is calculated by averaging over the molecules that cross the transition state in the direction of the product minimum, which, corresponds to the no-recrossing assumption discussed in Section 2.1.2.

To account for the no-recrossing assumption, the exact rate constant, k_f^{exact}, can be expressed as,

$$\mathrm{k}_f^{exact} = \alpha \mathrm{k}_f^{TST}, \tag{2.30}$$

where α is defined as the transmission coefficient, taking a value between zero and

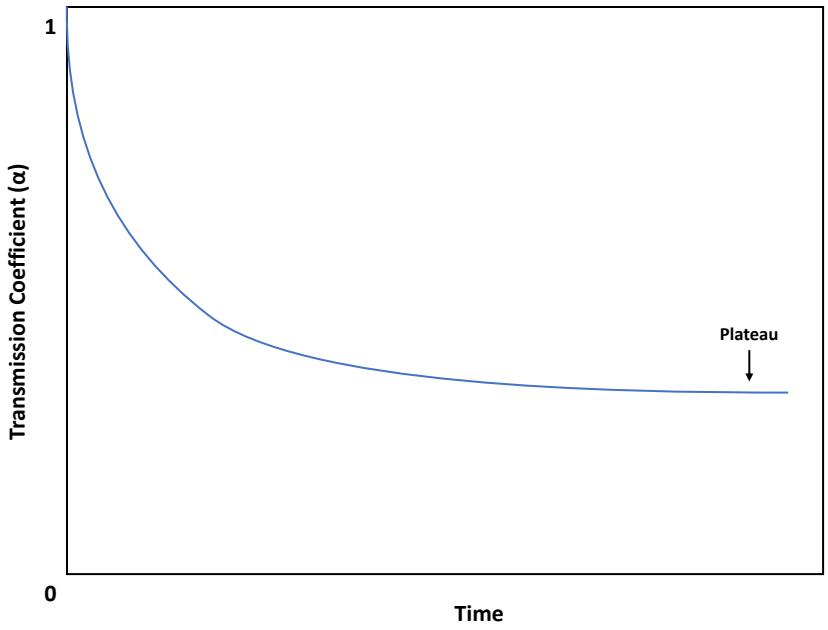

Figure 2.3: Typical plot of the transmission coefficient, α, as a function of time, t. The plateau corresponds to the transmission coefficient which can then be used to determine the exact rate.

unity, which accounts for trajectories which do not end up in the product minimum even after crossing the transition state.

Substituting Equation 2.28 and 2.29 into Equation 2.30 yields,

$$\alpha = \frac{\langle \theta\big[\xi(t)\big]\dot{\xi}(0)\delta\big[\xi(t)\big]\rangle}{\langle \theta\big[\xi(t)\big]\dot{\xi}(0)\delta\big[\xi(0)\big]\rangle}, \tag{2.31}$$

where the denominator corresponds to all molecules that cross the transition state at time $t = 0$ in the positive direction averaged and the numerator corresponds to all the molecules that cross the transition state at time $t = 0$ and finish in the product minimum at a time t. This nuance essentially accounts for any recrossing of the transition state barrier. At very short times, the ratio will be close to unity but as the time evolves and as more chances of recrossing occur, the ratio decreases. After a short time, all the molecules at the transition state at time $t = 0$ will have finished at either the reactant minimum or the product minimum, and so the ratio arrives to a plateau which then corresponds to the value of the transmission coefficient which can be multiplied to the TST rate constant to determine the exact rate constant, shown in Figure 2.3.

2.4 Reaction path Hamiltonian

2.4.1 Background

The reaction path Hamiltonian (RPH) was first derived by Miller, Handy, and Adam in 1980 in order to find a way to use a small but reasonable amount of calculations on the PES of a many-atom system in order to be best used for dynamical purposes.[85] At that time, most of the systems investigated, in the context of intramolecular dynamics, were tri-atomic due to the difficulty in calculating the PES using *ab initio* quantum chemistry. The PES for an N atom system depends on $3N-6$ coordinates and typically requires approximately 10 points on the surface in order to completely characterise it, resulting in 10^{3N-6} *ab initio* quantum chemistry calculations. It quickly becomes apparent how for $N > 4$ systems, the number of calculations becomes unfeasible and even impossible.[86]

The key idea behind the RPH lies in the concept of a reaction valley on the PES which can describe all of the mechanistic and dynamic steps accompanying a chemical reaction.[86] Miller, Handy and Adams described the reacting system in terms of a reaction path coordinate set which included a reaction coordinate s and $3K - L - 1$ complementary harmonic reaction valley coordinates where K is the number of atoms in a system and L is the number of overall translations and external rotations. This reaction valley can be described by determining, at each point s, the curvature of the valley floor in directions which are perpendicular to the reaction path. This can be done by considering that for a point on the reaction coordinate s, the energy $V(\mathbf{R})$ corresponds to a minimum in the $3K-L-1$ dimensional subspace orthogonal to the reaction path subspace. Once $V(\mathbf{R})$ is expanded to second-order, both the curvature and the steepness of the valley can be calculated, however the Hessian matrix at a point s is now expressed in mass-weighted coordinates and constructed by projecting out the rotations and translations of the reaction complex, and translations along the reaction path. The mass-weighted projected force constant matrix, or projected Hessian, at a point s can then be expressed as:

$$\mathbf{K}(s) = [\mathbf{I} - \mathbf{P}(s)]\mathbf{F}(s)[\mathbf{I} - \mathbf{P}(s)], \tag{2.32}$$

where $\mathbf{K}(s)$ is the mass-weighted projected force constant matrix, $\mathbf{I}$ is the identity matrix, $\mathbf{P}(s)$ is a projection matrix and $\mathbf{F}(s)$ is the Hessian matrix.

By diagonalising Equation 2.32, one obtains $3K - L - 1$ mass-weighted generalised normal modes $\boldsymbol{l_\mu}(s)$, the normal mode coordinates, $\boldsymbol{Q_\mu}(s)$, which measure the displacements along the directions of $\boldsymbol{l_\mu}(s)$, and their associated frequencies, $\boldsymbol{\omega_\mu^2}(s)$, and lastly $L+1$ frequencies equal to 0 which correspond to the translations,

rotations and motion along the reaction path,

$$\mathbf{K}(s)\mathbf{l}_\mu(s) = \boldsymbol{\omega}_\mu^2(s)\mathbf{l}_\mu(s). \tag{2.33}$$

The resulting generalised normal modes vectors are then orthogonal to the reaction path and span the $3K - L - 1$ dimensional subspace. Therefore, the normal mode coordinates, $\boldsymbol{Q_\mu}(s)$, are suited to describe the reaction valley, and the frequencies, $\boldsymbol{\omega_\mu^2}(s)$, can be used to describe the curvature and the steepness of the reaction valley walls. The reaction valley is labelled as harmonic because the potential, $\mathbf{V}$, is expanded to second order, and so each point, $\mathbf{x}_i$, in mass-weighted Cartesian coordinate space is expressed as:

$$\mathbf{x}_i = \mathbf{x}_i(s) + \sum_{\mu}^{3K-L-1} \mathbf{l}_{\mu,i}(s)\mathbf{Q}_\mu, \tag{2.34}$$

The original RPH of Miller, Handy and Adams,[85] which is also the one used throughout this work, is a classical Hamiltonian which is built around four assumptions.

1. The first assumption, which was briefly touched on, is that the reaction valley can be described as a harmonic reaction valley where a mass-weighted projected force-constant matrix, $\mathbf{K}(s)$, can be calculated at any point along the reaction path.

2. The second assumption ties in with the first with respect to the harmonic reaction valley. Because of the harmonic expansion of the valley potential, only the kinetic component of the RPH contains coupling terms. As a result, the RPH is an adiabatic Hamiltonian, meaning the frequencies, $\boldsymbol{\omega_\mu^2}(s)$, do not cross.

3. The third assumption consists of removing the rotations of the reaction complex in three dimensional space by assuming zero angular momentum. This excludes any rotational part and possible rotation-vibration coupling terms in the RPH.

4. Lastly, the fourth assumption is that the movement along the reaction path is slow relative to the transverse vibrational motion, also known as the vibrationally adiabatic assumption.

We note that these assumptions breakdown in some cases such as: in the event of strong anharmonicity for weak vibrations or at high temperatures which would

breakdown the harmonic approximation. However, based on these assumptions the original RPH takes the form of:

$$H[s, p_s, \{\boldsymbol{Q}_\mu\}, \{\boldsymbol{P}_\mu\}] = T[s, p_s, \{\boldsymbol{Q}_\mu\}, \{\boldsymbol{P}_\mu\}] + V[s\{\boldsymbol{Q}_\mu\}], \tag{2.35}$$

where $s, \{\boldsymbol{Q}_\mu\}$ corresponds to the reaction valley coordinates and $p_s, \{\boldsymbol{P}_\mu\}$ and corresponds to their conjugate momenta.

The total potential energy term, V, is calculated at a point on the reaction coordinate, s, by the potential energy at said point s in addition to harmonic displacements perpendicular to the reaction path.

$$V[s\{\boldsymbol{Q}_\mu\}] = V_0(s) + \frac{1}{2}\sum_{\mu}^{3K-L-1} \boldsymbol{\omega}_\mu^2(s)\mathbf{Q}_\mu^2(s), \tag{2.36}$$

where $V_0(s)$ is the potential energy.

The second term of the RPH, the kinetic energy term $T[s, p_s, \{Q_\mu\}$, is expressed as the following:

$$T[s, p_s, \{\boldsymbol{Q}_\mu\}] = \frac{1}{2}\frac{\left[p_s - \sum_\mu^{3K-L-1}\sum_\nu^{3K-L-1} \boldsymbol{B}_{\mu,\nu}(s)\boldsymbol{Q}_\mu(s)\boldsymbol{P}_\nu(s)\right]}{\left[1 + \sum_\mu^{3K-L-1} \boldsymbol{B}_{\mu,s}(s)\boldsymbol{Q}_\mu(s)\right]}, \tag{2.37}$$

where $\boldsymbol{B}_\mu, \nu(s)$ and $\boldsymbol{B}_\mu, s(s)$ are the Coriolis coupling and curvature coupling respectively.

The numerator of Equation 2.37 relates to the kinetic energy part of the movement along the reaction path, which includes coupling terms between reaction path and transverse motion. The second component of Equation 2.37 relates to the kinetic energy associated with movement orthogonal to the reaction path direction.

2.4.2 Derivation of the reaction path Hamiltonian

In order to derive the reaction path Hamiltonian a general F-dimensional Cartesian-like Hamiltonian is used without any angular momentum, as stated in the assumption in Section 2.4.1.

Let $\{x_i\}, i = 1, ..., F$ be the mass-weighted Cartesian coordinates, and so, the Hamiltonian for the system is

$$H(\mathbf{p},\mathbf{x}) = \sum_{i=1}^{F} \frac{1}{2} p_i^2 + V(x_i, ..., x_F), \tag{2.38}$$

where V is the potential energy of the system and p is the momentum of the system.

It is then assumed that the reaction path for a given reaction is known, and the normal mode analysis has been calculated using the tools such as *ab initio* quantum chemistry. As a result, $\{a_i(s)\}, i = 1, ..., F$, the Cartesian coordinates of the reaction path as a function of reaction coordinate s, the arc length along the reaction path, $a_i'(s)$, and the potential energy along the reaction path $V_0(s)$ are known. Furthermore, the normal mode frequencies $\omega_k^2, k = 1, ..., F-1$ as well as the matrix of eigenvectors $L_{i,k}(s), i, k = 1, ..., F$ are calculated by diagonalisation of the project force-constant matrix, where the projection matrix, $P = \mathbf{vv}$, is also known.

The potential energy, within a harmonic approximation of the reaction path, is then given by

$$V(s, Q_1, ..., Q_{F-1}) = V_0(s) + \sum_{k=1}^{F-1} \frac{1}{2} \omega_k(s)^2 Q_k^2, \tag{2.39}$$

where the term $k = F$ is not included within the sum as it is the zero eigenvalue which corresponds to the direction of the reaction path, and so the Fth eigenvector corresponds to the normalised gradient vector

$$L_{i,F}(s) = \nu_i(s) \propto -\left(\frac{\delta V(\mathbf{x})}{\delta x_i} \right)_{x=a}, \tag{2.40}$$

but also

$$L_{i,F}(s) = a_i'(s), \tag{2.41}$$

which follows by definition of arc length for displacements along the reaction path

$$ds^2 = \sum_{i=1}^{F} (dx_i)^2. \tag{2.42}$$

With the potential energy term determined, the reminder of the derivation consists of determining the kinetic energy term in terms of s, $\{Q_k\}$ and $p_s, \{P_k\}$. To do

so, a canonical transformation is used on the $2F$ old variables $(x_i), (p_i), i = 1, ..., F$ to the $2F$ new variables $(s, p_s), (Q_k), (P_k), k = 1, ..., F-1$ where the "old" Cartesian coordinates $\{x_i\}$ are now given in terms of the new variables $(s, \{Q_k\})$ by

$$x_i = a_i(s) + \sum_{k=1}^{F-1} L_{i,k}(s) Q_k \equiv x_i(s, \{Q_k\}). \tag{2.43}$$

Now the Cartesian coordinates $\{x_i\}$ of a general point in configuration space are given by the Cartesian coordinate of a point on the reaction path $\{a_i(s)\}$ and $F-1$ displacements, $\{Q_k\}$, orthogonal to the reaction path. Since the old coordinates are a function of only the new coordinates and not the new momenta, Miller *et al.*[85] expressed them as a function of the new momenta in the form of,

$$P_k = \sum_{i=1}^{F} p_i L_{i,k}(s), \tag{2.44}$$

$$p_s = -\sum_{i=1}^{F} p_i \left[a_i'(s) + \sum_{k=1}^{F-1} L'_{i,k}(s) Q_k \right]. \tag{2.45}$$

The next part of the derivation consists of solving Equation 2.44 and 2.45 for the old momenta $\{p_i\}$ in terms of the new variables $(s, p_s), (Q_k, P_k)$. Knowing that the kinetic energy T in terms of the old momenta is given by

$$T = -\sum_{i=1}^{F} \frac{1}{2} p_i^2, \tag{2.46}$$

an expression for the kinetic energy can be obtained in terms of the new variables. In order to simplify the process, Equation 2.45 can be re-written using Equation 2.42 as

$$p_s = -\sum_{i=1}^{F} p_i \left[\nu_i + \sum_{k=1}^{F-1} L'_{i,k}(s) Q_k \right]. \tag{2.47}$$

In order to solve Equation 2.44 and 2.45 for $\{p_i\}$, Equation 2.44 is multiplied by $L_{i,k}(s)$ and sum over k

$$\sum_{k=1}^{F} L_{j,k}(s)P_k = \sum_{i=1}^{F} p_i \sum_{k=1}^{F} L_{j,k}(s)L_{i,k}(s), \tag{2.48}$$

but unitarity of $\{L_{i,k}\}$ implies that

$$\sum_{k=1}^{F} L_{j,k}(s)L_{i,k}(s) = \sum_{k=1}^{F} L_{j,k}(s)L_{i,k}(s) - L_{j,F}(s)L_{i,F}(s) = \delta_{j,i} - \nu_j\nu_i, \tag{2.49}$$

so that Equation 2.48 becomes

$$\sum_{k=1}^{F} L_{j,k}(s)P_k = p_j - \nu_j \sum_{i=1}^{F} p_i\nu_i, \tag{2.50}$$

and so the old momenta $\{p_i\}$ are given as

$$p_i = \sum_{i=1}^{F} L_{i,k}(s)P_k + c\nu_i, \tag{2.51}$$

where c is determined by substituting Equation 2.51 into Equation 2.47 as

$$c = \frac{p_s - \sum_{l,k=1}^{F-1} Q_k P_l B_{k,l}(s)}{1 + \sum_{k=1}^{F-1} Q_k B_{k,F}(s)}, \tag{2.52}$$

where $B_{k,l}(s) = \sum_{i=1}^{F} L'_{i,k}(s)L_{i,l}(s)$. Using Equation 2.52 in Equation 2.51 gives the old momenta explicitly in terms of the new variables

$$p_i = \sum_{l=1}^{F-1} L_{i,l}(s)P_i + L_{i,F}(s)\frac{[p_s - \sum_{l,k=1}^{F-1} Q_k P_l B_{k,l}(s)]}{[1 + \sum_{k=1}^{F-1} Q_k B_{k,F}(s)]}. \tag{2.53}$$

Using the unitarity of $\{L_{i,}k\}$ again and substituting Equation 2.53 into Equation 2.37 gives the kinetic energy in terms of the new variables

$$T = \sum_{k=1}^{F-1} \frac{1}{2}P_k^2 + \frac{1}{2}\frac{[p_s - \sum_{l,k=1}^{F-1} Q_k P_l B_{k,l}(s)]}{[1 + \sum_{k=1}^{F-1} Q_k B_{k,F}(s)]}. \tag{2.54}$$

Finally, combining both the potential energy and kinetic energy terms expressed

in terms the reaction path coordinates and their conjugate momenta, the classic RPH is obtained

$$H(p_s, s, \{Q_k\}, \{P_k\}) = V_0(s) + \sum_{k=1}^{F-1}(\frac{1}{2}P_k^2\frac{1}{2}\omega_k(s)^2Q_k^2) + \frac{1}{2}\frac{[p_s - \sum_{l,k=1}^{F-1} Q_k P_l B_{k,l}(s)]}{[1 + \sum_{k=1}^{F-1} Q_k B_{k,F}(s)]}. \tag{2.55}$$

2.4.3 Insight provided by the reaction path Hamiltonian

The reaction path Hamiltonian allows for the possibility to gather mechanistic and dynamical information by investigating the terms present in Equation 2.55.[86] The terms in the RPH can be split into two categories: shape terms and coupling terms.

First, the shape terms are the classical potential V_0, which describes the height of the reaction path, and the vibrational frequencies which describe the width of the reaction valley. Second, the coupling terms are $B_{\mu,\nu}(s)$ (Coriolis coupling) and $B_{\mu,s}(s)$ (curvature coupling) which reflect the dynamic coupling between the reaction coordinate and the transverse vibrations, and the coupling between the transverse vibrations themselves respectively.

The coupling terms can play an important role in the dynamics of a reaction and, as such, exploring them allows for a more thorough understanding of the dynamics involved.[87,88] The magnitude of the Coriolis coupling indicates the amount of energy flow among the transverse vibrations, and so gives insight into the energy dissipation occurring during the reaction as a result of the energy transfer from one mode to another. As such, a high magnitude indicates a large amount of energy being dissipated during the reaction and *vice versa*. Alternatively, the magnitude of the curvature coupling accounts for the translational to vibrational energy transfer which occurs between the reaction path and the vibrational modes during the reaction. A larger curvature coupling indicates an increase in the coupling between the reaction path and the vibrational mode and thus the energy transfer from translation to vibration and *vice versa* is facilitated. Furthermore, the regions at which the reaction path curves significantly and thus the curvature coupling is large, are important, as that is where the translation to vibration energy transfer will take place. In the entrance channel, the vibrational modes which have a large coupling to the reaction path are known as *donating modes*, which means that energy flows from them to the reaction path and increase the reaction rate. In the exit channel, the vibrational modes with large coupling to the reaction path are known as *accepting modes*, which means that the energy flows from the reaction path to these vibrational modes.[86]

2.4.4 Constructing the reaction path Hamiltonian

The standard implementation of the RPH consists of two key components, as discussed in Section 2.4.1 and Section 2.4.2. These two are the MEP, which connects the reactant and product minima via a transition state and the Hessian matrix to be calculated along said MEP. This can be done for all points s along the MEP, however it is undesirable as the computational cost quickly escalates depending on the number of points on the path. Instead, the standard implementation of the reaction path Hamiltonian consists of only selecting a discrete number of points along the minimum energy path and interpolating through the points in order to get smooth curves for the functions present in the reaction path Hamiltonian.[87–89] At each intermediate image used along the reaction coordinate, s, to construct the RPH, the Hessian matrix, $\mathbf{F}(s)$, is calculated and, subsequently, the rotations and translations of the reaction complex and the MEP path vector are projected out using a projection matrix, $\mathbf{P}(s)$. This gives the mass-weighted projected force constant matrix or mass-weighted projected Hessian matrix, $\mathbf{K}(s)$, as:

$$\mathbf{K}(s) = [\mathbf{I} - \mathbf{P}(s)]\mathbf{F}(s)[\mathbf{I} - \mathbf{P}(s)]. \tag{2.56}$$

With the mass-weighted projected Hessian known, diagonalising and thus solving the eigenvalue problem for a given path point s becomes trivial in order to get the $(3K - L - 1)$ normal modes $\mathbf{L}(s)$ and their associated frequencies $\boldsymbol{\omega}^2(s)$:

$$\boldsymbol{\omega}^2(s) = \mathbf{L}(s)^{\mathrm{T}}\mathbf{K}(s)\mathbf{L}(s). \tag{2.57}$$

Finally, the vibrational coupling constants are determined. The curvature coupling constants $\mathbf{b}(s)$, which account for the curvature of the MEP, are determined by:

$$\mathbf{b}(s) = \mathbf{L}(s)^{\mathrm{T}}\mathbf{a}'(s), \tag{2.58}$$

where $\mathbf{a}'$ denotes the derivative of the normalised path tangent. The Coriolis coupling constants $\mathbf{B}(s)$, which describe the transfer of energy among the harmonic "bath" modes, are determined by:

$$\mathbf{B}(s) = \mathbf{L}(s)^{\mathrm{T}}\mathbf{L}'(s), \tag{2.59}$$

where $\mathbf{L}'(s)$ is the first derivative of the mass-weighted generalised normal modes. A prerequisite for using the RPH is that correct functions of $\omega_\mu(s)$ are determined, ordered and correlated properly along the reaction path in order to calculate the coupling constants. However, an adiabatic ordering of the frequencies can lead to

unphysical spikes in the coupling constant where transverse frequencies cross which becomes obvious when the Coriolis coupling can also be written in terms of the derivative of the mass-weighted projected Hessian $\mathbf{K}$:

$$\mathbf{B}_{ij}(s) = \frac{\mathbf{L}_j^{\dagger}(\mathbf{K}'(s))\mathbf{L}_i}{\boldsymbol{\omega}_i^2 - \boldsymbol{\omega}_j^2} \qquad i,j = 1, 3N-7, i \neq j. \tag{2.60}$$

From this formulation it is clear the matrix exhibits poles at degeneracies, which result in those unphysical spikes mentioned. To avoid these complications, a similar strategy to Peters *et al* is employed,[87] whereby a diabatic RPH is constructed by finding the permutation matrix at each image which maintains the character of eigenvectors across the reaction path. The permutation matrix is obtained by solving the linear assignment problem using the Hungarian algorithm,[90] maximising the trace of the overlap matrix $\mathbf{L}^{\dagger}(s_i)\mathbf{L}(s_{i+1})$ between an image at s_{i+1} from an already-permuted adjacent image at s. Whenever degeneracies occur between frequencies at an image, the diagonalization procedure returns vectors with one or more arbitrary angles of rotation that continue to satisfy the eigenvalue problem. In those circumstances, the rotation matrix which maximises the overlap between the degenerate vectors in the overlap matrix is found prior to the permutation of eigenvectors. A small caveat, however, lies when the rotations lead to a coordinate representation with off-diagonal terms in the Hessian matrix. In those rare cases, the off-diagonal elements are not evaluated as most frequency crossings are found to be 'accidental' (in the sense that the mixing angle is not substantial during the crossings). Although the Hessian remains diagonal, the permutation of eigenvectors along the RPH leads to the disappearance of poles in $\mathbf{B}$ via $\mathbf{L}'(s)$ in Equation (2.59). The result of a diabatic RPH is then a smoothly varying function for the coupling coefficients which facilitate dynamics calculations.

Overall, for a system with zero angular momentum comprising N atoms, the RPH takes the following form:

$$H(s, p_s, \mathbf{q}, \mathbf{p}) = \frac{(p_s - \mathbf{q}^T\mathbf{B}(s)\mathbf{p})^2}{2(1 + \mathbf{q}^T\mathbf{b}(s))} + \frac{1}{2}\mathbf{p}^2 + V_0(s) + \frac{1}{2}\mathbf{q}^T\boldsymbol{\omega}^2(s)\mathbf{q}, \tag{2.61}$$

where s denotes the reaction coordinate and p_s corresponds to its conjugate momentum. Furthermore, $\boldsymbol{q}$ denotes the orthogonal harmonic coordinates and $\boldsymbol{p}$ corresponds to their conjugate momenta. Once the information required for construction of the RPH has been computed at the series of images along the MEP, the RPH (and derivatives) can be evaluated at any reaction coordinate s by spline interpolations. As a result, the RPH of Equation 2.61 can subsequently be used to perform a full-dimensional dynamics simulation of the N-atom system as it moves along

the reaction coordinate s, whilst also accounting for energy flow to and from the transverse vibrational degrees-of-freedom.

Lastly, for reactions where one of the endpoint configurations describes a bound state, to stop the system from rolling off the PES and crashing the dynamics, we create a fictitious harmonic well along the reaction path by defining a normalised path tangent vector at the minimum in the basis of normal modes of the Hessian at the minimum. The resulting effective frequency along s is then given by $\omega_s^2 \approx \sum_i^{3N-7} \omega_i^2 c_i^2$ where c_i are the normal mode displacements of the normalised path tangent vector.

2.4.5 Reactive flux simulations

The RPH can be used in conjunction with MD simulations to determine absolute reaction rates and transmission coefficients,[87,88] which can, in principle, be combined with TST to calculate reaction rates.

Here, to determine dynamic transmission coefficients, we employ the standard classical flux-side time-correlation function, $C_{fs}^{cl}(t)$,[91] given by

$$C_{fs}^{cl}(t) = \frac{1}{2\pi\hbar} \int d\mathbf{p}\, d\mathbf{q}\, dp_s\, ds\; e^{-\beta H(s,p_s,\mathbf{q},\mathbf{p})} p_s \delta(s - s_0)\theta(s_t - s_0), \tag{2.62}$$

where $H(s, p_s, \mathbf{q}, \mathbf{p})$ is the RPH of Equation 2.61. Here, $\theta(x)$ is the Heaviside step function, s_0 is the position of the TS along the reaction-coordinate s, $\beta = \frac{1}{k_B T}$, where k_B is Boltzmann's constant, and $\delta(x)$ is the Dirac delta function. The function $C_{fs}^{cl}(t)$ is related to the classical reaction rate at temperature T, $\mathrm{k}^{cl}(T)$, through

$$\mathrm{k}^{cl}(T) Q_r(T) = \lim_{t \to t'} C_{fs}^{cl}(t), \tag{2.63}$$

where t' is a suitable plateau time for the reaction under study and $Q_r(T)$ is the reactant partition function. Similarly, the TST rate constant is related to the $t \to 0^+$ limit of $C_{fs}^{cl}(t)$,

$$\mathrm{k}^{TST}(T) Q_r(T) = \lim_{t \to 0_+} C_{fs}^{cl}(t). \tag{2.64}$$

Finally, the dynamic transmission coefficient $\alpha(T)$, is given by

$$\alpha(T) = \frac{\mathrm{k}^{cl}(T)}{\mathrm{k}^{TST}(T)}. \tag{2.65}$$

The flux-side correlation function $C_{fs}^{cl}(t)$ can be computed using Equation 2.62 by initializing MD trajectories at the TS (such that $\mathrm{s} = \mathrm{s}_0$), with the initial momenta $(p_s, \mathbf{p})$ and remaining positions $\mathbf{q}$ sampled from the Boltzmann distribution

calculated with the RPH of Equation 2.61.[92,93] Moreover, the artificial harmonic potential detailed above is added to the RPH to ensure that configurations sampled during MD simulations remain within the configuration space in which the RPH is well-defined. These trajectories are propagated forwards and backwards for a sufficiently long time-period that the $C_{fs}^{cl}(t)$ function would be expected to reach a plateau.[94,95] By averaging over a large number of these MD trajectories, the thermally-averaged $C_{fs}^{cl}(t)$ can be calculated, thereby allowing determination of the transmission coefficient $\alpha(T)$.

2.4.6 Bench marking against literature

In order to make sure that the reaction path Hamiltonian constructing methodology and its implementation with reactive flux simulation are correct, we bench marked the program against known literature where, for a given reaction, the transmission coefficient had been calculated using the RPH along with reactive flux simulations using the RPH. The reactions investigated were the interconversion of cyclohexane from chair to twist-boat by Peters *et al.*,[87] the Claisen rearrangement of allyl vinyl ether and the Diels-Alder reaction of cyclopentadiene with methyl vinyl ketone by Hu *et al.*[88]

For all reactions, we use a 15-image MEP obtained by running a CI-NEB[96] calculation. We then use the initial MEP (comprising 15 images) and use spline interpolation to generate a path with a total of 50 images; this expanded 50-image path was used to perform RPH simulations which means that 50 Hessian matrices were evaluated along the reaction-path.

Furthermore, for the reactive flux simulations, each set of initial coordinates and momenta were propagated using Hamilton's equations of motion determined from the RPH; the fourth-order Runge-Kutta (RK4) algorithm was used to numerically integrate the equations-of-motion using a time-step of 0.30 fs. For each reaction considered, we found that a different total simulation time was required to ensure that $C_{fs}^{cl}(t)$ had reached a plateau; typically, each trajectory required 0.5-3 ps simulation time, and a total of 10^4 trajectories were performed for each reactions. Under these conditions, we find that the typical standard error in the plateau values of the $C_{fs}^{cl}(t)$ function is 2×10^{-3}; this value is typically much smaller than any observed differences between the different simulation methods investigated below.

Interconversion of cyclohexane from chair to twist-boat

Peters *et al* had investigated the dynamics rate constant calculated with the RPH compared to VTST for the interconversion of cyclohexane from chair to twist-boat.[87] Despite VTST minimising the recrossing effects by using an alternative dividing

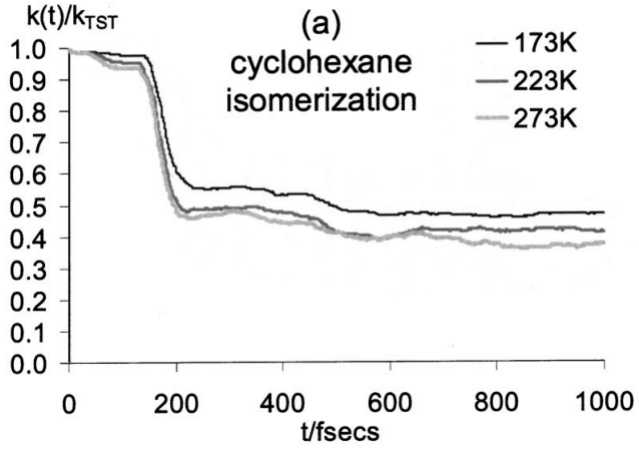

Figure 2.4: The transmission coefficient determined using the RPH approach of Peters *et al.* for the interconversion of cyclohexane from chair to twist-boat at 173K, 223K and 273K. Figure taken from the work and permission of Peters *et al.*[87]

surface along the reaction coordinate, it still remains a TST and as such may still not fully account for recrossing effects. The interconversion of cyclohexane from chair to twist-boat was chosen as an example as there had been evidence of ballistic trajectories that recross the dividing surface and this would be reflected in the transmission coefficient. Furthermore, there are 48 internal degrees of freedom which would be a challenging test case for the methodology of construction of the RPH.

The level of theory used by Peters *et al* was initially at the HF/6-31G level in order to find the saddle point on the PES using a Cerjan Miller TS from the chair configuration.[97] Following this, the steepest descent path was determined using the local quadratic approximation also at the HF/6-31G level and the stationary points were reoptimised at the B3LYP/6-31G level, and the forward and backward barrier heights were scaled to match the B3LYP/6-31G values. Finally, the MEPs were analysed within the standard RPH framework.

In order to determine the transmission coefficient, 0.95×10^6 Monte Carlo steps are used to generate an ensemble of 950 decorrelated trajectories at 173K, 223K and 273K. The classical equations of motion were derived from the RPH and were solved using an adaptive version of the fourth-order Runge-Kutta algorithm where the time step was adjusted based on $q(t)^T b[s(t)]$ and the difference between k_1 and k_2 evaluations in the Runge-Kutta algorithm. Moreover, the maximum timestep was one-twelfth of the fastest transverse vibration period.

The resulting transmission coefficient for the interconversion of cyclohexane from chair to twist-boat reported by Peters *et al.* is shown in Table 2.1 and Figure 2.4.[87]

In our bench mark test, we used the ORCA quantum chemistry package feature, NEB-TS,[98] in order to determine the MEP at the B3LYP/6-31G level of theory. Using the MEP, the transmission coefficient is determined using an ensemble of 10

Table 2.1: Transmission coefficient for the interconversion of cyclohexane from chair to twist-boat determined by Peters *et al.*[87]

Temperature (K)	$C_{fs}^{cl}(t)$ **plateau value**
173	0.47
223	0.41
273	0.37

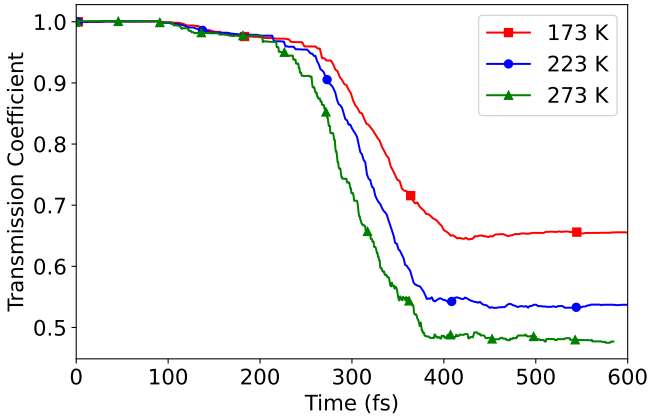

Figure 2.5: The transmission coefficient determined using our RPH approach for the interconversion of cyclohexane from chair to twist-boat at 173K, 223K and 273K.

000 trajectories at 173K, 223K and 273 K with a timestep of 0.30 fs. The resulting transmission coefficients using our implementation are shown in Table 2.2 and Figure 2.5.

Table 2.2: Transmission coefficient for the interconversion of cyclohexane from chair to twist-boat.

Temperature (K)	$C_{fs}^{cl}(t)$ **plateau value**
173	0.65
223	0.52
273	0.47

The transmission coefficients determined using our implementation of the RPH for the interconversion of cyclohexane at 173 K, 223 K and 273 K were 0.65, 0.52 and 0.47. Compared to the work done by Peters *et al.*,[87] the difference in transmission coefficient at 173 K, 223 K and 273 K was 0.18, 0.11 and 0.10. Despite these difference, both the trend (increasing temperature, the transmission coefficient decreases) and the shape of the flux-side correlation function over time is comparable. The differences in transmission coefficients could be attributed to the choice of timestep for the MD simulations. In the work done by Peters *et al.*, the time step was adjusted based on $q(t)^T b[s(t)]$ and the difference between k_1 and k_2 evaluations in the Runge-Kutta algorithm, whereas in our work we used a fixed timestep of 0.30 fs. Because

the values used by Peters *et al.* are dependent upon the MEP, and the transmission coefficient, which is calculated using these values, will differ slightly to if a explicit time-step was used.

Another difference lies within the method used to determine the reaction path with which the RPH is then constructed, and as a result subtle differences in the constructed RPH will lead to differences in the transmission coefficient determined.

Claisen rearrangement of allyl vinyl ether and Diels-Alder reaction of cyclopentadiene with methyl vinyl ketone

The next reactions used to benchmark our methodology were the Claisen rearrangement of allyl vinyl ether and Diels-Alder reaction of cyclopentadiene with methyl vinyl ketone, which had both been investigated for dynamical solvent effects within the framework of the RPH by Hu *et al.*[88] In both of the reactions, important dynamical solvent effects had been determined, with experimental data suggesting that the rate in water was accelerated by a factor of 1000 relative to the rate in gas-phase for the Claisen rearrangement and in the case of the Diels-Alder reaction the rate was accelerated by a factor of 730 in water relative to the rate in isooctane. In the case of the Diels-Alder reaction, dynamical effects had been studied by Voth *et al*[99] where they had developed an empirical PES allowing for solute motion based on gas phase electronic structure calculations. They then performed molecular dynamics simulations with this PES with explicit solvent and investigated the dynamical effects using the reactive flux method. Despite being a breakthrough study, the approach was not scalable as the development of a multidimensional PES and significant computational resources were necessary. This is why the dynamical solvent effects were investigated within the RPH framework as a computationally cheaper alternative.

In the Hu *et al.* paper, the level of theory used was B3LYP/6-31G** and the MEP was generated using the method of Schlegel *et al.*[88] The MEP was subsequently analysed within the RPH framework. However, in order to make the molecular dynamics simpler, only the orthogonal vibrational modes that are strongly coupled to the reaction coordinate are used. In order to determine the transmission coefficient, an ensemble of 10 000 trajectories at 298 K was used. The classical equations of motion were then derived from the RPH, and solved using the fourth-order Runge-Kutta algorithm, with a timestep of $\delta t = 0.012$ fs.

The resulting transmission coefficient for the Claisen rearrangement of allyl vinyl ether and Diels-Alder reaction of cyclopentadiene with methyl vinyl ketone in gas-phase conditions and also in the presence of two water molecules are shown in Table 2.3 below.

In both reactions, be it in gas-phase or in the presence of two water molecules, the transmission coefficient is close to unity indicating that there was little to no

Table 2.3: Transmission coefficients for the Claisen rearrangement of allyl vinyl ether and Diels-Alder reaction of cyclopentadiene with methyl vinyl ketone in gas-phase conditions and also in the presence of $2H_2O$ molecules, determined by Hu *et al.*[88]

Reaction	$C_{fs}^{cl}(t)$ **plateau value**
Claisen	0.995
Claisen/ $2H_2O$	0.991
Diels-Alder	0.950
Diels-Alder/ $2H_2O$	0.892

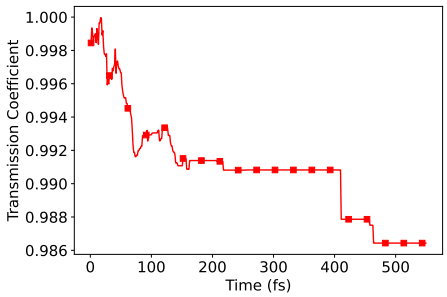

Figure 2.6: Transmission coefficient for the Claisen rearrangement of allyl vinyl ether in gas-phase using our RPH approach.

recrossing effects observed.

In our bench mark test, we used the ORCA quantum chemistry package feature, NEB-TS,[98] in order to determine the minimum energy path at the B3LYP/6-31G** level of theory, and to calculate the transmission coefficient an ensemble of 10 000 trajectories at 298 K was used. We note that in our implementation of the RPH, all vibrational modes were included in the construction of the RPH as well as the following simulations. Furthermore, instead of using explicit molecules of water, we use an implicit solvent model

The resulting transmission coefficient using our implementation of the RPH for the Claisen rearrangement of allyl vinyl ether and Diels-Alder reaction of cyclopentadiene with methyl vinyl ketone in gas-phase conditions and also in solvent-phase conditions using implicit solvent are shown in Table 2.4 and in Figures 2.6 - 2.9.

Table 2.4: Transmission coefficients for the Claisen rearrangement of allyl vinyl ether and Diels-Alder reaction of cyclopentadiene with methyl vinyl ketone in gas-phase conditions and also in the presence of 2H2O molecules using our implementation of the RPH.

Reaction	$C_{fs}^{cl}(t)$ **plateau value**
Claisen	0.986
Claisen/solvent	0.978
Diels-Alder	0.442
Diels-Alder/solvent	0.897

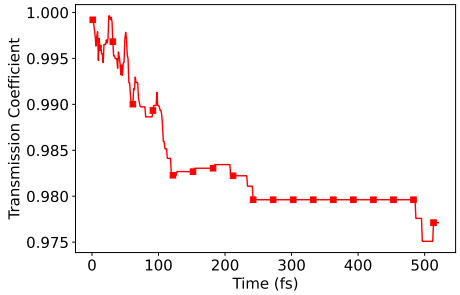

Figure 2.7: Transmission coefficient for the Claisen rearrangement of allyl vinyl ether in solvent-phase using our RPH approach and implicit solvent.

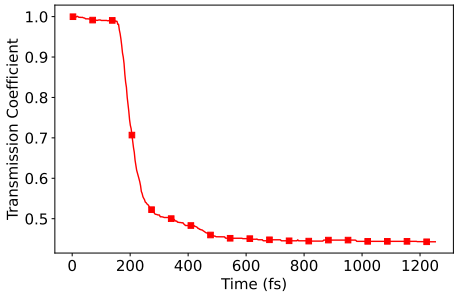

Figure 2.8: Transmission coefficient for the Diels-Alder reaction of cyclopentadiene with methyl vinyl ketone in gas-phase using our RPH approach.

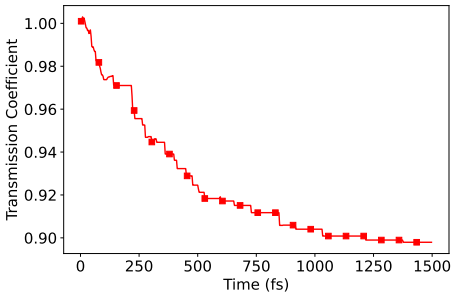

Figure 2.9: Transmission coefficient for the Diels-Alder reaction of cyclopentadiene with methyl vinyl ketone in solvent-phase using our RPH approach and implicit solvent.

The calculated transmission coefficient using our implementation of the RPH resulted in transmission coefficients comparable to Hu *et al.*[88] in all reactions but one. For the Claisen rearrangement, in both gas-phase and with solvent effects, the difference in transmission coefficient to the transmission coefficient reported by Hu *et al.* was 0.009 and 0.013 respectively. The transmission coefficients for the Claisen rearrangement did not result in a plateau, however, the simulations ended at around 500 fs and the transmission coefficient was still essentially unity and so the final value was taken as the transmission coefficient. For the Diels-Alder reaction in both gas-phase and with solvent effects, the difference in transmission coefficient to the transmission coefficient reported by Hu *et al.* was 0.508 and 0.005 respectively.

Comparatively, the transmission coefficients determined using our implementation of the RPH resulted in very similar magnitudes to the work of Hu *et al.* for three of the four calculations. The transmission coefficient which was significantly different was the Diels-Alder in gas-phase transmission coefficient. This difference can be attributed to the fact that they only used the orthogonal vibrational modes strongly coupled to the reaction coordinate as opposed to all of them like in our implementation. Using all of the vibrational modes will result in different coupling constants as opposed to only using a select number of vibrational modes, and with coupling constants affecting dynamics, the final transmission coefficient will then also be effected. We also note that, in the case of the work of Hu *et al.*, the transmission coefficient for the Diels-Alder reaction with two water molecules did not match previous studies done by Voth *et al*[99] of 0.67 showing the sensitivity of the RPH approach.

Chapter 3

RPH and update Hessian schemes

> Preoccupied with a single leaf... you won't see the tree. Preoccupied with a single tree... you'll miss the entire forest. Don't be preoccupied with a single spot. See everything in it's entirety... effortlessly. That is what it means to truly "see".
>
> *Vagabond*, Takehiko Inoue

Summary

The reaction path Hamiltonian, when used in conjunction with molecular dynamics simulation, can be used to derive dynamically corrected reaction rates. Nonetheless, the requirement of accurate Hessian matrices along the reaction path represents a significant obstacle in the applicability of the reaction path Hamiltonian in both larger systems and higher accuracy *ab initio* calculations. A possible alternative to this requirement lies within the concept of update Hessian schemes, a popular concept already used in numerical optimisation problems whereby an approximate Hessian is updated using only gradient evaluations via a generalised secant method. In this Chapter, several update Hessian schemes belonging to two distinct families, quasi-Newton methods and compact finite difference methods, were used on three different types of reactions in order to assess whether the transmission coefficient calculated from a reaction path Hamiltonian constructed using approximate Hessian matrices is comparable to the transmission coefficient calculated from a reaction path Hamiltonian constructed using analytical *ab initio* Hessian matrices.

3.1 Introduction

The requirement of calculating the Hessian matrix represents a substantial computational bottleneck in constructing the reaction path Hamiltonian (RPH),[85] whether it is being calculated at for a discrete number of points along the reaction path or, for the entire reaction path. When compared to an energy gradient evaluation, a Hessian evaluation is significantly more costly, and can take up to 10 times the computational cost depending on the level of theory used for the calculation.[100] This imposes some limitations to the systems that can be investigated using the RPH and to the level of accuracy of the calculations; furthermore, the potential expense of these repeated Hessian evaluations is not compatible with ongoing efforts to merge automated reaction discovery and accurate rate evaluations.[16,21,46,47,50,101,102] With Hessian updating methods being increasingly popular and successful in geometry optimisation calculations,[103–108] transition state (TS) searches,[109,110] potential energy surface (PES) interpolation[111,112] and reaction path following methods,[113] their potential applicability to the RPH method should be explored.

In this Chapter, we consider seven different update Hessian schemes, implemented in different ways within the RPH framework in order to calculate transmission coefficients for chemical reactions. The wider context of this Chapter is to assess how the RPH, constructed using update Hessian schemes, could be used as an alternative to TST, going beyond the usual assumptions (see Section 2.1.2), for high-throughput computation of reaction rates.

3.1.1 Quasi-Newton update Hessian schemes

The update Hessian schemes which are the most commonly used are those known as quasi-Newton methods,[114,115] where only the gradient of the objective function to be determined is needed at each step. By measuring the changes in gradients, quasi-Newton methods construct a model of the objective function that is a good enough approximation to achieve superlinear convergence. Compared to other optimisation methods like steepest descent, the improvement is very noticeable, especially on difficult problems. Moreover, since Hessian calculations are not required, quasi-Newton methods can sometimes be more efficient than Newton's method.

The most popular quasi-Newton update Hessian method is the Broyden–Fletcher–Goldfarb–Shanno method (BFGS).[116–119] The BFGS method is typically only used in minimisation problems such as geometry optimisation calculations or path optimisation problems due to its property whereby the resulting Hessian matrix remains positive definite. This property is necessary in minimisation problems because the Hessian matrix at a converged minimum will only ever have positive eigenvalues and so the Hessian matrix will be a positive definite matrix. Another advantage

of using the BFGS method is the very effective self-correcting properties which it possesses. If the Hessian matrix incorrectly estimates the curvature in the objective function and slows down the iteration, then the Hessian approximation typically corrects itself within a few steps. In order to be used for saddle-point optimisation problems as well as minimization problems, the BFGS method was modified into what is known as the transition state BFGS (TS-BFGS) update Hessian scheme,[120] defined in Equation 3.2. This is done by including a vector in the formula which is a function of both the product of the Hessian matrix and the change in coordinates, and the change of gradient vectors.

$$\Delta\mathbf{H}_{\text{BFGS}} = \frac{\mathbf{H}_k\Delta\mathbf{x}(\Delta\mathbf{x}^{\text{T}})\mathbf{H}_k}{\Delta\mathbf{x}\mathbf{H}_k\Delta\mathbf{x}} - \frac{\Delta\mathbf{g}\Delta\mathbf{g}^{\text{T}}}{\Delta\mathbf{g}\Delta\mathbf{x}}, \tag{3.1}$$

$$\begin{aligned}\Delta\mathbf{H}_{\text{TS-BFGS}} = {} & \frac{(\Delta\mathbf{g}-\mathbf{H}_k\Delta\mathbf{x})((\Delta\mathbf{g}^{\text{T}}\Delta\mathbf{x})\Delta\mathbf{g}+(\Delta\mathbf{g}^{\text{T}}|\mathbf{H}_k|\Delta\mathbf{g})|\mathbf{H}_k|\Delta\mathbf{g})^{\text{T}}}{((\Delta\mathbf{g}^{\text{T}}\Delta\mathbf{x})^2+(\Delta\mathbf{g}^{\text{T}}|\mathbf{H}_k|\Delta\mathbf{g})^2)} + \\ & \frac{((\Delta\mathbf{g}^{\text{T}}\Delta\mathbf{x})\Delta\mathbf{g}+(\Delta\mathbf{g}^{\text{T}}|\mathbf{H}_k|\Delta\mathbf{g})|\mathbf{H}_k|\Delta\mathbf{g})(\Delta\mathbf{g}-\mathbf{H}_k\Delta\mathbf{x})^{\text{T}}}{((\Delta\mathbf{g}^{\text{T}}\Delta\mathbf{x})^2+(\Delta\mathbf{g}^{\text{T}}|\mathbf{H}_k|\Delta\mathbf{g})^2)} - \\ & \frac{(\Delta\mathbf{g}^{\text{T}}\Delta\mathbf{x}-\Delta\mathbf{g}^{\text{T}}\mathbf{H}_k\Delta\mathbf{g})}{((\Delta\mathbf{g}^{\text{T}}\Delta\mathbf{x})^2+(\Delta\mathbf{g}^{\text{T}}|\mathbf{H}_k|\Delta\mathbf{g})^2)^2} \\ & \cdot((\Delta\mathbf{g}^{\text{T}}\Delta\mathbf{x})\Delta\mathbf{g}+(\Delta\mathbf{g}^{\text{T}}|\mathbf{H}_k|\Delta\mathbf{g})|\mathbf{H}_k|\Delta\mathbf{g})(\Delta\mathbf{g}^{\text{T}}\Delta\mathbf{x})\Delta\mathbf{g}+(\Delta\mathbf{g}^{\text{T}}|\mathbf{H}_k|\Delta\mathbf{g})|\mathbf{H}_k|\Delta\mathbf{g})^{\text{T}}),\end{aligned} \tag{3.2}$$

where $\Delta\mathbf{g} = \mathbf{g}_{k+1} - \mathbf{g}_k$ is the gradient difference between the new and old configurations, $\Delta\mathbf{x} = \mathbf{x}_{k+1} - \mathbf{x}_k$ is the vector containing the difference in the $3N$ Cartesian coordinates between the new and old configurations and $\mathbf{H}_k$ is the Hessian matrix at the old configuration.

Another popular quasi-Newton update Hessian method is the symmetric rank-1 method (SR1)[121] and is defined in Equation 3.3:

$$\Delta\mathbf{H}_{\text{SR1}} = -\frac{(\Delta\mathbf{g}-\mathbf{H}_k\Delta\mathbf{x})(\Delta\mathbf{g}-\mathbf{H}_k\Delta\mathbf{x})^{\text{T}}}{(\Delta\mathbf{g}-\mathbf{H}_k\Delta\mathbf{x})^{\text{T}}\Delta\mathbf{x}}. \tag{3.3}$$

Unlike the BFGS method where the updated Hessian matrix differs from its previous iteration by a rank-2 matrix and the updated Hessian matrix maintains positive definiteness, the SR1 method is a rank-1 update that does not guarantee that the updated matrix maintains positive definiteness. Good numerical results have been achieved using the SR1 method to update the Hessian matrix, however there is a drawback to the method and that lies within the denominator of the equation which can sometimes approach zero.[108,122,123] In such cases, the rank-

1 update does not provide enough freedom to create the updated Hessian matrix with all the desired characteristics, and instead a rank-2 correction would be better. Despite this, the SR1 method has reasons to be considered for updating Hessian matrices. First, the drawback linked to the denominator can be prevented and, second, when the method is functioning, the updated Hessian matrices generated by the SR1 method tend to be very good approximations when compared to *ab initio* Hessian matrices, and sometimes even better than the BFGS method. Lastly, in quasi-Newton methods, the curvature condition cannot be fulfilled and so the BFGS update is ill-advised - as such the SR1 method is preferred as it reflects the indefiniteness in the Hessian matrix.

The Powell-symmetric-Broyden (PSB)[124] method is another popular quasi- Newton update Hessian method which is part of the Broyden class like the BFGS method, and is defined in Equation 3.4.

$$\Delta H_{\mathrm{PSB}} = \frac{(\Delta \mathbf{g} - \mathbf{H}_k \Delta \mathbf{x}) + (\Delta \mathbf{g} - H_k \Delta \mathbf{x})^{\mathrm{T}}}{\Delta \mathbf{x}^{\mathrm{T}} \Delta \mathbf{x}} - \frac{\Delta \mathbf{x}^{\mathrm{T}} (\Delta \mathbf{g} - \mathbf{H}_k \Delta \mathbf{x})(\Delta \mathbf{g} - \mathbf{H}_k \Delta \mathbf{x})^{\mathrm{T}}}{\Delta \mathbf{x}^{\mathrm{T}} \Delta \mathbf{x}^2}. \tag{3.4}$$

The advantage of using the PSB method, over say the BFGS method, and the reason for its popularity is based on the fact that it preserves the symmetry of the Hessian matrix, without necessarily imposing positive definiteness, it can achieve superlinear convergence, as well as satisfying the secant equation. The secant method is a requirement for quasi-Newton update Hessian schemes which states that given the displacement s_k and the change of gradients y_k, the secant equation requires that the matrix B_{k+1} map s_k into y_k.[122] Moreover, unlike the SR1 method, the PSB method does not have the same drawback as the latter with respect to the denominator.

The last of the quasi-Newton update Hessian method considered to be used with the RPH is the Bofill[125] method and is given by Equation 3.5. The Bofill method consists of a combination of the SR1 and PSB methods using weights. The Bofill method has been tested against other methods and has shown to work quite well, especially when TS structures are involved.[120,125]

$$\Delta \mathbf{H}_{\mathrm{Bofill}} = (1 - \phi) \Delta \mathbf{H}_{\mathrm{SR1}} + \phi \Delta \mathbf{H}_{\mathrm{PSB}}, \tag{3.5}$$

where the weighting function ϕ is

$$\phi = 1 - \left(\frac{(\Delta \mathbf{x}^{\mathrm{T}}(\Delta \mathbf{g} - \mathbf{H}_k \Delta \mathbf{x}))^2}{\Delta \mathbf{x}^2 (\Delta \mathbf{g} - \mathbf{H}_k \Delta \mathbf{x})^2} \right). \tag{3.6}$$

3.1.2 Compact finite difference update Hessian schemes

High-accuracy update Hessian schemes have recently been developed particularly for direct dynamics where the PES is determined on-the-fly and a high level of accuracy is desirable, therefore these higher-accuracy update Hessian schemes have also been considered here, in the context of the RPH dynamics.[123] This new family of update Hessian scheme is based on the second-order equation derived using compact finite difference (CFD)[126–130] and, as long as the potential energy is sufficiently smooth, the second-order equation will remain valid in all cases up to an $\mathrm{O}|\Delta \mathbf{x}|^3$ error compared to an $\mathrm{O}|\Delta \mathbf{x}|^2$ error for quasi-Newton update Hessian schemes. When used for chemical dynamics simulations, these CFD update Hessian schemes improved the accuracy when they were implemented in a Hessian-based integration algorithm.[123]

The underlying theory of CFD update Hessian schemes consists of using CFD which is a high-order method for approximating differentiations of functions without using a larger stencil (more sampling points). CFDs then achieve this higher accuracy by including differentiated terms at more locations within the stencil. In the following Sections, three CFD update Hessian schemes (CFD-SR1, CFD-PSB and CFD-Bofill), defined in Equations 3.7 - 3.11, are used to determine the Hessian matrices for RPH calculations and their performance in the context of RPH dynamics is assessed and compared to their quasi-Newton counterparts (SR1, PSB and Bofill).

$$\Delta \mathbf{H}_{\text{CFD-SR1}} = \frac{\mathbf{R}\mathbf{R}^T}{\mathbf{R}^T \Delta \mathbf{x}}, \tag{3.7}$$

$$\Delta \mathbf{H}_{\text{CFD-PSB}} = \frac{\Delta \mathbf{x}\mathbf{R}^T + \mathbf{R}\Delta \mathbf{x}^T}{\|\Delta \mathbf{x}\|^2} - \frac{\mathbf{R}\Delta \mathbf{x}^T}{\|\Delta \mathbf{x}\|^4} \Delta \mathbf{x}\Delta \mathbf{x}\mathbf{R}^T, \tag{3.8}$$

$$\Delta \mathbf{H}_{\text{CFD-Bofill}} = (1 - \phi)\Delta \mathbf{H}_{\text{CFD-SR1}} + \phi \Delta \mathbf{H}_{\text{CFD-PSB}}, \tag{3.9}$$

where the weighting function ϕ is

$$\phi = 1 - \frac{(\mathbf{R}\Delta \mathbf{x}^T)^2}{\|\mathbf{R}\|^2 \|\Delta \mathbf{x}\|^2}, \tag{3.10}$$

where $\mathbf{R}$ is

$$\mathbf{R} = 2\Big(\Delta\mathbf{g} - \mathbf{H}_k(\Delta\mathbf{x})\Big), \tag{3.11}$$

where just like in the quasi-Newton update Hessian schemes, $\Delta\mathbf{g} = \mathbf{g}_{k+1} - \mathbf{g}_k$ is the gradient difference between the new and old configurations, $\Delta\mathbf{x} = \mathbf{x}_{k+1} - \mathbf{x}_k$ is the vector containing the difference in the $3N$ Cartesian coordinates between the new and old configurations and $\mathbf{H}_k$ is the Hessian matrix at the old configuration.

3.2 Implementation of update Hessian schemes with the RPH

Within the RPH strategy, all of these update Hessian schemes are straightforward to implement, given an initial Hessian matrix. We also note that these update schemes are suitable to the problem of propagating Hessian matrices for systems which cross potential energy barriers, as they have been used for TS optimization problems.[120,123,131]

In the following sections, we consider several different routes to Hessian propagation along the MEP, with the aim of reducing the computational burden of calculating the Hessian matrices along the MEP whilst still providing an accurate estimate of the transmission coefficient. These different methods for propagating the Hessian along the MEP, shown in Figure 3.1, were the following: (i) a single ended update Hessian starting from the reactant (or product) minimum, (ii) analytical Hessian matrices calculated at both the reactant and product minima, with Hessian matrices along the MEP given by a weighted average based on the distance from either the reactant minima and the product minima, (iii) two single ended update Hessians starting from the reactant and product minima ending at the TS, and (iv) a single ended update Hessian starting from the TS to the reactant and (v) a single ended update Hessian starting from the TS to the product minima. Propagation schemes (i), (iii) and (iv) are straightforward implementations of the update Hessian equations shown in Equations 3.2 - 3.9; starting from an analytical Hessian matrix at one end-point of the MEP or from the TS, the update Hessian schemes can be used to calculate approximations to the Hessian matrices for the internal images along the MEP, using the Hessian matrix at the previous image as a starting point.

In the case of approach (ii), we note that, at any internal image along the MEP, let this be a point i, the weighted average over updated Hessian matrices from the

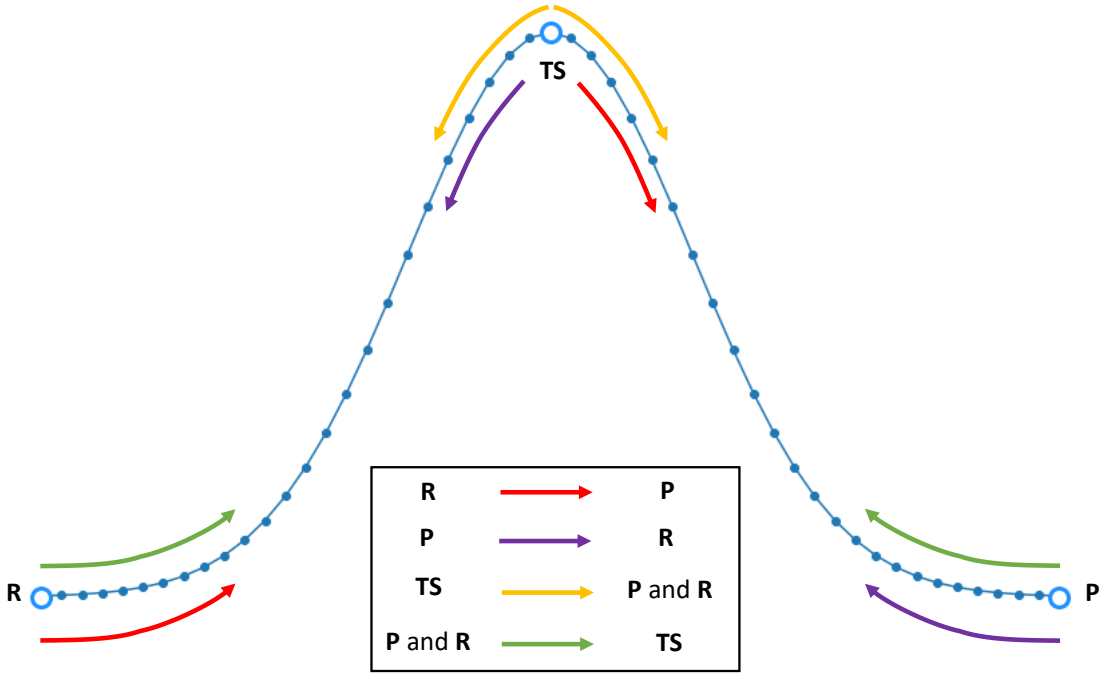

Figure 3.1: An illustration depicting the different approaches used to propagate the update Hessian schemes along the reaction path. These are; (i) a single ended update Hessian starting from the reactant (R) and ending at the product (P), (ii) a single ended update Hessian starting from P and ending at R, (iii) a weighted average of (i) and (ii), (iv) a single ended update Hessian starting at the saddle-point (TS) and ending at R, and lastly, (v) a single ended update Hessian starting at the saddle-point (TS) and ending at P

reactants or products is calculated as

$$\mathbf{H}_{\text{weighted average}} = \frac{N - \mathrm{i}}{N - 1}\mathbf{H}_{\mathrm{i}}^{\mathrm{r}} + \frac{\mathrm{i} - 1}{N - 1}\mathbf{H}_{\mathrm{i}}^{\mathrm{p}}, \tag{3.12}$$

where N is the total number of images along the MEP, $\mathbf{H}_{\mathrm{i}}^{\mathrm{r}}$ is the Hessian matrix propagated from the analytical Hessian matrix at the reactant minimum where $i = 2, ..., N-1$, $\mathbf{H}_{\text{N-i}}^{\mathrm{p}}$ is the Hessian matrix propagated from the analytical Hessian matrix at the product minimum. As an aside, we note that an alternative definition of the weighting in Equation 3.12 could instead use the values of the reaction-coordinates s at each image, rather than image index; however, in our current scheme, where spline-interpolation is used to create a series of closely-spaced images along the MEP, we find that the weights calculated using s instead of image-index are practically identical, as confirmed in Table S1 in the Appendix.

Finally, we note that each of the different propagation schemes can, in principle, be combined with any of the update Hessian schemes considered here. In practice, we find that most of these combinations of different propagation/update schemes

yield very poor results except for the double-ended approach; this point is discussed further below. As such for propagation schemes (iii) and (iv) in particular, we only use one update Hessian scheme which resulted in the closest approximations to the standard approach when the double-ended approach was used.

3.3 Application of Quasi-Newton update Hessian schemes with RPH dynamics

The four different quasi-Newton update Hessian schemes (SR1, PBS, Bofill and TS-BFGS) were implemented in the RPH framework in order to obtain transmission coefficients on three reaction systems: interconversion of cyclohexane from chair to twisted-boat conformer (R1), addition of nitrous oxide to ethene (R2), and 1,1-insertion of CO into the Co–C bond in the Heck and Breslow mechanism of hydroformylation.[132] These reactions were selected because recrossing effects were found to be significant; as a result, the impact of update Hessian should be simpler to observe. Furthermore, each of these reactions represents a different "reaction class", including isomerization without bond breaking/forming (R1), bimolecular addition (R2), and intramolecular shift reaction (R3); by studying different reaction types, we hope to draw firmer conclusions about the accuracy of the different update Hessian and propagation schemes considered here.

For all reactions, we use a 15 image MEP obtained by running a CI-NEB[96] calculation, and subsequently calculate the RPH using these images. For the standard RPH simulation method, this means that 15 Hessian matrices were evaluated along the reaction-path, whereas a maximum of two Hessian-matrix evaluations are required in all of the update Hessian schemes. Furthermore, in order to check the convergence, we perform additional calculations that use the initial MEP (comprising 15 images) and use spline interpolation to generate a path with a total of 50 images; this expanded 50-image path was also used to perform RPH simulations using both standard and update Hessian approaches. As such, below we compare two sets of results arising from simulations with either 15 or 50 images points in the RPH constructions. For the update Hessian schemes, the use of 50 discrete points along the MEP helps ensure that the so-called restricted-step condition,[125] which suggests that the PES variation due to harmonic approximation should be comparable to the true PES variation for update Hessian schemes to be applicable, is obeyed to an acceptable level across the MEPs for all reactions considered below (This is also confirmed in Table S2 in the Appendix).

The first two reactions were investigated using density functional theory (DFT) with the B3LYP functional[133–136] and 6-31G basis set.[137,138] The third reaction used

B3LYP with a 6-31G(d,p) basis set.[139,140] The choice of PES here is motivated by our desire to work on the same level of theory as previous simulations for the same reactions;[33,87] furthermore, we note that all of the methods discussed here can be used in combination with any PES method which provides energies, gradients and Hessian matrices. For the MD simulations, the first two reactions were performed at a temperature of 273 K, the third reaction was performed at a temperature of 423 K. For reference, the "standard" approach used to determine the transmission coefficient for all reactions consisted of calculating an analytical Hessian matrix at the 15 or 50 images along the MEP, and subsequently interpolating all discrete elements needed for the RPH.

For each reaction described below, $C_{fs}^{cl}(t)$ (described in Section 2.3, was evaluated using the RPH approximated with different propagation and update schemes. Initial RPH images along the MEP were obtained for each of the different reactions considered here by using the climbing-image nudged elastic band method,[96] as described below.

For the different choices of propagation/update schemes considered below, $C_{fs}^{cl}(t)$ was evaluated by sampling initial coordinates and momenta from the Boltzmann distribution for the underlying RPH. Each of these trajectories started at the dividing surface, defined by $s = 0$. Each set of initial coordinates and momenta were propagated using Hamilton's equations of motion determined from the RPH; the fourth-order Runge-Kutta algorithm was used to numerically integrate the equations-of-motion using a time-step of 0.30 fs. For each reaction considered, we found that a different total simulation time was required to ensure that $C_{fs}^{cl}(t)$ had reached a plateau, as shown in the results below; typically, each trajectory required 0.5-3 ps simulation time, and a total of 10^4 trajectories were performed for each of the different RPH update/propagation schemes considered below. Under these conditions, we find that the typical standard error in the plateau values of the $C_{fs}^{cl}(t)$ function is 2×10^{-3}; this value is typically much smaller than any observed differences between the different simulations methods investigated below.

To understand the relative performance of the different double-ended update Hessian schemes considered here, we investigated the predicted vibrational frequencies along the MEP, as well as the curvature and Coriolis coupling constants along the MEP (using 50 images). The aim was to use this information to explain the relative performance of the quasi-Newton update Hessian schemes, SR1, PSB, Bofill and TS-BFGS.

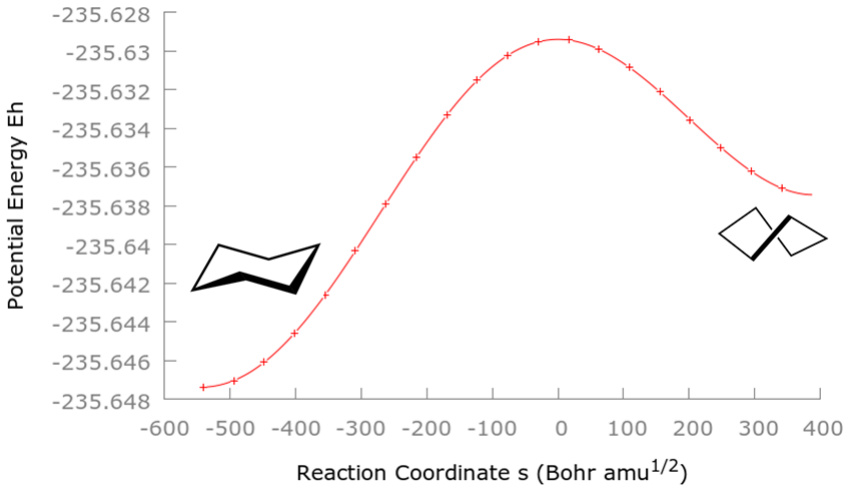

Figure 3.2: Interconversion of cyclohexane from chair to twist-boat conformer.

3.3.1 Interconversion of cyclohexane: from chair to twisted-boat

The first reaction studied was the interconversion of cyclohexane from chair conformer to twist-boat conformer, shown in Figure 3.2. As discussed below, $C_{fs}^{cl}(t)$ (and transmission coefficient α) were calculated for the four update Hessian schemes using *only* the double-ended propagation scheme; the calculated $C_{fs}^{cl}(t)$ are shown in Figure 3.3 and Figure 3.4, and compared to that obtained using the standard approach. Using the standard approach with the RPH, the $C_{fs}^{cl}(t)$ drops sharply at $\sim$ 200 fs and plateaus at $\sim$ 400 fs. In both sets of results (15 and 50 MEP points), when compared to the standard approach, the four update Hessian schemes all follow a very similar profile, with a steep initial decrease in $C_{fs}^{cl}(t)$ and then a smooth plateau after $\sim$ 350 fs. The PSB, Bofill and TS-BFGS updates in particular, look nearly identical, both underestimating the plateau value by approximately the same amount. This suggests that the PSB term in the Bofill update scheme was weighted more than the SR1 term, effectively making the Bofill update Hessian very similar to the PSB update Hessian. When 15 MEP points are used for RPH construction, all update Hessian schemes are very close to the standard approach. In the case of the 50 MEP points (Figure 3.4), the plateaus for the PSB, Bofill and TS-BFGS are relatively the same as they are when 15 MEP points are used, indicating some level of convergence already, however the SR1 update Hessian method results in a different plateau value.

Table 3.1 shows the transmission coefficient calculated for all four Hessian approaches for the interconversion of cyclohexane for 50 and 15 MEP points. The standard approach results in a $C_{fs}^{cl}(t)$ plateau value of 0.50 and 0.43 for 50 and 15 MEP points, respectively, whereas the plateau value for the SR1, PSB, Bofill, TS-

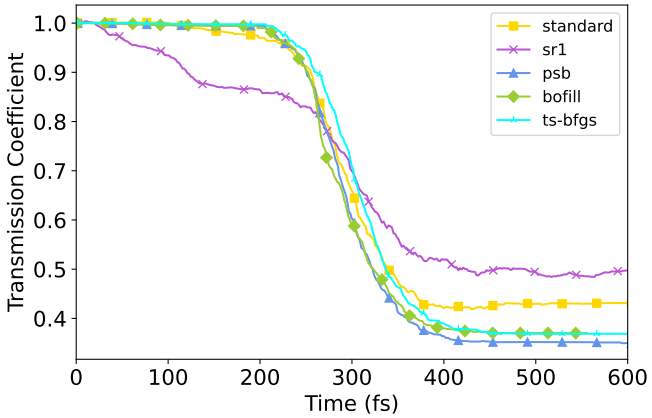

Figure 3.3: Normalized flux-side correlation function computed using the RPH with different update Hessian schemes for the interconversion of cyclohexane using 15 MEP discrete points. Results are shown for the analytical Hessian (gold squares), SR1 (purple crosses), PSB (blue triangles), Bofill (green diamonds) and TS-BFGS update Hessian schemes (cyan empty triangles).

BFGS update Hessian schemes were 0.66 (0.49), 0.41 (0.35), 0.44 (0.37) and 0.39 (0.37), respectively. Note that the transmission coefficient plateau values in brackets are for the 15 point MEP. Based on these results, the TS-BFGS, Bofill and PSB update Hessians performed better than the SR1 update Hessian when the transmission coefficient was determined using 50 MEP points. However, as noted above, because the Bofill update Hessian resembles the PSB update Hessian for this reaction, the estimate given for the plateau value by the Bofill update is very close to that of the PSB update (and the standard approach). The SR1 update Hessian underestimates the contributions from recrossing to the transmission coefficient, with a plateau value of 0.66, compared to the 0.50 plateau value using the standard approach. Based on the results shown in Fig 3.3 and 3.4, convergence does not seem to improve with the increase in points along the MEP. One would expect that adding more discrete points along the MEP increases the characterisation of the MEP, however, when propagating an approximate Hessian, this may not be the case. Instead, this may be a case of error cancellation, whereby, as there are more discrete points, the error in the approximate Hessian being propagated accumulates.

Table 3.1: Transmission coefficients for the interconversion of cyclohexane calculated with the RPH using different Hessian methods with 50 MEP points. Parentheses show results for simulations performed using 15 MEP points for RPH construction.

RPH Hessian method	$C_{fs}^{cl}(t)$ **plateau value**
Standard	0.50 (0.43)
SR1	0.66 (0.49)
PSB	0.41 (0.35)
Bofill	0.44 (0.37)
TS-BFGS	0.39 (0.37)

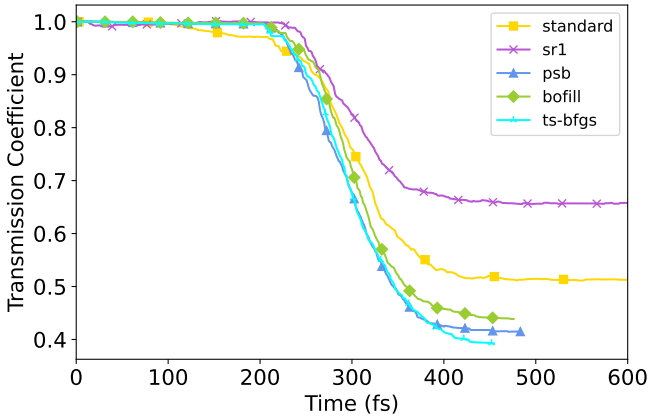

Figure 3.4: Normalized flux-side correlation function computed using the RPH with different update Hessian schemes for the interconversion of cyclohexane using 50 MEP discrete points. Results are shown for the analytical Hessian (gold squares), SR1 (purple crosses), PSB (blue triangles), Bofill (green diamonds) and TS-BFGS update Hessian schemes (cyan empty triangles).

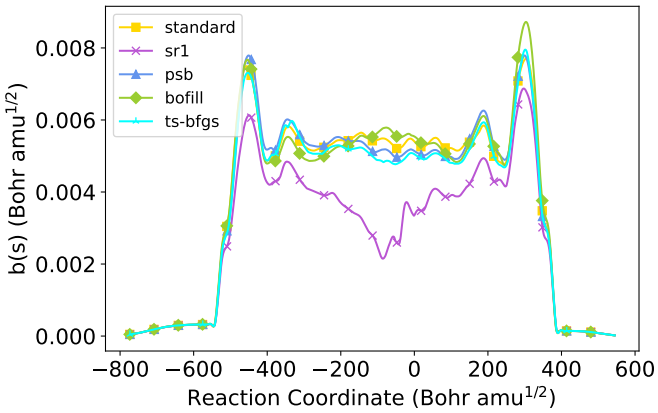

Figure 3.5: Total curvature coupling along the reaction coordinate s for the interconversion of cyclohexane (R1).

Figures 3.5 and 3.6 show the total absolute value of the curvature coupling and total absolute value of the Coriolis coupling along the MEP, providing some insights into how these coupling factors influence the observed dynamics. As shown in Equation (2.58), the curvature coupling describes the dynamic coupling between the reaction path and vibrational modes; in other words, it describes the extent of energy transfer between translational and vibrational degrees-of-freedom. On the other hand, the Coriolis coupling describes the transfer of energy between vibrational modes, highlighting energy dissipation, as shown in Equation (2.59).

In Figures 3.5 and 3.6, possible reasons as to why the PSB Bofill and TS-BFGS update Hessian method perform better than the SR1 update Hessian method start to become a little clearer. With regards to the curvature coupling in Figure 3.5, it can be seen that, in the case of the PSB, Bofill and TS-BFGS update schemes,

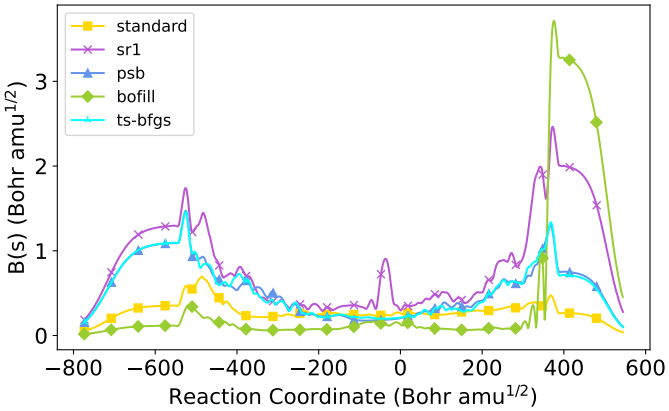

Figure 3.6: Total Coriolis coupling along the reaction coordinate s for the interconversion of cyclohexane (R1).

the coupling values given by the different update Hessian schemes are similar, both in magnitude and trend, to that observed in the standard approach (using analytic Hessian matrices along the MEP). However, in the case of the SR1 approach, this update scheme fails to correctly estimate the curvature coupling values between $s = -400$ Bohr amu$^{1/2}$ and $s = 400$ Bohr amu$^{1/2}$, especially before the TS ($s = 0$), where there is a significant "dip" in coupling value.

In Figure 3.6, we show the Coriolis coupling for all of the update Hessian schemes and the standard approach. The PSB, Bofill and TS-BFGS update Hessian schemes result in comparable values of the Coriolis coupling to the standard approach, particularly in the region of the TS ($s = 0$, where the dynamics is most relevant to the calculation of the transmission coefficient); this is then reflected in the fact that the associated transmission coefficients are close to that of the standard approach. On the other hand, the SR1 update Hessian fails to accurately approximate the transmission coefficient (Figure 3.4), with the transmission coefficient being too large. A plausible explanation for this can be linked to the sharp peak close to the TS in the Coriolis coupling of Figure 3.6; this larger value in coupling means that more energy is dissipated into the vibrational modes and thus, as mentioned previously, there is less energy to recross the energy barrier. As a result, the predicted SR1 transmission coefficient is too high for R1 (see Table 3.1).

Finally, the Hessian matrices used to construct the elements of the RPH have also been analysed by calculating the root mean square deviation between Hessian matrices generated in the standard approach and those from the update Hessian schemes. Furthermore, the full sets of frequencies determined by the standard approach and the update Hessian schemes using 50 MEP points are shown in Figures 1 - 5 in the Appendix. In Figure 3.7, we find that the root-mean-square deviations show a significant peak for the SR1 update Hessian at image 24, where the

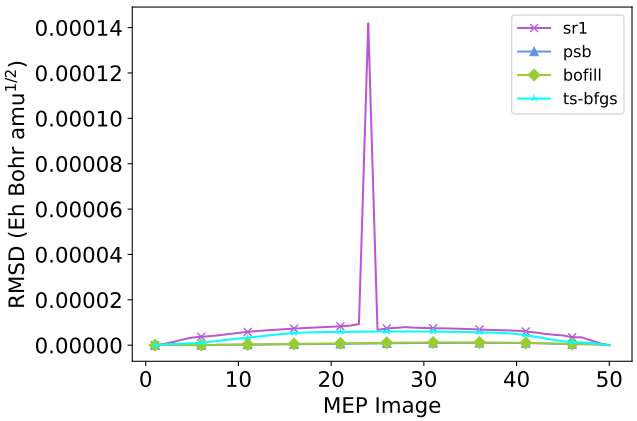

Figure 3.7: Hessian RMSD at each MEP discrete point in the cyclohexane isomerisation reaction (R1), used to construct using the RPH, between the standard approach and the update Hessian schemes.

error is significantly larger than the other methods. In Figures 1 - 5, all update Hessian schemes display similar magnitudes in the majority of frequencies along the reaction coordinate. The PSB, Bofill and TS-BFGS update Hessians result in near-identical frequencies with one another, with all three resulting in quite broad frequency variations for the higher normal modes in contrast to the very flat trends in the standard approach. These broad frequencies could reflect the error propagation due to the Hessian update being propagated from the minima, resulting in approximate Hessians along the MEP differing from the analytical Hessian. As a result, the frequencies are not exactly the same as the standard approach and are broader. The similarity between these three update Hessian schemes is also reflected in the transmission coefficient calculations, where they have similar values to one another too. The SR1 update Hessian resulted in some frequencies changing erratically along the reaction coordinate, providing another observation indicating that SR1 behaves qualitatively different compared to the other update schemes. This could be due to the one drawback of the SR1 update Hessian scheme, whereby the denominator of the equation can sometimes approach zero, which would lead to inaccurate approximate Hessians which would differ greatly to the standard approach.

3.3.2 Addition reaction of ethene and nitrous oxide

The second reaction studied was the addition of nitrous oxide to ethene to form oxadiazoline shown in Figure 3.8. The $C_{fs}^{cl}(t)$ functions were calculated using the standard approach and the four update Hessian schemes with both 15 and 50 MEP points, and are shown in Figures 3.9 and 3.10. Similar to the first reaction, the analytical Hessian approach results in a $C_{fs}^{cl}(t)$ which drops sharply at 200 fs and plateaus shortly after this time. The update Hessian schemes show qualitatively

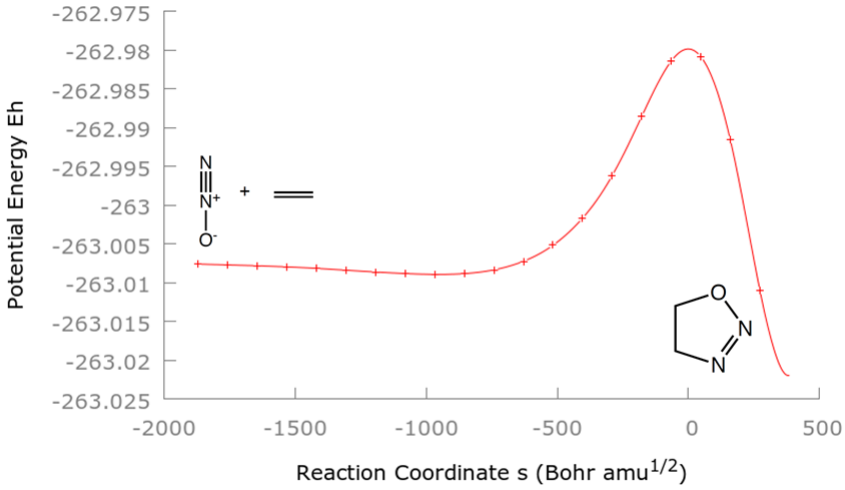

Figure 3.8: Addition of nitrous oxide to ethene.

similar behaviour, with all four showing a drop and a smooth plateau, consistent with the standard approach. When using 15 MEP points for RPH construction, all update Hessian approaches give similar results, as well as good agreement with the standard calculations. However, when 50 MEP points are used, only the TS-BFGS curve shows a reasonable level of agreement with the standard approach; the remaining update Hessian schemes generally over-estimate the transmission coefficient by around 50%.

The $C_{fs}^{cl}(t)$ plateau values for the four different Hessian schemes are shown in Table 3.2. The standard approach results in a transmission coefficient of 0.64 and 0.92 for 50 and 15 MEP points, with the SR1, PSB, Bofill and TS-BFGS update Hessians giving transmission coefficients of 0.91 (0.98), 0.87 (0.96), 0.87 (0.94) and 0.72 (0.95), respectively. Again, the transmission coefficient plateau values in brackets are for the 15 point MEP. All update Hessian schemes were close to the standard approach when 15 MEP points were used for the RPH. However, when a converged $C_{fs}^{cl}(t)$ is calculated using 50 MEP points, only the TS-BFGS Hessian method results in a plateau value close to the standard approach. Again, we note that the 50 MEP points do not necessarily increase the convergence when it comes to the update Hessian schemes, as it may actually increase the possibility of error propagation or error cancellation. The converged results show that the TS-BFGS update Hessian method performed better than its counterparts, with a difference of just 0.08 compared to the standard approach, which will be investigated further in this Section. Furthermore, for the SR1, PSB, and Bofill update Hessian schemes, the $C_{fs}^{cl}(t)$ plot seemingly exhibit qualitatively different features compared to TS-BFGS or the standard approach, perhaps indicating different initial dynamics.

Figure 3.11 and Figure 3.12 show the different couplings along the MEP for the addition of nitrous oxide to ethene (R2). In this case, Figure 3.11 shows that all

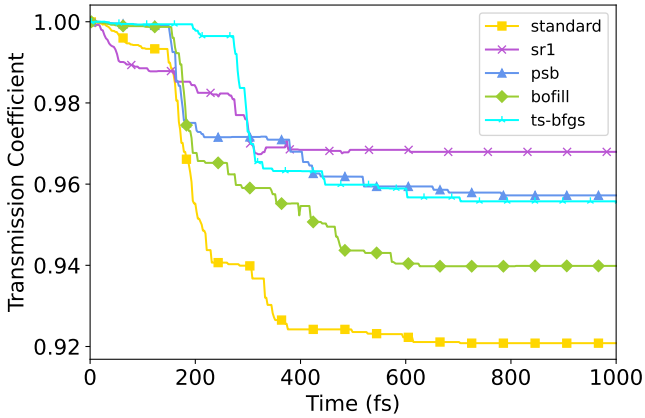

Figure 3.9: Normalized flux-side correlation function computed using the RPH with different update Hessian schemes for the addition of nitrous oxide to ethene using 15 MEP discrete points . Results are shown for the analytical Hessian (gold squares), SR1 (purple crosses), PSB (blue triangles), Bofill (green diamonds) and TS-BFGS update Hessian schemes (cyan empty triangles).

Table 3.2: Transmission coefficients for the addition of nitrous oxide to ethene calculated with the RPH using different Hessian methods with 50 MEP points. Parentheses show results for simulations performed using 15 MEP points for RPH construction.

RPH Hessian method	$C_{fs}^{cl}(t)$ **plateau value**
Standard	0.64 (0.92)
SR1	0.91 (0.98)
PSB	0.87 (0.96)
Bofill	0.87 (0.94)
TS-BFGS	0.72 (0.95)

update Hessian schemes can correctly approximate the broad shape of the curvature coupling along the MEP. For example, all methods show a "dip" near the TS ($s = 0$), with two large peaks on either side; furthermore, the behaviour on the "exit" channel, moving towards negative reaction-coordinate values, is also very similar across all update Hessian schemes (and compares well to the standard approach). As such, on the basis of Figure 3.11 alone, one might expect the transmission coefficient using all of the update Hessian schemes to be comparable to the standard approach, however as shown in Figure 3.10, this is not the case.

The Coriolis couplings in Figure 3.12 reveal important differences between the update Hessian schemes. Here, the standard approach results in small absolute values of the Coriolis coupling at the upper and lower limits of the MEP, with larger total Coriolis coupling in the region bound by $s = 500$ Bohr amu$^{1/2}$. With regards to the update Hessian schemes, the Coriolis couplings have some similarities between themselves, but also clear dissimilarities relative to the standard approach. Compared to the standard approach, the update Hessian schemes fail to correctly replicate the shape of the Coriolis coupling along the MEP; however, in the region

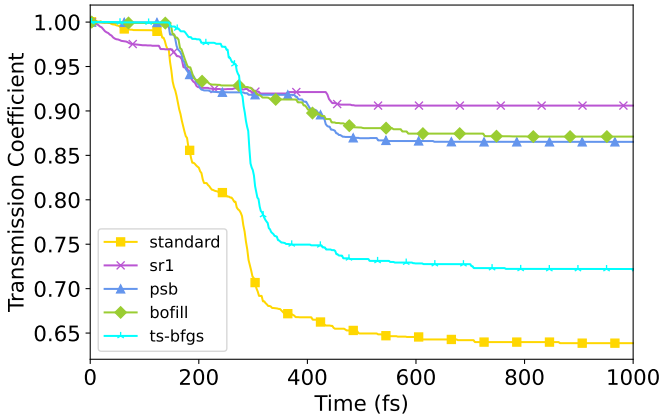

Figure 3.10: Normalized flux-side correlation function computed using the RPH with different update Hessian schemes for the addition of nitrous oxide to ethene using 50 MEP discrete points. Results are shown for the analytical Hessian (gold squares), SR1 (purple crosses), PSB (blue triangles), Bofill (green diamonds) and TS-BFGS update Hessian schemes (cyan empty triangles).

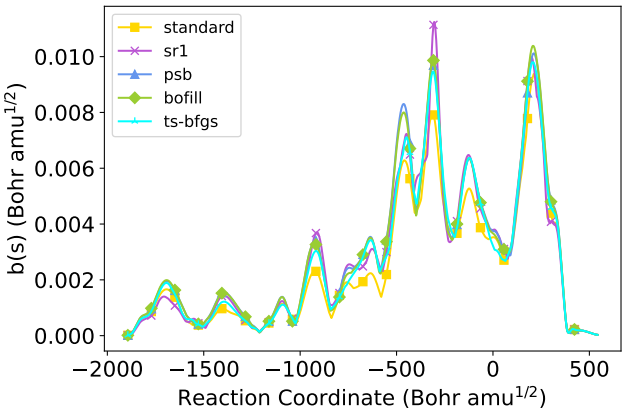

Figure 3.11: Total curvature coupling along the reaction coordinate s for the nitrous oxide (R2). addition to ethene (R2).

around the TS ($s = 0$), comparable coupling magnitudes are observed. Moving away from $s = 0$, it is clear, however, that the behaviour of SR1 is qualitatively different from the other coupling schemes, as also reflected in the calculated transmission coefficients (Table 3.2). In particular, on a qualitative level, the larger Coriolis coupling peaks for SR1 imply stronger energy dissipation into vibrational modes, which could lead to less recrossing along the reaction-coordinate s through the curvature coupling, coupling the reaction-coordinate to the vibrational modes, consistent with the calculated transmission coefficient. However, a similar analysis does not notably explain why the TS-BFGS method is more similar to the expected transmission coefficient for R2.

To better understand the relative behaviour of SR1 and TS-BFGS, Figure 3.13 shows the average value of the time-dependent reaction coordinate s (averaged over

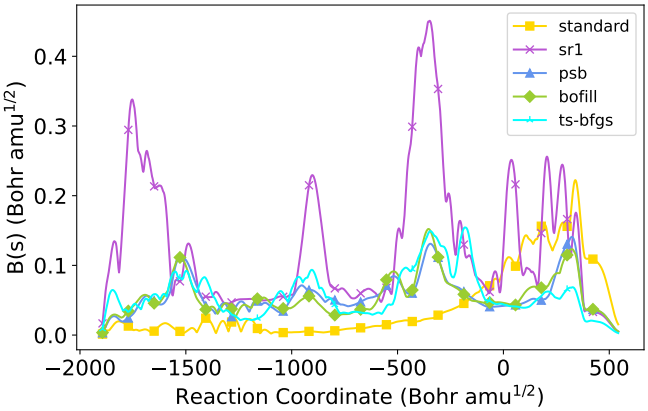

Figure 3.12: Total Coriolis coupling along the reaction coordinate s for the nitrous oxide addition to ethene (R2).

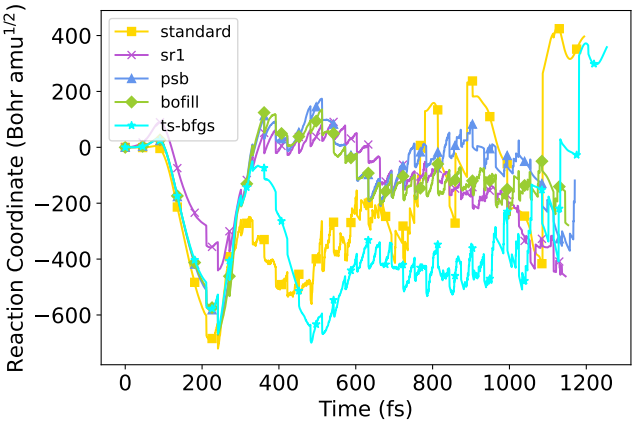

Figure 3.13: Average time-dependent value of the reaction coordinate s for R2 (nitrous oxide addition to ethene), calculated for all update Hessian schemes and the standard method. Results are averaged over 25×10^3 independent MD trajectories. We note that the somewhat jagged appearance of the lines is due to the different statistics of different points, given that not all trajectories run for the same length of time.

25×10^3 trajectories). The standard approach and the update Hessian schemes all exhibit the same behaviour up to about $t = 300$ fs; all start at the TS ($s = 0$), and briefly move towards the product region ($s < 0$) before subsequently heading back towards the region of the TS. At this point (around $t = 300$ fs), the average trajectories observed in the SR1, PBS and Bofill schemes then broadly cross into the product region ($s > 0$), whereas the average trajectory in the standard and TS-BFGS case returns towards the reactant region. These differences in trajectory behaviour along s then translate into differences in the calculated flux correlation functions (Figure 3.11) and transmission coefficients.

Figure 3.13 suggests that, when using TS-BFGS update Hessian, energy is being dissipated into the vibrational modes and away from the translational (s) degree-of-

freedom, particularly in the region from $s = -400$ Bohr amu$^{1/2}$ to $s = -100$ Bohr amu$^{1/2}$. To further confirm the important role of the Coriolis coupling in influencing these dynamics, we have also performed simulations for all update Hessian schemes, but with the Coriolis coupling factor $\mathbf{B}(s)$ set to zero. In these simulations, we find that all averaged time-dependent s trajectories become very similar, with TS-BFGS closely matching the three other update Hessian schemes behaviour observed in Figure 3.13. In other words, the Coriolis coupling term can be identified as the key factor resulting in observed differences in the behaviour of TS-BFGS.

Furthermore, in the region around $s = -100$ Bohr amu$^{1/2}$, where the TS-BFGS trajectories in Figure 3.13 begin to diverge from the other methods, we observe a corresponding peak in the Coriolis coupling plot (Figure 3.12), indicating a region of relatively strong coupling dispersing energy into vibrational modes. In combination with the observed similarity of dynamics along s when Coriolis coupling is removed, these observations suggest that the Coriolis coupling peak at $s = -100$ Bohr amu$^{1/2}$ may be significant in dissipating energy, resulting in the divergent trajectories of the TS-BFGS method relative to the other schemes.

It is worth noting that consideration of the Coriolis coupling peaks aligns with the observed dynamic behaviour of TS-BFGS, but this interpretation is less straightforward in the case of SR1. In particular, the SR1 Coriolis coupling shows a very strong coupling peak at $s = -340$ Bohr amu$^{1/2}$ which does not appear to significantly influence the dynamics along s (at least, when compared to the results obtained by the 'standard' method). Further investigation of the vibrational mode dynamics in the region of this peak shows that the averaged magnitudes of the squared normal-mode displacements, $\langle q^2 \rangle$, tend to be generally smaller for those modes exhibiting strong coupling (and so giving rise to the peak in Coriolis coupling). In contrast, the modes exhibiting strong Coriolis coupling in TS-BFGS at $s = -100$ Bohr amu$^{1/2}$ do exhibit relatively larger mode-displacements. Of course, a somewhat selective analysis of a few vibrational modes in a many-coupled-mode system cannot give the full picture; but we note that these simulations clearly highlight differences in the performance of the TS-BFGS method in this reaction, when compared to the other schemes considered here.

Lastly, we again look at the Hessian matrices used to construct the elements of the RPH, as well as the full sets of frequencies determined by the standard approach and the update Hessian schemes. Figure 3.14 shows the root-mean-square deviation between Hessian matrices generated in the standard approach and those from the update Hessian schemes, where, all of the update Hessian schemes are comparable in terms of absolute error values, but SR1 demonstrates significant peaks which differ to the other methods, suggesting significant differences in the SR1 Hessian matrix and that calculated by the standard approach possibly explained by the drawback of

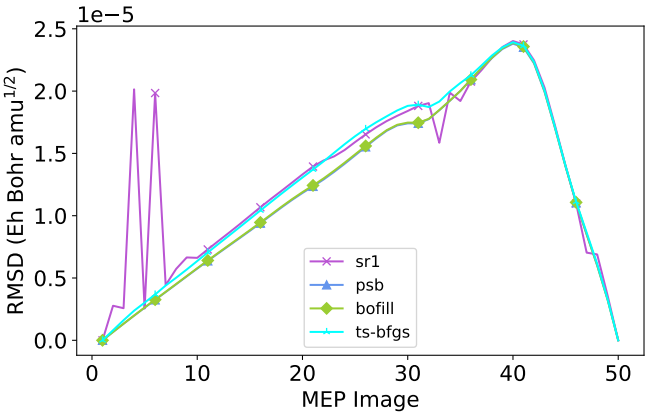

Figure 3.14: Hessian RMSD at each MEP discrete point in the nitrous oxide addition to ethene reaction (R2), used to construct using the RPH, between the standard approach and the update Hessian schemes.

the SR1 Hessian update scheme. In Figures 8-12 in the Appendix, we see a similar pattern, where, the PSB, Bofill, TS-BFGS update Hessian schemes result in near-identical frequencies and the SR1 update Hessian method resulting in frequencies which change drastically along the reaction coordinate. As such, these calculations provide some more evidence that the SR1 scheme is the least preferred of those considered here, and that the resulting transmission coefficient could be a result of error cancellation instead of accurate approximations.

3.3.3 1,1-insertion of CO into the Co–C bond in the Heck-Breslow hydroformylation mechanism

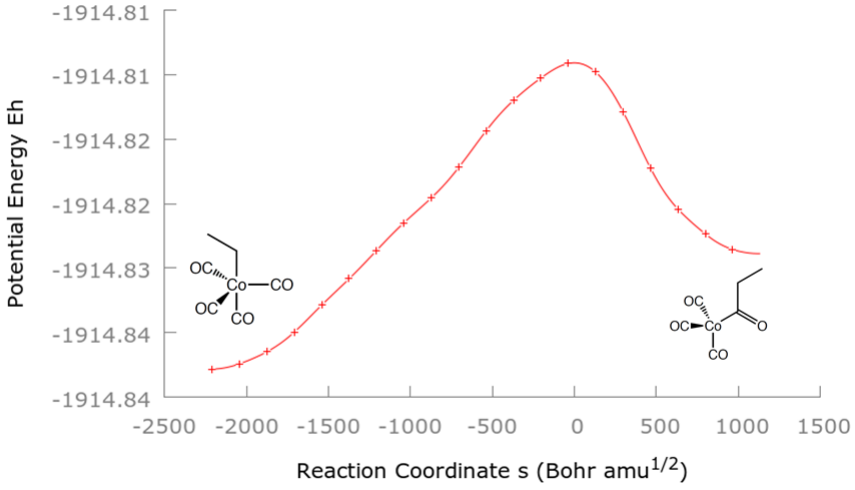

Figure 3.15: 1,1-insertion of CO into the Co–C bond in the Heck and Breslow mechanism of hydroformylation.

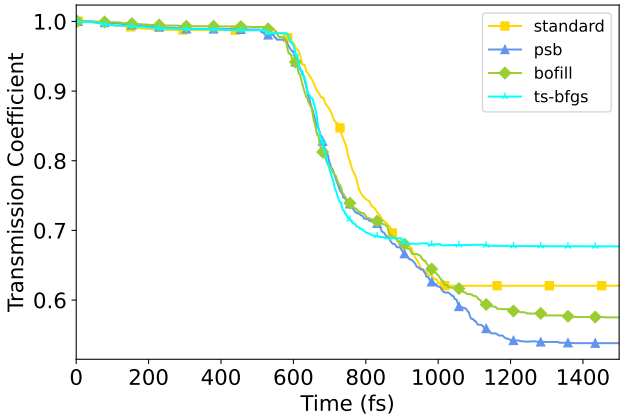

Figure 3.16: Normalized flux-side correlation function computed for CO insertion in the Heck-Breslow hydroformylation mechanism using the RPH with different update Hessian schemes using 15 MEP discrete points. Results are shown for the analytical Hessian (gold squares), SR1 (purple crosses), PSB (blue triangles), Bofill (green diamonds) and TS-BFGS update Hessian schemes (cyan empty triangles).

The third reaction studied was the 1,1-insertion of CO into the Co–C bond in the Heck-Breslow hydroformylation mechanism, shown in Figure 3.15. The calculated $C_{fs}^{cl}(t)$ are shown in Figure 3.16 and 3.17 for the four different Hessian schemes considered here. The timescale at which the lines plateau is significantly longer than in reactions R1 and R2, a feature which may be related to the more complex nature of this reaction, involving significant intramolecular atomic displacements. Despite this, the update Hessian schemes perform qualitatively quite well, with all four methods converging to plateaus on a similar time-scale to the standard approach. However, using 15 MEP points for the SR1 update Hessian results in a failure to calculate the transmission coefficient due to unstable MD trajectories, indicating that more images are required for the RPH construction and transmission coefficient calculation in this case. Furthermore, the standard method indicates that there is a significant amount of dynamic recrossing associated with this reaction, and similar trends are observed for all of the update Hessian schemes. Although there are some clear differences in the calculated $C_{fs}^{cl}(t)$ for the different update Hessians, the SR1, PSB and the Bofill update Hessian schemes demonstrate a plateau value that was very close to the standard approach, specifically when using 15 MEP points. When 50 MEP points are used, the PSB, Bofill and SR1 update Hessians demonstrate a plateau which is similar to that of the standard approach (especially when one considers the relatively long time-scale involved here compared to R1 and R2).

Table 3.3 shows the transmission coefficients for R3, calculated using the standard approach and the update Hessian schemes using 15 and 50 MEP points. Using the standard approach, the transmission coefficients were determined to be 0.62 and 0.74, for 15 and 50 images respectively. The PSB, Bofill and TS-BFGS update

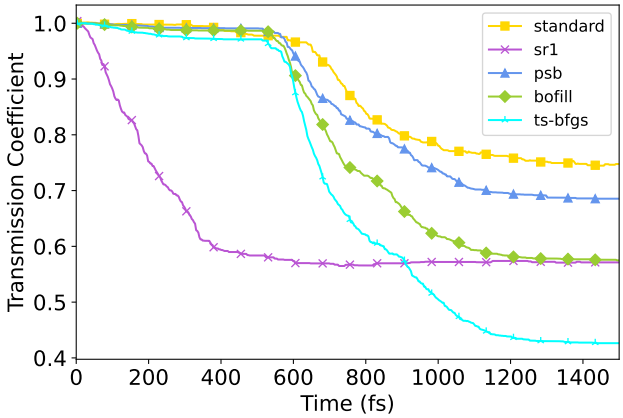

Figure 3.17: Normalized flux-side correlation function computed for CO insertion in the Heck-Breslow hydroformylation mechanism using the RPH with different update Hessian schemes using 50 MEP discrete points. Results are shown for the analytical Hessian (gold squares), SR1 (purple crosses), PSB (blue triangles), Bofill (green diamonds) and TS-BFGS update Hessian schemes (cyan empty triangles).

Table 3.3: Transmission coefficients for the 1,1-insertion of CO into the Co–C bond in the Heck-Breslow mechanism of hydroformylation calculated with the RPH using different update Hessian schemes with 50 MEP points. Parentheses show results from simulations using 15 images for RPH construction.

RPH Hessian method	$C_{fs}^{cl}(t)$ **plateau value**
Standard	0.74 (0.62)
SR1	0.57 (N/A)
PSB	0.68 (0.55)
Bofill	0.57 (0.57)
TS-BFGS	0.42 (0.68)

Hessians result in transmission coefficients which were very close to the standard approach,when 15 MEP points were used for the RPH, differing by just 0.07, 0.05 and 0.06 respectively. When 50 MEP points were used, the SR1, PSB and the Bofill performed best, with differences to the standard approach of 0.17, 0.06, and 0.17, respectively. The TS-BFGS update Hessian resulted in a transmission coefficient of 0.42 which differs from the standard approach by 0.32, a clear underestimation of the transmission coefficient. This could be likely due to some error propagation as a result of including more discrete points on the MEP, leading to the error in the approximate Hessian to increase with respect to the analytical Hessian.

Figure 3.18 and Figure 3.19 show the curvature coupling and the Coriolis coupling respectively along the MEP for the 1,1-insertion of CO into the Co–C bond in the Heck-Breslow mechanism of hydroformylation. Similarly to the addition of nitrous oxide to ethene, Figure 3.18 shows that all update Hessian schemes can correctly approximate the broad shape of the curvature coupling along the MEP, in the sense

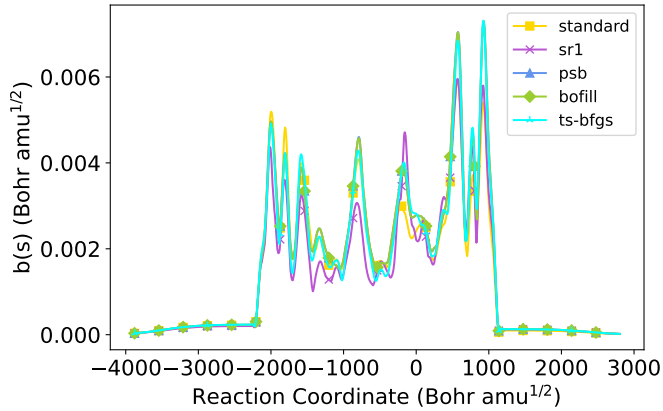

Figure 3.18: Total curvature coupling along the reaction coordinate s for 1,1-insertion of CO into the Co–C bond in the Heck-Breslow mechanism of hydroformylation (R3).

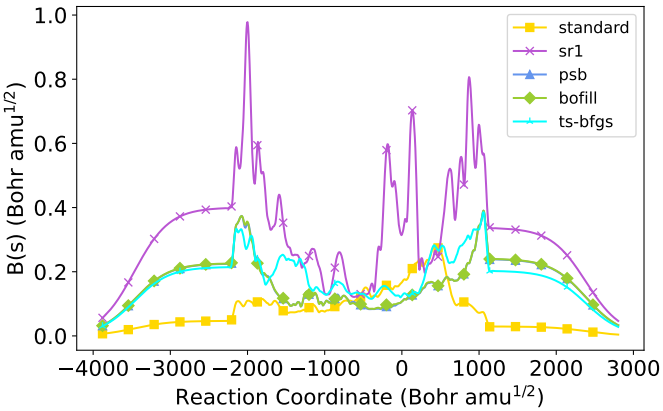

Figure 3.19: Total Coriolis coupling along the reaction coordinate s for the 1,1-insertion of CO into the Co–C bond in the Heck-Breslow mechanism of hydroformylation (R3).

that where the standard method exhibits a peak, so do the update Hessian schemes. Despite being similar in shape, it is clearer that there are differences in magnitude in the curvature couplings between the standard approach and the update Hessian schemes, which can already account for differences in the resulting transmission coefficients. Moreover, even between the update Hessian schemes a clearer divide is apparent between the SR1 scheme and the PSB, Bofill and TS-BFGS schemes. The SR1 scheme tends to underestimate or overestimate the curvature coupling peaks along the reaction coordinate compared to the other update Hessian scheme and the standard approach, which can explain why the resulting transmission coefficient converged so much quicker than the other schemes.

Fig 3.19 shows the Coriolis coupling along the reaction coordinate. In the standard approach, the Coriolis coupling has a value of ~ 0.1 in the region of s $= -1000$ Bohr amu$^{1/2}$ to s $= -500$ Bohr amu$^{1/2}$, and from then on in the region of s $= -500$

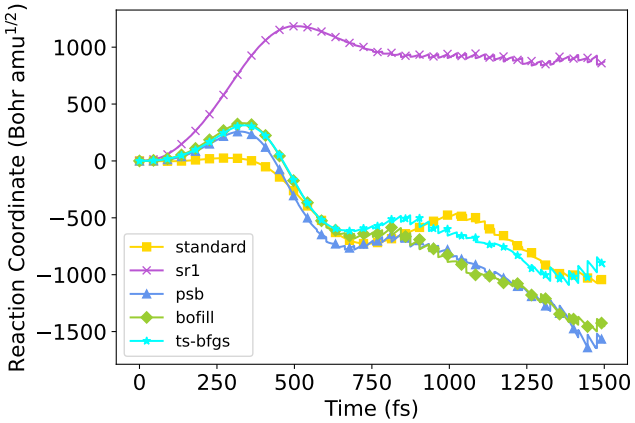

Figure 3.20: Average time-dependent value of the reaction coordinate s for R3 (1,1-insertion of CO into the Co–C bond in the Heck-Breslow mechanism of hydroformylation), calculated for all update Hessian schemes and the standard method. Results are averaged over 25×10^3 independent MD trajectories. We note that the somewhat jagged appearance of the lines is due to the different statistics of different points, given that not all trajectories run for the same length of time.

Bohr amu$^{1/2}$ to s = 500 Bohr amu$^{1/2}$, the Coriolis coupling value increase until it peaks at 0.3. Overall, no update Hessian schemes approximates the Coriolis coupling adequately across the reaction coordinate, in particular the SR1 scheme which significantly overestimate the Coriolis coupling along the reaction coordinate. The TS-BFGS scheme resulted in a Coriolis coupling with a larger magnitude than the standard approach, at s = −2000 Bohr amu$^{1/2}$ to −500 Bohr amu$^{1/2}$, however from s = −500 Bohr amu$^{1/2}$ to s = 500 Bohr amu$^{1/2}$ the magnitude is similar to the standard approach, especially at the peak s = 500 Bohr amu$^{1/2}$which is approximated well by the TS-BFGS scheme. From s = 500 onward, the TS-BFGS Coriolis coupling continues to increase, unlike the standard approach. The PSB and Bofill schemes resulted in near identical absolute Coriolis coupling along the reaction coordinate, with very slight minimal differences. In a similar way to the TS-BFGS scheme, they have peaks at s = 2000 Bohr amu$^{1/2}$ and s = 1000 Bohr amu$^{1/2}$ which are larger in magnitude than the standard approach. For the rest of the reaction coordinate, the resulting PSB and Bofill Coriolis coupling is similar to the standard approach (between s = −1500 Bohr amu$^{1/2}$ to s = 0 Bohr amu$^{1/2}$ but fails to correctly approximate the magnitude of the peak at s = 500 Bohr amu$^{1/2}$.

Similarly to R2, investigating the curvature and Coriolis coupling does not offer a clear explanation for the resulting update Hessian schemes transmission coefficients. As such, the average value of the time-dependent reaction coordinate s (averaged over 25×10^3 trajectories) is shown in Figure 3.20. It can be seen that for the standard approach and all of the update Hessian schemes besides the SR1 scheme, the average value of the time-dependent reaction coordinate behaves, qualitatively, in a very similar way. This would explain why that is also the case for the transmission

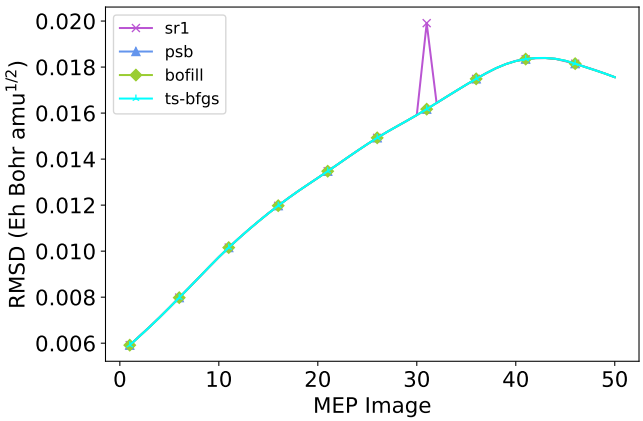

Figure 3.21: Hessian RMSD at each MEP discrete point in the the 1,1-insertion of CO into the Co–C bond in the Heck-Breslow mechanism of hydroformylation reaction (R3), used to construct using the RPH, between the standard approach and the update Hessian schemes.

coefficients. For all update Hessian schemes, the trajectories initially start a the TS ($s = 0$) and move towards the product region ($s > 0$), unlike the standard approach which, stays at the TS region. At $\sim$ 350 fs, the PSB, Bofill and TS-BFGS schemes go back towards the TS region, and at 400 fs continue towards the reactant region, at $s = 600$ just like the standard approach. Between 700 fs and 1000 fs, the standard approach gradually climbs back towards the TS region however, is stopped at s = 500 Bohr amu$^{1/2}$ and subsequently goes back to the reactant region, s = 1000 Bohr amu$^{1/2}$. The PSB, Bofill and TS-BFGS schemes follow a similar behaviour but do so earlier at 600 fs and subsequently plummet down towards the reactant region. Unlike the other update Hessian schemes, the SR1 scheme does not follow the same behaviour of the standard approach, where instead of returning to the TS region after 300 fs, the SR1 scheme goes deeper into the product region (s = 1000 Bohr amu$^{1/2}$), showing no similarities to the standard approach or any of the update Hessian schemes.

In Figure 3.17, the PSB and Bofill update Hessian schemes are very similar, which confirms what has been the trend already in the transmission coefficient and coupling constants. However, the slight differences in the Coriolis coupling between the PSB and Bofill schemes highlighted in Figure 3.20, result in the average value of the time-dependent reaction coordinate for the Bofill scheme to be more similar to that of the standard approach at $\sim$ 600 fs into the simulation which is when the transmission coefficient starts to converge. In comparison, at the same time ($\sim$ 600 fs), the PSB scheme is lower on the reaction coordinate than both the Bofill scheme and standard approach.

To complete the analysis, we look at the Hessian matrices used to construct the elements of the RPH by calculating the root mean square deviation between Hes-

sian matrices generated in the standard approach and those from the update Hessian schemes. In Figure 3.22, the root-mean-square deviations show that all update Hessian schemes have the same magnitude across the majority of images on the MEP. However, the SR1 update Hessian scheme has a peak at the 31st image on the MEP which is not the case for the other schemes, possibly explained by the drawback of the SR1 Hessian update scheme. Finally, Figures 15 - 19 in the Appendix show the full sets of frequencies determined by the standard approach and the update Hessian schemes. Similarly to R1, the PSB, Bofill and TS-BFGS update Hessian schemes all share a similar magnitude as well as broad frequency variations for certain modes compared to the flat frequencies in the standard approach, showing how the approximate Hessians using the update Hessian schemes differ to the analytical Hessian and can be seen in the frequencies.The SR1 update Hessian scheme on the other hand does not result in these broad frequency variations, however in the the case of some frequencies, it results in some very erratic behaviour whereby a frequency increases or decreases in magnitude very rapidly along the reaction coordinate. This, along with the other analysis, again shows that the SR1 update Hessian scheme has many issues and does not accurately approximate the components of the RPH.

3.3.4 Comparison of single-ended and double-ended update Hessian approaches

The double-ended update Hessian approach, the focus of the results in Section 3.3 so far, was compared to the suggested four single-ended update Hessian approaches for the same three reactions. The transmission coefficients for each reaction were plotted for the *product* single-ended update Hessian approach, the *reactant* single-ended update Hessian approach, "TSup" update Hessian approach and the "TSdown" update Hessian approach in Figures 3.22 - 3.24, Figures 3.25 - 3.27, Figures 3.28 - 3.30 and Figures 3.31 - 3.33 respectively. All calculations reported here used 50 images for RPH construction.

The product single-ended update Hessian approach had some relative success in approximating the transmission coefficients depending on the update Hessian schemes; however, this approach lacks consistency among the reactions. For the interconversion of cyclohexane from chair conformer to twist boat conformer (R1), the SR1 and Bofill update Hessian schemes performed better than their counterparts, having a similar plateau to that of the standard approach. Both the PSB and TS-BFGS update Hessian schemes were very similar to one another, just as in in the double-ended calculations above; however, in the product single-ended approach they both overestimate the contributions of recrossing to the transmission coefficient slightly. In reaction R2, the addition of nitrous oxide to ethene, the PSB and

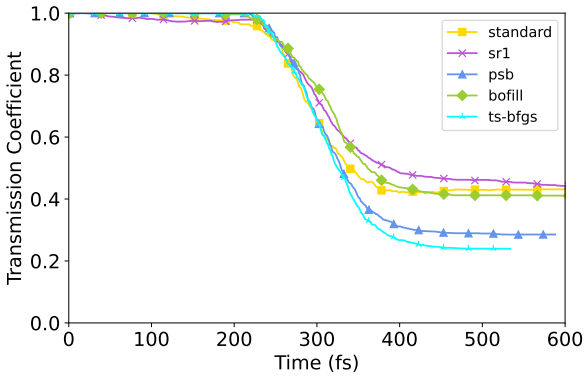

Figure 3.22: Normalized flux-side correlation function using the product single-ended update Hessian approach for interconversion of cyclohexane from chair to twisted-boat conformer (R1). Results are shown for the analytical Hessian (gold squares), SR1 (purple crosses), PSB (blue triangles), Bofill (green diamonds) and TS-BFGS update Hessian schemes (cyan empty triangles).

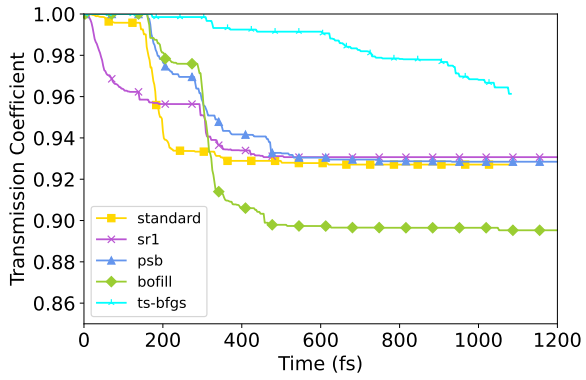

Figure 3.23: Normalized flux-side correlation function using the product single-ended update Hessian approach for addition of nitrous oxide to ethene (R2). Results are shown for the analytical Hessian (red ticks), SR1 (green crosses), PSB (blue stars) and Bofill update Hessians (purple square).

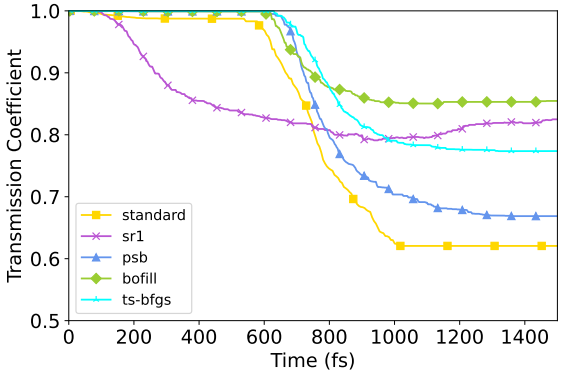

Figure 3.24: Normalized flux-side correlation function using the product single-ended update Hessian approach for 1,1-insertion of CO into the Co–C bond in the Heck-Breslow mechanism of hydroformylation (R3). Results are shown for the analytical Hessian (gold squares), SR1 (purple crosses), PSB (blue triangles), Bofill (green diamonds) and TS-BFGS update Hessian schemes (cyan empty triangles).

SR1 Hessian update schemes resulted in the same transmission coefficient as the standard approach. The TS-BFGS Hessian update scheme resulted in a transmission coefficient which did not reach a plateau and was not near the same value as the standard approach. The Bofill Hessian update scheme overestimated the recrossing effects by having a lower transmission coefficient value compared to the standard approach. Lastly, for the third reaction, all of the update Hessian schemes resulted in similar transmission coefficient plateaus to the standard approach. In particular, the PSB update Hessian method was very close to the standard approach transmission coefficient value. However, across these three reactions, there is no clear consistency indicating one update Hessian method being superior to another.

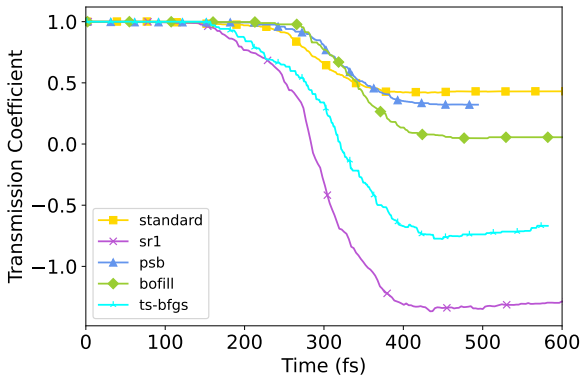

Figure 3.25: Normalized flux-side correlation function using the reactant single-ended update Hessian approach for interconversion of cyclohexane from chair to twisted-boat conformer (R1). Results are shown for the analytical Hessian (gold squares), SR1 (purple crosses), PSB (blue triangles), Bofill (green diamonds) and TS-BFGS update Hessian schemes (cyan empty triangles).

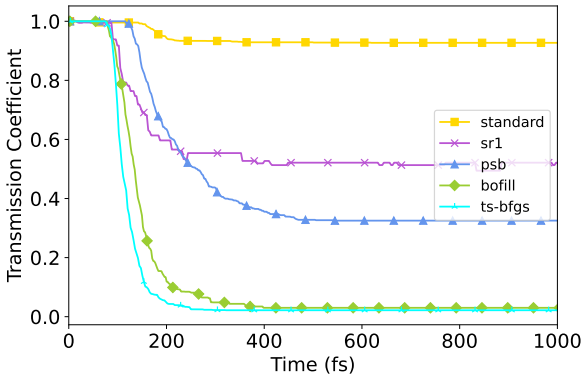

Figure 3.26: Normalized flux-side correlation function using the reactant single-ended update Hessian approach for addition of nitrous oxide to ethene (R2). Results are shown for the analytical Hessian (gold squares), SR1 (purple crosses), PSB (blue triangles), Bofill (green diamonds) and TS-BFGS update Hessian schemes (cyan empty triangles).

The results from the reactant single-ended update Hessian approach showed that using this approach was not adequate in order to determine the transmission coef-

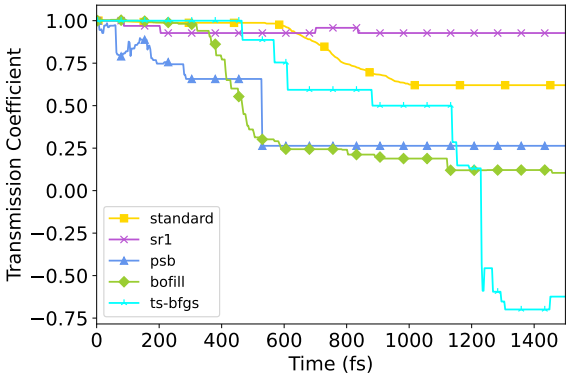

Figure 3.27: Normalized flux-side correlation function using the reactant single-ended update Hessian approach for 1,1-insertion of CO into the Co–C bond in the Heck and Breslow mechanism of hydroformylation (R3). Results are shown for the analytical Hessian (gold squares), SR1 (purple crosses), PSB (blue triangles), Bofill (green diamonds) and TS-BFGS update Hessian schemes (cyan empty triangles).

ficient for these reactions. For each reaction, the reactant single-ended approach drastically overestimated the recrossing contribution to the transmission coefficient. Moreover, the reactant single-ended update Hessian resulted in erroneous negative transmission coefficient in two reactions out of the three, clearly showing how this approach fails to capture the correct qualitative behaviour of the transmission coefficient.

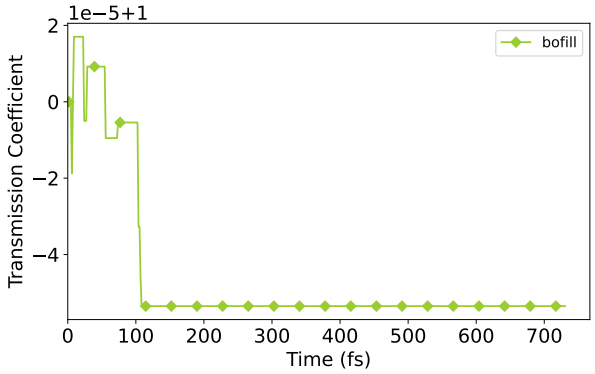

Figure 3.28: Normalized flux-side correlation function using the “TSup” update Hessian approach for interconversion of cyclohexane from chair to twisted-boat conformer (R1). Results are shown for the Bofill (green diamonds) update Hessian scheme.

For the final two propagation schemes, referred to as “TSdown” and “TSup”, we use the update Hessian scheme which resulted in the closest approximation to the standard approach when the double propagation scheme was used for each reaction. As such, we use the Bofill, TS-BFGS and PSB update Hessian schemes for R1, R2 and R3 respectively. The “TSup” Hessian propagation scheme resulted in transmission coefficients which were not comparable to the standard approach, and

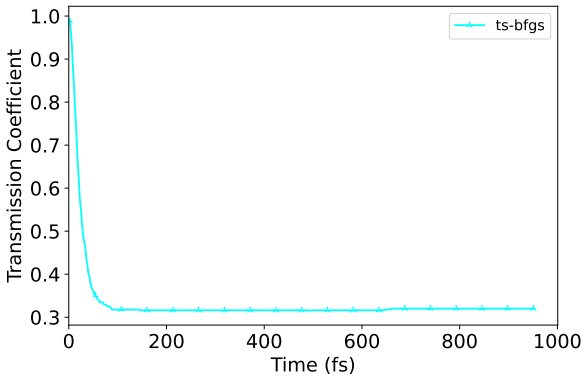

Figure 3.29: Normalized flux-side correlation function using the "TSup" update Hessian approach for addition of nitrous oxide to ethene (R2). Results are shown for the TS-BFGS update Hessian scheme (cyan empty triangles).

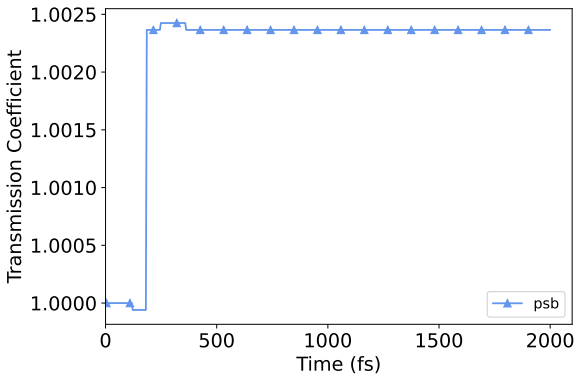

Figure 3.30: Normalized flux-side correlation function using the "TSup" update Hessian approach for 1,1-insertion of CO into the Co–C bond in the Heck and Breslow mechanism of hydroformylation (R3). Results are shown for the PSB (blue triangles) update Hessian scheme.

were poor representations of recrossing effects for the reactions. In R2, the transmission coefficient was significantly lower than the standard approach (0.32 compared to 0.64), and in R1 and R3, the transmission coefficient was negative and at unity respectively, whereas the standard approach results in a transmission coefficient of 0.50 and 0.74. The flaws of this propagation scheme is highlighted when looking at the frequencies, shown in Figures 6, 13 and 20 in the Appendix. In R1-R3, a significant number of frequencies become quite large along the reaction coordinate compared to what they should be when using the standard approach. Moreover, the frequencies tend to show sharp changes in amplitude which do not accurately represent the reactions but also will have an effect on the subsequent coupling constants which is why the transmission coefficients determined are far off. Similarly, the "TSdown" Hessian propagation scheme did not show any consistency across the three reactions. Only in R2 did the propagation scheme show success, with a transmission coefficient of 0.58 compared to 0.64 using the standard approach. For R1 and R3, the resulting transmission coefficients were 0.78 and 0.90 compared to 0.50 and 0.74 respectively. Despite this, as shown in Figures 7, 14 and 21, the resulting frequencies for each reaction were sensible, although quite flat, as opposed to the "TSup" propagation scheme, however this did not result in a transmission coefficient similar to that of the standard approach.

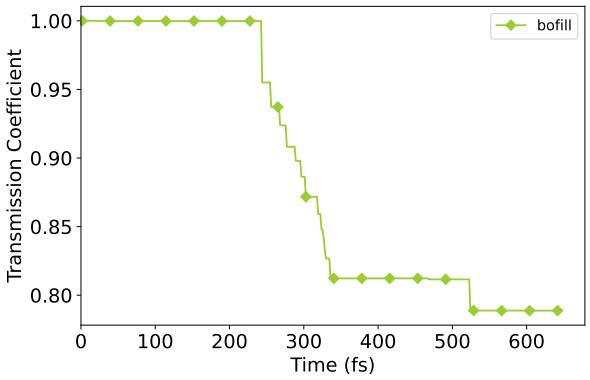

Figure 3.31: Normalized flux-side correlation function using the "TSdown" update Hessian approach for interconversion of cyclohexane from chair to twisted-boat conformer (R1). Results are shown for the Bofill (green diamonds) update Hessian scheme

In comparison, the results discussed in the previous subsection for the double-ended update Hessian approach show that the approach is more reliable than both of the single-ended update Hessian approaches. In particular, we emphasize that the labelling of starting-points for update Hessians as either reactants or products is arbitrary; as a result, the comparison of Figures 3.22 - 3.24, Figures 3.25 - 3.27 and in Figures 3.28 - 3.30 indicate that the predictability of the performance of the single-ended update Hessian schemes is poor. In other words, depending on whether one

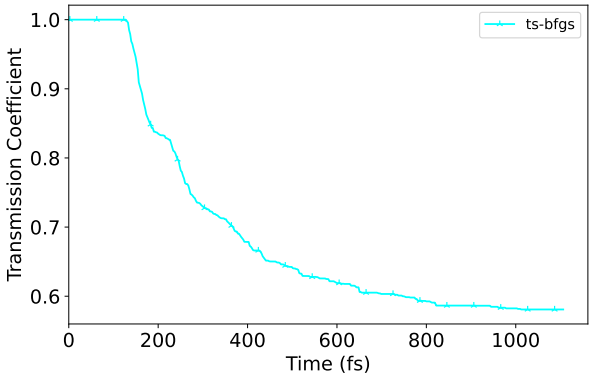

Figure 3.32: Normalized flux-side correlation function using the "TSdown" update Hessian approach for addition of nitrous oxide to ethene (R2). Results are shown for the update Hessian scheme (cyan empty triangles).

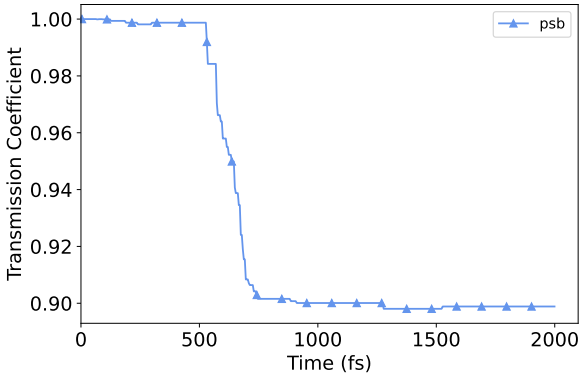

Figure 3.33: Normalized flux-side correlation function using the "TSdown" update Hessian approach for 1,1-insertion of CO into the Co–C bond in the Heck-Breslow mechanism of hydroformylation (R3). Results are shown for the PSB (blue stars) update Hessian

chooses to start from the reactants or the products, one can calculate quite different transmission coefficient values; this is particularly evident by comparing Figures 3.22 and 3.25. Furthermore, both the "TSup" and "TSdown" approaches are either, in the case of "TSdown", not consistent across the board or, in the case of "TSup", simply do not result in accurate transmission coefficients. As a result, we summarize that double-ended update Hessian schemes are greatly preferred over single-ended methods.

3.4 Application of compact-finite differences update Hessian schemes with RPH dynamics

In this section, we investigate the compact-Finite differences (CFD) update Hessian schemes, described in Section 3.1.2, to assess whether they result in better

approximations than the quasi-Newton update Hessian schemes, in the context of using them to construct the RPH and to determine the transmission coefficient via MD simulations. The three CFD update Hessian schemes considered here are the CFD-SR1, CFD-PSB and CFD-Bofill schemes.

The three different CFD update Hessian schemes were implemented in the RPH framework in order to obtain transmission coefficients on the same three reaction systems investigated in Section 3.3 and these were: interconversion of cyclohexane from chair to twisted-boat conformer (R1), addition of nitrous oxide to ethene (R2), and 1,1-insertion of CO into the Co–C bond in the Heck-Breslow mechanism of hydroformylation. As shown in 3.3, the Hessian propagation scheme which resulted in the most consistent results was the double-ended update Hessian approach, and so, this same approach is used in the following sections using the CFD update Hessian schemes. Furthermore, we use the same 50 image MEP and the same double-ended update Hessian propagation approach, used in Section 3.3, to perform RPH transmission coefficient calculations using CFD update Hessian schemes.

Lastly, all three reactions were investigated using the same computational methods and the same MD simulation parameters as they had been when using the quasi-Newton update Hessian schemes. As a reminder, the first two reactions were investigated using DFT with the B3LYP functional[133–136] and 6-31G basis set.[137,138] The third reaction used B3LYP with a 6-31G(d,p) basis set.[139,140] For the MD simulations, the first two reactions were performed at a temperature of 273 K, the third reaction was performed at a temperature of 423 K and the final two reactions were performed at a temperature of 298 K.

3.4.1 Interconversion of cyclohexane: from chair to twisted-boat

The calculated $C_{fs}^{cl}(t)$ (and α, the transmission coefficient) for the interconversion of cyclohexane from chair to twisted-boat using the standard approach and the CFD update Hessian schemes are shown in Figure 3.34. In Figure 3.34, all update Hessian schemes follow the same qualitative behaviour relative to the standard approach, where $C_{fs}^{cl}(t)$ drops at $\sim$ 200 fs and then plateaus at $\sim$ 400 fs.

The transmission coefficients for all three update Hessian schemes and the standard approach are shown in Table 3.4. Similarly to using quasi-Newton update Hessian schemes, the CFD update Hessian schemes result in comparable transmission coefficients to the standard approach but also to their quasi-Newton update Hessian scheme counterparts. The CFD-SR1, CFD-PSB and CFD-Bofill schemes result in a transmission coefficient of 0.60, 0.44 and 0.40 respectively, compared to 0.50 for the standard approach. These results are near identical to the quasi-Newton

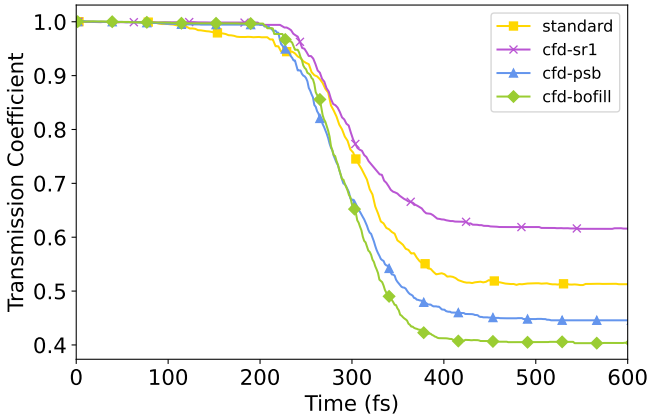

Figure 3.34: Normalized flux-side correlation function computed using the RPH with different update Hessian schemes for the interconversion of cyclohexane: from chair to twisted-boat using 50 MEP discrete points. Results are shown for the analytical Hessian (red ticks), CFD-SR1 (green crosses), CFD-PSB (blue stars), CFD-Bofill (purple square)

Table 3.4: Transmission coefficients for the interconversion of cyclohexane from chair to twisted-boat calculated with the RPH using different Hessian methods with 50 MEP points.

RPH Hessian method	$C_{fs}^{cl}(t)$ **plateau value**
Standard	0.50
CFD-SR1	0.60
CFD-PSB	0.44
CFD-Bofill	0.40

Hessian counterparts, with a difference of 0.06, 0.03 and 0.04 in the transmission coefficient between the CFD-SR1, CFD-PSB and CFD-Bofill update Hessian schemes and their quasi-Newton counterparts.

3.4.2 Addition reaction of ethene and nitrous oxide

The calculated $C_{fs}^{cl}(t)$ (and α, the transmission coefficient) for the addition reaction of ethene and nitrous oxide using the standard approach and the CFD update Hessian schemes are shown in Figure 3.35. In this reaction, the update Hessian schemes show some indication that there are recrossing effects, with $C_{fs}^{cl}(t)$ dropping at $\sim$ 200 fs just like the standard approach, however, unlike the standard approach, the $C_{fs}^{cl}(t)$ determined by the update Hessian schemes start to plateau earlier.

Table 3.5 shows the transmission coefficients for all three update Hessian schemes and the standard approach. The standard approach results in a transmission coefficient of 0.64, whereas the update Hessian schemes result in values of the transmission coefficient of 0.91, 0.81 and 0.83 for CFD-SR1, CFD-PSB and CFD-Bofill respectively. Similarly to R1, the transmission coefficients determined by the CFD update Hessian schemes are not so different to their quasi-Newton counterparts and do

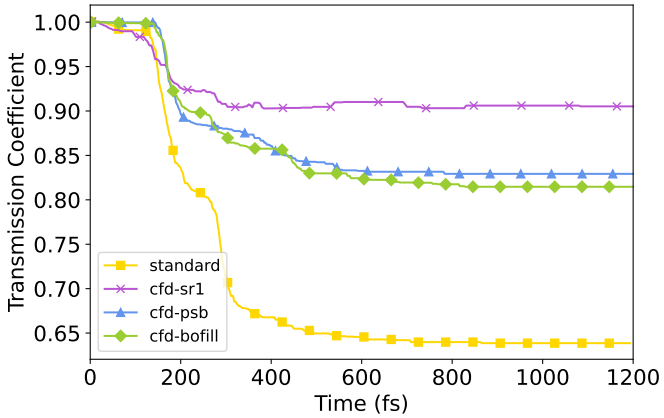

Figure 3.35: Normalized flux-side correlation function computed using the RPH with different update Hessian schemes for the addition reaction of ethene and nitrous oxide using 50 MEP discrete points. Results are shown for the analytical Hessian (red ticks), CFD-SR1 (green crosses), CFD-PSB (blue stars), CFD-Bofill (purple square)

Table 3.5: Transmission coefficients for the addition of nitrous oxide to ethene calculated with the RPH using different Hessian methods with 50 MEP points.

RPH Hessian method	$C_{fs}^{cl}(t)$ **plateau value**
Standard	0.64
CFD-SR1	0.91
CFD-PSB	0.81
CFD-Bofill	0.83

not correctly account for the recrossing effects determined when using the standard approach.

3.4.3 1,1-insertion of CO into the Co–C bond in the Heck-Breslow hydroformylation mechanism

The 1,1-insertion of CO into the Co–C bond in the Heck-Breslow hydroformylation mechanism is the final reaction investigated using the CFD update Hessian schemes. The calculated $C_{fs}^{cl}(t)$ (and α, the transmission coefficient) using the CFD update Hessian schemes is shown in Figure 3.36. Qualitatively, the CFD-PSB and CFD-Bofill update Hessian schemes have a similar behaviour to the standard approach, where $C_{fs}^{cl}(t)$ stays constant until it suddenly decreases until a plateau is reached at $\sim$ 1000 fs. On the other hand, the CFD-SR1 update Hessian scheme does not follow the same behaviour, instead, from the start $C_{fs}^{cl}(t)$ gradually decreases and plateaus earlier than the other schemes.

The transmission coefficients calculated by the update Hessian schemes and the standard approach are shown in Table 3.6. The standard approach resulted in a

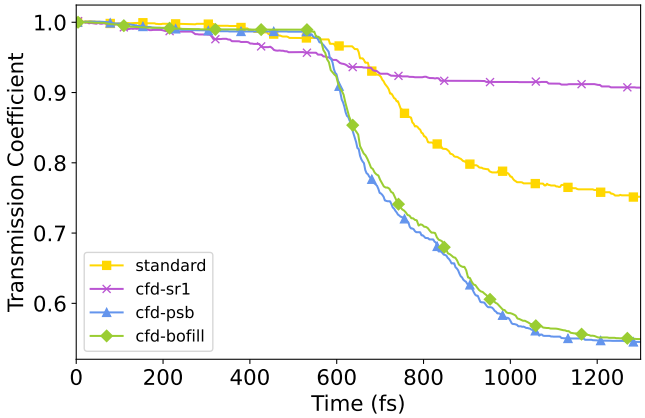

Figure 3.36: Normalized flux-side correlation function computed using the RPH with different update Hessian schemes for the 1,1-insertion of CO into the Co–C bond in the Heck-Breslow hydroformylation mechanism using 50 MEP discrete points. Results are shown for the analytical Hessian (red ticks), CFD-SR1 (green crosses), CFD-PSB (blue stars), CFD-Bofill (purple square)

Table 3.6: Transmission coefficients for the 1,1-insertion of CO into the Co–C bond in the Heck-Breslow hydroformylation mechanism calculated with the RPH using different Hessian methods with 50 MEP points.

RPH Hessian method	$C_{fs}^{cl}(t)$ **plateau value**
Standard	0.74
CFD-SR1	0.90
CFD-PSB	0.54
CFD-Bofill	0.55

transmission coefficient of 0.74, whereas the update Hessian schemes resulted in a transmission coefficient of 0.90, 0.54 and 0.55 for the CFD-SR1, CFD-PSB and CFD-Bofill schemes respectively. In this reaction, none of the update Hessian schemes managed to successfully account for the recrossing occuring in the reaction like the standard approach did, with the CFD-PSB and CFD-Bofill schemes overestimating the recrossing effects and the CFD-SR1 scheme underestimating the recrossing effects. In comparison to their quasi-Newton counterparts, some of the CFD update Hessian schemes resulted in different results of the transmission coefficients. The CFD-SR1 scheme resulted in a difference of 0.33 in the transmission coefficient compared to the SR1 scheme, and the CFD-PSB scheme resulted in a difference of 0.14 compared to the PSB scheme. The CFD-Bofill scheme on the otherhand resulted in a very similar transmission coefficient, with only a difference of 0.02 in the transmission coefficient compared to the Bofill scheme.

3.4.4 Relative computational cost of quasi-Newton update Hessian schemes

Based on the performances of each approach, the double-ended weighted average approach was selected in order to compare calculation times across the different Hessian treatments. Moreover, the CFD update Hessian schemes are not considered here as they did not result in substantial differences to their quasi-Newton counterparts and in the calculation times should be similar to their quasi-Newton counterparts. As noted in the Section 3.1, the RPH model requires calculation of multiple Hessian matrices at many discrete points along the MEP, which can be computationally-expensive; comparing calculation times across the different approaches is therefore of interest. Furthermore, we note that each of the schemes considered here (*i.e.* standard approach, SR1, PSB, Bofill and TS-BFGS) all use exactly the same underlying MEP configurations and, once the RPH is constructed, the sampling over MD trajectories is also exactly the same. As such, the calculation time difference between the different methods boils down to the time required to evaluate the Hessian matrices along the MEP.

Table 3.7: Comparison between the relative computational cost associated with calculating the Hessian matrices using the RPH and full analytical Hessian approach vs using the RPH and update Hessian schemes.

Hessian calculation type	R1	R2	R3
Standard	1	1	1
SR1	0.36	0.59	0.22
PSB	0.36	0.59	0.22
Bofill	0.36	0.59	0.22
TS-BFGS	0.36	0.59	0.22

Table 3.7 shows the relative computational costs for the four update Hessian schemes using the double-ended weighted average approach; times are given relative to the standard approach. We note that this comparison highlights the best case scenario whereby 15 analytical Hessians are enough to achieve convergence in the standard approach and 50 MEP points are used in the update Hessian approaches. As expected, all four update Hessian schemes provide a reduction in computational cost because they avoid explicit evaluation of the Hessian matrices at all internal images along the MEP. For the first two reactions, the interconversion of cyclohexane (R1) and the addition of nitrous oxide to ethene (R2), the update Hessian schemes all provide a substantial reduction in associated computational cost. For reaction R3, the 1,1-insertion of CO into the Co–C bond in the Heck and Breslow mechanism of hydroformylation, shows an even more significant reduction in computational cost, with all 4 update Hessian schemes resulting in a 78% reduction in computational cost. This is a result of the increased size of the system and the resulting additional

cost of evaluating the Hessian matrices directly using DFT; for larger, more complex systems, the benefits of using update Hessian schemes would be expected to become more apparent.

3.5 Conclusions

This Chapter has presented a comparative assessment of different update Hessian schemes to assess their accuracy in the context of determining reaction transmission coefficients using the RPH combined with MD simulations. For each reaction considered, a RPH calculation and MD simulation were performed using RPHs constructed from either 15 or 50 images. The RPH was implemented in several different ways: (1) the standard analytical Hessian approach, (2) a single-ended update Hessian starting from reactants, (3) a single-ended update Hessian starting from products, (4) a double-ended weighted-average update Hessian scheme, (5) a single-ended update Hessian starting from the TS towards both reactants and products and (6) a single-ended update Hessian starting from the reactants and products towards the TS. In addition, four types of quasi-Newton update Hessian schemes were assessed, namely: (1) SR1 update Hessian, (2) PSB update Hessian, (3) Bofill update Hessian and (4) TS-BFGS update Hessian as well as three types of CFD update Hessian schemes: (1) CFD-SR1 update Hessian, (2) CFD-PSB update Hessian and (3) CFD-Bofill update Hessian.

Transmission coefficients were obtained by calculating $C_{fs}^{cl}(t)$, which accounts for recrossing in chemical reactions. The method which most commonly resulted in qualitative and quantitative results similar to that of the standard approach was the double-ended weighted-average update Hessian. This method showed reasonable estimates for the transmission coefficients, unlike the case of the single-ended methods. For the double-ended weighted-average method, all four update Hessian schemes showed qualitative promise, in the sense that in all case studies, the update Hessian schemes resulted in a transmission coefficient which was affected by recrossing similar to the standard approach. In terms of the transmission coefficient calculated using 15 images, in all reactions, the update Hessian schemes resulted in quite similar values to those given by the standard approach. In the case of the transmission coefficients calculated from the 50 images, there was no update Hessian method which provided accurate and consistent results across all reactions considered. However depending on the reaction, the quasi-Newton update Hessian schemes, such as the PSB, Bofill and TS-BFGS schemes, generally resulted in reasonable transmission coefficients relative to that of the standard approach. In the case of the PSB update Hessian, calculated transmission coefficients were 0.41, 0.87 and 0.68 for R1-R3 respectively, compared to 0.50, 0.64 and 0.74 for the standard

approach, indicating how well it performed for R1 and R3. In the case of the Bofill update, the transmission coefficients were 0.44, 0.87 and 0.57 for R1-R3 respectively, performing well for R1 in particular. The SR1 update Hessian method had the least success, with transmission coefficients which had the largest differences to the standard approach, and in the case of R3, when 15 images were used, did not result in a transmission coefficient at all. Finally, the TS-BFGS update Hessian showed success in R1 and especially in R2, where it was the only update Hessian method which was close to the standard approach.

In an effort to determine more accurate and consistent transmission coefficients, CFD update Hessian schemes were investigated. Overall, the CFD update Hessian schemes were no different to their quasi-Newton counterparts, and resulted in similar or the same transmission coefficients across the three reactions. The CFD-SR1 update Hessian scheme resulted in a transmission coefficient of 0.60, 0.91 and 0.90 for R1, R2 and R3 respectively, compared to 0.66, 0.91 and 0.57 for the SR1 update Hessian scheme. Using the CFD-SR1 scheme did not result in improvements in getting a transmission coefficient closer to the standard approach, and confirmed that the CFD-SR1 scheme, just like the SR1 scheme, is not adequate for these types of calculations and would not be recommended in the context of transmission coefficient determination. Both the CFD-PSB and CFD-Bofill resulted in essentially the same transmission coefficients across the three reactions, but were also nearly identical to their quasi-Newton counterparts with the exception of the CFD-PSB scheme in R3. As such, there were no substantial improvements in using the CFD family of update Hessian schemes in the context of constructing the RPH and running MD simulations for these reactions in particular. This could be due to either; there not being enough images used to update the Hessian matrix, as the CFD method requires the potential energy to be adequately smooth, or simply the increase in accuracy offered from the CFD method is not necessary for the reactions investigated using the quasi-Newton update Hessian schemes.

Several RPH parameters were investigated and compared to the standard approach. The harmonic vibrational frequencies at the TS were correctly represented by both the standard approach and all of the update Hessian schemes. The curvature coupling along the reaction-coordinate was also correctly represented by both the standard approach and all update Hessian schemes, although we noted that the SR1 scheme appears to give worse agreement with the standard scheme than the other update Hessians, in line with poorer transmission coefficient results (particularly for R1). Similarly, for the Coriolis coupling, we find that the majority of update Hessian schemes considered here give relatively good agreement with the standard method (at least in magnitude and broad trend), but the SR1 scheme is again found to be the outlier, often exhibiting spuriously large peaks in coupling. Combined together,

consideration of the curvature couplings, Coriolis couplings, and the vibrational frequencies shown in the Appendix demonstrates that SR1 is not recommended for general use; for the other schemes, we find that there is nothing to particularly recommend one over the other. Finally, as expected, we also showed that the relative computational cost of the four update Hessian schemes was less than that of the standard approach for all three reactions considered.

The simulations performed here consider just a single temperature, but it is worth noting the influence of temperature. While the construction of the RPH is temperature-independent, being based on information from MEP calculations, the flux correlation functions and corresponding recrossing factors will depend on temperature through the generation of initial conditions and the impact of these initial conditions on the generated trajectories. At high temperature, one would expect the implicit harmonic approximations in RPH to begin to become less accurate as anharmonicity becomes important, regardless of the method chosen to construct the RPH model; in addition to the differences already noted at a single temperature, this would give rise to an additional temperature-dependence to the comparison between different RPH schemes. However, for the purposes of this Chapter, we have already shown that there are significant differences between different RPH construction methods, even if one just considers a single temperature.

To summarize, this Chapter has demonstrated that update Hessian schemes can be used to construct the RPH and subsequently run MD simulations to determine quantitative transmission coefficients for complex chemical reactions. Such schemes can reduce the computational cost associated with rate calculations using RPH methods; the double-ended schemes used here are also compatible with automated reaction discovery workflows, where it is common that geometry optimization of reactants and products, and MEP-finding, are often straightforward, whereas TS location can be challenging. The double-ended scheme tested here does not explicitly require a TS configuration or Hessian matrix.

Chapter 4

Dynamical Effects in Cobalt Catalytic Cycles

> If you desire one thing for so long, it's a given that you'll miss other things along the way. That's how it is ... that's life
>
> *Berserk*, Kentaro Muira

Summary

This Chapter focuses on using the reaction path Hamiltonian (RPH) coupled with molecular dynamics simulations in order to account for, if any, dynamical effects to the reaction rate in organometallic catalysis. The organometallic catalytic cycle investigated is the Heck-Breslow hydroformylation process for the production of aldehydes from alkenes using a cobalt catalyst. The RPH-derived reaction rates, as well as TST-derived reaction rates, were used to perform kinetic Monte Carlo simulations in order to derive the rate law for the catalytic cycles being investigated. The analysis showed that recrossing effects were observed in several of the reactions in the catalytic cycle. However, the subsequent kinetic simulations did not show much difference between using TST reaction rates and RPH reaction rates, specifically in the final rate law for the catalytic cycle. Moreover, the difference between gas-phase conditions and solvent-phase conditions was also minimal. Further investigation of the kinetic simulation, comparing the differences between TST and RPH reactions rates for all species, showed little to no differences in the initial species but a slight decrease in magnitude for the time evolution of the concentrations of the intermediate species using TST reaction rates.

4.1 Introduction

Homogenous catalysis represents an important field in the worldwide chemical industry.[141–143] As such, the drive to develop molecular catalysts with improved turnover frequency, higher selectivity, and better resistance to degradation is ever present in chemistry research. Until recently, the complete *de novo* design of molecular catalysts using computational chemistry meant using an existing catalyst as a starting point,[144] however the development of automated reaction discovery (ARD) methods which can construct complex and detailed chemical reaction networks (CRNs) has greatly improved the computational aided catalysis designs.[49,145–147]

With the help of ARD methods characterising the complete catalytic cycle, rate constants defining the important steps in a catalytic cycle, typically calculated using a form of TST, and the rate law have become easier to determine.[48,147,148] However as detailed in Section 2.1.2, the assumptions in TST, specifically the so-called no-recrossing assumption, can lead to an inaccurate description of the rate constant for a given reaction.[87] With rate constants, and subsequently, rate laws being vital to the description of a catalytic cycle and by proxy the performance of a catalysis, calculating these as accurately as possible, by taking into account recrossing factors, is essential for developing and investigating new catalysts. Furthermore, to the best of our knowledge, recrossing effect have not been investigated in this context and thus would be an interesting application of the RPH framework for reaction rate determination.

In the well studied Heck-Breslow hydroformylation[132,149] process using a cobalt catalyst (Figure 4.1) we have shown that in Chapter 3, that in at least one of the reaction steps, there is a certain amount of recrossing happening as reflected by the transmission coefficient. As a result, in this Chapter, we investigate the complete Heck-Breslow hydroformylation catalytic cycle using a cobalt catalyst both in gas-phase and in solvent using the RPH framework detailed in 2.4.4 to determine the reaction rates and ultimately the rate law of the catalytic cycle.

4.2 Heck-Breslow hydroformylation cobalt catalysis

The RPH approach, described in Section 2.4.4, is used for each step of the Heck-Breslow hydroformylation process for the production of aldehydes from alkenes using a cobalt catalyst where a TS is formed between the reactants and the products, shown in Figure 4.2, to determine the dynamically correct reaction rates for each reaction step.

For all reactions, the reactant and product structures were obtained from Martínez-

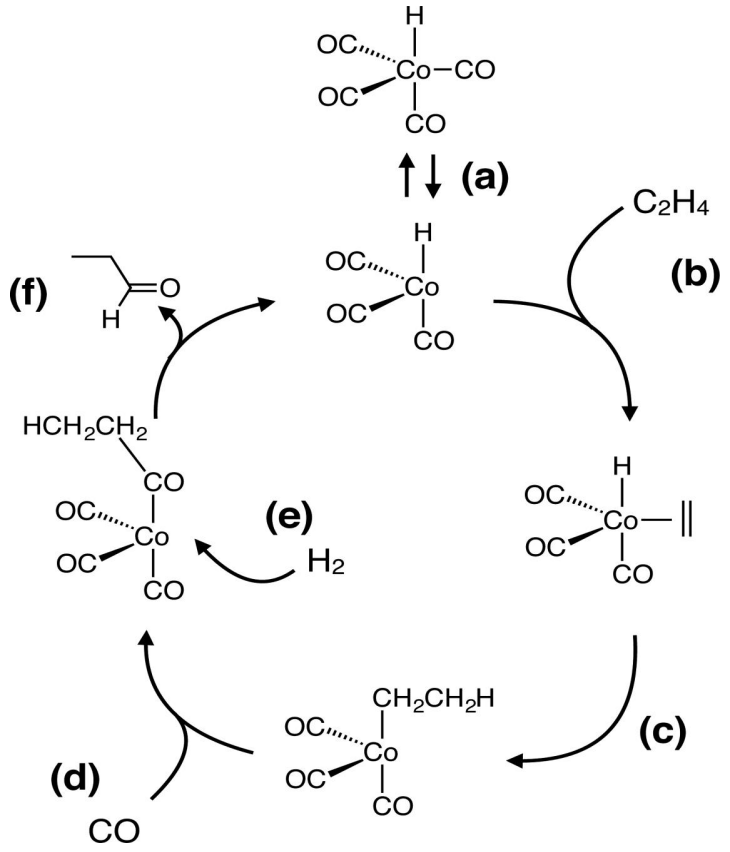

Figure 4.1: An illustration depicting the Heck–Breslow mechanism for alkene hydroformylation using a cobalt catalyst. The initial species $HCo(CO)_4$ undergoes CO dissociation (a) to generate the active catalyst. Subsequently, (b) the alkene coordinates and (c) inserts into the Co–H bond. Coordination and insertion (d) of CO is followed by addition of molecular hydrogen, H_2 (e). Finally, reductive elimination leads to formation of the product aldehyde and regeneration of the catalyst (f). Figure taken from the work and permission of Habershon[49]

Núñez *et al.*[147] and a 15 image MEP was obtained by running a NEB[96] calculation using the NEB-TS feature in the ORCA quantum chemistry package.[98] We then use the initial MEP (comprising 15 images) and use spline interpolation to generate a path with a total of 50 images; this expanded 50-image path was used to perform RPH simulations which means that 50 Hessian matrices were evaluated along the reaction-path.

For reactions where one of the endpoint configurations describes a bound state, we create a fictitious harmonic well along the reaction path by defining a normalized path tangent vector at the minimum in the basis of normal modes of the Hessian at the minimum, as explained in detail in Section 2.4.4. This artificial harmonic potential is added to the RPH to ensure that configurations sampled during MD simulations remain within the configuration space in which the RPH is well-defined.

All of the reactions in the catalytic cycle were investigated using density functional theory (DFT) with the B3LYP functional[133–136] and a 6-31G(d,p) basis set.[139,140]

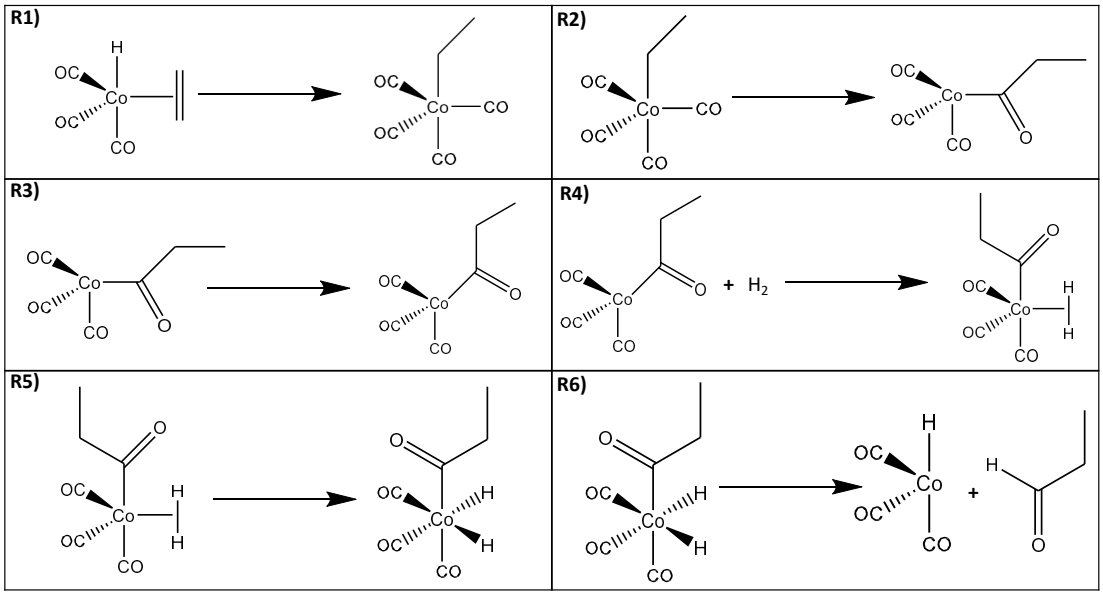

Figure 4.2: An illustration showing the reactions of Heck–Breslow mechanism for alkene hydroformylation using a cobalt catalyst studied using the RPH approach. Where the reactions labelled a to f are referred in the text as R1-R6.

The choice of PES here is motivated by our desire to have the same PES as previous simulations for the same reactions performed at this same level of theory.[48,147] For the MD simulations, all reactions in the catalytic cycle were simulated at a temperature of 423K, which was the same temperature used in literature[48,147] and experiments.[150] Using the standard RPH, analytical Hessians were calculated along the MEP were obtained for the six different reactions, shown in Figure 4.2, involved in the catalytic cycle in both gas-phase and solvent-phase using the ORCA quantum chemistry package NEB-TS feature and are shown in Figure 22-33 in the Appendix. For solvent-phase calculations, an implicit solvent model was used to represent toluene, specifically the conductor-like polarisable continuum model (CPCM).

The flux-side correlation function, $C_{fs}^{cl}(t)$, was evaluated by sampling initial coordinates and momenta from the Boltzmann distribution for the underlying RPH. Each of these trajectories started at the dividing surface, defined by $s = 0$. Each set of initial coordinates and momenta were propagated using Hamilton's equations of motion determined from the RPH; the fourth-order Runge-Kutta (RK4) algorithm was used to numerically integrate the equations-of-motion using a time-step of 0.30 fs. For each reaction considered, we found that a different total simulation time was required to ensure that $C_{fs}^{cl}(t)$ had reached a plateau, as shown in the results below, and a total of 10^4 trajectories were performed. Under these conditions, we find that the typical standard error in the plateau values of the $C_{fs}^{cl}(t)$ function is 2×10^{-3}; this value is typically much smaller than any observed differences between the different simulations methods investigated below.

4.2.1 Gas-phase dynamics

Transmission coefficients

In this section, we calculate the reaction rate for each reaction in gas-phase shown in Figure 4.2 using conventional TST. Furthermore, we also use the RPH framework to determine the transmission coefficient from the MEPs determined, shown in Figure 22-27 in the Appendix, which can then be combined to the TST reaction rate in order to determine the dynamically correct reaction rate.

The transmission coefficients, for each reaction, determined using the RPH framework are shown in Table 4.1.

Table 4.1: Transmission coefficients for the reactions investigated of the Heck–Breslow mechanism for alkene hydroformylation using a cobalt catalyst studied using the RPH approach in gas-phase.

Reaction	$C_{fs}^{cl}(t)$ **plateau value**
R1	0.86
R2	0.66
R3	0.97
R4	0.26
R5	0.50
R6	0.49

Across the six reactions, varying amounts of recrossing effects were observed. R4 had the largest amount of recrossing effects observed with a transmission coefficient of 0.26. R5 and R6 had a similar transmission coefficient of 0.50 and 0.49 respectively, whereas R3, R1 and R2 had transmission coefficients closer to unity, 0.97, 0.86 and 0.66 respectively, suggesting that recrossing effects were not as important for those reactions.

Kinetic studies

The reaction rates determined via conventional TST as well as the dynamically correct reaction rates determined via RPH for the reactions in gas-phase were used as the input for kinetic simulations. The time evolution of each chemical species involved in the catalytic cycle can be monitored using kinetic Monte Carlo simulations, assuming that the catalyst and starting materials are mixed and continuously stirred. The time-dependence of the concentration of the cobalt catalyst and the aldehyde product, using an initial concentration of 0.13284 mol dm^{-3} for the cobalt catalyst and 1.3284 mol dm^{-3} for the ethene, molecular hydrogen and carbon monoxide, are shown in Figure 4.3. In the Figure, the concentration of the cobalt catalyst, determined after using TST rates and RPH rates, remains stable in both cases which suggest that this structure is the resting state of the catalyst and is in agreement

with the literature.[147,148] Furthermore, we note that the difference between the time-dependent concentration using TST rates and RPH rates were minimal, only 0.00002 mol dm^{-3}, after one second.

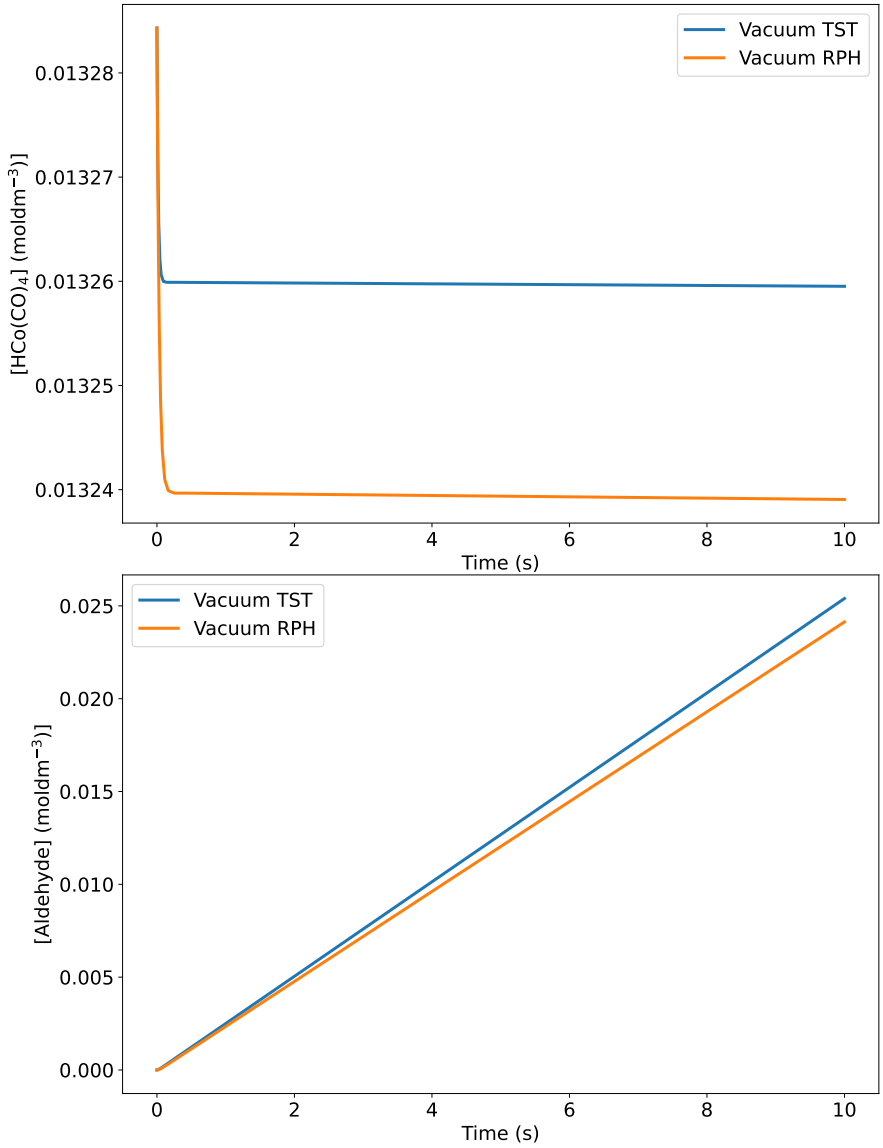

Figure 4.3: The time evolution of the concentrations of $HCo(CO)_4$ and the aldehyde product obtained using TST and RPH-derived reaction rates using the following initial concentrations: 0.13284 mol dm^{-3} for the cobalt catalyst and 1.3284 mol dm$^{-}3$ for the ethene, H_2 and carbon monoxide.

Moreover, the trend in time-dependence of the concentration of the aldehyde product also corresponds to what is reported in literature, when either TST rates were used or RPH rates. Initially, there is a short induction period, also observed experimentally,[150] and then the trend becomes linear for the rest of the time. In order to avoid the induction period, the rate is obtained from the slope of the line in the range of 1-10 seconds. The time-dependent concentration of the aldehyde

product was slightly smaller when the RPH rates were used, possibly suggesting that the recrossing effects shown in the transmission coefficient had an effect on the kinetics. We note that, compared to previous studies, the concentration of the aldehyde product is an order of magnitude greater. However, as noted by Ismail *et al.*, differences in energy barrier heights can cause significant impact on the resulting kinetics, especially if the energy barrier belongs to a reaction which is significant towards the resulting kinetics. In our case, for the reactions investigated, some of the energy barrier heights were slightly different to those reported in the literature, such as in R4 where the our energy barrier was $\sim$ 20 kJ/mol lower in energy or in R5 where the energy barrier was $\sim$ 8 kJ/mol lower.[54] These energy barrier height differences between the work presented here and Martínez-Núñez *et al.* can be explained by the difference in methodology used to determine the TSs. In this work, we use the reactant and product structures from Martínez-Núñez *et al.*[147] and run a NEB calculation using the NEB-TS method,[98] where the highest energy image will correspond to the TS. However, in the work done by Martínez-Núñez *et al.*, the TSs were determined using TSSCDS at the PM7 level of theory, and then re-optimized using the B3LYP/6-31G(d,p) level of theory.[133–136,139,140]

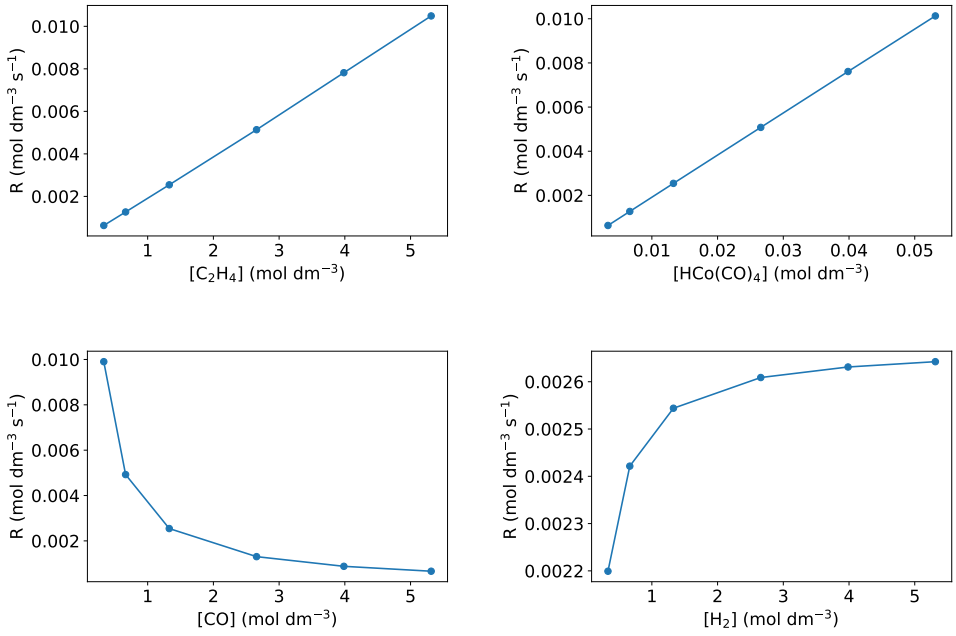

Figure 4.4: The rates of hydroformylation of the aldehyde product in gas-phase for various initial conditions using TST-derived reaction rates.

Following the kinetic Monte Carlo simulations, the rate law for hydroformylation in gas-phase using either TST-derived reaction rates or RPH-derived reaction rates can be determined. Figure 4.4, shows the dependence of the TST-derived reaction

rates on the concentrations of the cobalt catalyst and the starting materials (ethene, molecular hydrogen and carbon monoxide). With respect to the concentration of the ethene, the reaction rates derived from TST is first-order, which is also what is reported in literature and experimental.[147,148,150] Moreover, the reaction rates with respect to the concentration of the cobalt catalyst was also first order, which is also what is reported in literature if the experimental catalyst ($Co_2(CO)_8$) is not involved in the kinetic simulations, as is the case here. On the other hand, with respect to the concentration of carbon monoxide, the reaction rate was inversely proportional, best fitted with Equation 4.1, which is also reported in literature;[147]

$$R = \frac{a_1}{(1 + a_2[CO] + a_3[CO]^2)}, \tag{4.1}$$

where a_1, a_2 and a_3 are constants.

Finally, the reaction rate with respect to the molecular hydrogen (H_2) is fractional, 0.1, which differed from literature and experiments, which reported in the vicinity of 0.4 and 0.6 respectively.[147,148] This is most likely due to the difference in the energy barrier in R4, which consists of the addition of hydrogen to the cobalt complex, heavily impacting the concentration evolution of molecular hydrogen. As such, the rate law for the hydroformylation using a cobalt catalysis in gas-phase and using TST-derived reaction rates is shown in Equation 4.2;

$$R = \frac{[\mathrm{H_2}]^{0.1}[\mathrm{cat}][\mathrm{ethene}]}{(1 + a_1[\mathrm{CO}] + a_2[\mathrm{CO}]^2)}. \tag{4.2}$$

In Figure 4.5, the dependence of the RPH-derived reaction rates on the concentrations of the cobalt catalyst and the starting materials (ethene, H_2 and carbon monoxide) are shown. The results using RPH-derived reaction rates were very similar to what was obtained when TST-derived reaction rates were used. In terms of both ethene and the cobalt catalyst, the reaction rates with respect to the concentration was first-order with almost no differences in magnitudes. Furthermore, for both carbon monoxide and molecular hydrogen, the same trends were observed. The reaction rate with respect to the concentration of carbon monoxide was inversely proportional and could be defined by Equation 4.1, and the reaction rate with respect to the concentration of molecular hydrogen was also fractional, 0.11, which differed slightly from the results obtained using TST-derived reaction rates.

The resulting rate law for the hydroformylation using a cobalt catalysis in gas-phase but using RPH-derived reaction rates is shown in Equation 4.3.

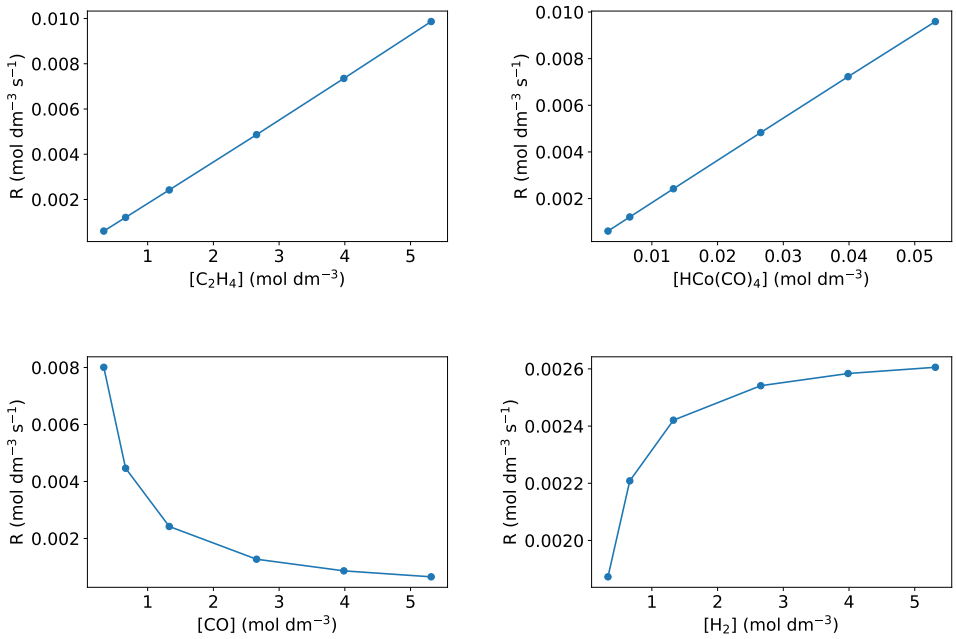

Figure 4.5: The rates of hydroformylation of the aldehyde product in gas-phase for various initial conditions using RPH-derived reaction rates.

$$R = \frac{[H_2]^{0.11}[\text{cat}][\text{ethene}]}{(1 + a_1[\text{CO}] + a_2[\text{CO}]^2)}. \tag{4.3}$$

Overall, the differences between using RPH-derived reaction rates which account for recrossing effects compared to TST-derived reactions rates were minimal in terms of the final rate law equation. In both cases, for the catalyst, ethene and carbon monoxide, the rate law was first-order, first-order and inversely proportional respectively. In terms of the molecular hydrogen, whilst both methods resulted in a fractional relation, the value was slightly different, 0.1 for the TST reaction rates compared to 0.11 for the RPH reaction rates. This suggests that the recrossing effects reflected by the transmission coefficients in Table 4.1, were not significant enough to significantly impact the kinetic simulations performed.

4.2.2 Solvent-phase dynamics

Transmission coefficients

In this section, we calculate the reaction rate for each reaction, shown in Figure 4.2, using conventional TST in solvent-phase using an implicit solvent model. Furthermore, we also use the RPH framework on the same reactions using the same implicit

solvent model to determine the transmission coefficient from the MEPs determined, shown in Figure 28-33 in the Appendix, which can then be combined to the TST reaction rate in order to determine the dynamically correct reaction rate.

The transmission coefficients, for each reaction, determined using the RPH framework are shown in Table 4.2.

Table 4.2: Transmission coefficients for the reactions investigated of the Heck–Breslow mechanism for alkene hydroformylation using a cobalt catalyst studied using the RPH approach in solvent-phase using an implicit solvent model.

Reaction	$C_{fs}^{cl}(t)$ **plateau value**
R1	0.93
R2	0.79
R3	0.94
R4	0.46
R5	0.40
R6	0.72

The transmission coefficients determined for the six reactions in solvent-phase using an implicit solvent model were much closer to unity than the transmission coefficients in gas-phase. For R4, the transmission coefficient, which showed large amounts of recrossing in gas-phase (0.26), was 0.46. For R1, R2, R3 and R6, the transmission coefficients were 0.93, 0.79, 0.94, and 0.72 respectively, all of which were equal or larger than their gas-phase counterparts. Lastly, R5 was the only other reaction which had a noticeable difference in the transmission coefficient in solvent-phase and gas-phase, 0.40 and 0.50 respectively.

The differences between the solvent-phase and gas-phase transmission coefficients can be attributed to the differences in the resulting MEPs shown in Figures 22-33 in the Appendix. As the RPH is constructed using information of the MEP, the differences on the MEP which arise from using an implicit solvent model will result in different coupling constants and thus the RPH will be different and so will the transmission coefficients. This follows how solvents can effect dynamics, and is explained in detail in Section 2.1.2, whereby there may be transfer in energy between the solvent and system reducing the amount of recrossing as there is less energy to recross the dividing surface. Furthermore, the system may bump into the solvent molecules at different points along the MEP, thus influencing the dynamics. However, this would have to be investigated with explicit solvents and not implicit solvents, to observe these effects.

Kinetics Studies

The reaction rates determined via conventional TST as well as the dynamically correct reaction rate determined via RPH for the reactions in solvent-phase using an

implicit solvent were used as input for kinetic simulations. The time-dependence of the concentration of the cobalt catalyst and the aldehyde product, using an initial concentration of 0.13284 mol dm^{-3} for the cobalt catalyst and 1.3284 mol dm^{-3} for the ethene, H_2 and carbon monoxide, are shown in Figure 4.6. In the figure, the concentration of the cobalt catalyst, determined after using TST rates and RPH rates, remains stable again in both cases and is also in agreement with the literature.[147,148] The difference between the time-dependent concentration using TST rates and RPH rates were minimal, only 0.00006 mol dm^{-3}, after one second.

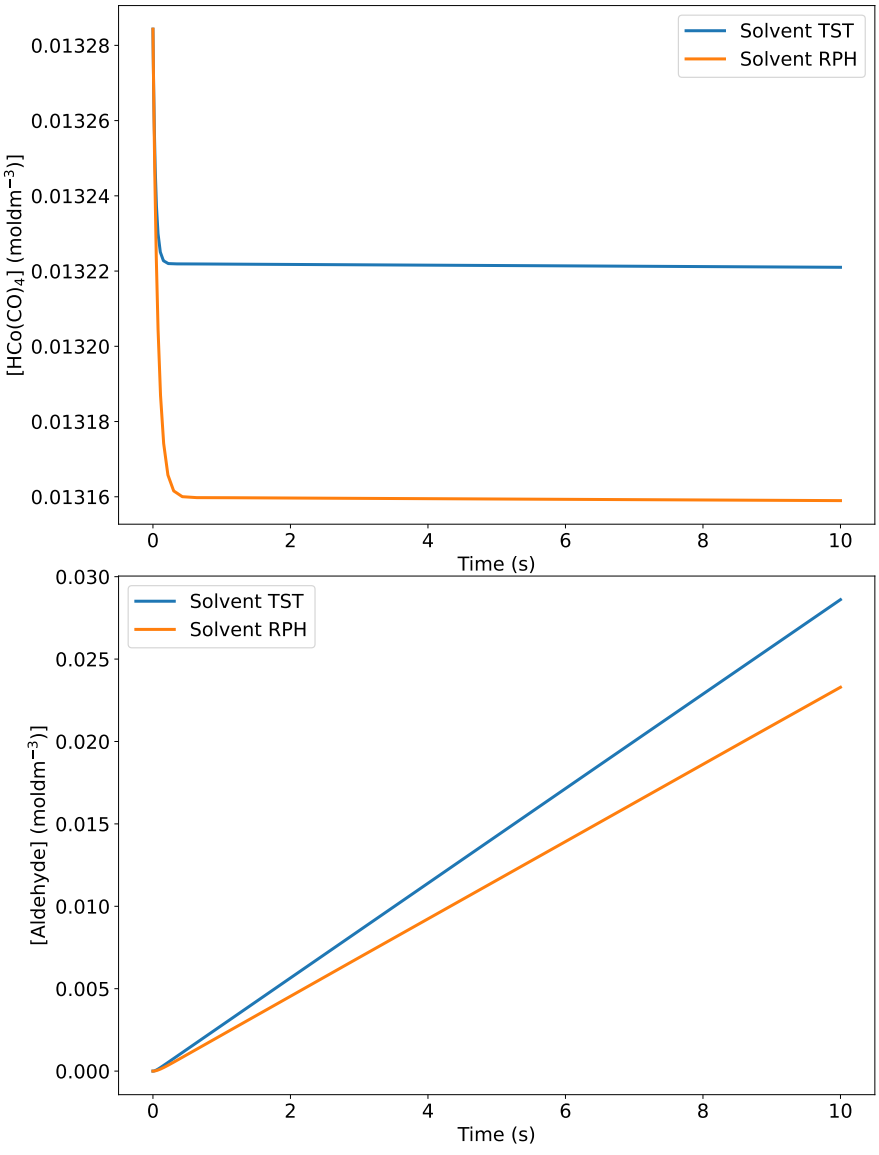

Figure 4.6: The time evolution of the concentrations of $HCo(CO)_4$ and the aldehyde product obtained using TST and RPH-derived reaction rates using the following initial concentrations: 0.13284 mol dm^{-3} for the cobalt catalyst and 1.3284 mol dm^{-3} for the ethene, H_2 and carbon monoxide.

The trend in time-dependence of the concentration of the aldehyde product in

solvent-phase is very similar to that in gas-phase and also corresponds to what is reported in literature, when either TST rates or RPH rates are used.[147,148] Similarly to the gas-phase results, there is a short induction period, and then the trend becomes linear for the rest of the time. Again, the time-dependent concentration of the aldehyde product using the RPH rates is smaller than when TST rates were used. This could also result in the recrossing effects having an influence on the kinetic simulations. The rate is obtained from the slope of the line in the range of 1-10 seconds, like in gas-phase conditions. The concentration of the aldehyde product was also a magnitude larger than reported in the literature, but the same as the gas-phase results we presented Section in 4.2.1. Again, this suggests that the energy barrier differences between our work and the literature (for example for R4), leads to a noticeable impact upon the concentration of the aldehyde product. An effect that has been reported in previous literature.[54]

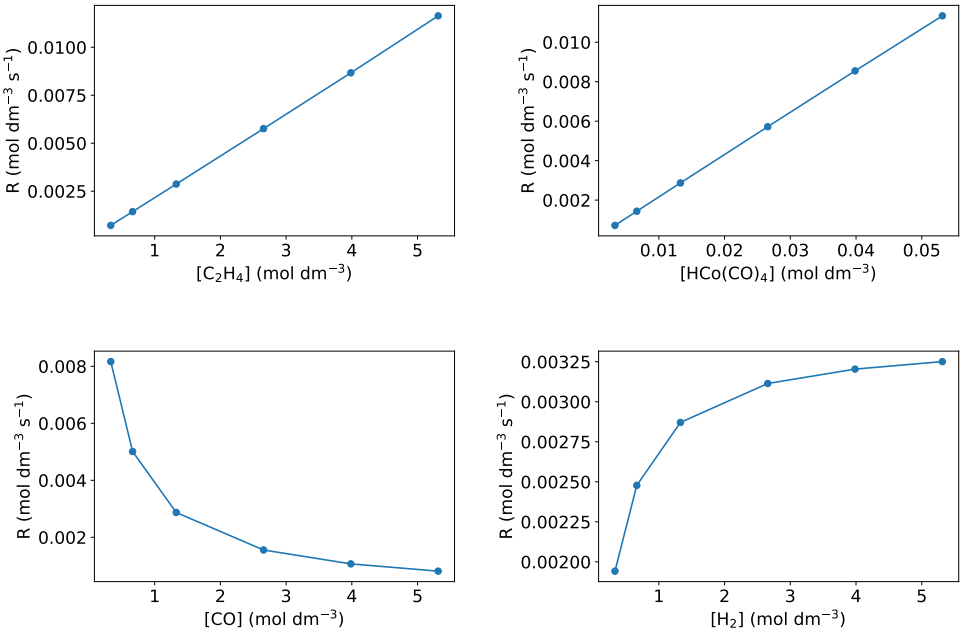

Figure 4.7: The rates of hydroformylation of the aldehyde product in solvent-phase for various initial conditions using TST-derived reaction rates.

With the TST-derived reaction rates and the RPH-derived reaction rates, the rate law for hydroformylation in solvent-phase can be determined. In Figure 4.7, we show the dependence of the TST-derived reaction rates on the concentrations of the cobalt catalyst and the starting materials (ethene, molecular hydrogen and carbon monoxide) in solvent-phase. Compared to the results in gas-phase using TST-derived reaction rates, the trends shown in solvent-phase using TST-derived reaction rates do not differ much. The reaction rate with respect to the concentration

of ethene was first-order, and the reaction rate with respect to the concentration of the cobalt catalyst was first-order just like the results shown in gas-phase. The reaction rate with respect to concentration of carbon monoxide was also inversely proportional and could be fitted with the same equation used for the gas-phase TST reaction rates result, Equation 4.1. Lastly, the reaction rate with respect to the concentration of the molecular hydrogen was also fractional, however the value was different, 0.17 instead of 0.06 in gas-phase and using TST reaction rates.

And so, the rate law for the hydroformylation using a cobalt catalysis in solvent-phase and using TST-derived reaction rates is shown in Equation 4.4;

$$R = \frac{[\mathrm{H_2}]^{0.17}[\mathrm{cat}][\mathrm{ethene}]}{(1 + a_1[\mathrm{CO}] + a_2[\mathrm{CO}]^2)}. \tag{4.4}$$

The dependence of the RPH-derived reaction rates with respect to the concentrations of the cobalt catalyst and the starting materials (ethene, molecular hydrogen and carbon monoxide) in solvent-phase is shown in Figure 4.8. Again, the results are very similar to the results already reported in this Chapter, whether it is in gas-phase or solvent-phase or depending on which reaction rates are used.

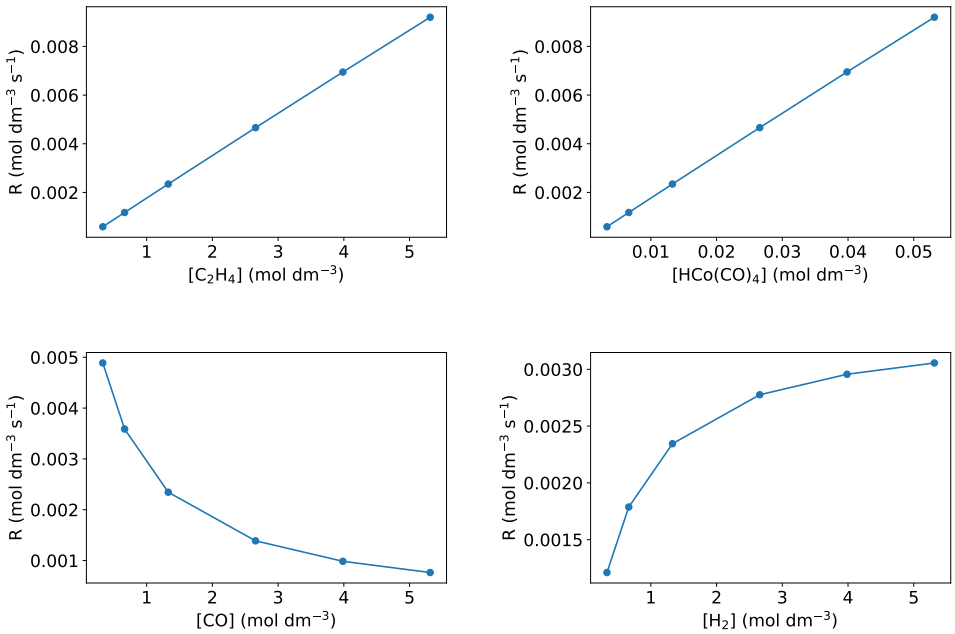

Figure 4.8: The rates of hydroformylation of the aldehyde product in solvent-phase for various initial conditions using RPH-derived reaction rates.

The reaction rates with respect to the concentration of ethene and the cobalt catalyst when using RPH-derived reaction rates are both first-order. The reaction

rate with respect to the concentration of carbon monoxide using RPH-derived reaction rates is also inversely proportional, and again, can be defined by the same equation, reported above, Equation 4.1. Finally, the reaction rate with respect to the concentration of molecular hydrogen is fractional, with a value of 0.3, differing slightly from the gas-phase results and the solvent-phase result using TST-derived reaction rates.

The rate law for the hydroformylation using a cobalt catalysis in solvent-phase and using RPH-derived reaction rates is shown in Equation 4.4;

$$R = \frac{[\mathrm{H_2}]^{0.3}[\mathrm{cat}][\mathrm{ethene}]}{(1 + a_1[\mathrm{CO}] + a_2[\mathrm{CO}]^2)}. \tag{4.5}$$

Similarly, to the gas-phase results, the differences between using TST-derived reaction rates and RPH-derived reaction rates on the final rate law equation in solvent-phase were minimal. The only differences were linked to the reaction rate with respect to the concentration of molecular hydrogren which increased slightly when RPH reaction rates were used. This could suggest that the recrossing effects determined via the transmission coefficients in Table 4.2 had little influence on the kinetic simulations performed.

4.3 Comparing TST and RPH reaction rate effects on the kinetic simulations

The differences between using TST-derived reaction rates and RPH-derived reaction rates in either gas-phase or solvent-phase were rather negligible, with only the reaction rate with respect to the concentration of molecular hydrogen being different in terms of the magnitude of the fit. The reaction rate with respect to the concentration of carbon monoxide, the cobalt catalyst and ethene were inversly proportional, first-order and first-order respectively, using either TST-derived reaction rates or RPH-derived reaction rates.

This would suggest that the recrossing effects reflected by the transmission coefficients determined in Tables 4.1 and 4.2 for the reactions investigated had little to no effect on the resulting kinetic simulations. In Figure 4.9, the time evolution of the concentrations of all the species in the hydroformylation catalytic cycle in gas-phase obtained using TST and RPH reaction rates using the following initial concentrations: 0.13284 mol dm^{-3} for the cobalt catalyst and 1.3284 mol dm^{-3} for the ethene, molecular hydrogen and carbon monoxide. Across all the species, the same trends are observed in the time evolution of the concentrations between TST reaction rates

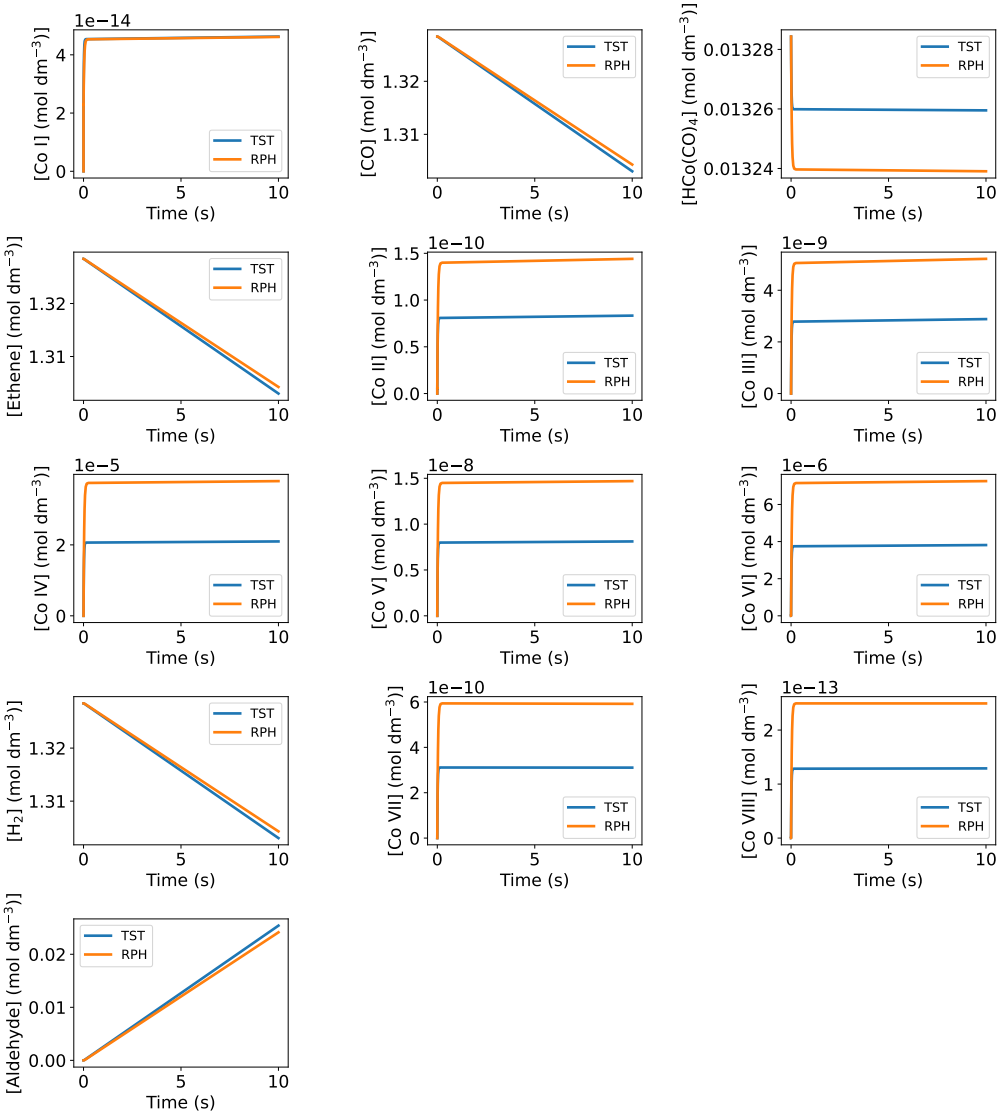

Figure 4.9: The time evolution of the concentrations of all the species involved in the catalytic cycle in the gas-phase, obtained using TST and RPH-derived reaction rates using the following initial concentrations: 0.13284 mol dm^{-3} for the cobalt catalyst and 1.3284 mol dm^{-3} for ethene, H_2 and carbon monoxide.

and RPH reaction rates. In terms of the initial species, carbon monoxide, molecular hydrogen, ethene and the cobalt catalyst, the difference in TST reaction rates and RPH reaction rates is negligible as the same trends are followed. In terms of the intermediate structures involved in the catalytic cycle, the trends in the time evolution of the concentrations is the same, however, the magnitude is lower for the TST-derived reaction rates, with the exception of the Co I species.

In Figure 4.10, the time evolution of the concentrations of all the species in the hydroformylation catalytic cycle in solvent-phase obtained using TST and RPH reaction rates using the following initial concentrations: 0.13284 mol dm^{-3} for the cobalt catalyst and 1.3284 mol dm^{-3} for the ethene, molecular hydrogen and carbon

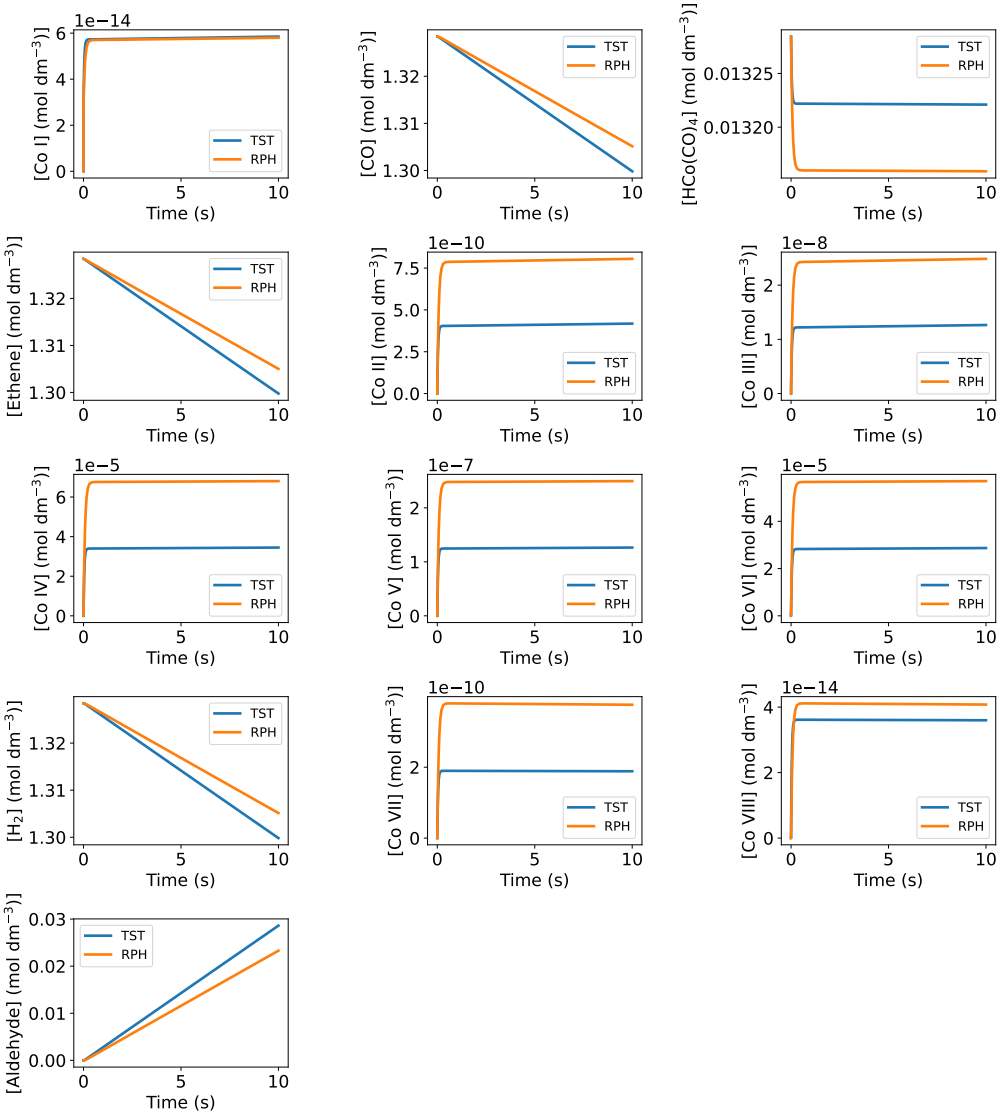

Figure 4.10: The time evolution of the concentrations of all the species involved in the catalytic cycle in solvent-phase, obtained using TST and RPH-derived reaction rates using the following initial concentrations: 0.13284 mol dm^{-3} for the cobalt catalyst and 1.3284 mol dm^{-3} for the ethene, H_2 and carbon monoxide respectively.

monoxide respectively. Similarly to the results shown in gas-phase, the differences in TST-derived reactions rates and RPH-derived reaction rates are almost negligible. Just like in gas-phase, for the initial species, the trends are very much the same for both TST reaction rates and RPH reactions rates with minimal differences. Similarly to the gas-phase results, the time evolution of the concentrations when using TST reaction rates and RPH reaction rates follow the same trends for the intermediate species formed in the catalytic cycle. Although, when using TST reaction rates, the time evolution of the concentrations were smaller in magnitude.

These results, in both gas-phase and solvent-phase, highlight the fact that there were in fact differences based on whether TST reaction rates or RPH reaction rates

were used. While not obvious, the magnitude of the time evolution of the concentrations for the intermediate species, in both gas-phase and solvent-phase, was smaller when using TST reaction rates compared to RPH reaction rates. However, in terms of the initial species, cobalt catalyst and ethene, molecular hydrogen and carbon monoxide, the differences between TST reaction rates and RPH reaction rates were minimal. Based on these results, the rate law being practically identical when using TST reaction rates or RPH reaction rates could be due to the time evolution of the concentrations for the initial species being effectively the same in both cases.

4.4 Conclusions

This Chapter showcased how the RPH approach can be used to determine reaction rates for a catalytic cycle and subsequently use these reaction rates to run kinetic simulations to determine the rate law. As is often the case, in the context of rate laws for catalytic cycles, TST is typically used to determine reaction rates. However, TST fails to account for recrossing effects and so, the time evolution of concentration for the various species may not be accurately described if recrossing effects are present during a catalytic cycle.

In this Chapter, we investigated the Heck–Breslow mechanism for alkene hydroformylation using a cobalt catalyst in both gas-phase and solvent-phase. We used both TST-derived reaction rates and RPH-derived reaction rates and subsequently ran kinetic simulations to derive the rate law for the catalytic cycle. For the gas-phase results, the TST and RPH-derived reaction rates resulted in close to the same rates of hydroformylation of the aldehyde product and also close to the same rate law, shown in Equations 4.2 and 4.3. In terms of the solvent-phase results, the TST and RPH-derived reaction rates also resulted in close to the same rates of hydroformylation of the aldehyde product and rate law, shown in Equations 4.4 and 4.5.

When an implicit solvent model was used to describe the solvent-phase, the differences in the rates of hydroformylation of the aldehyde product between gas-phase and solvent-phase were negligible. Moreover, the rate law determined in both gas-phase and solvent-phase was very similar, with only the rates of hydroformylation of the aldehyde product for molecular hydrogen having increased. This does agree with literature where it is stated that, for this system in particular, the Heck–Breslow mechanism for alkene hydroformylation using a cobalt catalyst, solvent effects are unimportant and would not have a significant effect upon the reaction rate.[147,148]

Finally, we investigated the differences between TST-derived reaction rates and RPH-derived reaction rates for the time evolution of the concentrations for each species involved in the catalytic cycle. This showed that while there were no signifi-

cant differences in the trends observed overall, the magnitude between TST and RPH reaction rates for intermediate species differed more than for the initial species.

Chapter 5

Initial Reaction Path Generation Methods

> It doesn't mean, it will be exactly the same. Maybe you aren't a shadow on the water but instead, a fish that breaches the water's surface.
>
> *Berserk*, Kentaro Muira

Summary

In this Chapter, two novel reaction-path finding methods, Projected Navigation String Method (P-NSM) and Adiabatic Navigation String Method (A-NSM), are presented in order to generate good approximate initial reaction paths which can then be used as a starting point to determine the minimum energy path (MEP) via a nudged elastic band (NEB) calculation. When compared to other popular methods such as the Image Dependent Pair Potential (IDPP) method and Root Mean Square Deviation Push-Pull (RMSD-PP), the P-NSM and A-NSM performed the same if not better, in terms of distance between the initial reaction path and the MEP, and in terms of the number of force evaluations needed for subsequent NEB refinement. This Chapter first begins with a brief introduction behind the importance of the MEP, followed by the theory of the methods used in this Chapter. Secondly, P-NSM and A-NSM are used on a set of model reactions as examples and compared to IDPP and RMSD-PP. Finally, the parameters used in P-NSM and A-NSM are discussed and their effect on the resulting initial reaction path is explored in detail.

5.1 Introduction

The minimum energy path (MEP) is a necessary and key concept when analysing chemical reactions and describing their dynamics and mechanisms.[16,36,87,151–157] The MEP is defined as the lowest energy path which connects specified reactants and products of a given reaction on the potential energy surface (PES), and is essential when investigating kinetic and thermodynamic properties.[67,85,94,158–160] As such, determining the MEP is typically the first step when analysing any reactive chemistry such as organometallic homogeneous catalysis,[46,48–50,161–166] heterogeneous catalysis[167–171] and drug discovery.[172–174] As a note for this Chapter, we acknowledge that the reaction path finding methods discussed in this Chapter do not necessarily find the MEP but instead, a more accurate description would be that they find a steepest descent path from a saddle point to minima which can be referred to as an intrinsic reaction coordinate (IRC).[175] However, for the sake of this Chapter, we refer to these paths as the MEP.

5.1.1 Nudged elastic band

The necessity of the MEP for reactive chemistry has motivated the development of many methods designed to find the MEP. Perhaps the most popular method used to determine MEPs is the nudged elastic band (NEB) method, where a series of nodes along a string is used to representing the reaction path.[96,176,177] The nodes along this string correspond to intermediate configurations along the reaction pathway where each node is connected to one another via spring forces which help keep the nodes in place and equally spaced.

At each iteration of a NEB calculation, all the nodes which make up the reaction path are relaxed to the MEP. This is done by minimizing the forces arising from the underlying potential energy surface (PES) perpendicular to the string, and the forces due to artificial harmonic spring terms acting parallel to the string. In order to project the forces, the tangent along the string $\hat{\boldsymbol{\tau}}$ is calculated as the unit vector to the higher energy neighbouring node. As a limit, a linear interpolation between the vectors to neighbouring nodes is used so that the direction of the tangent does not change so suddenly, and so the NEB calculation is more stable as artificial kinks in the high force regions of the path are avoided. The final NEB force, $\boldsymbol{F}_i^{NEB}$, acting on each node can then, simply be described by Equation 5.1;

$$\boldsymbol{F}_i^{NEB} = \boldsymbol{F}_i^{g\perp} + \boldsymbol{F}^{S\parallel}, \tag{5.1}$$

where $F_i^{\perp}$ is defined as the forces arising from the PES perpendicular to the band,

$$\boldsymbol{F}_i^{\perp} = \boldsymbol{F}_i - (\boldsymbol{F}_i \cdot \hat{\boldsymbol{\tau}}_{\boldsymbol{i}})\hat{\boldsymbol{\tau}}_{\boldsymbol{i}}, \tag{5.2}$$

and $F^{S\parallel}$ is defined as the forces from the artificial harmonic spring terms acting parallel to the band,

$$\boldsymbol{F}^{S\parallel} = k(|\boldsymbol{r}_{i+1} - \boldsymbol{r}_i| - |\boldsymbol{r}_i - \boldsymbol{r}_{i-1}|)\hat{\boldsymbol{\tau}}_{\boldsymbol{i}}, \tag{5.3}$$

where r_i is the position of the ith image and k is a defined spring constant.

Once the NEB calculation has converged and the MEP is determined, the highest-energy node can, usually, be used as a start for transition-state (TS) searching algorithms in order to subsequently use transition-state theory (TST) to derive reaction rates.[28,32,67,87,98,178–180] The climbing image nudged elastic band method (CI-NEB) is a modification to the standard NEB method where the highest-energy node is brought closer to the saddle point during the calculation, which avoids having to run two separate optimizations or to interpolate to find the saddle point.[96] This is achieved by having the spring forces acting on the highest-energy node set to zero, enabling the node to climb to the saddle point via a reflection in the force along the tangent, shown in Equation 5.4 allowing for convergence towards the TS configuration,

$$\boldsymbol{F}_l^{CI} = \boldsymbol{F}_l - 2\boldsymbol{F}_l \cdot \hat{\boldsymbol{\tau}}_l \hat{\boldsymbol{\tau}}_l, \tag{5.4}$$

where l is the highest-energy node.

5.2 Limitations of the NEB method

Despite the simple implementation and efficacy of the NEB method, there are still some disadvantages. First, the method is reliant on an adequate spring constant in order to converge to the MEP. If the spring constant is too large, the condition number of the optimization problem can become very large resulting in a slow convergence to the MEP. If the spring constant is too small, the node spacing can become quite erratic resulting in a poor description of the reaction path.[159] Second, the NEB method requires a good initial path as a starting point, which is usually done via a linear interpolation, linear synchronous transit (LST) interpolation,[181,182] or using the image dependent pair potential (IDPP) method.[157] Linear interpolation and LST interpolation typically tend to result in a decent initial reaction path

guess, however, for some reactions, both methods can result in bad initial reaction paths which either lie far from the MEP or have images along the path where atoms come much too close together, leading to large atomic forces. As such, a bad initial reaction path can result in either a slow convergence to the MEP, or in some cases, in unrealistic chemical structures which lead to electronic structure calculations not being able to determine potential energy and forces. On one hand, the former will inevitably lead to the number of force evaluations (defined by number of nodes along the path multiplied by the number of NEB iterations) to increase significantly as will the associated computational cost. On the other hand, the latter can be avoided by using chemical intuition. However, while choosing appropriate bond lengths and angles for the interpolation or assessing the sensibility of the interpolation can be done in some cases, it is not always an option when investigating new chemistry or complex reaction networks.[155] Going beyond using an interpolation between reactant and product minima or a similar method to generate an initial path for NEB, several methods have emerged where an extra term is added to the electronic energy of a system guiding the system along the PES as the energy function is minimised. These methods, along with IDPP, are discussed more in detail in the following Sections.

5.3 Image dependent pair potential

The image dependent pair potential (IDPP) method is a popular alternative to the traditional linear interpolation used in initial reaction path calculations.[157] With IDPP, an interpolation of all pair distances between atoms is done for each of the "images" along the reaction path where the energy minima representing the initial and final states of the transition are defined as α and β. Where the interpolated distance between atoms i and j for image k is,

$$d_{i_j}^{\kappa} = d_{i_j}^{\alpha} + k(d_{i_j}^{\beta} - d_{i_j}^{\alpha})/p, \tag{5.5}$$

where $d_{i_j} = \sqrt{\sum_{\sigma}(r_{i,\sigma} - r_{j,\sigma})^2}, \sigma = x, y, z$ is the distance between coordinates, r, of atoms i and j, and the index k denotes the image number in the path and runs from 1 to p $-$ 1.

The squared norm of the difference between the coordinates of an image and the target interpolated pair distance values are then used as the energy of that image in a NEB-like optimisation process. In essence, for each image, the pair distances are used as target values, for which the initial reaction path can then be made to match as closely as possible. The energy function at each image then takes the form,

$$E_K^{IDPP}(R_K) = \sum_i^N \sum_{j>i}^N w(d_{ij}) \left(d_{ij}^{\kappa} - \sqrt{\sum_{\sigma} (\boldsymbol{r}_i(R_K) - \boldsymbol{r}_j(R_K))^2} \right)^2 \tag{5.6}$$

where R_K are the Cartesian coordinates of the Kth image, $r_i(R_K)$ and $r_j(R_K)$ are the Cartesian coordinates of the ith atom in the Kth image and w is a weighting function. A weighting function is used so that short distances between atoms are prioritised as these typically represent stronger interactions between the atoms as opposed to atoms which are far apart and weakly interacting.

While the IDPP method provides significant improvement over a linear interpolation in generating an initial reaction path, the method can sometimes create extremely distorted intermediate structures along the paths which leads to instability and convergence issues. For example, in the work by Zhu *et al.*,[155] it was demonstrated that in the imidazole hydrogen migration reaction, the IDPP interpolation resulted in a reaction path similar to the MEP but with the presence of a kink in the path. Moreover, this kink did not disappear even when the convergence threshold was increased, highlighting that the IDPP convergence behavior is not always robust. Furthermore, in the ring formation in dehydro Diels-Alder reaction, the IDPP interpolation failed to result in a reaction path highlighting that for reactions with many structural changes, such as ring closure and large torsional displacements in this case, IDPP interpolation may not result in a reaction path.[183]

5.4 Root mean square deviation-push-pull

The root mean square deviation-push-pull (RMSD-PP) is another method used to approximate initial reaction path calculations, where the main advantage lies in the rapid estimation of these initial reaction paths.[184,185] The underlying theory of the RMSD-PP method is rather simple and consists of adding two Gaussian biasing potentials to the electronic energy of a system, one which "pushes" the system away from the reactant structure and another which "pulls" the system towards the product structure. The total energy of the system is then defined by Equation 5.7.

$$E_{total} = E_{total}^{elec} + k_{push} e^{-\alpha \Delta r^2} + k_{pull} e^{-\alpha \Delta p^2}, \tag{5.7}$$

where k_{pull} is a constant which represents the pulling strength and is positive, k_{pull} is a constant which represents the pushing strength and is negative, α is a weight parameter and Δr^2 and Δp^2 are the root mean square deviations (RMSD) between the current structure and the reactant and product, respectively.

The RMSD-PP methodology starts from the reactant and goes towards the product, where at each step, the energy function (Equation 5.7) is geometry optimised and the final relaxed geometry is saved. Following this, each saved geometry is re-optimised with three optimisation steps without the biasing potentials added to the total energy function. All the final geometries and their energies then correspond to a reaction path linking the reactant to the product. This procedure is repeated two more times with increasing push/pull strengths and the best reaction path is then used to start TS searching calculations. The best reaction path is then determined following the procedure outlined by Grimme,[184] which is a path where the RMSD of the end structure and the input product structure is less than 0.3 Bohr while using the smallest absolute values of k_{pull} and k_{pull} .

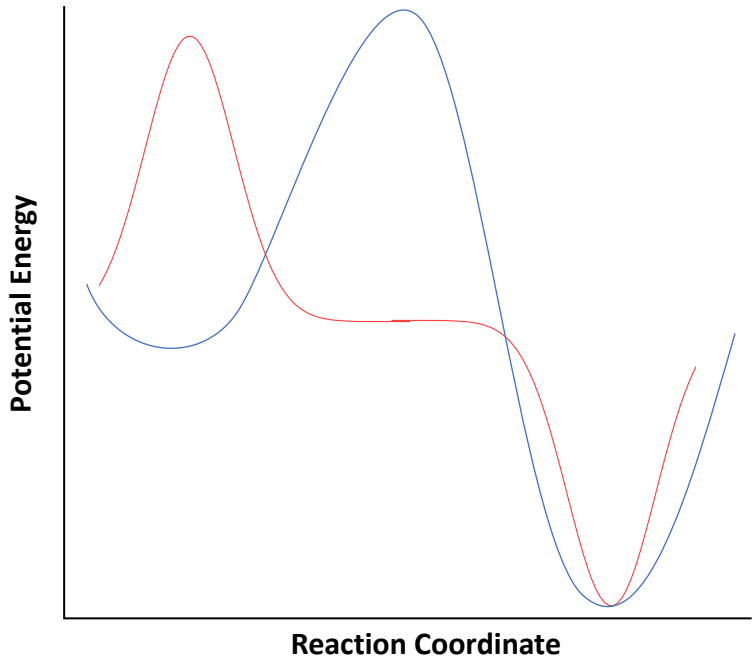

Figure 5.1: An illustration depicting the main idea behind the RMSD-PP method, whereby, two Gaussian functions (red) are used to, initially, push the system from the reactant minimum (blue) above the saddle point and then, subsequently pull the system into the product minimum (blue). Once the system has been pushed or pulled by the Gaussians, the system is minimised without the Gaussians so that it can roll as close as possible to the MEP.

5.5 Adiabatic mapping

Adiabatic mapping is a simple method which has been used to determine reaction paths in QM/MM studies of enzymes and proteins.[186,187] The method consists of initially defining a geometric coordinate to model the reaction, either a bond length, dihedral angle or a combination of bond lengths. Then, at fixed values of the reaction coordinate from reactants to products, a reaction path is mapped

out as the system's energy is minimised with an added term which restrains the reaction coordinate using a harmonic potential with a force constant. A version of the adiabatic method, is called the restrained distance (RESD), where the distance between atoms is used as the restraint. The energy function which is minimised at each step along the reaction coordinate is then:

$$E_{total} = E_{total}^{elec} + \sum_{j}^{N} \frac{1}{2} \mathrm{k}_j \Big(\sum_{I}^{M_j} a_{ij} |R_{1ij} - R_{2ij}| - d_j \Big)^2, \tag{5.8}$$

where k_j is the force constant, a_{iJ} is a weighting function, $R_{1ij} - R_{2ij}$ is an interatomic distance and d_j is a distance parameter which is systematically modified in small increments until the interatomic distance corresponds to the product interatomic distance.

Similarly to other reaction path finding methods, the maximum energy value in the approximate reaction path corresponds to the approximate TS location and can be used for subsequent TS optimisation.

The adiabatic method is typically used to model reactions where only a small number of chemical and structural changes occur, for example in the reaction involving chorismate to prephenate in the enzyme chorismate mutase or in the mechanism of the aromatic hydroxylation of phenol by a flavin dependent phenol hydroxylase.[188,189] Furthermore, the adiabatic method may overestimate energy barriers if the atom movements connected to the reaction are not included in the reaction coordinate, meaning that the choice of the reaction coordinate is crucial.

5.6 The climber method

The climber method was developed as a morphing method to be used to understand the pathways that a protein follows between stable conformations.[190] The method uses harmonic restraints which are added to the total energy function which effectively pulls the inter-residue distances of a starting conformer to a target conformer as the function is minimised at each step. The total energy of the system is then defined by Equation 5.9,

$$E_{total} = E_{total}^{elec} + k_{\mathrm{spring}} G \Big[\sum_{i} \sum_{j} F(d_{ij}) \Big], \tag{5.9}$$

where $F(d_{ij})$ is a function defined as $(d_{ij}^2 - D_{ij}^2)^2/(2(d_{ij}^2 + D_{ij}^2))$, d_{ij} and D_{ij} are the distances between atoms i and j in the moving and target structures respectively,

and G is a function which relates the distance deviation between the current and target conformers to the restraint energy.

Furthermore, in the climber method, at each step, the amount moved by the starter conformer to the target conformer is measured by the change in coordinate root-mean square deviation (cRMSD). If the amount moved is too small and the cRMSD between the current and target structures has not decreased by the desired amount, then k_{spring} is increased in the next step. Similarly, if the amount moved is too large and the cRMSD change is sufficient, then k_{spring} is reduced in the next step. As such, k_{spring} is a self-adjusting variable which ensures that at each step, the conformation can move to the target conformation at an approximate constant rate.

5.7 Artificial force induced reaction

The artificial force induced reaction (AFIR) is a single ended method where the idea consists of either pushing molecular fragments together or pulling them apart and is typically used to explore the PES for stable molecular geometries of a reaction.[191] This is achieved by adding a linear function of the distance between molecular fragments to the electronic energy. The total energy for a system comprising of fragment A and fragment B is then defined by Equation 5.10,

$$E_{total} = E_{total}^{elec} + \rho\alpha \frac{\sum_{i\epsilon A} \sum_{j\epsilon B} \omega_{ij} r_{ij}}{\sum_{i\epsilon A} \sum_{j\epsilon B} \omega_{ij}}, \tag{5.10}$$

where ρ takes a value of 1 to push the molecular fragments together or 0 to pull them apart, r_{ij} corresponds to the distances between atom i in the fragment A and atom j in the fragment B and ω corresponds to a weight where closer atom pairs are weighted stronger than distant atom pairs. The weighting function is defined as,

$$\omega_{ij} = \left[\frac{(R_i + R_j)}{r_{ij}} \right]^6, \tag{5.11}$$

where $(R_i + R_j)$ is the sum of the covalent radii of atoms i and j.

The parameter α corresponds to the mean force that acts on two atoms in their direct collision on the Lennard–Jones potential with collision energy γ, in the area from the minimum to the saddle point and is defined by the following,

$$\alpha = \frac{\gamma}{\left[2^{\frac{1}{6}} - \left(1 + \sqrt{1 + \frac{\gamma}{\epsilon}}\right)^{\frac{2}{6}}\right] R_0}, \tag{5.12}$$

where R_0 and ϵ correspond to the the standard Ar-Ar parameters of the Lennard-Jones potential, as suggested by the authors[191], and γ is a parameter chosen by users based approximately on the highest TS energies searched or based on if experimental conditions are known.

As such the added AFIR term to the electronic energy effectively eliminates the energy barrier along reaction paths, allowing for the system to reach either reactant or product minima wells fairly easily. The reaction path generated after using AFIR is labelled the AFIR path and while this path traverses low energy regions of the TS, we note that the highest energy point on the AFIR is often a good guess for the actual TS. A reaction path can then be determined using the TS as a starting point and running an IRC calculation.

5.8 Navigation string method

In this Chapter, we borrow concepts from the field of autonomous navigation with mobile robots, in an effort to determine accurate initial MEPs rapidly while keeping the computational cost, associated to the number of force evaluations, as small as possible. Autonomous navigation with mobile robots has been a field which has generated increased interest over the years due to technological advances and the rise of deep learning.[192,193]Autonomous navigation with mobile robots can deal with problems linked to area coverage and exploration, surveillance and problems requiring robots to move efficiently in an environment with obstacles or other constraints. Within this area of research, the idea of motion planning in unknown environments describes a robot equipped with a sensor trying to optimally go from an initial point to a final point with no prior knowledge of the environment and limited information being fed to it. This is achieved by using a navigation function which typically refers to a function of position, velocity, acceleration and/or time determined by a sensor which is then used to drive the robot from the initial to the final point in the most optimal way. The idea of using a navigation function to drive the system from one point to another is appealing as one can easily view the PES as the unknown environment the robot has to explore before finding the optimal path and the MEP as the optimal path a robot then takes. For the rest of the Chapter, we use and illustrate perhaps the simplest implementation of a navigation function used in motion planning in unknown environments.

5.8.1 Method

Navigation string method

In both the projected navigation string method (P-NSM) and adiabatic navigation string method (A-NSM), the underlying theory consists of adding a so-called navigation function biasing potential to the electronic energy of a system, with the total energy of the system at a node k now being defined in Equation 5.13. This navigation function essentially pushes the system across the PES from a user defined starting structure towards the target end structure.

$$E^{k}_{\text{total}} = E^{\text{elect}}_{\text{k}} + E^{\text{nav}}_{\text{k}}, \tag{5.13}$$

where $E^{\text{nav}}_{\text{k}}$ is defined in Equation 5.14

$$E^{\text{nav}}_{k} = k_{\text{nav}}(|R_k - R_{\text{end}}| - \rho_{\text{k}})^2, \tag{5.14}$$

where k_{nav} is the navigation force constant which acts as the driving force that pushes the system towards the end node, R_k are the Cartesian coordinates of the current node k, R_{end} are the Cartesian coordinates of the end node and ρ_{k} is the distance between the Cartesian coordinates of a starting point (typically the reactant) and an end point (typically the product) defined in Equation 5.15,

$$\rho_{\text{k}} = \frac{\sqrt{r^2_{\text{start}} - r^2_{\text{end}}}}{\text{k}}, \tag{5.15}$$

where r_{start} are the coordinates of the starting point (reactants), r_{end} are the coordinates of the end point (products) and k is the current node.

The method used for the P-NSM and A-NSM to determine the reaction path has the same initial step, which is to determine the distance between the Cartesian coordinates of an optimised starting point and an optimised end point, defined as ρ. Subsequently a user defined number of nodes is iteratively grown from a single end and optimised while minimising the energy function defined in Equation 5.13, from the starting point configuration until the end point configuration is reached. Once the end point configuration is reached, we select 10 evenly spaced nodes from the NSM generated reaction path, which make up the final initial reaction path which will be used for the NEB refinement. The general NSM algorithm is shown in a flowchart in Figure 5.2. Throughout this work, we have used the steepest descent method with a parameterised step-size to minimise the energy function, however we note that other optimising algorithms could be used. The only difference between

the P-NSM and A-NSM lies within how the forces from the PES are described when added to the forces of the navigation function. In P-NSM, the tangential forces of the PES are projected out, leaving just the forces perpendicular to the PES, (Equation 5.16). In A-NSM, no projection is done to the forces. The projected forces in P-NSM are:

$$\boldsymbol{F}_k^{\perp} = \boldsymbol{F}_k - (\boldsymbol{F}_k \cdot \hat{\boldsymbol{\tau}})\hat{\boldsymbol{\tau}}, \tag{5.16}$$

where $\mathbf{F}_k$ are the forces acting on the system at node k and $\hat{\boldsymbol{\tau}}$ is the tangent between the start node and the end node.

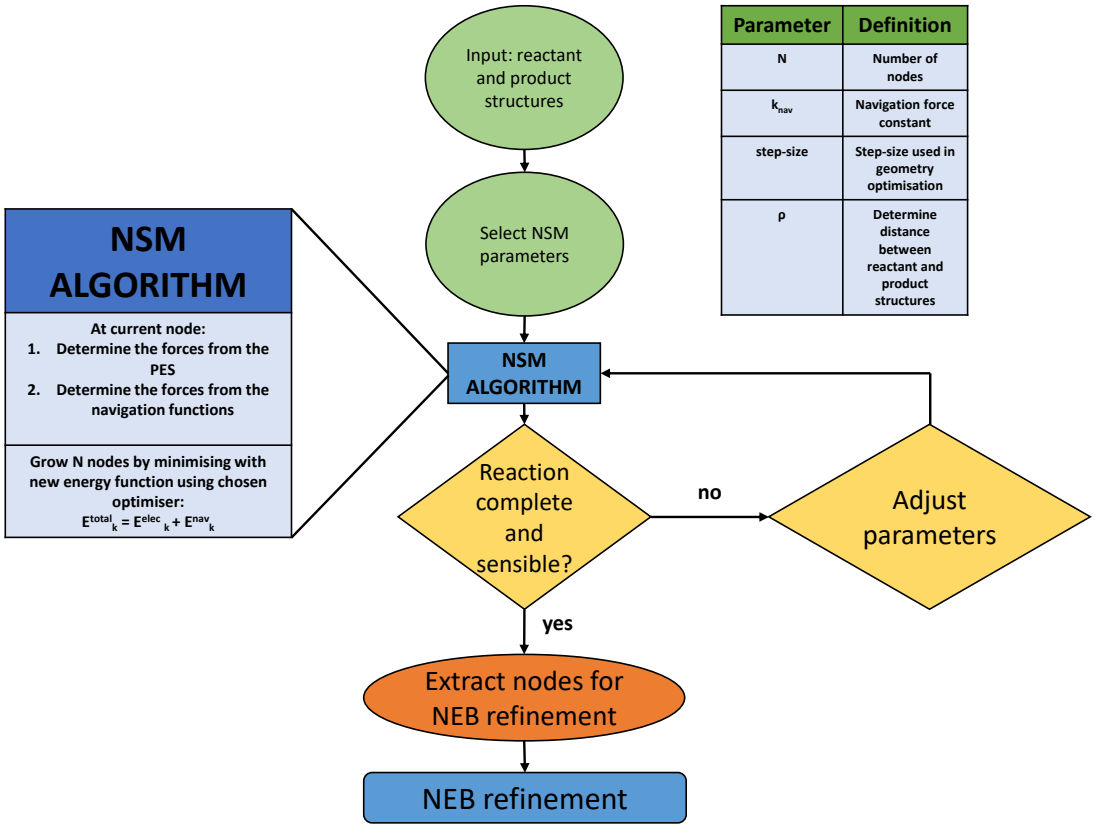

Figure 5.2: Algorithm flowchart for the navigation string method with parameter definitions.

Demonstration for the Müller-Brown PES

As proof of concept, we choose to investigate the Müller-Brown PES, a well known two-dimensional benchmark system often used to to investigate optimization algorithms and reaction-path finding methods, in order to illustrate the P-NSM algorithm for a two-dimensional problem.[9] The Müller-Brown PES is defined in Equation 5.17;

$$V(x,y) = \sum_{i=1}^{4} A_i e^{a_i(x-x_i^0)^2 + b_i(x-x_i^0)(y-y_i^0) + c_i(y-y_i^0)^2}, \tag{5.17}$$

where,

$$\mathbf{A} = [-200.0, -100.0, -170.0, 15.0] \quad \mathbf{a} = [-1.0, -1.0, -6.5, 0.7]$$
$$\mathbf{b} = [0.0, 0.0, 11.0, 0.6] \quad \mathbf{c} = [-10.0, -10.0, -6.5, 0.7]$$
$$\mathbf{x^0} = [1.0, 0.0, -0.5, -1.0] \quad \mathbf{y^0} = [0.0, 0.5, 1.5, 1.0].$$

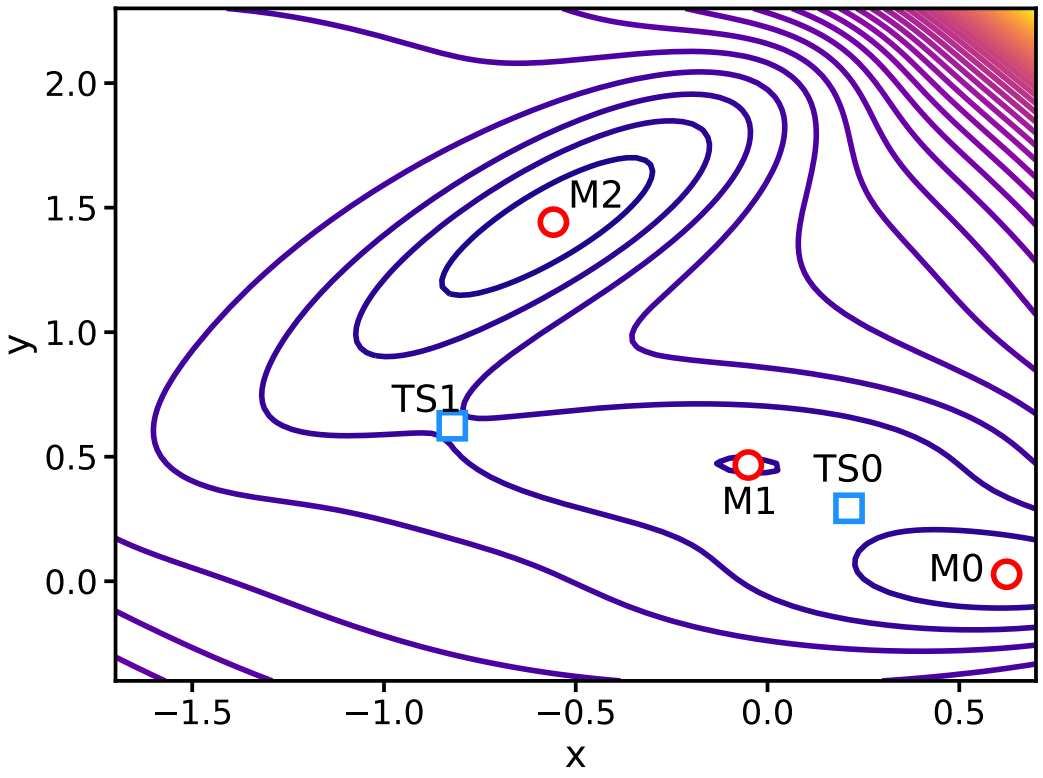

Figure 5.3: Müller-Brown potential energy surface featuring the three minima labelled M0, M1, M2 and the two TSs labelled TS0 and TS1.

The resulting Müller-Brown PES is shown in Fig 5.3, where there are three local minima (labelled, M0, M1 and M2) and two TS (labelled TS0 and TS1). Motion from the minimum M0 to the minimum M1 involves crossing a TS0 which roughly sits on a direct linear path connecting M0 to M1 and as such an initial approximate path for that reaction could be simply achieved using linear interpolation. In comparison, the motion from M1 to M2 which crosses TS1 is much more curved and thus determining a good initial reaction path approximation is a more challenging problem and so the focus here will be on this path.

The P-NSM algorithm is used between the minima M1 and M2 using $N = 25$, $k_{\text{nav}} = 80$ and a step-size of 0.003. The approximate reaction path determined by

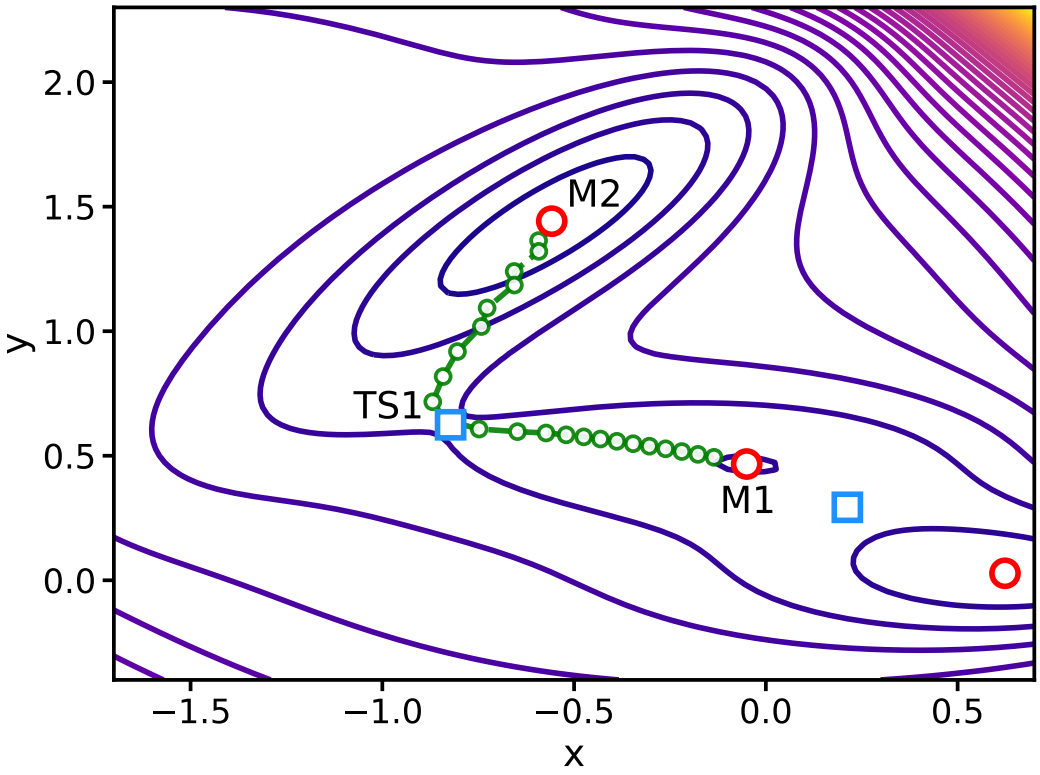

Figure 5.4: Navigation string method used on the Müller-Brown potential energy surface between point M1 and M2 crossing TS1.

the P-NSM algorithm results in a smooth reaction path which crosses the point TS1 and smoothly joins the minimum M2, as shown in Figure 5.4.

5.8.2 Further tests of the A-NSM and P-NSM algorithms

In the following, we use the A-NSM and P-NSM algorithms to generate initial MEP approximations for seven different molecular systems, shown in Figure 5.5. In each case, we use the A-NSM and P-NSM algorithms to generate an initial reaction path, and then, the standard NEB algorithm is used to refine the initial reaction path to determine the MEP.[96] Relevant calculation details of the A-NSM and P-NSM algorithm (N, k_{nav} and a step-size used for optimisation) are given for each individual reaction, however, energy gradient and potential energy evaluations were performed using semi-empirical PM3 calculations.[194]

The parameters used for the A-NSM and P-NSM calculations were determined from multiple test runs, however we note that after experimenting with various parameter values we have found that using a number of nodes of $20-50$, a navigation force constant of $0.05-0.1$ and a step-size of $0.25-0.75$ is a good starting point to determine initial reaction paths.

For all reactions, the NEB refinement was done with the following parameters,

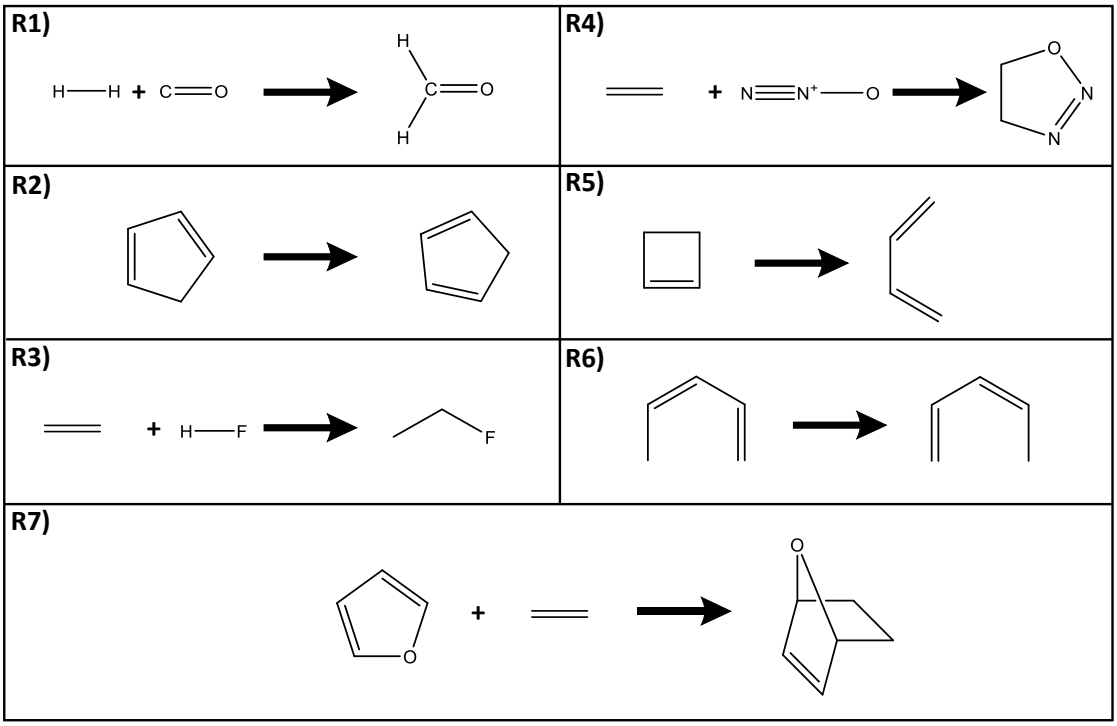

Figure 5.5: Reactions investigated using the A-NSM and P-NSM algorithms where a) is the formation of formaldehyde (R1), b) is the cyclopentene hydrogen transfer reaction (R2), c) is the addition of ethene and hydrofluoric acid (R3), d) is the addition of ethene and nitrous oxide (R4), e) is the ring opening of cyclobutene (R5), f) is the penta-1,3-diene hydrogen transfer reaction (R6) and g) is a Diels-Alder reaction (R7).

PM3 semi-empirical energy evaluations, a harmonic spring constant of $k_{spring} = 0.02$ $E_h a_0^{-2}$, and the calculations were performed until the root-mean-square force on atoms along the reaction path was less than 0.005 $E_h a_0^{-2}$. Finally, all electronic structure calculations were performed using the ORCA quantum chemistry package at the PM3 level of electronic structure theory.

Furthermore, we note that each of these reactions represents a different "reaction class", including hydrogen transfer reactions (R2 and R6), an isomerization reaction (R5) and bimolecular additions (R1, R3, R4 and R7); by studying different reaction types, we hope to show the applicability of the A-NSM and P-NSM algorithms to generate good initial reaction paths for a wide spectrum of reactions.

Lastly, we would like to note that for most of the reactions investigated in this section, the P-NSM and the A-NSM methods resulted in the same initial reaction path and MEP. As such, in the Figures shown in this section, the A-NSM initial reaction path and the subsequent MEP may not be visible.

Formaldehyde formation (R1)

We first consider the formation of formaldehyde, H_2CO, from direct reaction of molecular hydrogen, H_2, with carbon monoxide, CO. In terms of the parameters of the A-NSM and P-NSM methods, we used $N = 40$ nodes, $k_{\text{nav}} = 0.085$ and a step-size of 0.75.

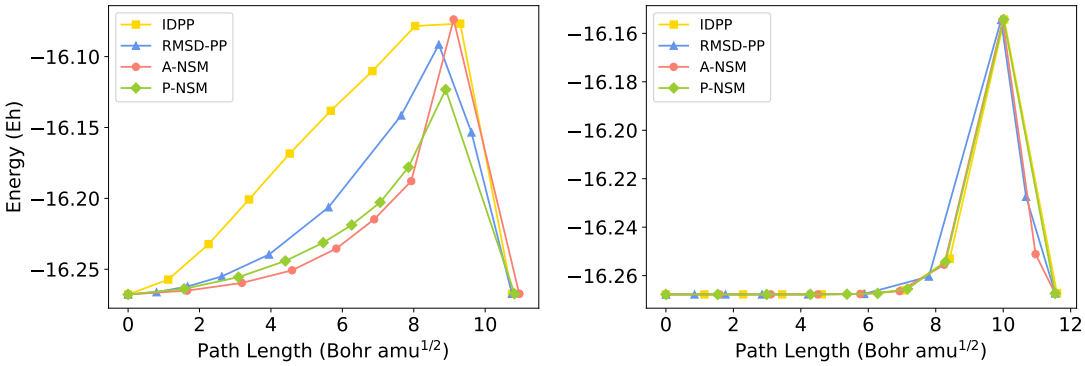

Figure 5.6: Energy profiles of the initial reaction paths (left) and MEPs (right) for the formation of formaldehyde reaction determined using different reaction path finding methods. Results are shown for the IDPP method (yellow squares), the RMSD-PP method (blue triangles), A-NSM (red circles) and P-NSM (green diamonds). The points on the plot represent the "images" used for NEB.

Figure 5.6 shows the initial approximate reaction calculated using the IDPP, RMSD-PP, A-NSM and P-NSM methods and the resulting MEP after using these initial reaction paths for NEB refinement. In the first instance, the resulting MEP determined after NEB refinement, was the same for all four methods, which indicated that the initial reaction paths calculated were all close enough to the expected MEP. The potential energy along the MEP is constant at $\sim$ -16.26 E_h until 8 Bohr, where it sharply increases towards the TS at $\sim$ -16.16 E_h and then again sharply decreases to the product at $\sim$ -16.26 E_h.

When looking at the calculated initial approximate reaction paths, shown in Figure 5.6 (left), it is clear that there are some differences between each method. Out of the four methods used, the initial reaction path calculated by the IDDP method was the worst. In the IDPP initial reaction path, the potential energy linearly increases from the reactant to the saddle point where it shortly plateaus, then it sharply decreases to the product, as opposed to how the potential energy is described in the MEP. Moreover, when comparing the saddle point, the saddle point on the IDPP initial reaction path is located just before 10 Bohr at $\sim$ -16.075 E_h and is also significantly less defined than the saddle point on the converged MEP. For the RMSD-PP method, the initial reaction path was an improvement and looked a bit more like the MEP than the IDPP method. In the RMSD-PP initial reaction path,

the potential energy increases more gradually along the reaction path and has a more defined saddle point at $\sim$ -16.100 E_h. Both, the A-NSM and P-NSM methods, resulted in very similar initial reaction paths, where the potential energy gradually increases along the reaction path but closer to what it looks like in the MEP. The biggest difference between the A-NSM initial reaction path and the P-NSM initial reaction path is in the saddle point, where in former method the saddle point has a potential energy value of $\sim$ -16.075 E_h and in the latter method the saddle point has a potential energy value of $\sim$ -16.125 E_h which is the closest, out of the four methods, to the saddle point on the MEP.

Cyclopentene hydrogen transfer (R2)

The second example considered is the hydrogen transfer reaction on a cyclopentene molecule. The parameters used for both the A-NSM and P-NSM method were the following: $N = 30$ nodes, $k_{\text{nav}} = 0.085$ and a step-size of 0.75.

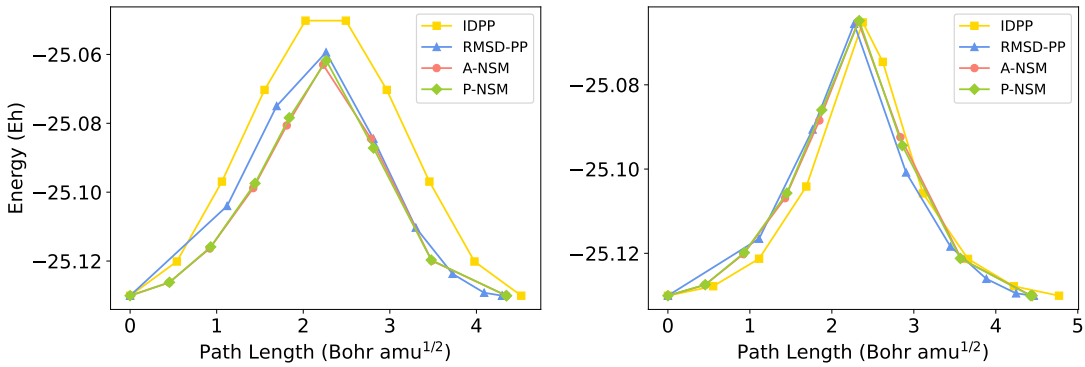

Figure 5.7: Energy profiles of the initial reaction paths (left) and MEPs (right) for the cyclopentene hydrogen transfer reaction determined using different reaction path finding methods. Results are shown for the IDPP method (yellow squares), the RMSD-PP method (blue triangles), A-NSM (red circles) and P-NSM (green diamonds). The points on the plot represent the "images" used for NEB.

The calculated initial reaction paths for all four methods, as well as the MEP determined using NEB refinement for each method are shown in Figure 5.7. Similarly to the first reaction studied, all methods resulted in initial reaction paths which, when using NEB refinement, converged to the same MEP. This indicates that, again, all methods resulted in good initial reaction paths to be used a starting point to find the MEP. The resulting MEP shown in Figure 5.7 shows that the potential energy increases quickly from the reactant to the TS at 2.5 on the reaction path with a potential energy of $\sim$ -25.07 E_h and then decreases quickly to the product.

In Figure 5.7, the initial reaction paths for the four methods are shown. The IDPP method resulted in the worst initial reaction path compared to the other

method. It managed to accurately depict the potential rapidly increasing along the reaction path, from the reactant to the saddle point and then the product. However, unlike the MEP, the saddle point in the IDPP initial reaction path is much less defined, and is higher in energy, $\sim$ -25.05 E_h as opposed to $\sim$ -25.07 E_h. The three other methods; RMSD-PP, A-NSM and P-NSM, all resulted in almost the same initial reaction path, which were very similar to the MEP. However the RMSD-PP initial reaction path differed slightly in the first half of the reaction path, where the potential energy is slightly higher than the A-NSM or P-NSM method. The saddle point in those calculated initial reaction paths had a potential energy value of $\sim$ -25.06 E_h which was closer to the potential energy of the saddle point in the MEP.

Addition of hydrofluoric acid to ethene (R3)

The third example considered is an addition reaction between hydrofluoric acid and ethene. The parameters used for the A-NSM and P-NSM method were the same, and were the following: $N = 40$ nodes, $k_{\text{nav}} = 0.075$, and a step-size of 0.75.

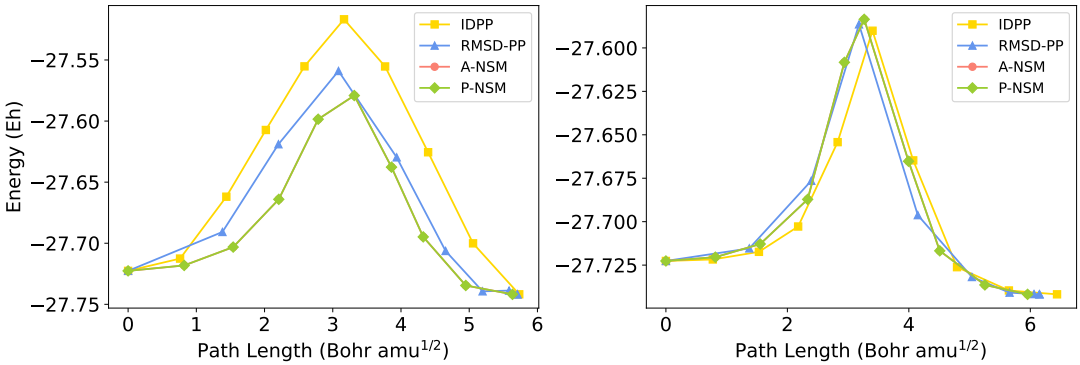

Figure 5.8: Energy profiles of the initial reaction paths (left) and MEPs (right) for the addition of hydrofluoric acid to ethene reaction determined using different reaction path finding methods. Results are shown for the IDPP method (yellow squares), the RMSD-PP method (blue triangles), A-NSM (red circles) and P-NSM (green diamonds). The points on the plot represent the "images" used for NEB.

The MEPs for this reaction, determined by NEB refinement using initial reaction paths for each method, are shown in Figure 5.8. All of the initial reaction paths, when used as a starting point for a NEB calculation, converged to the same MEP which suggests that all of the initial reaction paths were a good starting point for a NEB calculation. The MEP for this reaction is quite similar to R2, whereby the potential energy quickly increases from the reactant until the TS and then quickly decreases to the product. The TS is well defined, between 3 and 4 on the reaction coordinate with a potential energy value of $\sim$ -27.58 E_h.

The calculated initial reaction paths for all four methods are shown in Figure 5.8. The IDPP initial reaction path resulted in a quite broad reaction path as opposed to the sharp MEP it converges to. Furthermore, the saddle point potential energy is the highest out of the four methods, 27.50 E_h as opposed to $\sim$ -27.58 E_h, although we note that it did get the position of the saddle point along the path relatively correct. The RMSD-PP initial reaction path was similar in shape to that determined by the IDPP method, but differed in terms of the magnitude of the potential energy, whereby the RMSD-PP initial reaction path was lower in potential energy. The saddle point is located in the same position along the reaction path as the IDPP initial reaction path, but the potential energy value is lower, $\sim$ -27.56 E_h. Lastly, the A-NSM and P-NSM methods resulted in exactly the same path (resulting in the A-NSM line not being visible in Figure 5.8) and, out of the four methods, resembled the MEP the most, be it in shape and potential energy magnitude. The A-NSM and P-NSM initial reaction path was the least broad and the position of the saddle point was closest to the MEP as well as the potential energy value, $\sim$ -27.57 E_h compared to $\sim$ -27.58 E_h.

Addition of nitrous oxide and ethene (R4)

The fourth example considered is another addition reaction, between nitrous oxide and ethene. The parameters for the A-NSM and P-NSM methods were the same, and were the following: $N = 40$ nodes, $k_{\text{nav}} = 0.075$, and a step-size of 0.75.

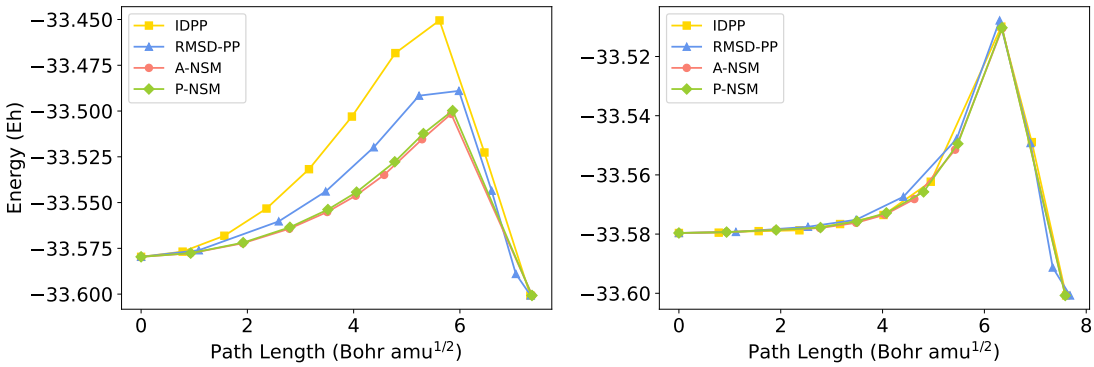

Figure 5.9: Energy profiles of the initial reaction paths (left) and MEPs (right) for the addition of nitrous oxide and ethene reaction determined using different reaction path finding methods. Results are shown for the IDPP method (yellow squares), the RMSD-PP method (blue triangles), A-NSM (red circles) and P-NSM (green diamonds). The points on the plot represent the "images" used for NEB.

In Figure 5.9, the calculated initial reaction paths for each method as well as the NEB refinement using these paths to determine the MEP are shown. In Figure 5.9, all of the initial reaction paths calculated converged to the same MEP, indicating

that they were all good starting points for the NEB refinement calculation. The MEP for this reaction looks similar to that of R1, where the potential energy is flat for the first half of the MEP and then quickly increases to the a well defined TS, at 6 on the MEP with a potential energy value of $\sim$ -33.51 E_h, before quickly decreasing to the product.

Out of the four methods used to calculate the initial reaction paths, shown in Figure 5.9, the IDPP initial reaction path was the one which least resembled the MEP. The potential energy in the IDPP initial reaction path is larger and and increased rapidly in the first half of the reaction path as opposed to how it is in the MEP. In terms of the saddle point, the position is slightly before 6, which is close to the position of the saddle point in the MEP, and has a potential value of $\sim$ -33.46 E_h as opposed to $\sim$ -33.51 E_h in the MEP. The RMSD-PP method resulted in a better initial reaction path than the IDPP method, whereby the maximum potential energy was lower in magnitude and increased less rapidly in the first half of the reaction path like the MEP. Unlike the IDPP initial reaction path, the saddle point in the RMSD-PP initial reaction path is not well defined compared to that of the MEP but is closer in magnitude to the saddle point on the MEP, $\sim$ -33.50 E_h. The A-NSM and P-NSM methods resulted in essentially the same initial reaction path, which was also the most similar to the MEP. The potential energy in the first half is the lowest compared to IDPP and RMSD-PP methods, although not flat like the MEP, and the position of the saddle point as well as the potential energy value is very close to how the saddle point is described in the MEP.

Cyclobutene ring opening (R5)

The fifth example considered is the cyclobutene ring opening reaction. The parameters for the A-NSM and P-NSM methods were the same, and were the following: $N = 40$ nodes, $k_{\text{nav}} = 0.075$, and a step-size of 0.75.

For each initial reaction path finding method, the calculated initial reaction path and the MEP determined using a NEB refinement calculation with the initial reaction path as a starting point are shown in Figure 5.10. The results of the NEB refinement calculation show that the MEP was determined for all of the initial reaction paths, which indicates that all four methods resulted in initial reaction paths which were a good starting point for the NEB refinement. The potential energy described by the MEP starts by quickly increasing from the reactant to a well defined TS where it then decreases to the product.

The initial reaction paths calculated by the four methods for this reaction, shown in Figure 5.10, all resulted in very close approximations of the MEP. The RMSD-PP initial reaction path was the least like the MEP, in particular the saddle point described by the RMSD-PP initial reaction path, which had a higher potential

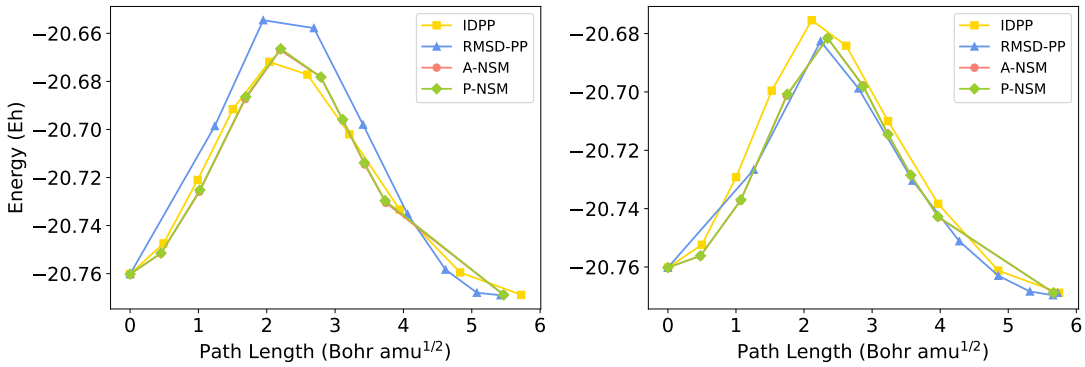

Figure 5.10: Energy profiles of the initial reaction paths (left) and MEPs (right) for the cyclobutene ring opening reaction determined using different reaction path finding methods. Results are shown for the IDPP method (yellow squares), the RMSD-PP method (blue triangles), A-NSM (red circles) and P-NSM (green diamonds). The points on the plot represent the "images" used for NEB.

energy value of $\sim$ -20.66 E_h and was also not as defined as it is in the MEP. The initial reaction paths determined using the A-NSM and P-NSM method resulted in the same paths (resulting in the A-NSM line not being visible in Figure 5.10), which also resembled the MEP quite well both in terms of shape of the path but also the potential energy value of the saddle point, $\sim$ -20.67 E_h compared to $\sim$ -20.68 E_h in the MEP. Lastly, the IDPP method resulted in a similar initial reaction path as the A-NSM and P-NSM methods, however the potential energy value of the saddle point in the initial reaction path is closer to the the resulting MEP.

Penta-1,3-diene hydrogen transfer (R6)

The second to last example considered is the hydrogen transfer on a penta-1,3-diene molecule. The parameters for the A-NSM and P-NSM methods were the same, and were the following: $N = 40$ nodes, $k_{\text{nav}} = 0.075$, and a step-size of 0.75.

The initial reaction paths calculated by the four reaction path finding methods as well as the MEPs determined by subsequent NEB refinements are shown in Figure 5.11. In this reaction, the NEB refinement resulted in slightly different MEPs, although still somewhat similar. The position of the TS along the reaction path slightly differed as well as the magnitude of the potential energy associated to the TS. The TS on the MEP determined using the RMSD-PP, A-NSM/P-NSM and IDPP path had a potential energy value of $\sim$ -26.19 E_h, $\sim$ -26.19 E_h and $\sim$ -26.20 E_h respectively, at a path length of 3.5, 4.5 and 4 respectively.

In terms of the initial reaction paths calculated using the four different methods, only A-NSM and P-NSM resulted in a similar potential energy for the saddle point compared to the MEP, however, the initial reaction paths for all methods were broader in shape as opposed to the MEPs which were much sharper. The RMSD-

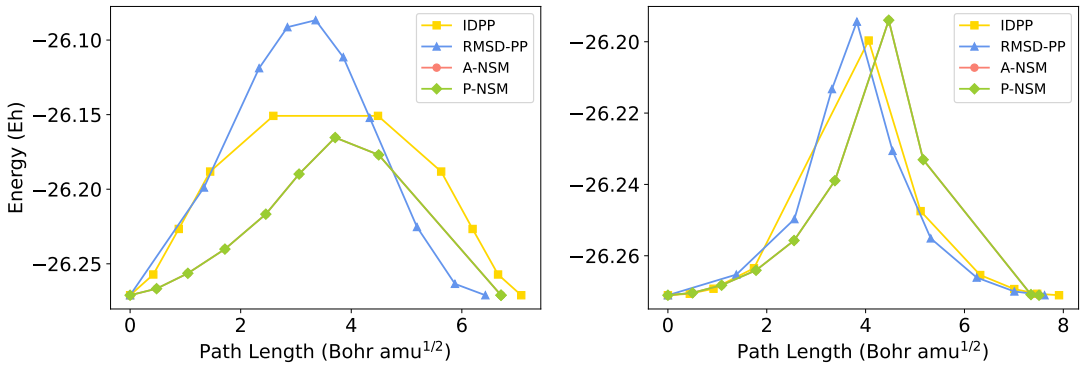

Figure 5.11: Energy profiles of the initial reaction paths (left) and MEPs (right) for the penta-1,3-diene hydrogen transfer reaction determined using different reaction path finding methods. Results are shown for the IDPP method (yellow squares), the RMSD-PP method (blue triangles), A-NSM (red circles) and P-NSM (green diamonds). The points on the plot represent the "images" used for NEB.

PP method resulted in a broad initial reaction path, where the saddle point was much larger in potential energy compared to the MEP, $\sim$ -26.10 E_h compared to $\sim$ -26.20 E_h. A reason for this significant energy difference to the MEP, but also with the other methods, could be due to the method itself. The Gaussian used to both push and pull the system may have been too strong, effectively bringing the system into an unfeasible region of the PES, higher in energy than where the MEP is. The IDPP method resulted in an initial reaction path which was lower in potential energy compared to the RMSD-PP method, however the reaction path was significantly broad and poorly described the saddle point. Instead of a sharp saddle point like in the MEP, the IDPP initial reaction path had two nodes which had the highest potential energy ($\sim$ -26.150 E_h). Lastly, the initial reaction paths determined by the A-NSM and P-NSM methods were exactly the same (resulting in the A-NSM line not being visible in Figure 5.11) and were the lowest in potential energy. Moreover, the saddle point was the sharpest compared to both the RMSD-PP and IDPP methods, and is also the closest in terms of potential energy compared to the MEPs, $\sim$ -26.175 E_h compared to $\sim$ -26.19 E_h or $\sim$ -26.20 E_h.

Diels-Alder Reaction (R7)

The final example investigated is the Diels-Alder reaction. In terms of the parameters used, for both A-NSM and P-NSM, the number of nodes N was 35, the step-size was 0.75 and the navigation force constant, k_{nav} was 1.25.

In Figure 5.12, the initial reaction paths determined using the four reaction path finding methods and the subsequent NEB refined path leading to the converged MEP are shown. In this example, all of the reaction path finding methods resulted in initial reaction paths which successfully converged to the MEP. In the MEP,

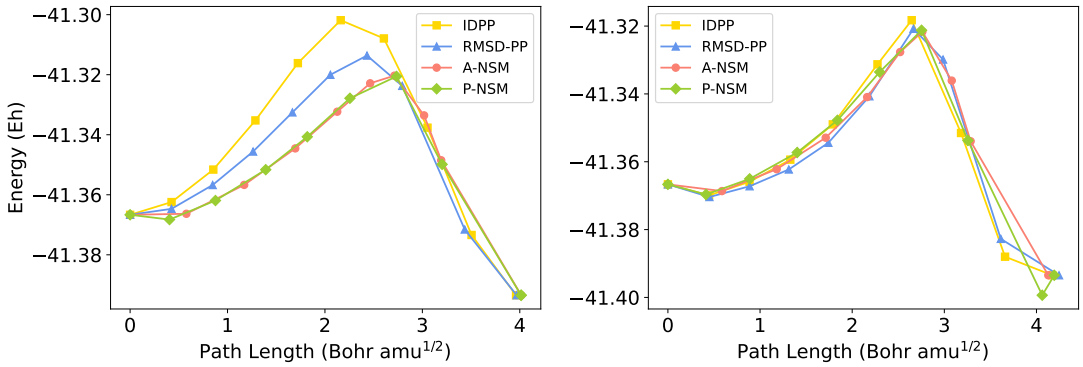

Figure 5.12: Energy profiles of the initial reaction paths (left) and MEPs (right) for the diels-Alder Reaction. reaction determined using different reaction path finding methods. Results are shown for the IDPP method (yellow squares), the RMSD-PP method (blue triangles), A-NSM (red circles) and P-NSM (green diamonds). The points on the plot represent the "images" used for NEB.

starting from the reactant region, the potential energy slightly decreases before gradually increasing towards the TS located just before the path length of 3 and with a potential energy of $\sim$ -41.32 E_h. Once the TS is reached, the potential energy decreases rapidly to the product region.

The initial reaction path obtained as a result of using the IDPP method was the least similar to the resulting MEP. In the IDPP initial reaction path, firstly, the position of the saddle point in terms of the path length is shorter than the MEP (2 as opposed to 3) and the potential energy associated with the saddle point is $\sim$ -41.30 E_h as opposed to $\sim$ -41.32 E_h. Secondly, the potential energy initially does not slightly decrease, on the contrary, it increases right from the start. The RMSD-PP method resulted in a better initial reaction path, with a saddle point at a path length of 2.5 with a potential energy of $\sim$ -41.32 E_h which was closer to what the MEP looked like. Similarly to the IDPP initial reaction path, there was no initial dip in potential energy at the start of the reaction path. The P-NSM and A-NSM initial reaction paths were very similar to one another but also similar to what the MEP looked like. The saddle point was located at a path length between 2.5 and 3, with a potential energy of $\sim$ -41.32 E_h. Furthermore, the initial reaction path determined by P-NSM did show the dip in potential energy at the start of the reaction path like in the MEP, however the A-NSM did not.

5.8.3 Assessing the performances of each initial reaction path finding method

In order to further assess the performance of both the A-NSM and P-NSM methods in comparison to the RMSD-PP and IDPP methods, we look at the distance between the initial approximated reaction paths to the MEP for each method and for each

reaction discussed so far. The resulting distance between the initial approximated reaction paths to the MEP for each method and for each reaction is plotted in Figure 5.13. We also note that typically, the shorter the distance between the initial reaction path and the MEP would suggest that the initial reaction path was a good starting point for the MEP. However, as will be discussed later in this Section, a shorter distance between the initial reaction path and the MEP does not always lead to quicker convergence to the MEP.

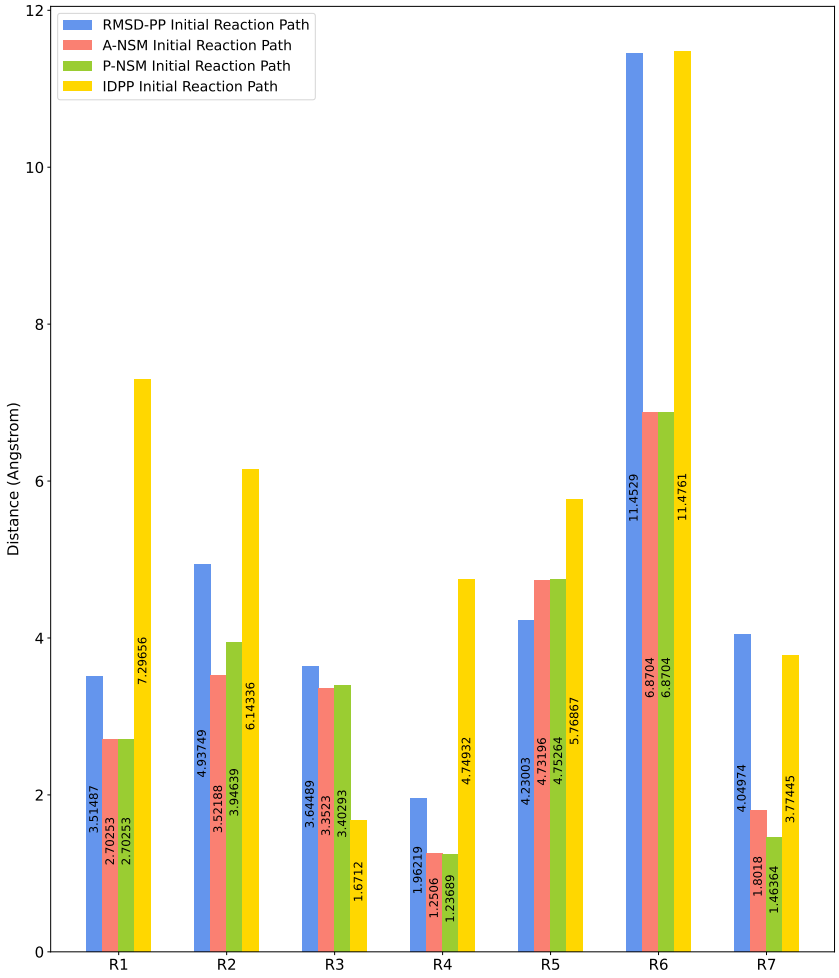

Figure 5.13: Comparing distances between the initial paths determined by each method to the MEP for each reaction. Results are shown for the IDPP method (yellow), the RMSD-PP method (blue), A-NSM (red) and P-NSM (green).

Overall, based on Fig 5.13, both the P-NSM and A-NSM methods result in closer distances between the initial approximate reaction path and the MEP for four out of the seven reactions. In the other two reactions, despite not resulting in the shortest distances, the P-NSM and A-NSM methods result in distances that are

very comparable to the other methods. The RMSD-PP method also resulted in good initial approximate reaction paths close to the MEP, for R1, R3 and R4, however, even in the best case, the P-NSM and A-NSM methods outperform it. Lastly, the IDPP results in the longest distances between initial approximate reaction paths to the MEP for all reactions except R3. However, for R3, we note that the IDPP method results in the closest initial approximate reaction path which is 50% shorter than the other methods.

Another way to assess the performance of these initial reaction path finding methods, other than comparing the distance between the initial approximate reaction path and the resulting MEP for each method, is to compare the number of force evaluations for both the initial approximate reaction path calculation and the subsequent NEB refinement calculation in order to give insight into how accurate the initial reaction path was but also as to how cost efficient the method is. As mentioned in the introduction (Section 5.1), for initial reaction path finding methods such as the ones explored in this Chapter, the computational cost is linked to the number of force evaluations needed to obtain a reaction path. Therefore, the ideal initial reaction path finding method will have a minimal number of force evaluations needed to calculate the initial reaction path and a minimal number of force evaluations required for the subsequent NEB refinement to determine the MEP.

The number of force evaluations needed for each method to determine the initial approximate reaction path as well as the number of force evaluations needed for the subsequent NEB refinement is shown in Fig 5.14. For all of the reactions, the P-NSM and A-NSM methods have similar or the exact same number of force evaluations needed for the initial approximate reaction path, and more importantly, this number is low, ranging from only 18 force evaluations for R5 to 38 and 58 force evaluations for the P-NSM and A-NSM method respectively for R1. Furthermore, the NEB refinement after using an initial approximate reaction path calculated by either the P-NSM or A-NSM method results in the smallest number of force evaluations for all reactions except for R5 and R7. This is clearly seen with R12 which represent perhaps the hardest MEP to determine out of the seven reactions, and even then, both the P-NSM and A-NSM methods outperform the RMDS-PP and IDPP methods, where the difference between the P-NSM and RMSD-PP is 270 force evaluations and 222 force evaluations between P-NSM and IDPP, and the difference between the A-NSM and RMSD-PP is 180 force evaluations and 132 force evaluations between A-NSM and IDPP.

When looking at the RMSD-PP method, it does not need many force evaluations in order to determine a good initial approximate reaction path. For R2, R3 and R4, the RMSD-PP method has a similar number of force evaluations as the P-NSM and A-NSM methods, however for R1, R5, R6 and R7 the number of force evaluations

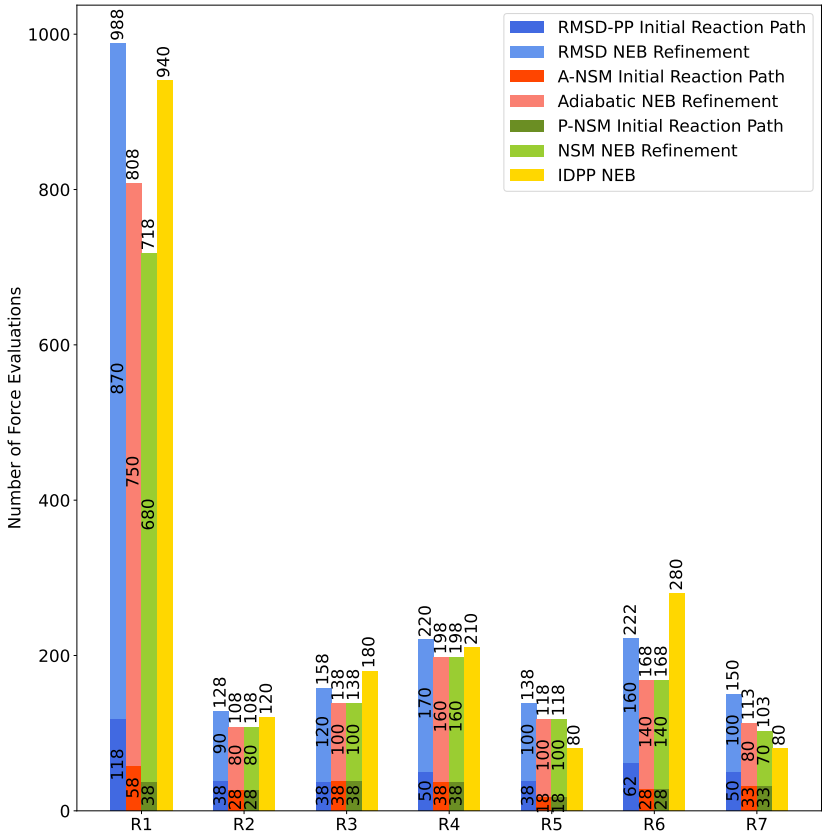

Figure 5.14: Comparing the number of force evaluations used by each method for the initial approximate reaction path and for the subsequent NEB refinement to determine the MEP, for each reaction. Results are shown for the IDPP method (yellow), the RMSD-PP method (blue), A-NSM (red) and P-NSM (green).

tends to be double what P-NSM and A-NSM require. In terms of NEB refinement, for all reactions except for R1, the number of force evaluations using a RMSD-PP initial reaction path is only slightly more than when a P-NSM or A-NSM initial reaction path is used. However for R1, the calculated initial reaction path is not close enough to the MEP and this is reflected by the large number (870) of force evaluations needed to converge to the MEP.

Similarly to the RMSD-PP method, the IDPP method results in about the same total number of force evaluations for all reactions except for R5 and R7, where it has the lowest total number of force evaluations needed for the initial reaction path to converge to the MEP. Only 80 force evaluations for both reactions compared to 138, 118 and 118 force evaluations for the RMSD-PP, A-NSM and P-NSM methods for R5 and 150, 113 and 103 force evaluations for the RMSD-PP, A-NSM and P-NSM methods for R7. In both reactions, there is no simultaneous large amplitude motion of many atoms which could possibly explain why the IDPP method resulted in a lower number of force evaluations. For the other reactions, just like with the RMSD-PP method, the IDPP method requires more force evaluations than either the P-NSM or A-NSM method, although we note that the difference in the number of force evaluations is not always substantial such as in R2, R3 and R4. In R1, the IDPP method results in a number of force evaluation that is considerably larger than the A-NSM or P-NSM methods, where 940 total force evaluations are needed to determine the MEP as opposed to 808 and 718 total force evaluations respectively.

5.9 Using the navigation string method for transition state searching

With both NSM methods (A-NSM and P-NSM) generating approximate reaction paths comparable to the MEP, in this section, we explore using the highest-energy node in these initial reaction paths as the starting point of TS optimisation calculation. For all of the reactions (R1-R7), we take the highest-energy node of the initial reaction path generated by P-NSM, RMSD-PP and IDPP, and use it as a starting point for a subsequent TS optimisation. We then compare TS found by TS optimisation to the TS of the respective MEP determined by P-NSM, RMSD-PP and IDPP. We use only the highest-energy nodes as a result of P-NSM as reaction path generated resulted in the same or better reaction paths than A-NSM. To assess the results, we investigate the following:

1. Whether or not the TS optimisation has converged using the highest-energy node.

2. The number of iterations needed to converge the TS.

The results of the TS optimisation using the highest-energy nodes of the reaction paths generated by the three reaction path finding methods (P-NSM, RMSD-PP, IDPP) are shown in Tables 5.1 - 5.3.

Table 5.1: Assessing the results of using the highest-energy node in the P-NSM generated reaction path as starting point for a TS optimisation and comparing it to the TS on the MEP.

Reaction	Converged	Number of Cycles
R1	No	NA
R2	Yes	14
R3	Yes	28
R4	Yes	17
R5	Yes	22
R6	No	NA
R7	Yes	58

Table 5.2: Assessing the results of using the highest-energy node in the RMSD-PP generated reaction path as starting point for a TS optimisation and comparing it to the TS on the MEP.

Reaction	Converged	Number of Cycles
R1	No	NA
R2	Yes	12
R3	Yes	17
R4	Yes	20
R5	Yes	176
R6	Yes	22
R7	Yes	12

Table 5.3: Assessing the results of using the highest-energy node in the IDPP generated reaction path as starting point for a TS optimisation and comparing it to the TS on the MEP.

Reaction	Converged	Number of Cycles
R1	No	NA
R2	Yes	12
R3	Yes	19
R4	Yes	28
R5	Yes	22
R6	Yes	25
R7	Yes	15

When the highest-energy node from the P-NSM generated reaction path is used as a starting point for TS optimisation, for five out of the seven reactions, the TS optimisation successfully converged to the correct TS which lies on the MEP. In terms of number of cycles needed to reach convergence, the minimum amount was for R2 where only 14 cycles were needed, the maximum was for R7 were 58 cycles

were needed and the average number of cycles was 28. The energy difference for the converged TSs was in the order of magnitude of 10^{-11} or lower with the exception of R7 where the energy difference had a magnitude of 10^{-9}, however we confirmed that this was in fact the correct TS after running an intrinsic reaction coordinate (IRC) calculation which resulted in the correct reactant and product structures.

Comparatively, when the highest-energy node from the RMSD-PP generated reaction path is used, the TS was found for all of the reactions with the exception of R1. The minimum number of cycles need to reach convergence was 12 for R4, the maximum number of cycles was 176 for R2 and the average number of cycles needed was 43. Lastly, when the highest-energy node from the IDPP generated reaction path is used, the TS is found for all reactions with exception of R1. Moreover, the minimum number of cycles needed to reach convergence was 12 for R3, the maximum number of cycle was only 28 for R4 and the average number of cycles was also low, 20.

These results show that, as well as generating good initial reaction paths, the highest-energy node on the NSM reaction path can be used as a starting point for subsequent TS optimisation calculations. For five out of the seven reactions, TS optimisation calculations converged to the correct TS on the MEP, whereas for the other two reactions, TS optimisation calculations failed to converge to any TS. Furthermore, the average number of cycles needed to find the TS was comparable to when the highest-energy node from a RMSD-PP or IDPP reaction path was used for TS optimisation, although, the latter methods resulted in one more converged correct TS. For the individual reactions, specifically R2-R4, the number of cycles needed to converge to the correct TS was similar for all three methods suggesting that the highest-energy node was a good initial guess for the TS. As such, using the highest-energy node from the P-NSM generated reaction path can be a good starting point for TS optimisation as the results were comparable both in terms of convergence and number of cycles needed to reach convergence. Moreover, with the added benefit that the P-NSM generated reaction path typically requires a lower number of force evaluation needed to generate said reaction paths.

Finally, Figure 5.15 shows the difference between the structure of the highest energy node on the initial reaction path to the TS found on the MEP for each respective method, P-NSM, RMSD-PP and IDPP. Ideally, the structure of the highest energy node on the generated initial reaction path would be as close to identical to the TS found on the MEP. And so a large difference in structure would suggest the starting point, the highest-energy node on the initial reaction path, is a sub-optimal starting point for TS optimisation. The differences between the structure of the highest energy node on the initial reaction path generated by P-NSM to the TS found on the MEP, were the smallest across five of the seven reactions, with R5

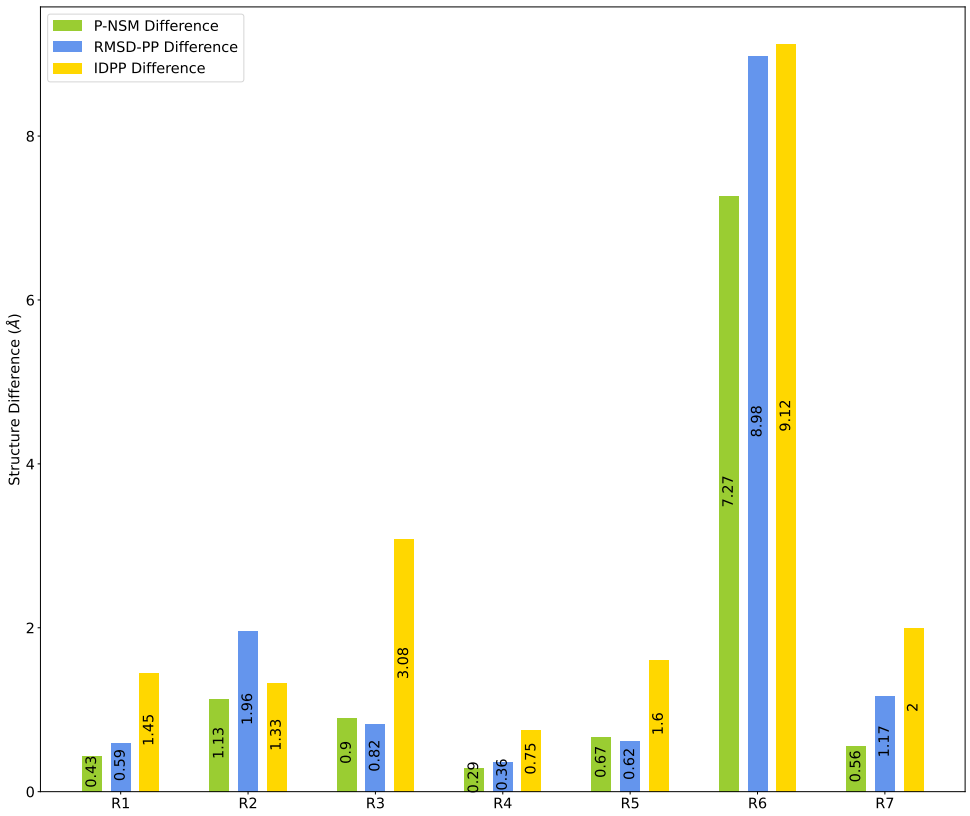

Figure 5.15: Comparison between the difference of the structure of the highest energy node on the initial reaction path to the TS found on the MEP for each respective method, P-NSM (green), RMSD-PP (blue) and IDPP (yellow).

being very similar to the RMSD-PP result. The differences between the structure of the highest energy node on the initial reaction path generated by RMSD-PP to the TS found on the MEP were quite similar to the P-NSM results, and in the case of R3 and R5, the RMSD-PP results were only slightly better. Lastly, the differences between the structure of the highest energy node on the initial reaction path generated by IDPP to the TS found on the MEP were the largest compared to P-NSM and RMSD-PP, with the exception of R2 where the difference was smaller than the RMSD-PP results. These results highlight how close the initial structure of the highest energy node on the P-NSM generated reaction path is to the TS on the MEP, compared to RMSD-PP and IDPP.

5.10 Parameter optimisation

In this section we investigate the parameters involved in the P-NSM method and observe how varying them effects the resulting initial reaction path approximation. The parameters investigated are the number of nodes in the reaction path, the step-size used in the optimisation step and the navigation force constant which is used to drive the system from the reactant region to the product region. Note that the points used in the Figures presented in this Section are there for visual aid purposes and do not signify anything. We note that investigating these three parameters was done by keeping the remaining two parameters constant, and as such, these results showcase the effect of the varied parameter in the context of these constant parameters. However, these results show the general behaviour of what would happen when one of these three parameters is varied and so a general understanding can be obtained. We also want to note that while the behaviour demonstrated by changing these parameters is predictable, it is still worth investigating in order to get a better understanding of the method.

5.10.1 Number of nodes

We first investigate the effect of varying the number of nodes in the initial reaction path approximation by only changing the number of nodes while keeping the other parameters constant for each run. Three reactions are used to demonstrate the effect of varying the number of nodes parameter; these are: the addition of nitrous oxide (R4), formaldehyde formation (R1) and penta-1,3-diene hydrogen transfer (R6). A total of five runs are done for each reaction, where the number of nodes changes between 10, 30, 50, 100, and 200 and the other parameters remain the same. For R1, the k_{nav} is 0.175 and the step-size is 0.5, for R2 the k_{nav} is 0.15 and the step-size is 0.75, for R3 the k_{nav} is 0.075 and the step-size is 0.75.

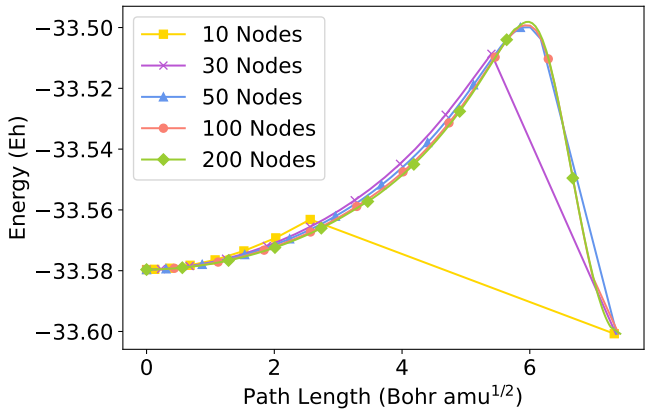

Figure 5.16: Comparing the effect of varying the number of nodes on the initial reaction path approximation for R4. Results are shown for 10 nodes (yellow), 30 nodes (purple), 50 nodes (blue), 100 nodes (red) and 200 nodes (green).

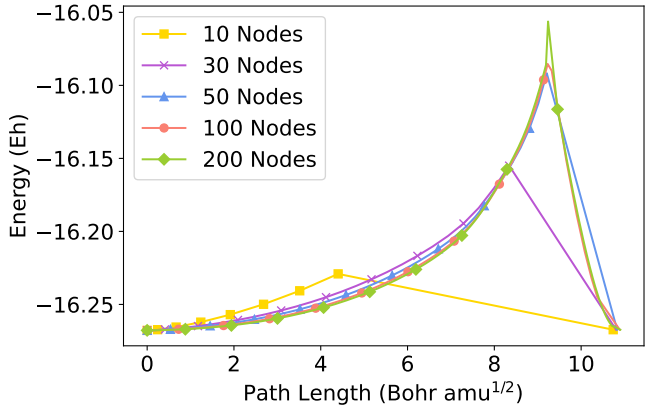

Figure 5.17: Comparing the effect of varying the number of nodes on the initial reaction path approximation for R1. Results are shown for 10 nodes (yellow), 30 nodes (purple), 50 nodes (blue), 100 nodes (red) and 200 nodes (green).

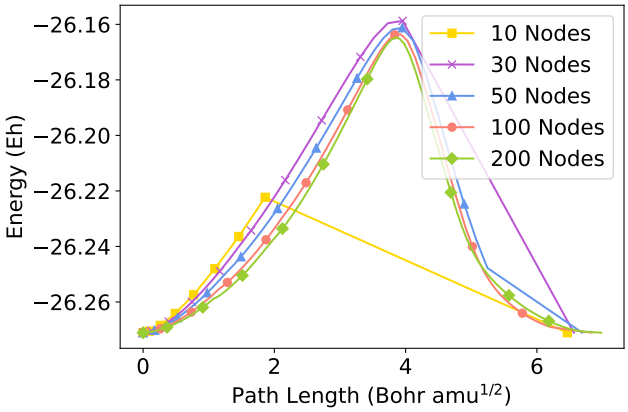

Figure 5.18: Comparing the effect of varying the number of nodes on the initial reaction path approximation for R6. Results are shown for 10 nodes (yellow), 30 nodes (purple), 50 nodes (blue), 100 nodes (red) and 200 nodes (green).

The effect of changing the number of nodes for the P-NSM calculation for each of the three reactions is shown in Figures 5.16 - 5.18. For all of the reactions, the addition of nodes for the calculation has a positive effect, typically by 100 nodes, as it enables for a better and smoother description of the reaction path. On the other hand, with the same k_{nav} and step-size parameters, using 10 or 30 nodes was not enough to describe the reaction path. In R1, using 50, 100 and 200 nodes for the P-NSM calculation results in a smooth reaction path where the saddle point is well-described, whereby the steep saddle point is clearly defined in the case of 200 nodes. However, both 10 and 30 nodes are not enough to get the complete reaction path, as the penultimate node is too far away from the product node resulting in a linear interpolation between the two nodes. In R2, using 200 nodes results in the smoothest reaction path, even finding the saddle point between the reactant and the product. Using 100 nodes results in a similar reaction path as 200 nodes in terms of smoothness of the reaction path, however the potential energy of the saddle point is slightly lower when compared to using 200 nodes. Using 50 nodes results in a smooth reaction path, but it is not enough to the find the saddle point. Furthermore, after the saddle point, the reaction path is no longer smooth but instead results in a sharp linear interpolation between the saddle point node and the final node. Lastly, in the case of using 30 or 10 nodes, neither cases result in a complete reaction path for the reaction, failing to even reach the region where the saddle point should be. In R3, using either 200 or 100 nodes results in essentially the same smooth reaction path, with the same saddle point region. Similarly, using 50 nodes, results in the same smooth reaction path, with the only difference in the final part of the reaction path which is sharp unlike when 100 or 200 nodes are used. Unlike the other reactions, in R3, using 30 nodes is enough to reach the saddle point region, however after that, the reaction path becomes quite sharp. Lastly, using 10 nodes, like in the other two reactions, is not enough to get a full description of the reaction path or of the saddle point.

In summary, increasing the number of nodes, while keeping the other parameters constant, in a P-NSM calculation in order to determine reaction path will result in a smoother reaction path which better describes the reaction as well as the saddle point region. In all reactions a minimum of 50 nodes was necessary in order to define a full reaction path. Using 100 and 200 nodes resulted in the smoothest reaction path for all reaction, whereas using 10 or 30 nodes was not enough to get a fully described reaction path.

5.10.2 Step-size

We now look at how varying the step-size in the optimisation step affects the resulting reaction path determined using P-NSM, while keeping the other parameters, the number of nodes and navigation force constant, constant. To do so, we use the same reactions as in 5.10.1, which are the addition of nitrous oxide (R1), formaldehyde formation (R2) and penta-1,3-diene hydrogen transfer (R3). For each reaction, a total of five P-NSM calculations are done with varying step-sizes: 0.05, 0.10, 0.30, 0.50, 0.75. In terms of the other parameters, the number of nodes and navigation force constant is 50 and 1.0 respectively for R1 and R2, and 50 and 0.15 respectively for R3.

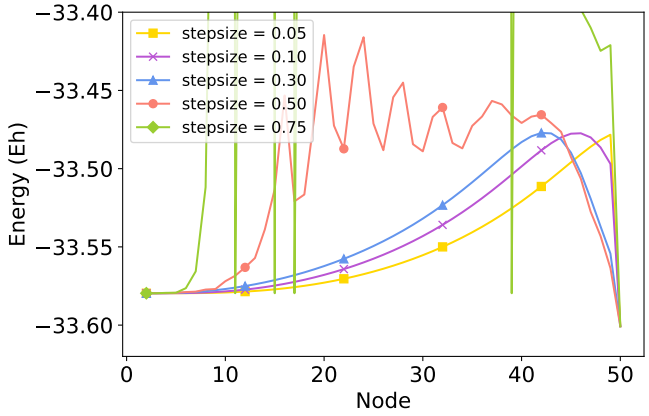

Figure 5.19: Comparing the effect of varying the step-size on the initial reaction path approximation for R1. Results are shown for a step-size of 0.05 (yellow), 0.10 (purple), 0.30 (blue), 0.50 (red) and 0.75 (green).

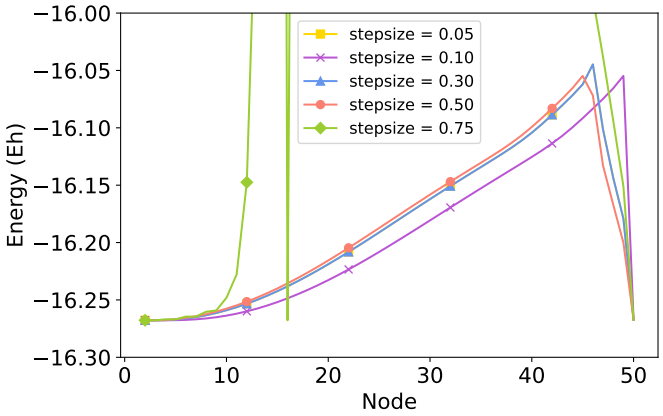

Figure 5.20: Comparing the effect of varying the step-size on the initial reaction path approximation for R2. Results are shown for a step-size of 0.05 (yellow), 0.10 (purple), 0.30 (blue), 0.50 (red) and 0.75 (green).

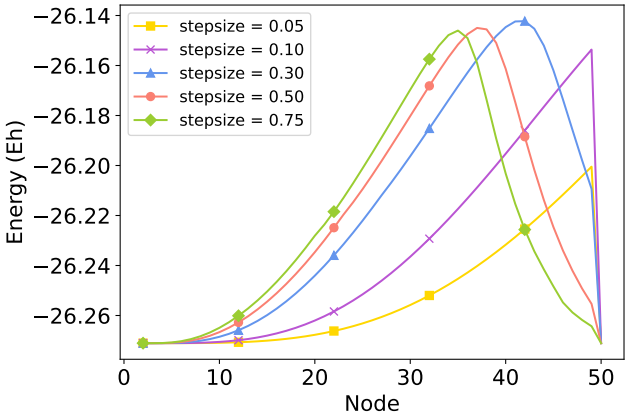

Figure 5.21: Comparing the effect of varying the step-size on the initial reaction path approximation for R3. Results are shown for a step-size of 0.05 (yellow), 0.10 (purple), 0.30 (blue), 0.50 (red) and 0.75 (green).

The effect of varying the step-size during the optimisation step on the resulting reaction path is shown in Figure 5.19 - 5.21. Overall, all three reactions have one step-size where the reaction path becomes fully described, whereas the other four are either not large enough to smoothly reach the final node or too large and the reaction path starts to become very ill-defined. In R1, the larger step-sizes, 0.75 and 0.50, both result in ill-defined reaction paths where the potential energy varies greatly along the reaction path, sometimes even oscillating too. On the other hand, the two smaller step-sizes, 0.10 and 0.05, do not allow for a full description of the reaction path with the smallest step-size not even finding the saddle point region. The most optimal step-size in this scenario was 0.30 as it was large enough to completely describe the reaction path and the saddle point region, but not too large so as to become sharp and erratic. In R2, only the largest step-size, 0.75, results in an ill-defined reaction path, where the potential energy at certain points along the path is considerably higher than the rest. None of the step-sizes investigated ended up being able to describe the reaction path completely, however, using a step-size of 0.30 enabled the saddle point region to be found as well as the reaction path to be described pretty well. Similarly, a step-size of 0.50 describes the reaction path quite well too, however the saddle point is not as clearly defined as it is when using a step-size 0.30. Lastly, both a step-size of 0.10 and 0.05 were not adequate to describe the reaction path or to find the saddle point region. In both cases, the step-size was too small which meant that less of the reaction path was described. In R3, the smaller step-sizes, 0.05 and 0.10, are too small to be able to describe the reaction path completely as well as finding the saddle point. Using a step-size of 0.30 we are able to see the saddle point region being described on the reaction path, however this step-size is not enough to completely describe the rest of the reaction

path. The final two step-sizes, 0.50 and 0.75, both manage to find the saddle point region and describe the reaction path almost completely in a very smooth fashion, although a slightly larger step-size could be considered to describe the very end of the reaction path.

In summary, for all reactions, a certain step-size was required to completely describe the reaction path smoothly as well as to find the saddle point region when all other parameters were kept constant. On one hand, using a large step-size such as 0.75 results in an ill-defined reaction path where the potential can spike to uncharacteristically large values, such as in R1 and R2. However, in R3, using a step-size of 0.75 does not result in an ill-defined reaction path, but instead in a smooth and well-described reaction path due to the fact that for that reaction, the navigation force constant was lower than R1 and R2. On the other hand, using small step-sizes, such as 0.05 or 0.10, is not enough and falls short to completely describe the reaction path and to find the saddle point. The most optimal step-size across the three example reactions, for the given parameters, was typically either 0.30 or 0.50, as these were large enough to completely describe a smooth reaction path and also correctly define the saddle point region.

5.10.3 Navigation force constant

The final parameter we investigate is now the magnitude of the navigation force constant, which effectively acts as the driving force from the reactant to the product in a P-NSM calculation. The same reactions used in Section 5.10.1 and 5.10.2 were used to investigate how varying the magnitude of the navigation force constant would affect the resulting reaction path. These were the addition of nitrous oxide (R1), formaldehyde formation (R2) and penta-1,3-diene hydrogen transfer (R3). Five different navigation force constants were used; 0.125 au, 0.25 au, 0.50 au, 1.0 au and 2.0 au for R1 and R2, and 0.15625 au, 0.3125 au, 0.625 au, 1.25 au and 2.0 au for R3. For each run, the number of nodes and step-size were kept constant with values of 10 and 0.75 respectively for R1, 15 and 0.75 respectively for R2 and 10 and 0.50 respectively for R3.

The resulting reaction paths for each reaction using varying magnitudes of the navigation force constant are shown in Figures 5.22 - 5.24. Across all reactions, increasing the magnitude of the navigation force constant does not necessarily mean that the reaction path is better described, on the contrary, the navigation force constant only describes the magnitude of the force pulling the reactant system towards the product system. Therefore, one can imagine that, at times and depending on the magnitude of this force, the system will be pulled through unfeasible regions of the PES away from the MEP. In the case of R1, Figure 5.22 shows that with the

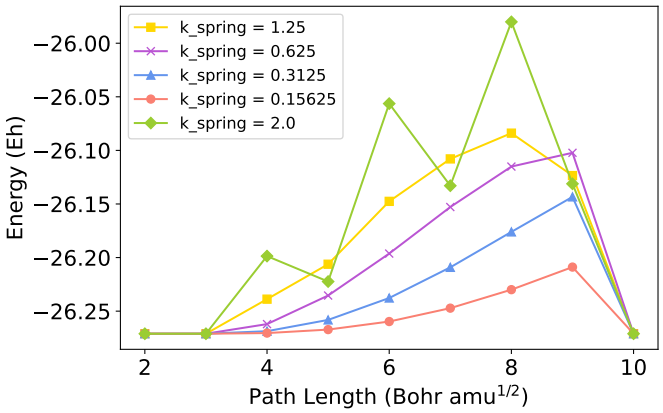

Figure 5.22: Comparing the effect of varying the navigation force constant on the initial reaction path approximation for R1. Results are shown for a navigation force constant of 1.0 au (yellow), 0.50 au (purple), 0.25 au (blue), 0.125 au (red) and 2.0 au (green).

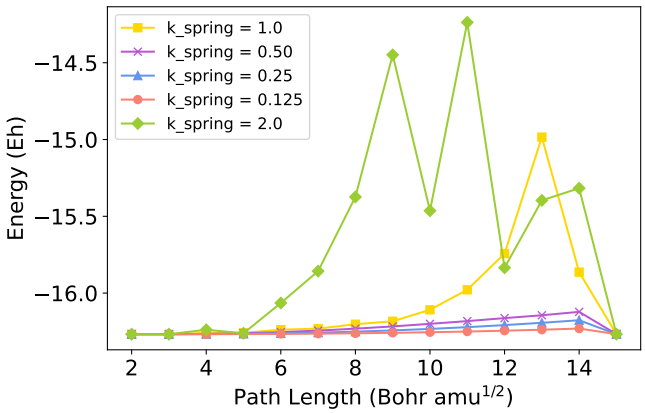

Figure 5.23: Comparing the effect of varying the navigation force constant on the initial reaction path approximation for R2. Results are shown for a navigation force constant of 1.0 au (yellow), 0.50 au (purple), 0.25 au (blue), 0.125 au (red) and 2.0 au (green).

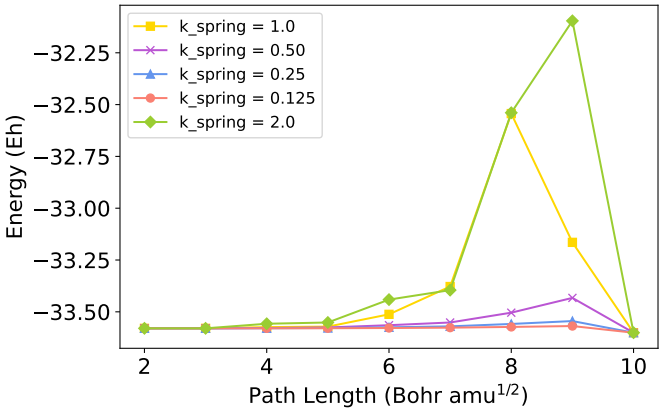

Figure 5.24: Comparing the effect of varying the navigation force constant on the initial reaction path approximation for R3. Results are shown for a navigation force constant of 1.25 au (yellow), 0.625 au (purple), 0.3125 au (blue), 0.15625 au (red) and 2.0 au (green).

given parameters, when the larger navigation force constants are used, such as 1.0 au or 2.0 au, the larger magnitude means that the force becomes significant and the system is dragged through regions of high potential energy starting at the sixth node, which are not representative of the MEP. Similarly, when a magnitude of 0.50 au is used for the navigation force constant, the force is still quite significant as the resulting reaction path has regions of higher potential energy, between the seventh and tenth node, compared to the actual MEP. On the other hand, when a small navigation force constant is used, the magnitude of the force is not strong enough to drag the system accurately towards the product. For this reaction, with the given parameters, the most optimal navigation force constant was that with a magnitude of 0.25 au, as it was large enough to drag the system towards the product through a feasible path on the PES.

Similarly to R1, using large navigation force constants in R2 results in the reaction paths which are ill-defined and unstable, in the case of 2.0 au, or unfeasible reaction paths with higher potential energy than what the MEP should be, as is the case when a magnitude of 1.0 au is used. Also similarly, using a small navigation force constant like 0.125 au or 0.25 au is not enough for the resulting reaction path to reach the right values of potential energy like the MEP. As such, in this example, the optimal navigation force constant is 0.50 au, as the reaction path is very similar to the MEP in terms of potential energy especially with where the saddle point lies.

In the case of R3, Figure 5.24 shows that as the magnitude of the navigation force constant is increased, the better the reaction path is described until the magnitude becomes too large whereby the reaction becomes unstable and ill-defined. Using a smaller navigation force constant such as 0.15625 au, 0.3125 au, or 0.625 au, results in the reaction path not being fully described, especially the saddle point region. This is due to the fact that as a result of the navigation force constant being small, the force is not strong enough to drag the system completely towards the product, and so either the force needs to be stronger or more nodes are necessary. When a navigation force constant of 1.25 au is used, the reaction path is better described and the saddle point region becomes clear and defined, suggesting this navigation force constant is optimal for this step-size and number of nodes.

These results showcase the importance of the navigation force constant in determining a good reaction path. If the navigation force constant is too small, then the force will not be enough for the system to be dragged from the reactant towards the product, but if the navigation force constant is too large, then the force will be too strong and will drag the system through unfeasible regions of the PES resulting in a reaction path which is not close to the MEP. These results also highlight how the navigation force constant is system dependent as, for the example reactions R1, R2 and R3, a navigation force constant of 0.50 au, 0.25 au and 1.25 au respectively was

optimal when used with the corresponding step-size and number of nodes.

5.11 Conclusions

This Chapter has introduced the projected navigation string method (P-NSM) and the adiabatic navigation string method (A-NSM), two novel and simple approaches which use the simplest concept of a navigation function to find good approximate initial reaction paths and subsequently the MEP using NEB refinement. In these methods, nodes are iteratively grown from the reactant to the product using a navigation force constant acting as the driving force in addition to either the projected forces of the PES (P-NSM) or the unprojected forces of the PES (A-NSM).

In order to test these two methods, seven reactions were investigated using the P-NSM and A-NSM and compared to current methods such as IDPP and RMSD-PP. With the exception of one reaction, the formation of formaldehyde, both P-NSM and A-NSM resulted in the same approximate initial reaction path, indicating that whether using the projected forces of the PES or the unprojected forces of the PES did not affect the resulting reaction path. The distance between initial reaction path and MEP as well as number of force evaluations were two properties used to determine the performance of the reaction path finding methods. In terms of the distance between the initial reaction path and MEP, both P-NSM and A-NSM outperformed RMSD-PP and IDPP in six out of the seven reaction examples, with the initial reaction path being closer to the MEP. In terms of the number of force evaluations, we looked at number of force evaluations needed for the approximate initial reaction path as well as the number of force evaluations needed for the subsequent NEB refinement. The initial reaction paths determined using P-NSM and A-NSM needed the same amount of force evaluations when compared to the RMSD-PP method in all reactions with one exception, in the formation of formaldehyde. In the formation of formaldehyde reaction, the P-NSM and A-NSM needed less than half of the number of force evaluations for the determination of the initial reaction path. The number of force evaluations needed for the subsequent NEB refinement were slightly lower (typically a difference of 10 or 20) than RMSD-PP in all of the seven reactions and lower than IDPP in five out of the seven reactions. The biggest difference in the NEB refinement between P-NSM/A-NSM and RMSD-PP or IDPP was also in the formaldehyde formation reaction, where the number of force evaluations needed was over 100 less compared to RMSD-PP and over 200 less when compared to IDPP.

Furthermore, the highest energy node of the P-NSM generated reaction path was investigated in the context of using it as a starting point for TS optimisation and compared to the highest energy node of both IDPP and RMSD-PP generated reaction paths. When the highest energy node from the P-NSM generated reaction path

as a starting point for TS optimisation, the results showed that the TS optimisation converged to the TS on the MEP for five out of the seven investigated reactions, compared to six out of seven when using the highest energy node from the IDPP and RMSD-PP reaction paths. Moreover, in terms of the number of cycles needed to converge to the TS on the MEP, the lowest result was 14 cycles and the largest result was 58, which were comparable to the IDPP, 12 and 28, and RMSD-PP, 12 and 22. Lastly, we compared the initial structures of the highest energy nodes from the P-NSM, IDPP and RMSD-PP reaction paths, to the TS on the respective MEP. The results here showed that, across all of the reactions investigated, the difference between the structure of the highest energy node on P-NSM generated reaction path to the TS on the MEP was the smallest. This again, highlighted that in addition to determining good initial reaction paths at a lower computational cost than IDPP and RMSD-PP, the P-NSM highest energy node could be used for TS optimisation and converge to the TS at a similar or better rate.

The three parameters involved in both the P-NSM and A-NSM were also investigated to see how they affect the resulting approximate initial reaction path using three of the example reactions from Section 5.8.2. In general, increasing the number of nodes needed for a P-NSM or A-NSM calculation had a positive effect whereby the reaction path resulted in being better described especially the saddle point region. However, at a certain point, increasing the number of nodes resulted in diminishing returns and became unnecessary and a waste of computational cost. In terms of step-size, in the examples investigated with the given parameters, using a small step-size meant that the system never reached the end-point and so the reaction path was not well described. On the other hand, a large step-size meant that the reaction path would become unstable and ill-defined. As such, a middle-ground was found to be optimal in the given conditions when investigating those chosen reactions. Lastly, varying the navigation force constant showed that using too small of a force resulted in the system not being able to be dragged to the end point (similarly to when a small step-size is used) and that too large a force resulted in the system being dragged in unfeasible regions of the PES (typically of high potential energy) away from the MEP. Furthermore, results of varying the navigation force constant also showed that it was reaction dependent and that the magnitude could differ depending on the reaction investigated.

The P-NSM and A-NSM outlined here offers several advantages as a method to determine good approximate initial reaction paths close to the MEP. Firstly, these methods only require geometry-optimized structures as inputs and the reaction paths produced result in good approximations of the MEP as well as strong initial guesses for subsequent NEB refinement. Secondly, the approach is very simple as there is no need for constraint optimisation or any re-parametrisation steps. Instead, by just

minimising the energy function with the added navigation function term is enough to generate the initial MEP approximation. Thirdly, there is no need to carry out any interpolation between the reactant and the product and as such, problems such as non-intuitive chemical structures with unrealistic inter-atomic distances or non-adequate accounts of dihedral angles can be avoided. Lastly, it is worth mentioning that this input information could be calculated at a lower level of *ab initio* theory as a computationally inexpensive route to generating an initial MEP approximation, before further refinement at a higher level of *ab initio* theory.

Chapter 6

Conclusion

> I cannot pray for their safety, but I will pray that they are sleeping slaves and when they wake, that these sleeping slaves shall fulfill some purpose.
>
> *JoJo's Bizarre Adventure Golden Wind*, Hirohiko Araki

Summary

This Chapter summarises the methods and results shown in this work and the conclusions that can be drawn from them for efficient and accurate automated reaction discovery. In addition, we explore potential future improvements and new avenues to the methods discussed in this work.

6.1 Summary and conclusions

In the context of automated reaction discovery (ARD) whereby connectivity matrices are used to build chemical reaction networks (CRNs), current screening methods typically involve using chemical intuition in order to sort through unfeasible and unreasonable changes in the connectivity matrix which would translate to unlikely CRNs. Whether it is screening the connectivity matrix changes during the ARD process or sorting through the resulting sequence of connectivity matrix changes once the ARD process has finished, chemical intuition in the form of reaction paths and the associated energy barrier or reaction rates is often used. Popular methods, while they have there merits, are sometimes not adequate or do not describe the complete reaction and as such they do not allow for fast, efficient and accurate ARD. Methods used for reaction path finding,include nudged elastic band (NEB), growing string method (GSM) and freezing string method (FSM), and while they do result in accurate minimum energy paths (MEP), the computational cost associated with the number of force evaluations required scales badly with large and complex chemical reactions. For determination of reaction rates and rate constants, transition state theory (TST) is a method commonly used however the no-recrossing assumption can introduce a significant error in those cases where recrossing effects do in fact occur (such as that caused by significant solvent interactions or in inter-conversion reactions) resulting in an inaccurate description of the chemical reaction.

We had outlined several aims and objectives at the beginning of this work that would be explored and discussed. These were the following:

1. Implement the RPH into a functional code where transmission coefficients and reaction rates can be determined.

2. Integrate several different update Hessian schemes into the RPH framework in order to reduce the computational cost but keep the accuracy of the calculation.

3. Explore dynamical effects in organometallic catalysis using the RPH approach.

4. Develop novel methods to generate reaction paths which can be used as good initial guesses for subsequent MEP refinement.

5. Compare and contrast the resulting reaction paths generated by the novel methods developed to current initial reaction path finding methods.

6. Compare and contrast the TS optimisation capabilities using the resulting reaction paths generated by the novel methods developed to current initial reaction path finding methods.

As such, in this work, we have proposed various methods which can be used as alternatives to popular methods in ARD as a way to efficiently and accurately screen through the large number of changes which can occur in the connectivity matrix throughout a chemical reaction. As a substitute to TST, we have shown that the reaction path Hamiltonian (RPH) can be used to account for recrossing effects which could take place in a chemical reaction. In this work we implemented the RPH into a functional code whereby transmission coefficients and reaction rates could be determined. The approach was as follows, once the MEP of a chemical reaction is determined, the RPH can subsequently be constructed over a number of discrete points on the path to provide an accurate description of the MEP. Following this, combining the constructed RPH with molecular dynamics (MD) simulations and thermal-averaging over a number of MD trajectories initiated at the TS results in the evaluation the flux-side correlation function. However, in this form, the RPH does not computationally scale well for large and complex CRNs as the determination of the *ab initio* Hessian matrix at every discrete point on the path represents a significant bottleneck.

We have shown that the RPH construction can be further accelerated by using a variety of Hessian update schemes, which significantly reduces the need for *ab initio* Hessian matrices at discrete points along the path. In this investigation, we compared the resulting transmission coefficients determined using seven different Hessian update schemes, four quasi-Newton Hessian update schemes and three compact-finite difference (CFD) Hessian update schemes, to using the standard RPH approach on three chemical reactions. Furthermore, the way the Hessian update schemes were implemented and propagated were explored using different approaches labelled as single-ended from the reactant, single-ended from the product, double-ended, "TSup" and "TSdown". Across all of the reactions investigated using Hessian update schemes, the propagation approach which had the most success, at least in qualitative terms, was the double-ended propagation approach which resulted in a transmission coefficient similarly affected by recrossing effects like the standard implementation of the RPH.

When quasi-Newton Hessian update schemes were used, there was no scheme which provided accurate and consistent transmission coefficients across the reactions studied. However this is not to say that they did not perform well as, depending on the reaction, some schemes resulted in similar transmission coefficients to the standard approach. Particularly the Powell-symmetric-Brodyen (PSB), and Bofill Hessian update schemes which resulted in very similar transmission coefficients to the standard approach for R1 and R3 and the transition-state-BFGS (TS-BFGS) Hessian update scheme which resulted in very similar transmission coefficients to the standard approach for R1 and especially R2 where none of the other schemes man-

aged to accurately depict the recrossing effects like the standard approach. On the other hand, the symmetric-rank-1 (SR1) scheme did somewhat under perform, having the largest differences between calculated transmission coefficients and standard approach transmission coefficients. We also showed that, for the reactions studied, the compact finite difference (CFD) Hessian update schemes did not result in better transmission coefficients than the quasi-Newton Hessian update schemes, but in fact just resulted in essentially the same transmission coefficient as there quasi-Newton counter-parts indicating that the added accuracy provided by CFD Hessian update schemes was negligible for these reactions studied. We also note that the relative computational cost of the four Hessian update methods was less than that of the standard approach for all three reactions considered, thus significantly reducing the bottleneck that limited the RPH in the context of ARD.

To understand and rationalise the performance of the Hessian update schemes investigated, we looked at Hessian matrices, harmonic vibrational frequencies, coupling constants and MD trajectories all of which are either key parameters used in the construction of the RPH or part of MD simulations. For all of the quasi-Newton Hessian update schemes, the harmonic vibrational frequencies at the transition state (TS) were correctly represented when compared to the standard approach. Moreover, the curvature coupling along the reaction path, which involves the harmonic vibrational frequencies, was also correctly represented by the PSB, Bofill and TS-BFGS schemes when compared to the standard approach, suggesting that these Hessian update schemes were suitable for harmonic vibrational frequencies determination. The SR1 Hessian update scheme however, typically had regions along the reaction path where the curvature coupling was either much larger in magnitude compared to the standard approach or was simply ill-defined, which also correlated with poor transmission coefficients across the reactions studied. As for the Coriolis coupling, the majority of the Hessian update schemes somewhat agreed with the standard approach at least in terms of magnitude and broad trend, but again, the SR1 scheme resulted in large peaks in some regions of the reaction path unlike the standard approach. Furthermore, we also highlighted the link between the Coriolis coupling and transmission coefficient as the Hessian update scheme which resulted in a Coriolis coupling closer to that using the standard approach, would then have similar MD trajectories resulting in a similar transmission coefficient. Lastly, analysis of the Hessian root-mean-square-deviation (RMSD) at each MEP discrete point for each reaction showed that, again, the SR1 scheme displayed sudden large error spikes as opposed to the other Hessian update schemes, as did the analysis of the frequencies as a function of the reaction coordinate which also showed abnormal fluctuations. Analysing of all these parameters, we demonstrated that SR1 is not the best Hessian update scheme and can not be recommended to be used in the

context of the RPH, whereas for the other schemes, we found that there was none which could be recommended over another however analysis of the Coriolis coupling could indicate which scheme would perform better.

Using the RPH approach, we investigated dynamical effects in organometallic catalysis using the Heck–Breslow mechanism for alkene hydroformylation with a cobalt catalyst in both gas-phase and solvent-phase as a case study. Both TST reaction rates and RPH reaction rates, to account for any recrossing effects, were used on the reactions with barriers involved in the catalytic cycle. The results showed that there were recrossing effects in several reactions, both in gas-phase and solvent-phase, with transmission coefficients not being unity. Subsequently, kinetic simulations were done in order to determine the rate law and the results showed near identical rate laws for both TST derived reaction rates and RPH derived reaction rates in both gas-phase and solvent-phase, which matched with literature and experimental. This suggested that, firstly, the implicit solvent model used to simulate the solvent-phase did not affect the dynamics greatly and that secondly, the dynamical effects described by the RPH reaction rates did not significantly affect the rate law either. As such, we investigated the time evolution of the concentrations for the species involved in the catalytic cycle, in order to see whether or not the TST results would differ from the RPH results. The results showed that for the initial species (the catalyst, molecular hydrogen, carbon monoxide and ethene), both TST and RPH reaction rates resulted in similar values for the time evolution of the concentrations. In terms of the intermediate species, while the trend in time evolution of the concentrations was identical, the magnitude using TST reaction rates was slightly smaller than using RPH reaction rates. Moreover, we noted that dynamical effects linked to recrossing were worth considering as depending on the CRNs investigated, the minimal differences due to recrossing observed here would not always be the case.

To reduce the computational cost of reaction path finding methods used in ARDs which require a large number of force evaluations to determine the MEP, in this work, we presented two new methods to determine good initial approximate reaction paths which could be used as a starting point for subsequent refinement for MEP determination. The two methods we introduced, the projected navigation string method (P-NSM) and the adiabatic navigation string method (A-NSM), were built around the concept of using a navigation function to drive the system from one end of the potential energy surface (PES) to the other end of the PES. Initial approximate reaction paths determined by P-NSM and A-NSM were compared to other popular initial approximate reaction path methods, specifically the image dependent pair potential (IDPP) method and the root mean square deviation push-pull method (RMSD-PP), on seven example reactions. We looked at the distance between the

initial reaction path and the MEP determined by NEB refinement as well as the number of force evaluations required for the generation of the initial reaction path and the number of force evaluations required for the determination of the MEP. When compared to the IDPP and RMSD-PP method, both P-NSM and A-NSM generated initial approximate reaction paths closer to the MEP for six out of the seven reactions. We also showed that both P-NSM and A-NSM, required less force evaluations for the generation of the initial reaction path, but also for the NEB refinement to determine the MEP, for six out of the seven reactions when compared to the RMSD-PP method. Similarly, both P-NSM and A-NSM, required less force evaluations for the generation of the initial reaction path in addition to the NEB refinement than the IDPP method for five out of the seven reactions. The advantages of P-NSM and A-NSM were highlighted in two specific reactions studied, the formation of formaldehyde reaction and in the penta 1,3-diene hydrogen transfer reaction. The formation of formaldehyde reaction highlighted how the number of force evaluations needed for the generation of the initial reaction path was significantly lower for P-NSM and A-NSM compared to RMSD-PP as was the number of force evaluations needed for subsequent NEB refinement of the initial reaction path when compared to both RMSD-PP and IDPP. The penta 1,3-diene hydrogen transfer reaction on the other hand highlighted how much closer the initial reaction path generated by P-NSM and A-NSM was to the MEP determined by NEB refinement compared to either RMSD-PP and IDPP.

We investigated the number of nodes, step-size and navigation force constant, all of which are parameters used in P-NSM and A-NSM to understand the effects they had on the resulting initial approximated reaction path. For three example reactions, each parameter was tested with different magnitudes while the other two parameters were kept constant. Across all three reactions, increasing the number of nodes had a positive effect meaning that the initial approximated reaction path was described better, however in line with trying to keep the computational cost at a minimal, too many nodes would be detrimental. We showed that increasing the step-size and navigation force constant to large magnitudes had a negative effect on the generated initial reaction path as the reaction path became ill-describe and unfeasible, whereas decreasing them meant that the system would not reach the end point resulting in an incomplete reaction path, highlighting the sensitivity of the step-size and navigation force constant. We also emphasised that different reactions required different magnitudes for their parameters and as such, the investigation into the parameters of P-NSM and A-NSM could act as a troubleshooting guide.

Finally, we explored the possibility of using the highest energy image on the NSM generated reaction path as an initial guess for TS optimisation in order to find the TS. The results shown were encouraging as for five out seven of the reactions

investigated, the highest energy image lead to the TS found on the MEP. While it did not outperform RMSD-PP or IDPP, which managed to find the TS found on the MEP for six out of the seven reaction, the number of cycles required to find the TS was comparable. However, if the cost of the initial reaction path generation is taken into account, then the NSM offers a potentially cheaper alternative in terms of computational cost than either RMSD-PP and IDPP for TS optimisation.

6.2 Future work

Building upon the work using Hessian update schemes in the context of RPH rate calculations, demonstrating significant reduction in computational time and good approximations of the transmission coefficient, it can now be explored within ARD methods for screening purposes or to account for recrossing effects which would effect the reaction rate. Moreover, with the constant development of new and better update Hessian schemes, the implementation with the RPH will only get better and is worth exploring even more.

Furthermore, using the RPH alongside MD simulations for the study of organometallic catalysis successfully highlighted the importance of including recrossing effects in reaction rate calculations, both in gas-phase and using an implicit solvent model, as such using the same methodology for larger and more complex reactions or using an explicit model for solvation would be of value for accurate reaction rates and rate order equation.

Future work for the method itself would include, but is not limited to, development of better Hessian update schemes which can reproduce the Hessian as close as possible to the analytical approach so that the Coriolis coupling can be accurate, re-calculating analytical Hessian calculations after a certain amount of Hessian update steps, investigating better propagating methods and using a more chemically intuitive weighting scheme. Another Hessian propagation method could also be explored whereby three analytical Hessians are calculated at the minima and TS, and a Hessian update scheme is used to propagate a Hessian from the minima to the TS and back. This would allow for the region around the TS to be better described using the Hessian update schemes and potentially improve the transmission coefficient determined. Finally, another interesting alternative would be to apply the RPH, alongside Hessian update schemes, using a direct dynamics approach to even further reduce the computational cost, especially because Hessian update schemes have had much success when used in direct dynamics.

Further applications for the RPH approach, in the context of dynamical effects in organometallic catalysis, could be to expand upon the catalytic cycles investigated, focusing on some where recrossing effects might occur. Furthermore, investigating

the reactive flux in the kinetic network model would give a clearer picture of how recrossing effects affected the reactive flux specific to the reactions in the catalytic cycle. Lastly, using explicit solvent instead of implicit solvent to better account for solvent effects and how they would effect TST reaction rates and RPH reaction rates would be of value.

P-NSM and A-NSM both yielded excellent and promising results using quite a simple methodology which leaves room for improvement. A simple improvement for example, instead of using a predetermined number of nodes initially, the number of nodes could just grow until the system reaches the end node or a certain threshold. Furthermore, exploring the use of a variable navigation force constant which could increase or decrease depending on the position of the system on the PES or using attractive and repulsive wells at the start and end points represent possible improvements for the methods. Lastly, including optimisation steps after each node is generated or optimising the initial reaction path after generation like in the RMSD-PP method could also be investigated however this would increase the number of force evaluations and may not be desirable.

Finally, and perhaps the most important piece of future work, would be to implement these methods in the context of ARD in order to better describe CRNs. Using the NSM to determine the reaction paths, and subsequently the MEP at a lower computational cost, and using the computationally cheaper RPH with update Hessian schemes to better describe reaction rates. These two approaches could either be used to improve the screening of reactions found using ARD, or to be used after the CRN is built, to rapidly get chemical information about reaction rates, parameters or shape of the MEP.

Bibliography

[1] D. J. Auerbach, J. C. Tully, and A. M. Wodtke, *Natural Sciences* **1**, e10005 (2021).

[2] N. Basco and R. G. W. Norrish, *Canadian Journal of Chemistry* **38**, 1769 (2011).

[3] A. L. Schawlow and C. H. Townes, *Physical Review* **112**, 1940 (1958).

[4] T. H. Maiman, *Nature 1960 187:4736* **187**, 493 (1960).

[5] P. Casavecchia, *Reports on Progress in Physics* **63**, 355 (2000).

[6] D. R. Herschbach, G. H. Kwei, and J. A. Norris, *The Journal of Chemical Physics* **34**, 1842 (2004).

[7] F. T. Wall and J. J. Erpenbeck, *The Journal of Chemical Physics* **30**, 634 (2004).

[8] J. Simons, *An introduction to theoretical chemistry*, Cambridge University Press, 2003.

[9] D. Mehta, J. D. Hauenstein, and D. J. Wales, *The Journal of Chemical Physics* **138**, 171101 (2013).

[10] D. Angeli, *European Journal of Control* **15**, 398 (2009).

[11] V. Wakelam, I. W. M. Smith, E. Herbst, J. Troe, W. Geppert, H. Linnartz, K. Oberg, E. Roueff, M. Agundez, P. Pernot, H. M. Cuppen, J. C. Loison, and D. Talbi, *Space Science Reviews* **156**, 13 (2010).

[12] S. Rangarajan, R. R. Brydon, A. Bhan, and P. Daoutidis, *Green Chemistry* **16**, 813 (2014).

[13] F. Pietrucci and A. M. Saitta, *Proceedings of the National Academy of Sciences of the United States of America* **112**, 15030 (2015).

[14] Z. W. Ulissi, A. J. Medford, T. Bligaard, and J. K. Nørskov, *Nature communications* **8** (2017).

[15] G. N. Simm and M. Reiher, *Journal of Chemical Theory and Computation* **13**, 6108 (2017).

[16] G. N. Simm, A. C. Vaucher, and M. Reiher, *Journal of Physical Chemistry A* **123**, 385 (2019).

[17] D. Rappoport, *Journal of Physical Chemistry A* **123**, 2610 (2019).

[18] K. Sugiyama, Y. Sumiya, M. Takagi, K. Saita, and S. Maeda, *Physical Chemistry Chemical Physics* **21**, 14366 (2019).

[19] J. P. Unsleber and M. Reiher, *Annual Reviews* **71**, 121 (2020).

[20] P. Schwaller, D. Probst, A. C. Vaucher, V. H. Nair, D. Kreutter, T. Laino, and J.-L. Reymond, *ChemRxiv* (2020).

[21] A. L. Dewyer, A. J. Argüelles, and P. M. Zimmerman, *WIREs Computational Molecular Science* **8**, e1354 (2018).

[22] J. Zeng, L. Cao, M. Xu, T. Zhu, and J. Z. Zhang, *Nature Communications 2020 11:1* **11**, 1 (2020).

[23] W. Ji and S. Deng, *Journal of Physical Chemistry A* **125**, 1082 (2021).

[24] C. Robertson and S. Habershon, *Journal of Computational Chemistry* **42**, 761 (2021).

[25] C. W. Gao, J. W. Allen, W. H. Green, and R. H. West, *Computer Physics Communications* **203**, 212 (2016).

[26] A. F. de Almeida, R. Moreira, and T. Rodrigues, *Nature Reviews Chemistry* **3**, 589 (2019).

[27] L. P. Wang, A. Titov, R. McGibbon, F. Liu, V. S. Pande, and T. J. Martínez, *Nature chemistry* **6**, 1044 (2014).

[28] P. Zimmerman, *Journal of Chemical Theory and Computation* **9**, 3043 (2013).

[29] A. J. Nett, W. Zhao, P. M. Zimmerman, and J. Montgomery, *Journal of the American Chemical Society* **137**, 7636 (2015).

[30] J. A. Varela, S. A. Vázquez, and E. Martínez-Núñez, *Chemical Science* **8**, 3843 (2017).

[31] S. Kopec, E. Martínez-Núñez, J. Soto, and D. Peláez, *International Journal of Quantum Chemistry* **119**, e26008 (2019).

[32] E. Martínez-Núñez, *Physical Chemistry Chemical Physics* **17**, 14912 (2015).

[33] E. Martínez-Núñez, *Journal of Computational Chemistry* **36**, 222 (2015).

[34] K. Ohno and S. Maeda, *Physica Scripta* **78**, 058122 (2008).

[35] S. Maeda and K. Ohno, *The journal of physical chemistry. A* **109**, 5742 (2005).

[36] S. Maeda and K. Morokuma, *Journal of Chemical Theory and Computation* **7**, 2335 (2011).

[37] S. Maeda, T. Taketsugu, K. Ohno, and K. Morokuma, *Journal of the American Chemical Society* **137**, 3433 (2015).

[38] C. W. Coley, W. Jin, L. Rogers, T. F. Jamison, T. S. Jaakkola, W. H. Green, R. Barzilay, and K. F. Jensen, *Chemical Science* **10**, 370 (2019).

[39] J. N. Wei, D. Duvenaud, and A. Aspuru-Guzik, *ACS Central Science* **2**, 725 (2016).

[40] P. P. Plehiers, G. B. Marin, C. V. Stevens, and K. M. V. Geem, *Journal of Cheminformatics* **10**, 1 (2018).

[41] J. S. Schreck, C. W. Coley, and K. J. Bishop, *ACS Central Science* **5**, 970 (2019).

[42] S. Szymkuć, E. P. Gajewska, T. Klucznik, K. Molga, P. Dittwald, M. Startek, M. Bajczyk, and B. A. Grzybowski, *Angewandte Chemie International Edition* **55**, 5904 (2016).

[43] O. Engkvist, P. O. Norrby, N. Selmi, Y. hong Lam, Z. Peng, E. C. Sherer, W. Amberg, T. Erhard, and L. A. Smyth, *Drug discovery today* **23**, 1203 (2018).

[44] E. Pieri, D. Lahana, A. M. Chang, C. R. Aldaz, K. C. Thompson, and T. J. Martínez, *Chemical Science* **12**, 7294 (2021).

[45] A. Rodríguez, R. Rodríguez-Fernández, S. A. Vázquez, G. L. Barnes, J. J. P. Stewart, and E. Martínez-Núñez, *Journal of Computational Chemistry* **39**, 1922 (2018).

[46] C. Robertson and S. Habershon, *Catalysis Science Technology* **9**, 6357 (2019).

[47] C. Robertson, R. Hyland, A. J. D. Lacey, S. Havens, and S. Habershon, *Journal of Chemical Theory and Computation* **17**, 2307 (2021).

[48] S. Habershon, *The Journal of Chemical Physics* **143**, 094106 (2015).

[49] S. Habershon, *Journal of Chemical Theory and Computation* **12**, 1786 (2016).

[50] I. Ismail, H. B. V. A. Stuttaford-Fowler, C. O. Ashok, C. Robertson, and S. Habershon, *The Journal of Physical Chemistry A* **123**, 3407 (2019).

[51] R. J. Gillis and W. H. Green, *ChemSystemsChem* **2**, e1900051 (2020).

[52] C. A. Class, M. Liu, A. G. Vandeputte, and W. H. Green, *Physical Chemistry Chemical Physics* **18**, 21651 (2016).

[53] M. Keçeli, S. N. Elliott, Y. P. Li, M. S. Johnson, C. Cavallotti, Y. Georgievskii, W. H. Green, M. Pelucchi, J. M. Wozniak, A. W. Jasper, and S. J. Klippenstein, *Proceedings of the Combustion Institute* **37**, 363 (2019).

[54] I. Ismail, C. Robertson, and S. Habershon, *The Journal of Chemical Physics* **157**, 014109 (2022).

[55] G. H. Gu, C. Choi, Y. Lee, A. B. Situmorang, J. Noh, Y. H. Kim, and Y. Jung, *Advanced Materials* **32**, 1907865 (2020).

[56] C. A. Grambow, L. Pattanaik, and W. H. Green, *Journal of Physical Chemistry Letters* **11**, 2992 (2020).

[57] K. Takahashi and I. Miyazato, *Journal of Computational Chemistry* **39**, 2405 (2018).

[58] W. Jiang, X. Xing, X. Zhang, and M. Mi, *Renewable Energy* **130**, 1216 (2019).

[59] Q. Zhao and B. M. Savoie, *Nature Computational Science 2021 1:7* **1**, 479 (2021).

[60] K. Jorner, T. Brinck, P. O. Norrby, and D. Buttar, *Chemical Science* **12**, 1163 (2021).

[61] K. Mikami, *Polymer* **203**, 122738 (2020).

[62] J. Xu, X. M. Cao, and P. Hu, *Journal of Physical Chemistry C* **123**, 28802 (2019).

[63] S. Choi, Y. Kim, J. W. Kim, Z. Kim, and W. Y. Kim, *Chemistry – A European Journal* **24**, 12354 (2018).

[64] C. A. Grambow, L. Pattanaik, and W. H. Green, *Scientific Data 2020 7:1* **7**, 1 (2020).

[65] K. A. Spiekermann, L. Pattanaik, and W. H. Green, *Journal of Physical Chemistry A* **126**, 3976 (2022).

[66] M. G. Evans and M. Polanyi, *Transactions of the Faraday Society* **31**, 875 (1935).

[67] K. J. Laidler and M. C. King, *Journal of Physical Chemistry* **87**, 2657 (1983).

[68] K. J. Laidler, *Chemical Kinetics*, Haper Collins, 3rd edition, 1987.

[69] H. Eyring and M. Polanyi, *Zeitschrift fur Physikalische Chemie* **227**, 1221 (2013).

[70] W. F. Wynne-Jones and H. Eyeing, *The Journal of Chemical Physics* **3**, 492 (2004).

[71] E. Wigner, *Transactions of the Faraday Society* **34**, 29 (1938).

[72] J. B. Anderson, *The Journal of Chemical Physics* **58**, 4684 (1973).

[73] N. E. Henriksen and F. Y. Hansen, *Theories of Molecular Reaction Dynamics*, Oxford University Press, 2008.

[74] J. W. Tromp and W. H. Miller, *Journal of Physical Chemistry* **90**, 3482 (1986).

[75] D. G. Truhlar and B. C. Garrett, *Journal of Physical Chemistry* **96**, 6515 (1992).

[76] N. F. Hansen and H. C. Andersen, *Journal of Physical Chemistry* **100**, 1137 (1996).

[77] G. A. Voth, D. Chandler, and W. H. Miller, *The Journal of Chemical Physics* **91**, 7749 (1998).

[78] W. H. Thompson, *The Journal of Chemical Physics* **110**, 4221 (1999).

[79] D. G. Truhlar and B. C. Garrett, *Accounts of Chemical Research* **13**, 440 (1980).

[80] D. G. Truhlar, W. L. Hase, and J. T. Hynes, *Journal of Physical Chemistry* **87**, 2664 (1983).

[81] D. G. Truhlar and B. C. Garrett, *Annual Review of Physical Chemistry* **35**, 159 (1984).

[82] J. L. Bao and D. G. Truhlar, *Chemical Society Reviews* **46**, 7548 (2017).

[83] L. Onsager, *Physical Review* **37**, 405 (1931).

[84] T. Yamamoto, *The Journal of Chemical Physics* **33**, 281 (2004).

[85] W. H. Miller, N. C. Handy, and J. E. Adams, *The Journal of Chemical Physics* **72**, 99 (1980).

[86] E. Kraka, *Reaction Path Hamiltonian and its Use for Investigating Reaction Mechanisms*, John Wiley Sons, Ltd, 2002.

[87] B. Peters, A. T. Bell, and A. Chakraborty, *Journal of Chemical Physics* **121**, 4453 (2004).

[88] H. Hu, M. N. Kobrak, C. Xu, and S. Hammes-Schiffer, *Journal of Physical Chemistry A* **104**, 8058 (2000).

[89] M. Page and J. W. M. Jr., *The Journal of Chemical Physics* **88**, 922 (1998).

[90] H. W. Kuhn, *Naval Research Logistics Quarterly* **2**, 83 (1955).

[91] W. H. Miller, *J. Chem. Phys* **61**, 1823 (1974).

[92] R. A. Kuharski, D. Chandler, J. A. Montgomery, F. Rabii, and S. J. Singer, *Journal of Physical Chemistry* **92**, 3261 (1988).

[93] M. A. Wilson and D. Chandler, *Chemical Physics* **149**, 11 (1990).

[94] D. Chandler, *Introduction to Modern Statistical Mechanics*, volume 5, Oxford University Press, 1987.

[95] D. Chandler, *The Journal of Chemical Physics* **68**, 2959 (2008).

[96] G. Henkelman, B. P. Uberuaga, and H. Jónsson, *Journal of Chemical Physics* **113** (2000).

[97] C. J. Cerjan and W. H. Miller, *The Journal of Chemical Physics* **75**, 2800 (1998).

[98] V. Ásgeirsson, B. O. Birgisson, R. Bjornsson, U. Becker, F. Neese, C. Riplinger, and H. Jónsson, *Journal of Chemical Theory and Computation* **17**, 4929 (2021).

[99] Y. Pak and G. A. Voth, *Journal of Physical Chemistry A* **103**, 925 (1999).

[100] Y. Shao, L. F. Molnar, Y. Jung, J. Kussmann, C. Ochsenfeld, S. T. Brown, A. T. Gilbert, L. V. Slipchenko, S. V. Levchenko, D. P. O'Neill, R. A. DiStasio, R. C. Lochan, T. Wang, G. J. Beran, N. A. Besley, J. M. Herbert, C. Y. Lin, T. V. Voorhis, S. H. Chien, A. Sodt, R. P. Steele, V. A. Rassolov, P. E. Maslen, P. P. Korambath, R. D. Adamson, B. Austin, J. Baker, E. F. Byrd, H. Dachsel, R. J. Doerksen, A. Dreuw, B. D. Dunietz, A. D. Dutoi, T. R. Furlani, S. R. Gwaltney, A. Heyden, S. Hirata, C. P. Hsu, G. Kedziora, R. Z. Khaliullin, P. Klunzinger, A. M. Lee, M. S. Lee, W. Liang, I. Lotan, N. Nair, B. Peters, E. I. Proynov, P. A. Pieniazek, Y. M. Rhee, J. Ritchie, E. Rosta, C. D. Sherrill, A. C. Simmonett, J. E. Subotnik, H. L. Woodcock, W. Zhang, A. T. Bell, A. K. Chakraborty, D. M. Chipman, F. J. Keil, A. Warshel, W. J. Hehre, H. F. Schaefer, J. Kong, A. I. Krylov, P. M. Gill, and M. Head-Gordon, *Physical Chemistry Chemical Physics* **8**, 3172 (2006).

[101] P. M. Zimmerman, *J. Comput. Chem.* **34**, 1385 (2013).

[102] M. Foscato and V. R. Jensen, *ACS Catalysis* **10**, 2354 (2020).

[103] C. Gonzalez and H. B. Schlegel, *The Journal of Chemical Physics* **90**, 2154 (1989).

[104] C. Gonzalez and H. B. Schlegel, *Journal of Physical Chemistry* **94**, 5523 (1990).

[105] C. Gonzalez and H. B. Schlegel, *Journal of Chemical Physics* **95**, 5853 (1991).

[106] F. Eckert and H. J. Werner, *Theoretical Chemistry Accounts* **100**, 21 (1998).

[107] H. B. Schlegel, GEOMETRY OPTIMIZATION ON POTENTIAL ENERGY SURFACES, 1995.

[108] A. B. Birkholz and H. B. Schlegel, *Theoretical Chemistry Accounts* **135**, 84 (2016).

[109] H. B. Schlegel, *Journal of Computational Chemistry* **3**, 214 (1982).

[110] A. Denzel and J. Kästner, *Journal of Chemical Theory and Computation* **16**, 5083 (2020).

[111] T. J. Frankcombe, *The Journal of Chemical Physics* **140**, 114108 (2014).

[112] G. Richings, I. Polyak, K. Spinlove, G. Worth, I. Burghardt, and B. Lasorne, *http://dx.doi.org/10.1080/0144235X.2015.1051354* **34**, 269 (2015).

[113] H. P. Hratchian, M. J. Frisch, and H. B. Schlegel, *Journal of Chemical Physics* **133**, 224101 (2010).

[114] J. J. E. Dennis and J. J. Moré, *SIAM Review* **19**, 46 (1977).

[115] P. Hennig and M. Kiefel, *Journal of Machine Learning Research* **14**, 843 (2013).

[116] C. G. Broyden, *The Computer Journal* **12**, 94 (1969).

[117] R. Fletcher, *The Computer Journal* **13**, 317 (1970).

[118] D. Goldfarb, *Mathematics of Computation* **24**, 23 (1970).

[119] D. F. Shanno, *Mathematics of Computation* **24**, 647 (1970).

[120] J. M. Bofill, *International Journal of Quantum Chemistry* **94**, 324 (2003).

[121] B. A. Murtagh and R. W. H. Sargent, *The Computer Journal* **13**, 185 (1970).

[122] S. W. J. Nocedal, *Quasi-Newton Methods*, pp. 135–163, Springer New York, New York, NY, 2006.

[123] H. Wu, M. Rahman, J. Wang, U. Louderaj, W. L. Hase, and Y. Zhuang, *The Journal of Chemical Physics* **133**, 074101 (2010).

[124] M. J. Powell, *IMA Journal of Applied Mathematics (Institute of Mathematics and Its Applications)* **7**, 21 (1971).

[125] J. M. Bofill, *Journal of Computational Chemistry* **15**, 1 (1994).

[126] S. K. Lele, *Journal of Computational Physics* **103**, 16 (1992).

[127] R. E. Lynch and J. R. Rice, *Proceedings of the National Academy of Sciences* **75**, 2541 (1978).

[128] I. Singer and E. Turkel, *Computer Methods in Applied Mechanics and Engineering* **163**, 343 (1998).

[129] Y. Zhuang and X.-H. Sun, *Advances in Engineering Software* **31**, 585 (2000).

[130] Y. Zhuang and X.-H. Sun, *Journal of Computational Physics* **171**, 79 (2001).

[131] H. P. Hratchian and H. B. Schlegel, *Journal of Chemical Theory and Computation* **1**, 61 (2005).

[132] R. F. Heck and D. S. Breslow, *Journal of the American Chemical Society* **83**, 4023 (1961).

[133] A. D. Becke, *Physical Review A* **38**, 3098 (1988).

[134] C. Lee, W. Yang, and R. G. Parr, *Physical Review B* **37**, 785 (1988).

[135] A. D. Becke, *The Journal of Chemical Physics* **98**, 1372 (1993).

[136] P. J. Stephens, F. J. Devlin, C. F. Chabalowski, and M. J. Frisch, *Journal of Physical Chemistry* **98**, 11623 (1994).

[137] R. Ditchfield, W. J. Hehre, and J. A. Pople, *The Journal of Chemical Physics* **54**, 720 (1971).

[138] W. J. Hehre, K. Ditchfield, and J. A. Pople, *The Journal of Chemical Physics* **56**, 2257 (1972).

[139] P. C. Hariharan and J. A. Pople, *Theoretica Chimica Acta* **28**, 213 (1973).

[140] V. A. Rassolov, J. A. Pople, M. A. Ratner, and T. L. Windus, *Journal of Chemical Physics* **109**, 1223 (1998).

[141] G. Duca, *Introduction*, pp. 1–9, Springer Berlin Heidelberg, Berlin, Heidelberg, 2012.

[142] S. Bhaduri and D. Mukesh, *Homogeneous catalysis: mechanisms and industrial applications*, John Wiley & Sons, 2014.

[143] G. W. Parshall, S. D. Ittel, et al., *Homogeneous catalysis*, Wiley, 1992.

[144] K. N. Houk and P. H. Y. Cheong, *Nature 2008 455:7211* **455**, 309 (2008).

[145] M. Steiner and M. Reiher, *Topics in Catalysis* **65**, 6 (2022).

[146] E. S. Isbrandt, R. J. Sullivan, and S. G. Newman, *Angewandte Chemie International Edition* **58**, 7180 (2019).

[147] J. A. Varela, S. A. Vázquez, and E. Martínez-Núñez, *Chem. Sci.* **8**, 3843 (2017).

[148] L. E. Rush, P. G. Pringle, and J. N. Harvey, *Angewandte Chemie International Edition* **53**, 8672 (2014).

[149] G. Natta, R. Ercoli, S. Castellano, and F. H. Barbieri, *Journal of the American Chemical Society* **76**, 4049 (1954).

[150] J. R. Bourne, O. M. Kut, and J. Lenzner, *Industrial & Engineering Chemistry Research* **31**, 949 (1992).

[151] S. Kale, O. Sode, J. Weare, and A. R. Dinner, *Journal of chemical theory and computation* **10**, 5467 (2014).

[152] J. B. Brokaw, K. R. Haas, and J. W. Chu, *Journal of Chemical Theory and Computation* **5**, 2050 (2009).

[153] K. Ohno and S. Maeda, *Chemical Physics Letters* **384**, 277 (2004).

[154] L. Xie, H. Liu, and W. Yang, *The Journal of Chemical Physics* **120**, 8039 (2004).

[155] X. Zhu, K. C. Thompson, and T. J. Martínez, *The Journal of Chemical Physics* **150**, 164103 (2019).

[156] W. E, W. Ren, and E. Vanden-Eijnden, *Physical Review B* **66**, 052301 (2002).

[157] S. Smidstrup, A. Pedersen, K. Stokbro, and H. Jónsson, *The Journal of Chemical Physics* **140**, 214106 (2014).

[158] N. E. Henriksen and F. Y. Hansen, *Theories of Molecular Reaction Dynamics* , 262 (2008).

[159] B. Peters, A. Heyden, A. T. Bell, and A. Chakraborty, *The Journal of Chemical Physics* **120**, 7877 (2004).

[160] R. C. Majerus, C. Robertson, and S. Habershon, *The Journal of Chemical Physics* **155**, 204112 (2021).

[161] V. P. Ananikov, *Understanding organometallic reaction mechanisms and catalysis : computational and experimental tools*, WILEY-VCH Verlag, 2015.

[162] T. Sperger, I. A. Sanhueza, I. Kalvet, and F. Schoenebeck, *Chemical Reviews* **115**, 9532 (2015).

[163] T. Ziegler, L. Cavallo, and A. Bérces, *Organometallics* **12**, 3586 (1993).

[164] C. F. Huo, Y. W. Li, M. Beller, and H. Jiao, *Organometallics* **22**, 4665 (2003).

[165] A. Nova, D. J. Taylor, A. J. Blacker, S. B. Duckett, R. N. Perutz, and O. Eisenstein, *Organometallics* **33**, 3433 (2014).

[166] L. E. Rush, P. G. Pringle, and J. N. Harvey, *Angewandte Chemie International Edition* **53**, 8672 (2014).

[167] M. Stamatakis, *Journal of Physics: Condensed Matter* **27**, 013001 (2014).

[168] C. F. Goldsmith and R. H. West, *Journal of Physical Chemistry C* **121**, 9970 (2017).

[169] A. Alavi, P. Hu, T. Deutsch, P. L. Silvestrelli, and J. Hutter, *Physical Review Letters* **80**, 3650 (1998).

[170] A. Bruix, J. T. Margraf, M. Andersen, and K. Reuter, *Nature Catalysis* **2**, 659 (2019).

[171] X. Wang, C. Jia, E. Sharman, G. Zhang, X. Li, and J. Jiang, *Scientific Reports 2020 10:1* **10**, 1 (2020).

[172] Z. Cournia, B. Allen, and W. Sherman, *Journal of Chemical Information and Modeling* **57**, 2911 (2017).

[173] Z. Cournia, C. Chipot, B. Roux, D. M. York, and W. Sherman, *ACS Symposium Series* **1397**, 1 (2021).

[174] E. King, E. Aitchison, H. Li, and R. Luo, *Frontiers in Molecular Biosciences* **8** (2021).

[175] D. Sheppard and G. Henkelman, *Journal of Computational Chemistry* **32**, 1769 (2011).

[176] G. Mills and H. Jónsson, *Physical Review Letters* **72**, 1124 (1994).

[177] G. Mills, H. Jónsson, and G. K. Schenter, *Surface Science* **324**, 305 (1995).

[178] J. Baker, *Journal of Computational Chemistry* **7**, 385 (1986).

[179] N. Govind, M. Petersen, G. Fitzgerald, D. King-Smith, and J. Andzelm, *Computational Materials Science* **28**, 250 (2003).

[180] D. G. Truhlar, B. C. Garrett, and S. J. Klippenstein, *Journal of Physical Chemistry* **100**, 12771 (1996).

[181] T. A. Halgren and W. N. Lipscomb, *Chemical Physics Letters* **49**, 225 (1977).

[182] C. Peng and H. B. Schlegel, *Israel Journal of Chemistry* **33**, 449 (1993).

[183] X. Zhu, K. C. Thompson, and T. J. Martínez, *The Journal of Chemical Physics* **150**, 164103 (2019).

[184] S. Grimme, *Journal of Chemical Theory and Computation* **15**, 2847 (2019).

[185] M. H. Rasmussen and J. H. Jensen, *PeerJ Physical Chemistry* **2**, e15 (2020).

[186] K. P. Eurenius, D. C. Chatfield, B. R. Brooks, and M. Hodoscek, *International Journal of Quantum Chemistry* **60**, 1189 (1996).

[187] K. E. Ranaghan and A. J. Mulholland, *International Reviews in Physical Chemistry* **29**, 65 (2010).

[188] F. Claeyssens, K. E. Ranaghan, F. R. Manby, J. N. Harvey, and A. J. Mulholland, *Chemical Communications* , 5068 (2005).

[189] L. Ridder, A. J. Mulholland, I. M. Rietjens, and J. Vervoort, *Journal of the American Chemical Society* **122**, 8728 (2000).

[190] D. R. Weiss and M. Levitt, *Journal of molecular biology* **385**, 665 (2009).

[191] S. Maeda, Y. Harabuchi, M. Takagi, T. Taketsugu, and K. Morokuma, *The Chemical Record* **16**, 2232 (2016).

[192] S. L. M., *Planning Algorithms*, Cambridge University Press, 2006.

[193] I. Arvanitakis, K. Giannousakis, and A. Tzes, *2016 IEEE Conference on Control Applications, CCA 2016* , 493 (2016).

[194] J. J. P. Stewart, *Journal of Computational Chemistry* **10**, 209 (1989).

Appendices

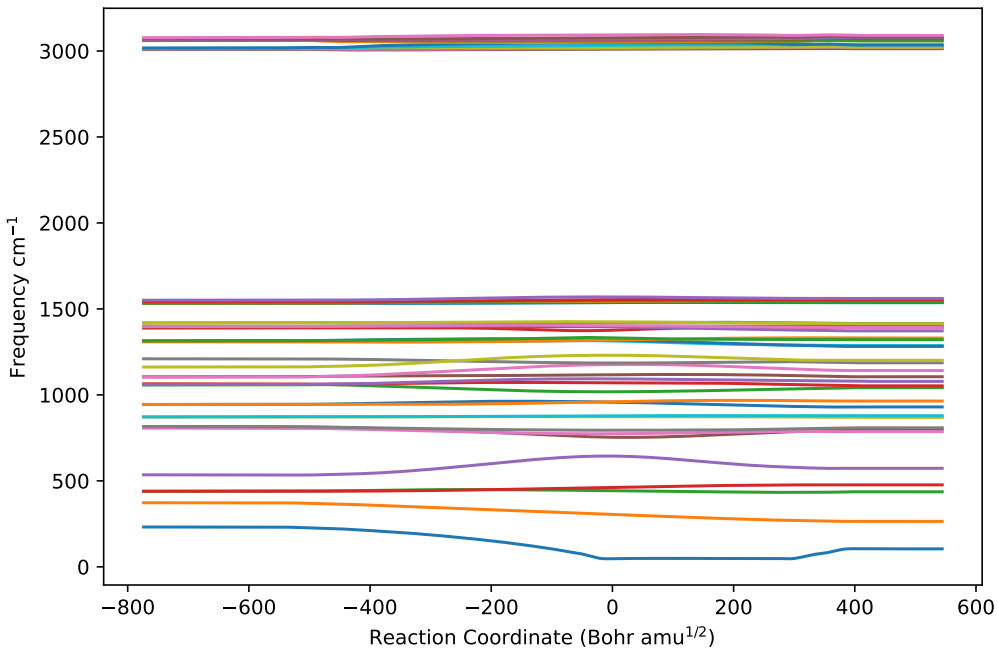

Figure 1: Calculated frequencies for reaction R1 as a function of reaction coordinate s using the standard calculation method with analytical Hessian matrices All calculations used 50 images for RPH construction.

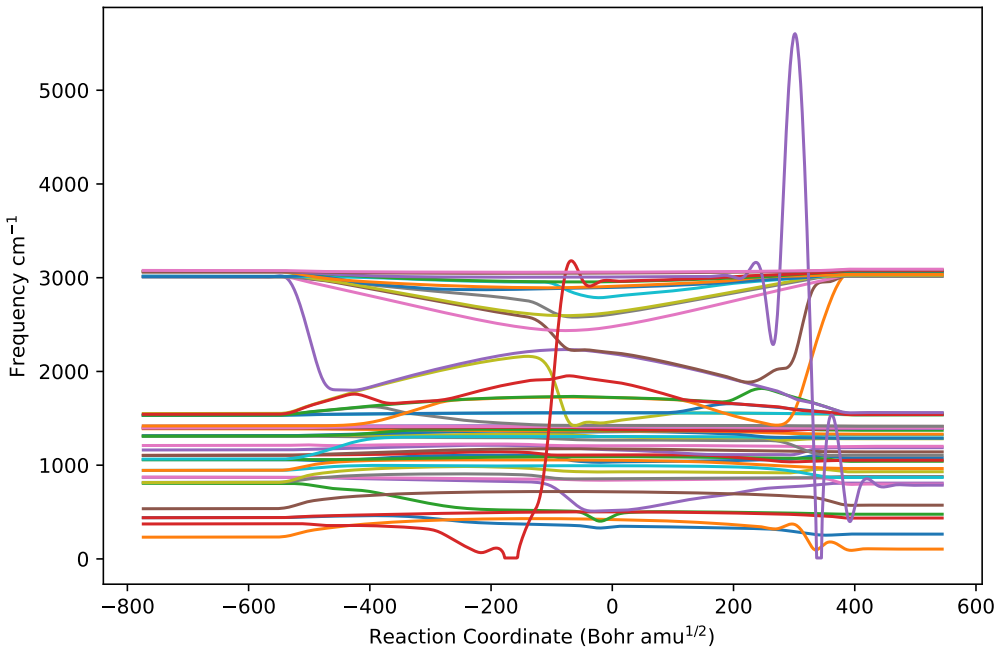

Figure 2: Calculated frequencies for reaction R1 as a function of reaction coordinate s using the SR1 method. All calculations used 50 images for RPH construction.

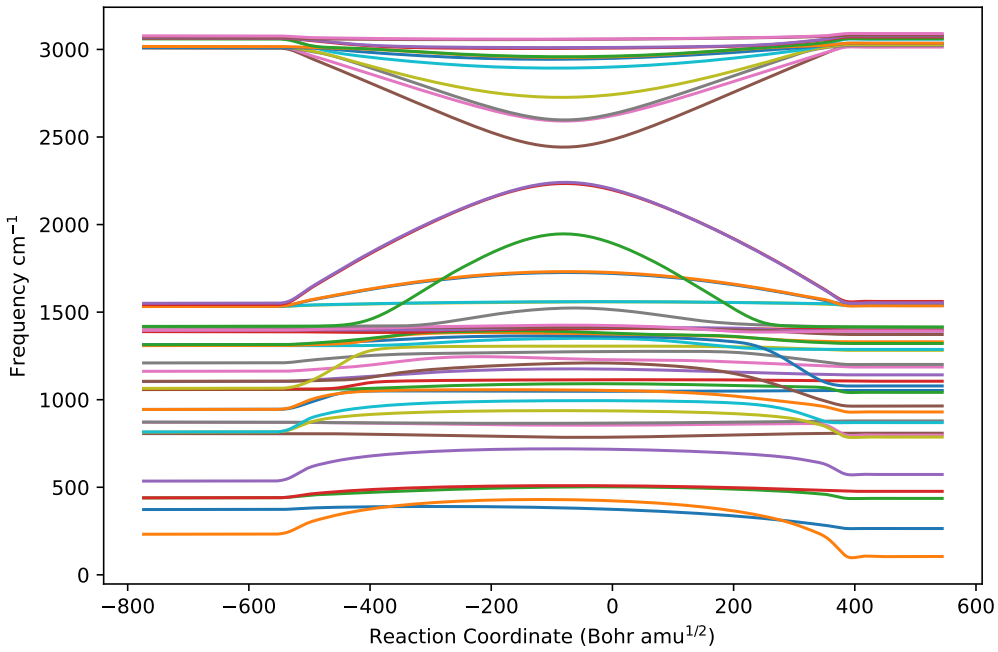

Figure 3: Calculated frequencies for reaction R1 as a function of reaction coordinate s using the PSB method. All calculations used 50 images for RPH construction.

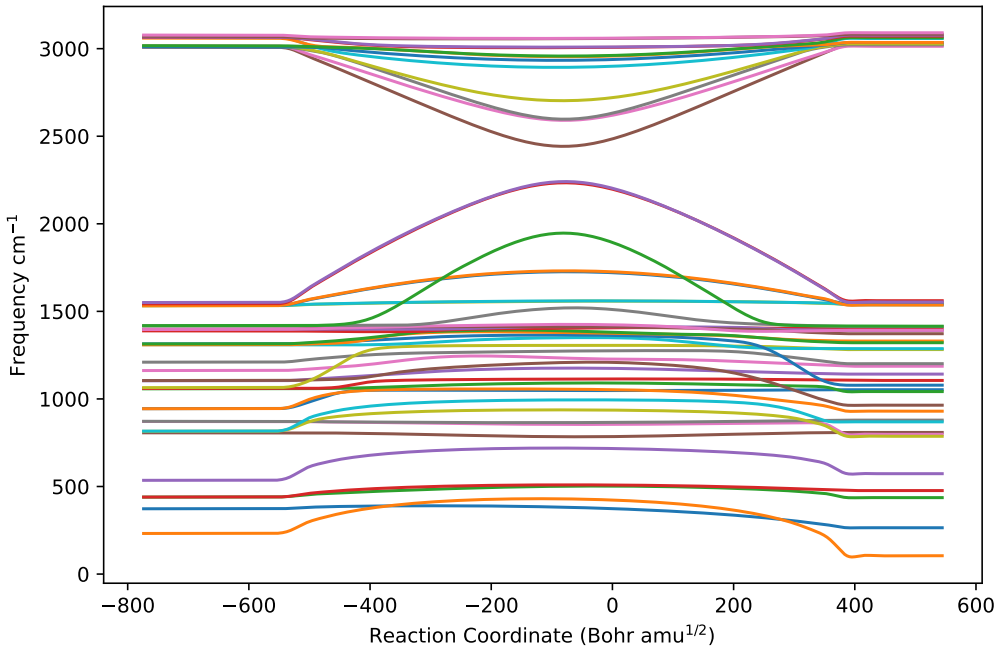

Figure 4: Calculated frequencies for reaction R1 as a function of reaction coordinate s using the Bofill method. All calculations used 50 images for RPH construction.

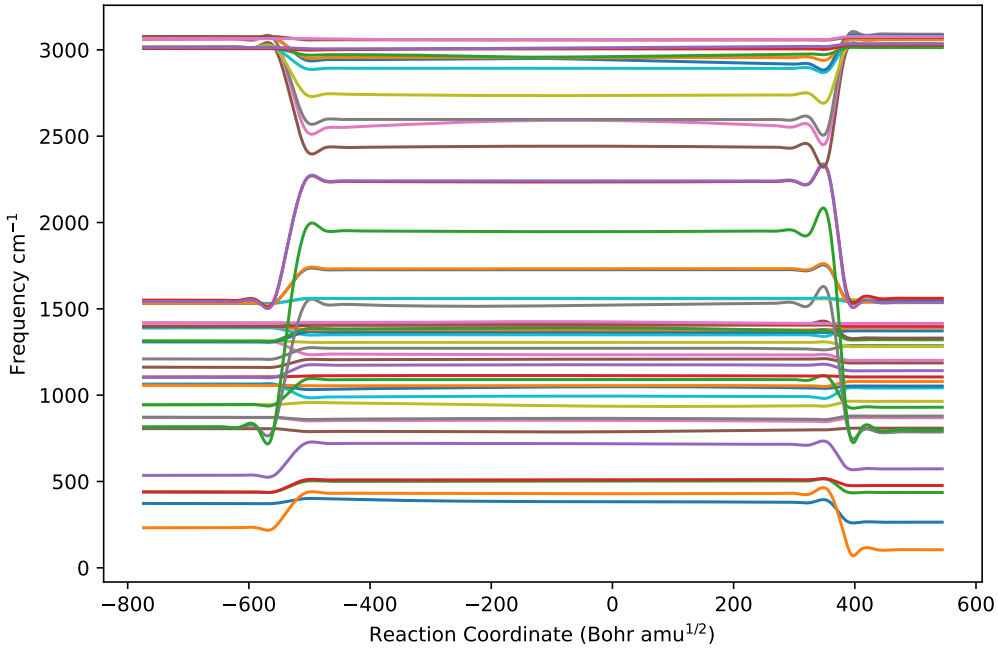

Figure 5: Calculated frequencies for reaction R1 as a function of reaction coordinate s using the TS-BFGS method. All calculations used 50 images for RPH construction.

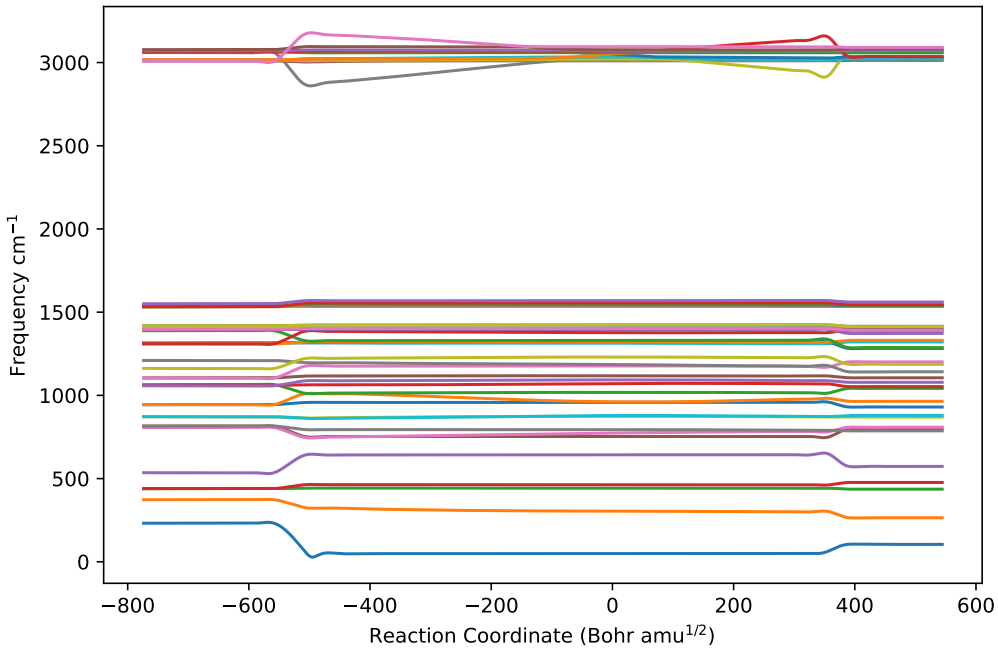

Figure 6: Figure S3: Calculated frequencies for reaction R1 as a function of reaction coordinate s using the Bofill method implemented using the "TSup" approach. All calculations used 50 images for RPH construction.

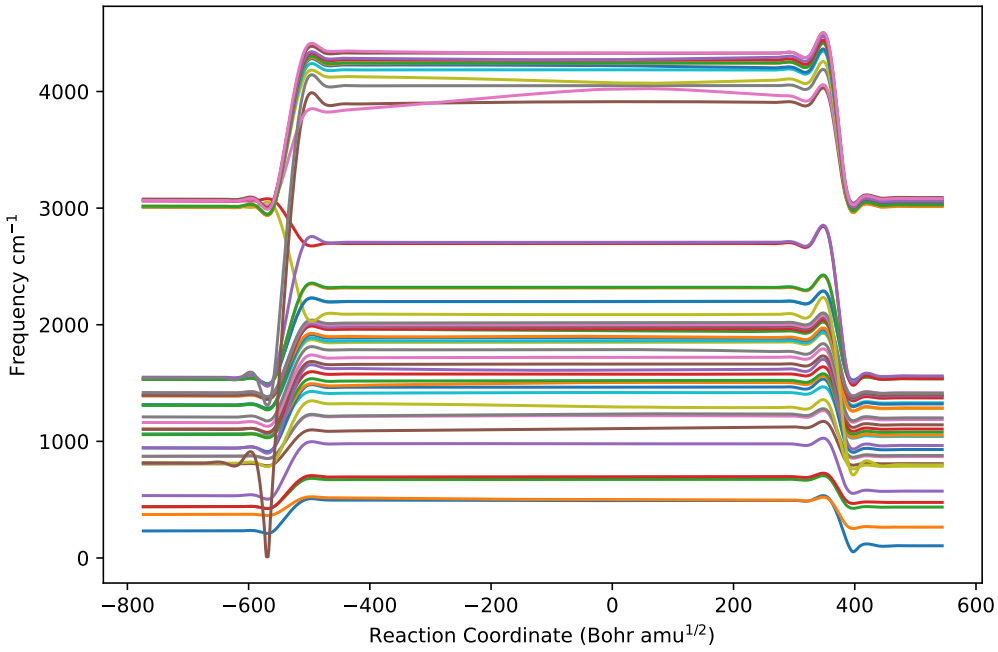

Figure 7: Calculated frequencies for reaction R1 as a function of reaction coordinate s using the Bofill method implemented using the "TSdown" approach. All calculations used 50 images for RPH construction.

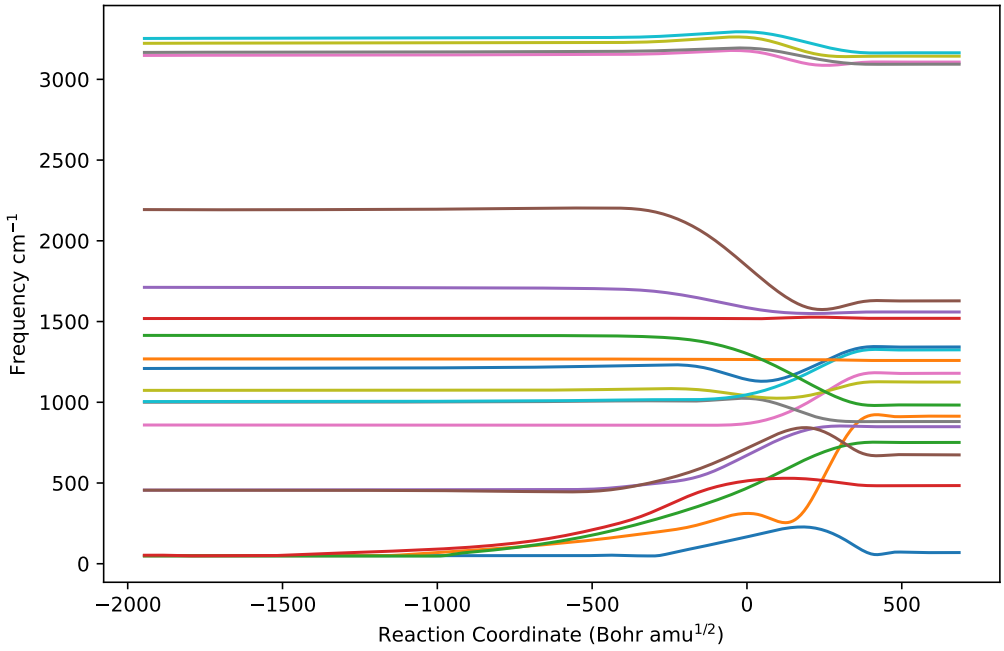

Figure 8: Calculated frequencies for reaction R2 as a function of reaction coordinate s using the standard calculation method with analytical Hessian matrices All calculations used 50 images for RPH construction.

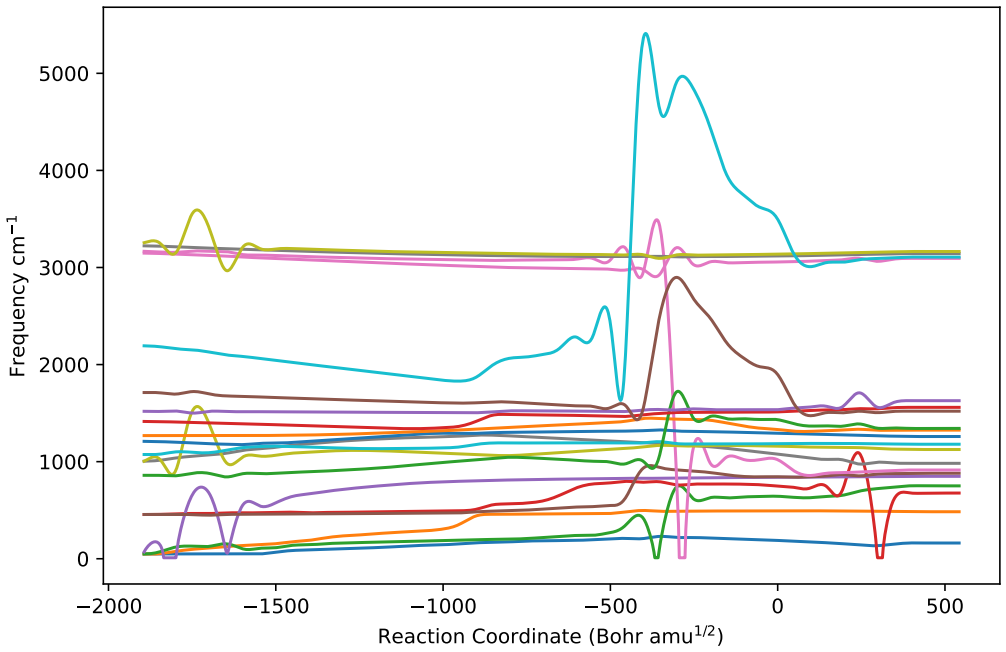

Figure 9: Calculated frequencies for reaction R2 as a function of reaction coordinate s using the SR1 method. All calculations used 50 images for RPH construction.

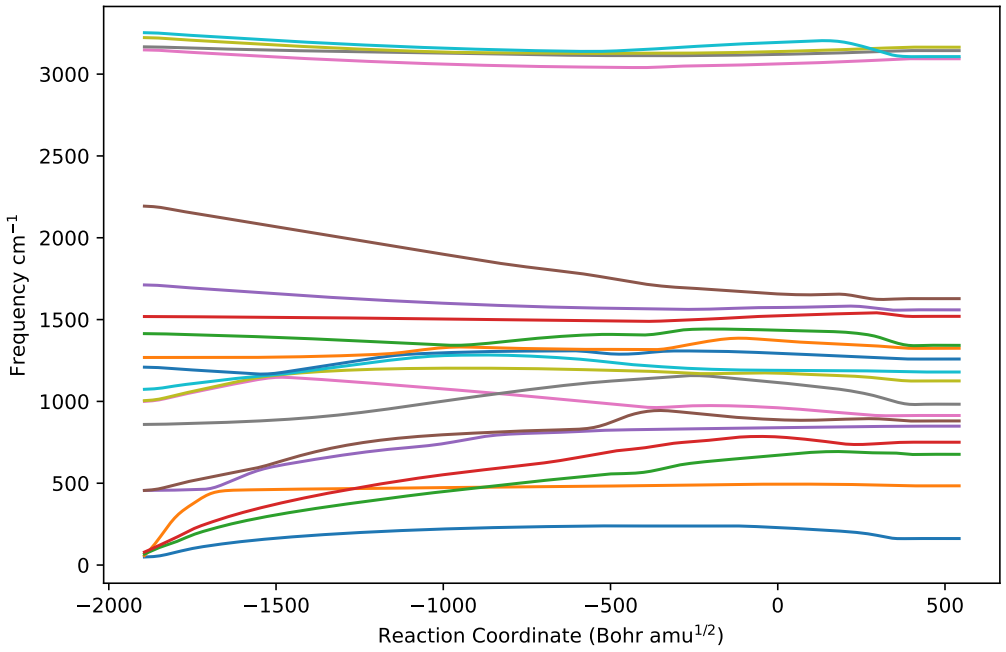

Figure 10: Calculated frequencies for reaction R2 as a function of reaction coordinate s using the PSB method. All calculations used 50 images for RPH construction.

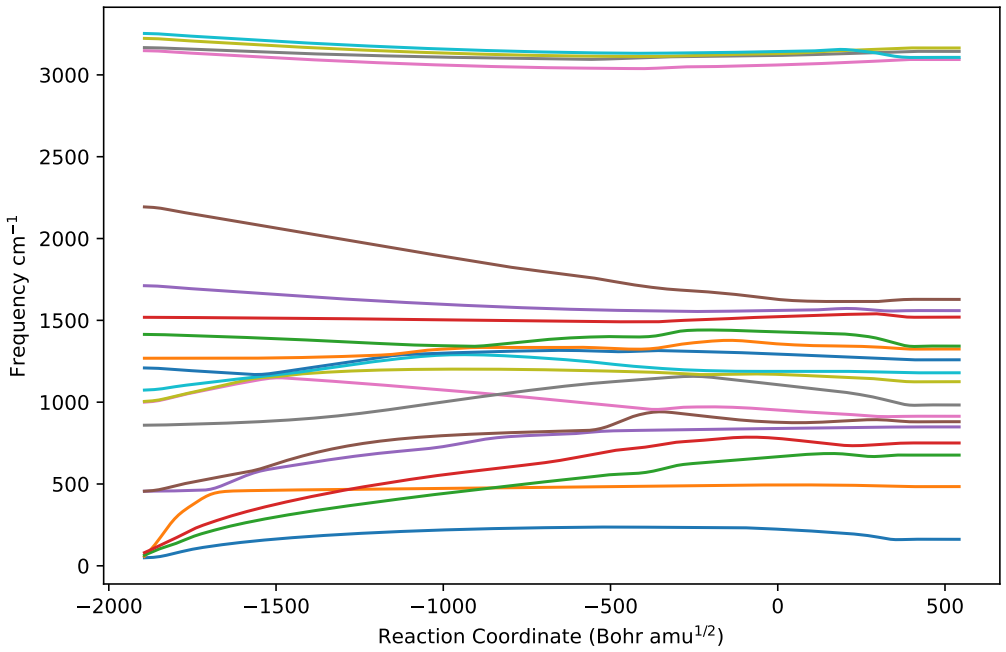

Figure 11: Calculated frequencies for reaction R2 as a function of reaction coordinate s using the Bofill method. All calculations used 50 images for RPH construction.

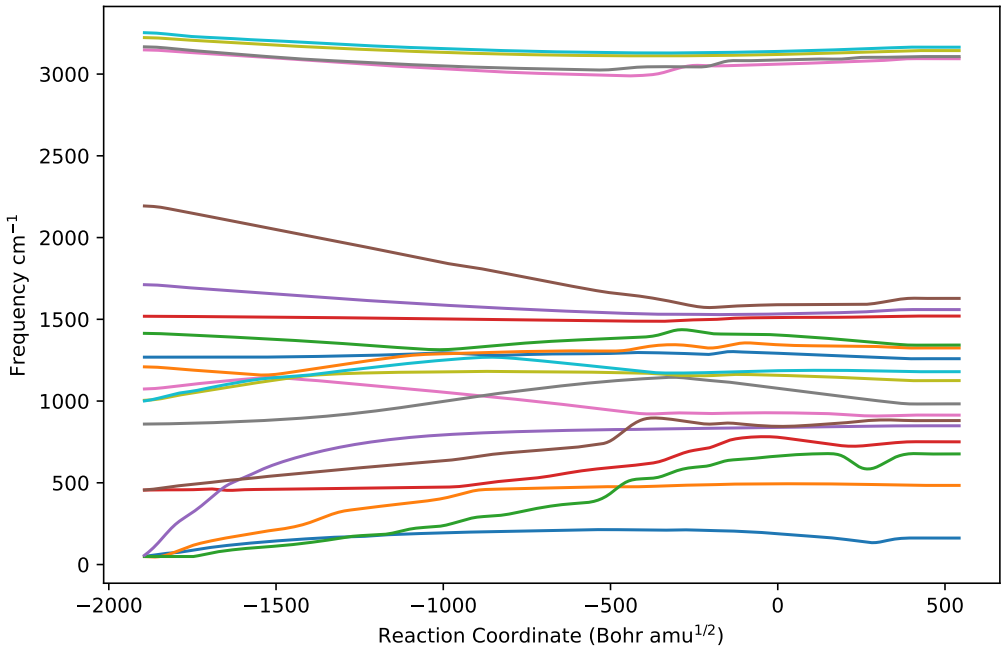

Figure 12: Calculated frequencies for reaction R2 as a function of reaction coordinate s using the TS-BFGS method. All calculations used 50 images for RPH construction.

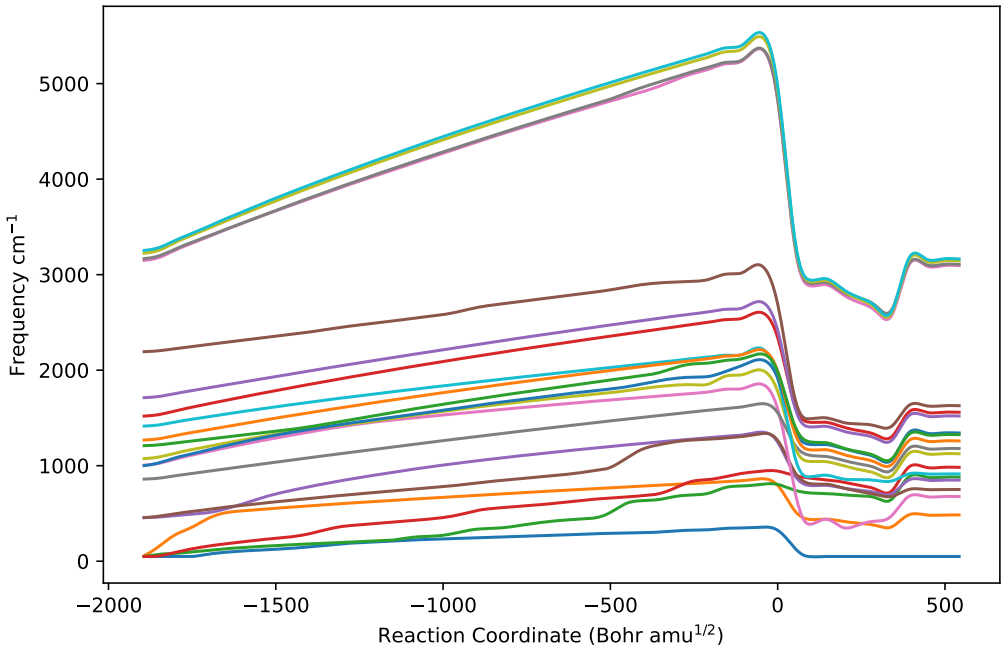

Figure 13: Calculated frequencies for reaction R2 as a function of reaction coordinate s using the TS-BFGS method implemented using the "TSup" approach. All calculations used 50 images for RPH construction.

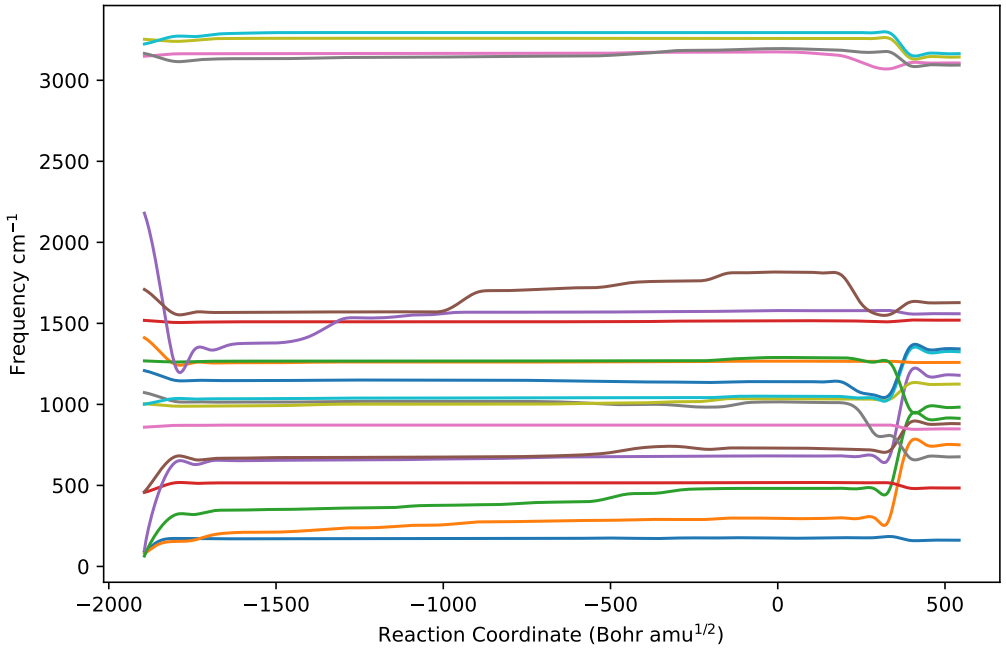

Figure 14: Calculated frequencies for reaction R2 as a function of reaction coordinate s using the TS-BFGS method implemented using the "TSdown" approach. All calculations used 50 images for RPH construction.

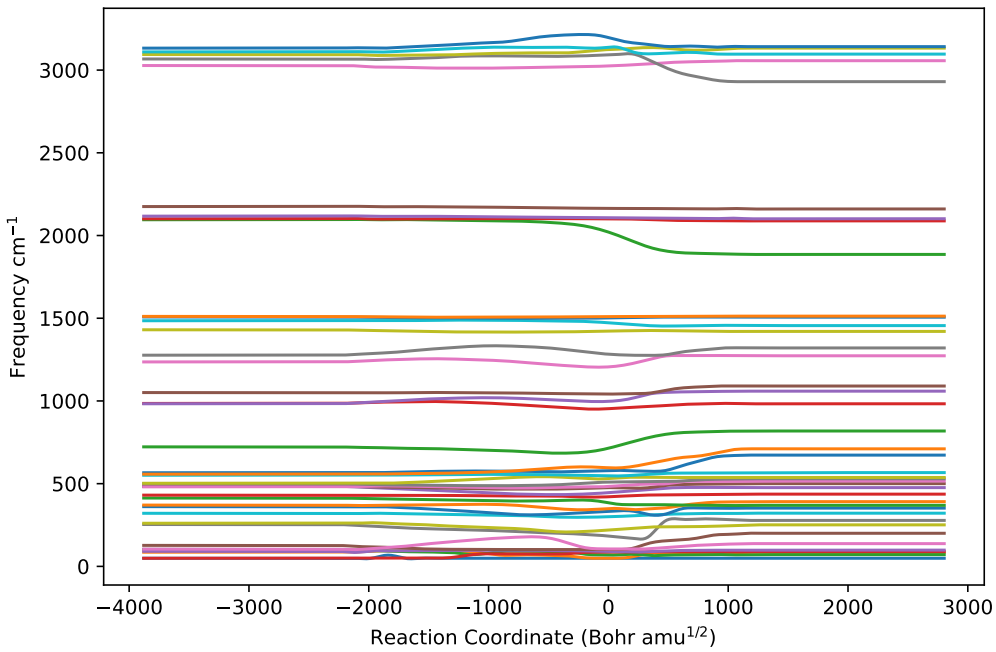

Figure 15: Calculated frequencies for reaction R3 as a function of reaction coordinate s using the standard calculation method with analytical Hessian matrices All calculations used 50 images for RPH construction.

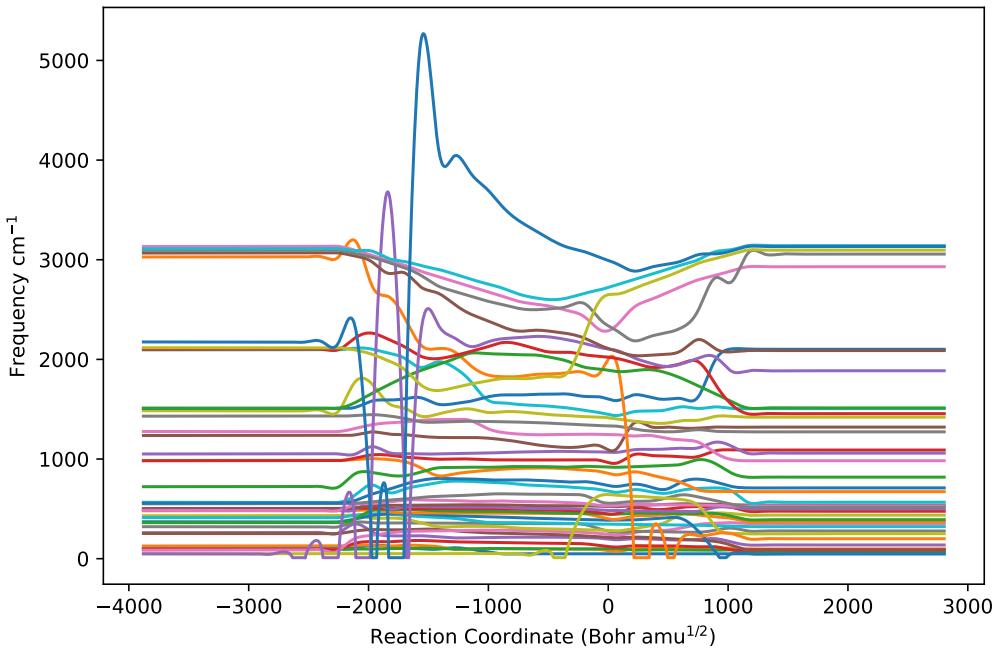

Figure 16: Calculated frequencies for reaction R3 as a function of reaction coordinate s using the SR1 method. All calculations used 50 images for RPH construction.

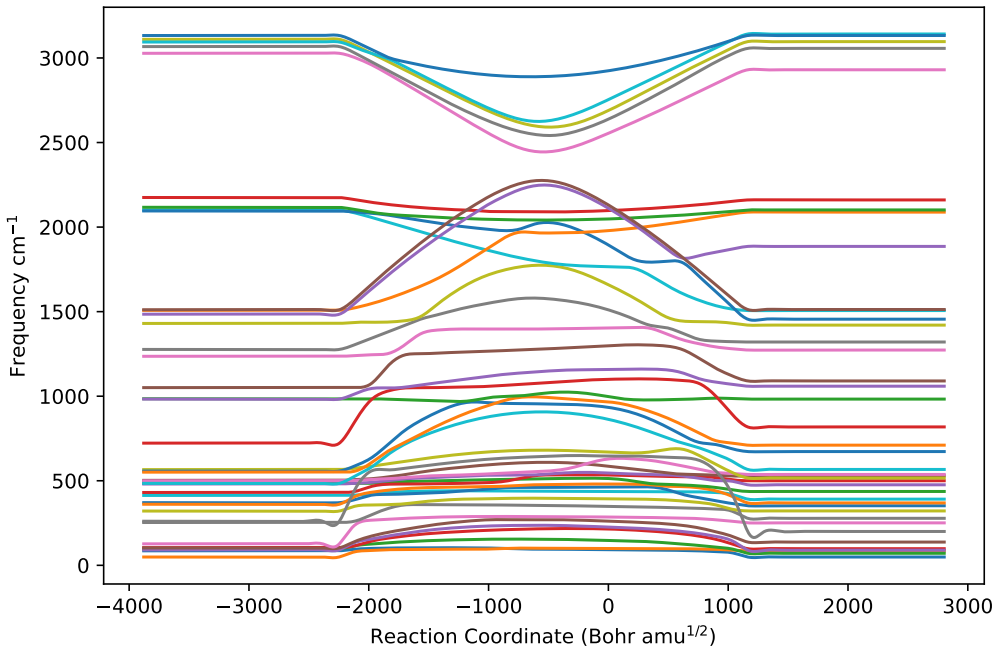

Figure 17: Calculated frequencies for reaction R3 as a function of reaction coordinate s using the PSB method. All calculations used 50 images for RPH construction.

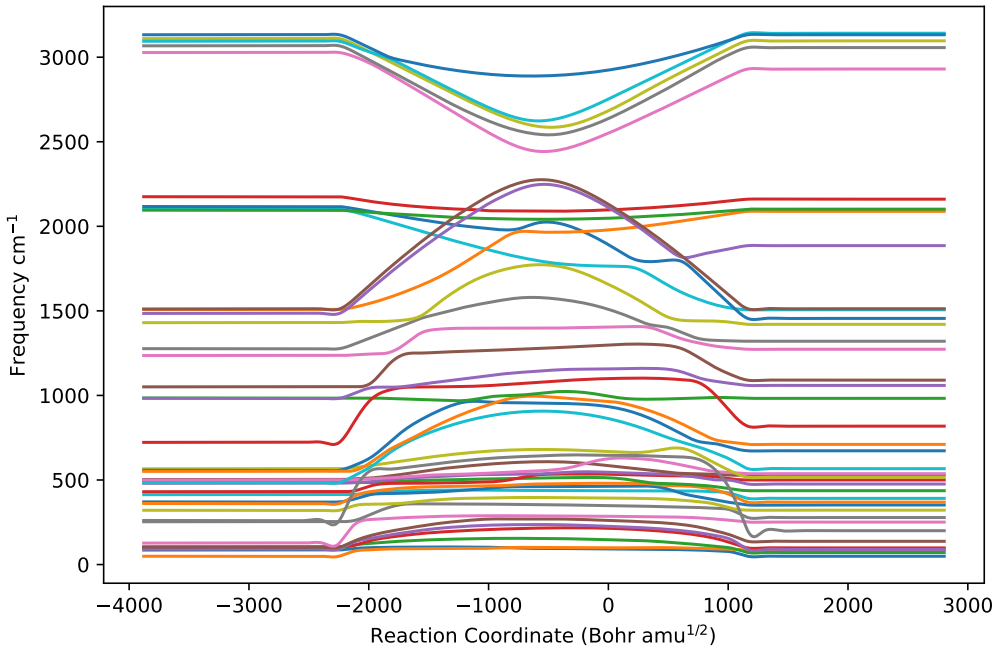

Figure 18: Calculated frequencies for reaction R3 as a function of reaction coordinate s using the Bofill method. All calculations used 50 images for RPH construction.

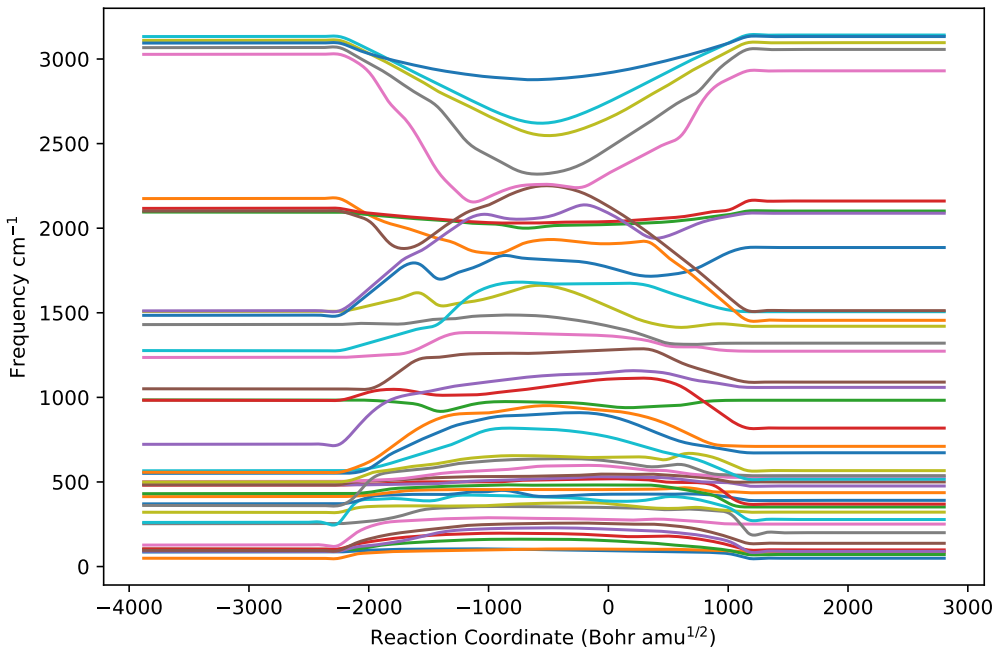

Figure 19: Calculated frequencies for reaction R3 as a function of reaction coordinate s using the TS-BFGS method. All calculations used 50 images for RPH construction.

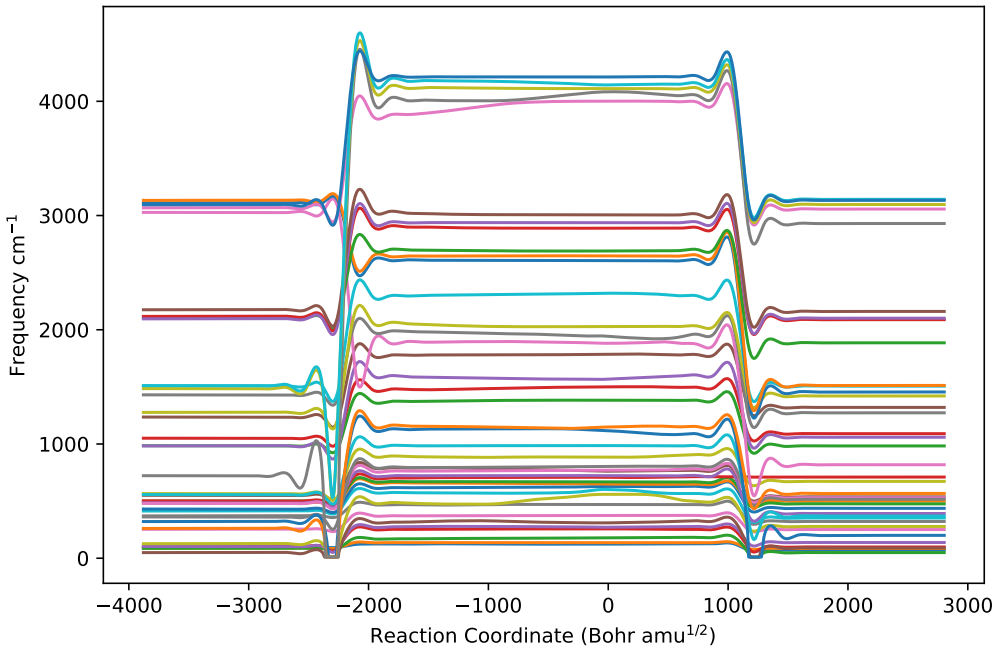

Figure 20: Calculated frequencies for reaction R3 as a function of reaction coordinate s using the PSB method implemented using the "TSup" approach. All calculations used 50 images for RPH construction.

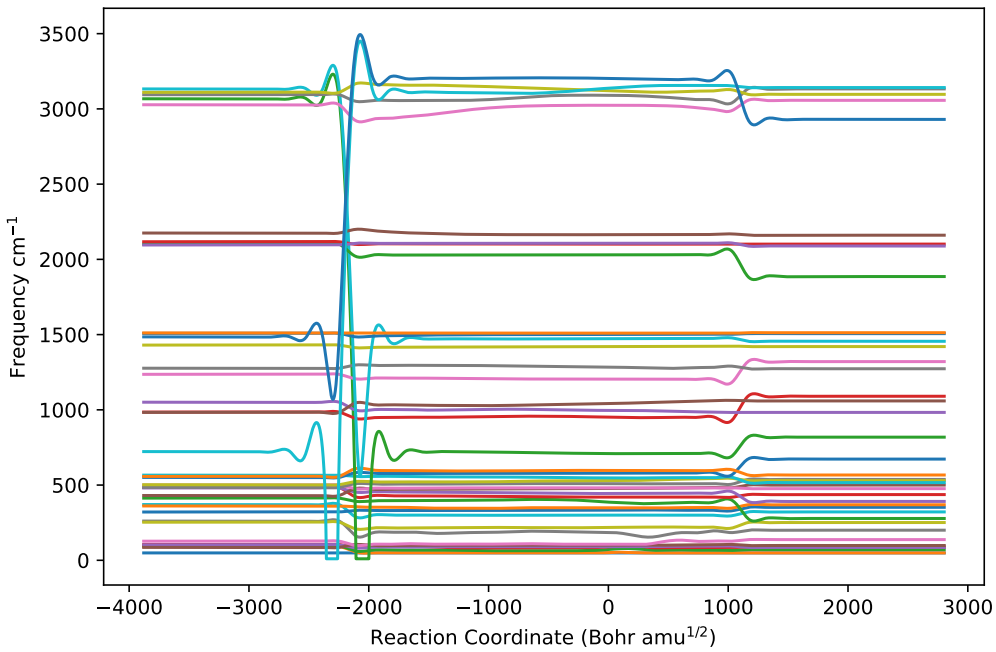

Figure 21: Calculated frequencies for reaction R3 as a function of reaction coordinate s using the PSB method implemented using the "TSdown" approach. All calculations used 50 images for RPH construction.

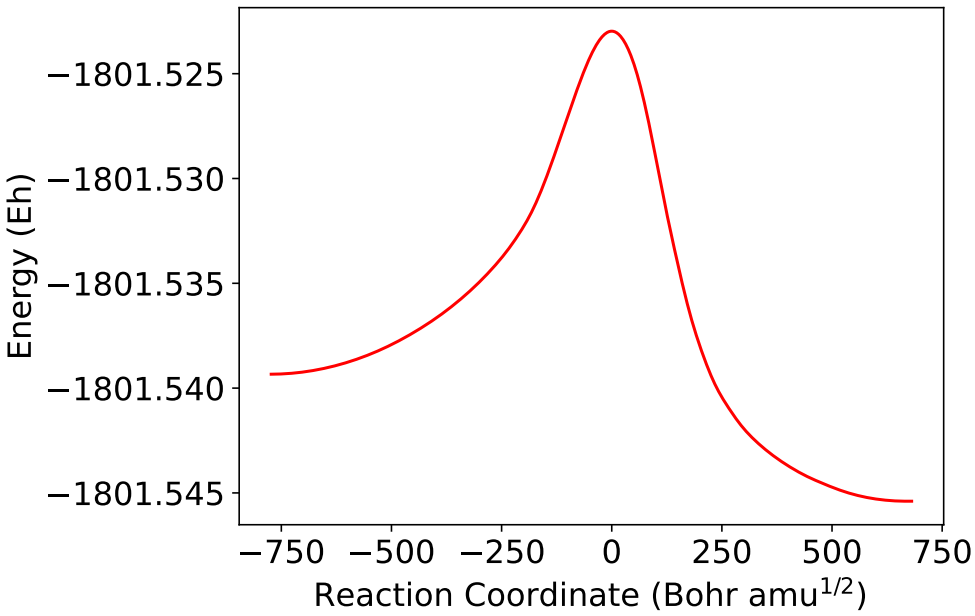

Figure 22: MEP for R1 in the reactions investigated for the Heck–Breslow mechanism for alkene hydroformylation using a cobalt catalyst in gas-phase.

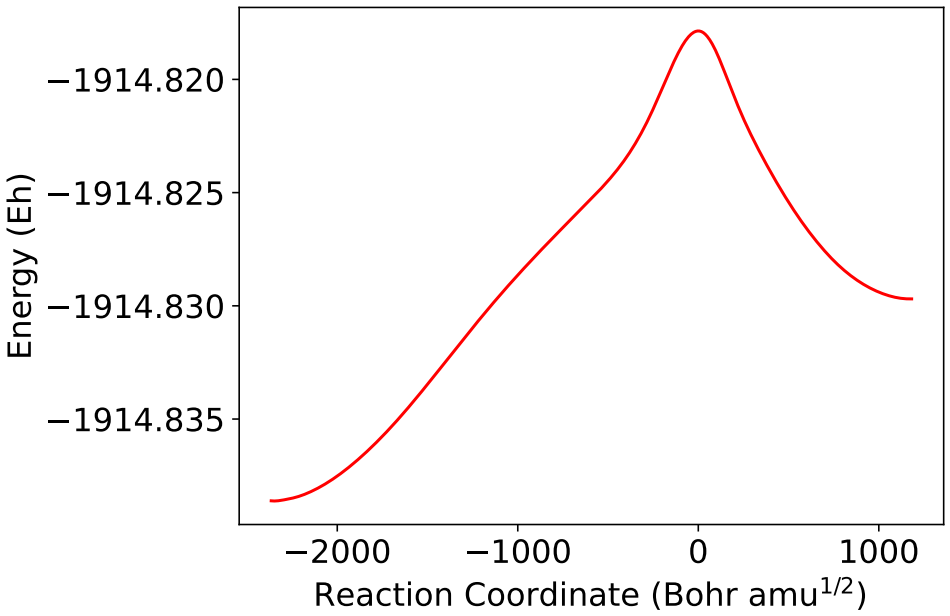

Figure 23: MEP for R2 in the reactions investigated for the Heck–Breslow mechanism for alkene hydroformylation using a cobalt catalyst in gas-phase.

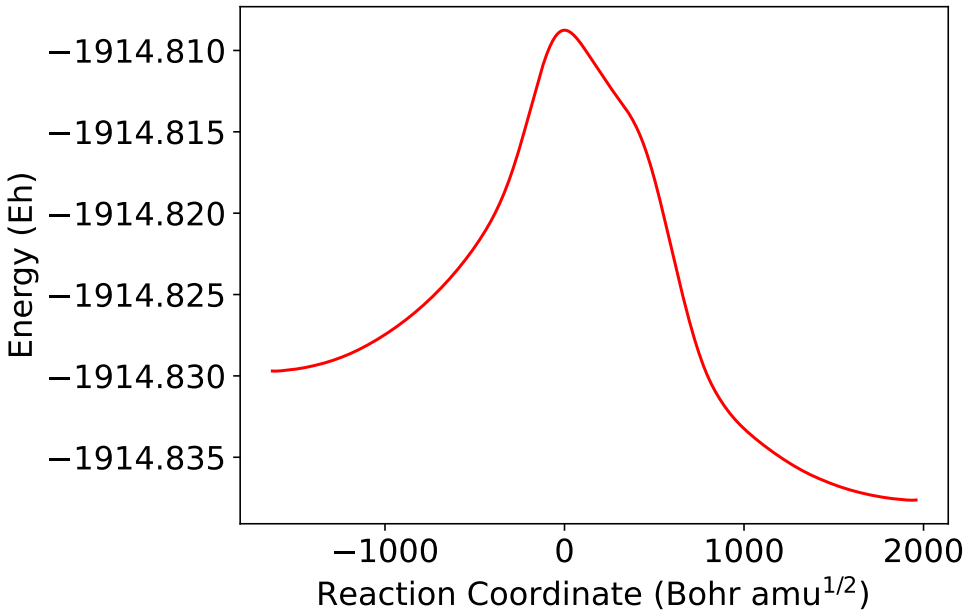

Figure 24: MEP for R3 in the reactions investigated for the Heck–Breslow mechanism for alkene hydroformylation using a cobalt catalyst in gas-phase.

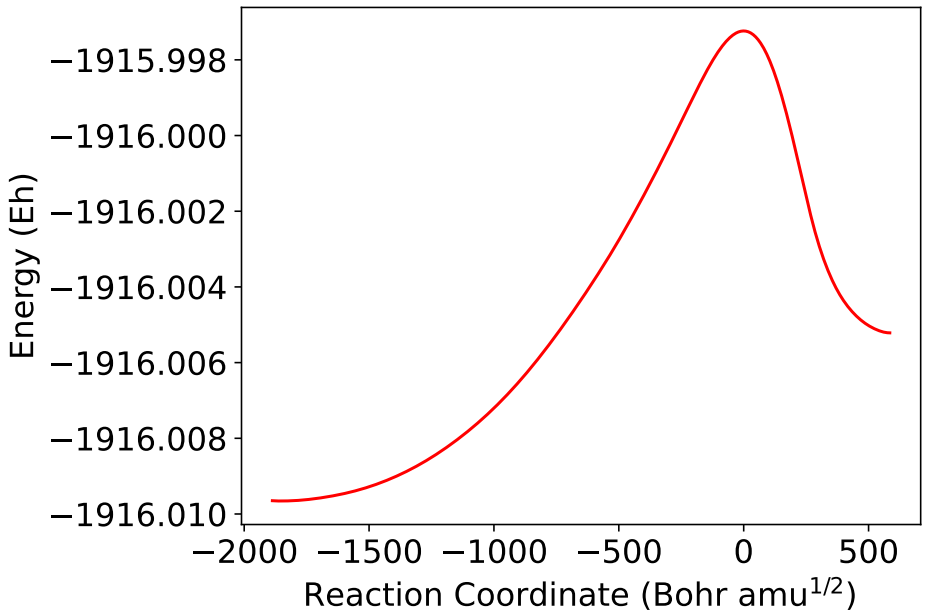

Figure 25: MEP for R4 in the reactions investigated for the Heck–Breslow mechanism for alkene hydroformylation using a cobalt catalyst in gas-phase.

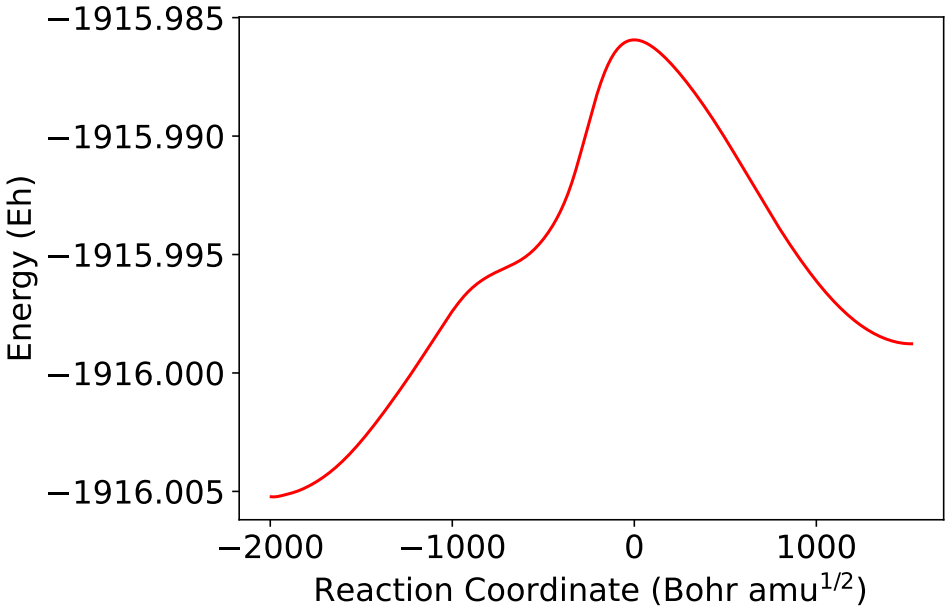

Figure 26: MEP for R5 in the reactions investigated for the Heck–Breslow mechanism for alkene hydroformylation using a cobalt catalyst in gas-phase.

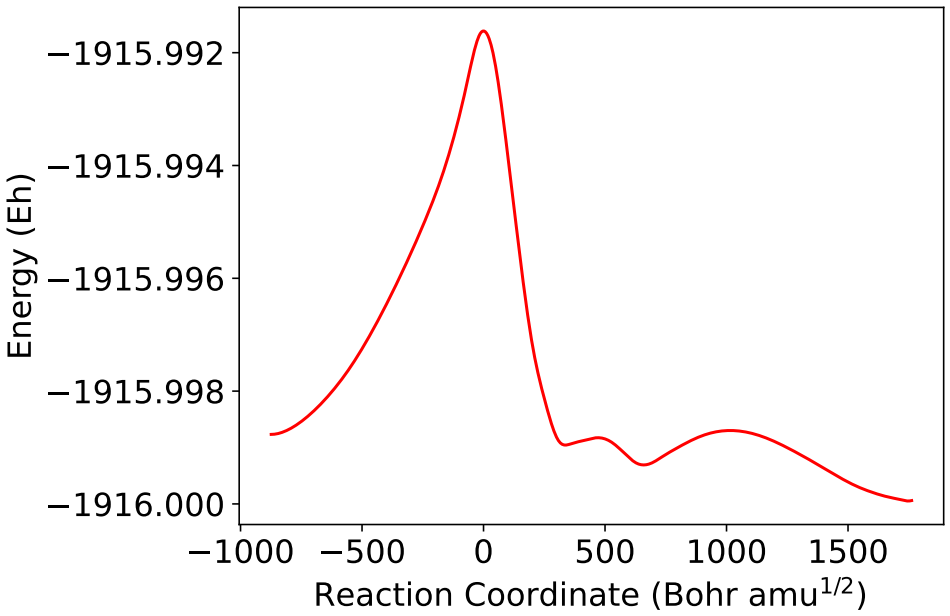

Figure 27: MEP for R6 in the reactions investigated for the Heck–Breslow mechanism for alkene hydroformylation using a cobalt catalyst in gas-phase.

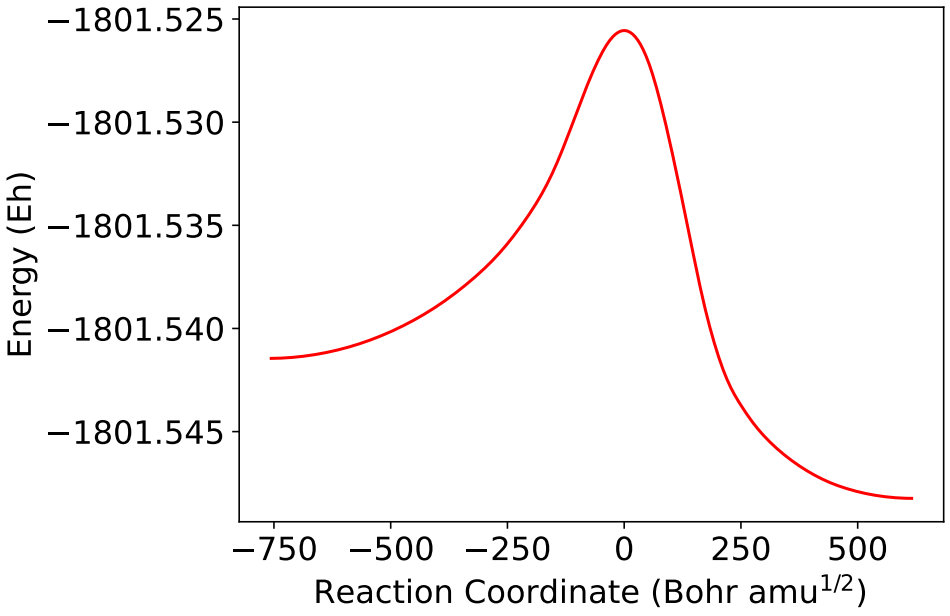

Figure 28: MEP for R1 in the reactions investigated for the Heck–Breslow mechanism for alkene hydroformylation using a cobalt catalyst in solvent-phase.

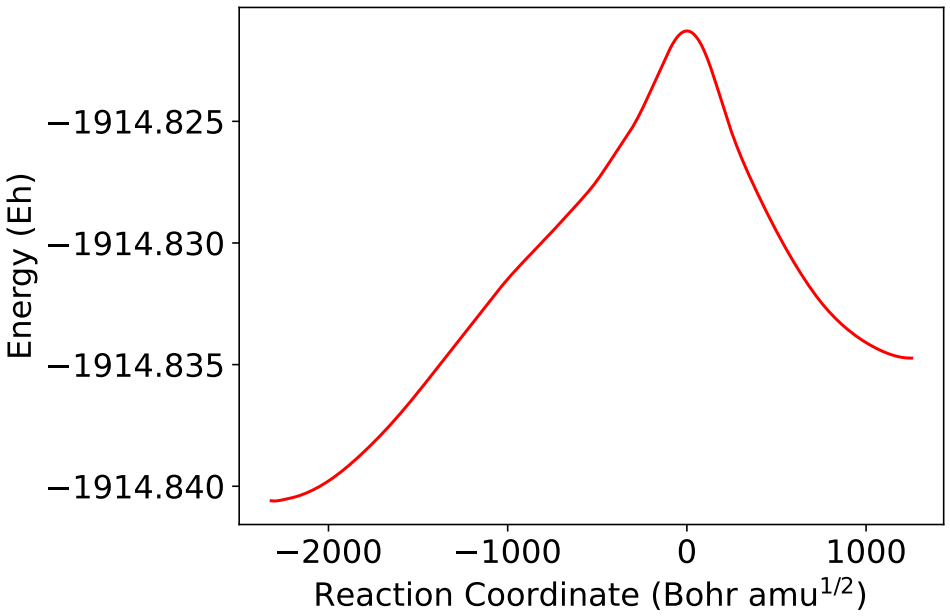

Figure 29: MEP for R2 in the reactions investigated for the Heck–Breslow mechanism for alkene hydroformylation using a cobalt catalyst in solvent-phase.

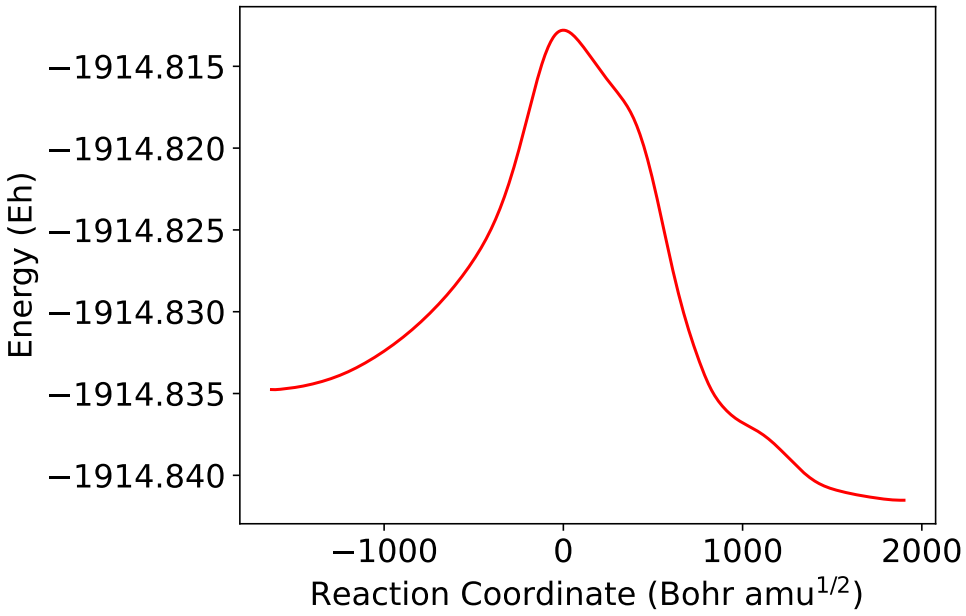

Figure 30: MEP for R3 in the reactions investigated for the Heck–Breslow mechanism for alkene hydroformylation using a cobalt catalyst in solvent-phase.

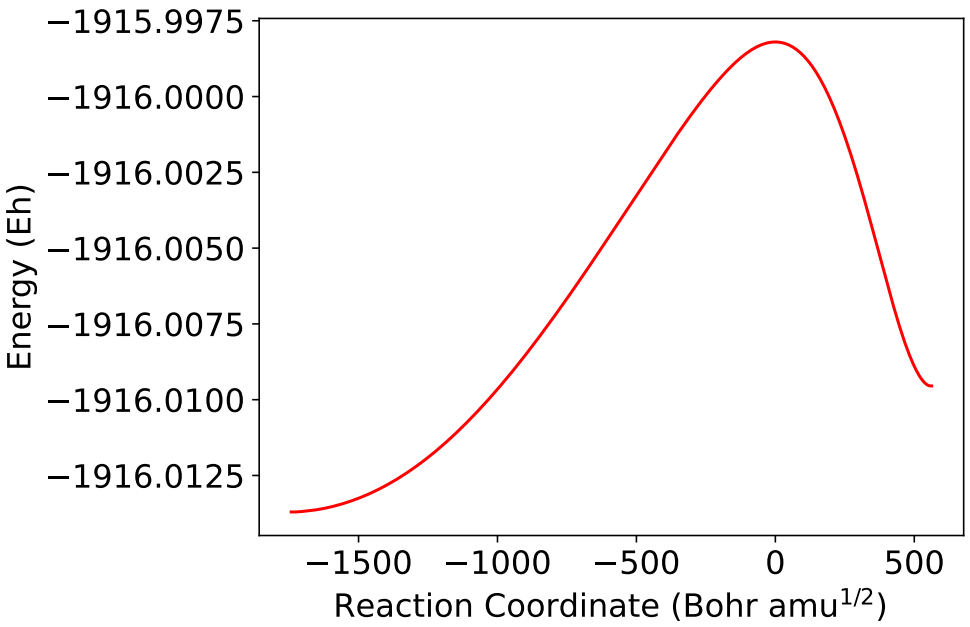

Figure 31: MEP for R4 in the reactions investigated for the Heck–Breslow mechanism for alkene hydroformylation using a cobalt catalyst in solvent-phase.

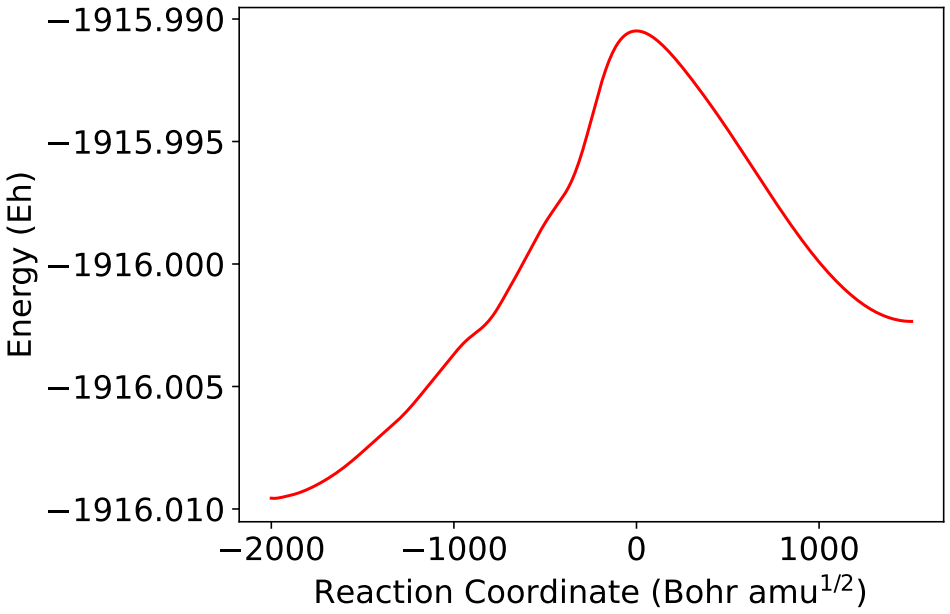

Figure 32: MEP for R5 in the reactions investigated for the Heck–Breslow mechanism for alkene hydroformylation using a cobalt catalyst in solvent-phase.

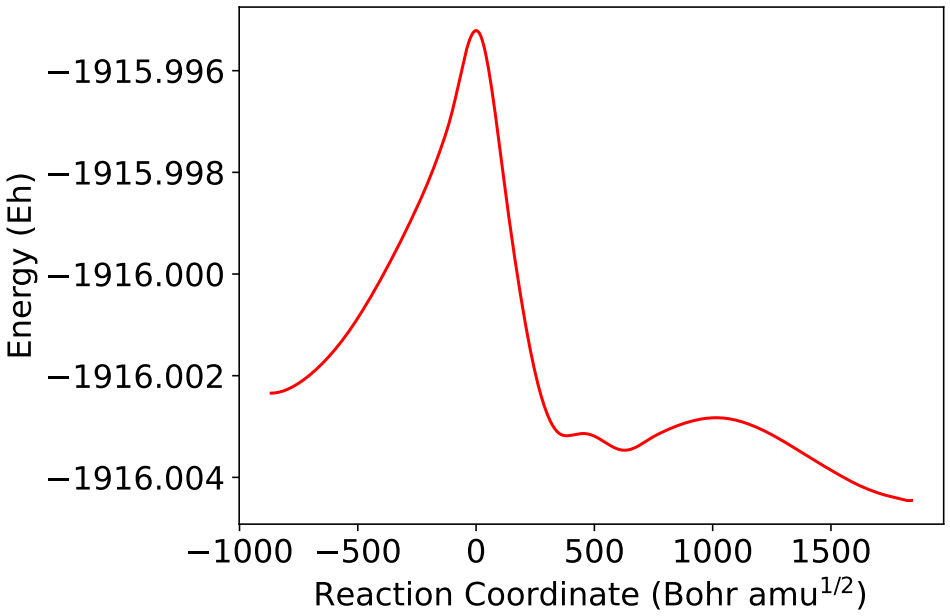

Figure 33: MEP for R6 in the reactions investigated for the Heck–Breslow mechanism for alkene hydroformylation using a cobalt catalyst in solvent-phase.